Atomic Force Microscopy Studies of Protein Interactions With Lipid Membranes

by

George Richard Heath

Submitted in accordance with the requirements for the degree of
Doctor of Philosophy

The University of Leeds
School of Physics & Astronomy

Sep 2014

The candidate confirms that the work submitted is his own, except where work which has formed part of jointly-authored publications has been included. The contribution of the candidate and the other authors to this work has been explicitly indicated below. The candidate confirms that appropriate credit has been given within the thesis where reference has been made to the work of others.

Chapter 4 is based on work accepted for publication within;

Heath, G. R., Roth, J., Connell, S. D., & Evans, S. D. (2014). Diffusion in Low Dimensional Lipid Membranes. *Nano letters*. (Articles ASAP (Web): August 28, 2014)

In this publication G.R. Heath was responsible for acquisition and analysis of data and wrote the first drafts of the manuscript. J. Roth performed simulations. S.D. Evans and S.D. Connell are the academic supervisors of G.R. Heath.

Chapter 5 is based on and work published within;

Connell, S. D., Heath, G., Olmsted, P. D., & Kisil, A. (2013). Critical point fluctuations in supported lipid membranes. Faraday Discuss. 161, 91-111.

In this publication G.R. Heath was responsible for acquisition and analysis of the majority of data and co-wrote the first drafts of the manuscript with S.D. Connell. A Kisil captured the AFM images in Figure 10 (not included in this thesis). P.D. Olmsted provided assistance with theoretical understanding of the experimental results. S. D. Connell supervised the work and presented the paper the Faraday Discussions meeting.

Chapter 5 is also based on work in preparation for submission to Physical Review Letters;

Heath, G. R., Evans, S. D. & Connell, S. D. (2014). Nanoscale Dynamics of Model Lipid Raft Systems Revealed by High-Speed AFM.

In this publication G.R. Heath was responsible for acquisition and analysis of data and wrote the first draft of the manuscript. S.D. Evans and S.D. Connell are the academic supervisors of G.R. Heath.

Chapter 6 is based around a manuscript in preparation for Langmuir;

Heath, G. R., Johnson, B. R., Connell, S. D., & Evans, S. D. (2014) Localization of the Actin Binding Transmembrane Protein Ponticulin in Phase Separated Model Membranes.

In this publication G.R. Heath was responsible for acquisition and analysis of data and wrote the first draft of the manuscript. Benjamin RG Johnson purified ponticulin, provided advise with actin handling and assisted with actin purification. S.D. Evans and S.D. Connell are the academic supervisors of G.R. Heath.

Chapter 7 is based on work published within;

Heath, G. R., Johnson, B. R., Olmsted, P. D., Connell, S. D., & Evans, S. D. (2013). Actin Assembly at Model-Supported Lipid Bilayers. Biophysical Journal, 105(10), 2355-2365.

In this publication G.R. Heath was responsible for acquisition and analysis of data and wrote the first drafts of the manuscript. Benjamin RG Johnson provided advise with actin handling and assisted with actin purification. P.D. Olmsted provided assistance with theoretical modelling of experimental results. S.D. Evans and S.D. Connell are the academic supervisors of G.R. Heath.

Chapter 8 is based on work published within;

Heath, G. R., Abou-Saleh, R. H., Peyman, S. A., Johnson, B. R., Connell, S. D., & Evans, S. D. (2014). Self-assembly of actin scaffolds on lipid microbubbles. Soft Matter, 10(5), 694-700.

In this publication, G.R. Heath was responsible for acquisition and analysis of data and wrote the first draft of the manuscripts. R.H. Abou-Saleh and S.A Peyman are independent research fellows who assisted the candidate in microbubble fabrication and characterisation. S.D. Evans and S.D. Connell are the academic supervisors of G.R. Heath.

Acknowledgements

Firstly I would like to thank my supervisors Professor Stephen Evans and Dr Simon Connell whose expertise, knowledge, inspiration and guidance has been invaluable. I appreciate the encouragement to work on many exciting and challenging projects as well as the independence given to me to follow my own scientific interests. I am also grateful for the encouragement and persuasion to speak at and present my work at conferences and meetings wherever possible, allowing me to overcome my fears of public speaking.

Thank you also to members of the Molecular and Nanoscale Physics group - especially Peng Bao, Johannes Roth, Radwa Abou-Saleh and Matthew Cheetham for their technical expertise and support. Thanks to Benjamin Johnson for his help and advice in the lab, with actin systems and protein purification in general. I would also like to thank Professor Peter Olmsted for help with theoretical modeling and understanding.

I would like to give special thanks to my girlfriend, Riva for her endless support, patience and words of encouragement, celebrating the good times whilst keeping my head up through the hard times. Thank you must also go to my son, Samuel for keeping me sane throughout the last 4 years and my Dad for inspiring my interest in science since before I can remember and for encouraging me to study physics instead of mathematics.

Abstract

The behaviour of biological components in cellular membranes is vital to the function of cells however many vital phenomena associated with membrane functions are not yet fully understood. Supported lipid bilayers provide a model of real cellular membranes. This thesis examines how increasing the complexity of model lipid bilayers through changes in lipid composition, membrane protein content and cytoskeletal interactions can be used to extract significant biological information with biophysical techniques and analysis. The atomic force microscope (AFM) is a powerful tool in the study of biological systems allowing both three dimensional sub-nanometer resolution and mechanical interrogation under physiological conditions. The recent arrival of high-speed atomic force microscopy has transformed the information and processes which can be obtained, enabling direct imaging of biomolecular processes in real time.

The work in this thesis shows that the AFM cannot only be used to investigate membranes but also deposit them *in situ* at lateral scales comparable to their height. Studies of confining lipid and protein diffusion in these quasi-one dimensional systems shows confinement reduces mobility of lipid with important implications on the behaviour of pores and defects cellular membranes. Studies of lipid phase behaviour of compositions thought be simplified models of the cell membrane lipid content show evidence that the small “raft” domains detected in real cells are not stable equilibrium phase separated domains, but non-equilibrium compositional fluctuations. Actin polymerisation induced at positively charged bilayers in non-polymerising conditions provides new insight into polymerisation processes whilst also describing a simple novel method to create “synthetic” robust actin-membrane scaffolds with controllable coverage. This polymerisation process was then applied to coating of lipid microbubbles for combined ultrasound imaging and drug delivery applications. The addition of the actin coating increased bubbles lifetimes, stability, elasticity and stiffness whilst allowing the attachment of model drug carriers.

Table of Contents

List of Tables

List of Figures

Abbreviations

ADP	Adenosine Diphosphate
ATP	Adenosine Triphosphate
AFM	Atomic Force Microscopy
BSA	Bovine serum albumin
FRAP	Fluorescence Recovery After Photobleaching
FRET	Förster resonance energy transfer
GUV	Giant Uni-lamellar Vesicle
GPI	GlycoPhosphatidylInositol
GDP	Guanosine Diphosphate
GTP	Guanosine Triphosphate
HS-AFM	High Speed Atomic Force Microscopy
MLV	Multi-Lamellar Vesicle
NMR	Nuclear magnetic resonance
PC	PhosphatidylCholine
PE	PhosphatidylEthanolamine
PS	PhosphatidylSerine
PDMS	Polydimethylsiloxane
QCM-D	Quartz Crystal Microbalance with Dissipation
SAM	Self-Assembled Monolayer
SUV	Small Uni-lamellar Vesicle
SLB	Supported Lipid Bilayer
SPR	Surface Plasmon Resonance
TEM	Transmission electron microscopy
VdW	Van der Waals

Chapter 1
Introduction

1.1 Introduction

Containing thousands of different lipids, proteins and other molecules, bio-membranes provide cells with a highly sophisticated dynamic, semi-permeable barrier that controls the flow of nutrients, the creation of electrical and chemical potentials and communication. As this is such an important structure, it is not surprising that the majority of drugs specifically target either the membrane or proteins within it. Similarly, disorders in the membrane and its supporting actin cytoskeleton can lead to numerous diseases from Alzheimer's to Cystic Fibrosis to Muscular Dystrophy. This thesis is focused on using atomic force microscopy (AFM) to create, study and model the underlying physics of simplified cell-membranes, including lipid phase behaviour, mechanisms of protein interaction and engineering drug delivery systems.

1.2 The Cell

Originating from the Latin *cella,* meaning "small room", cells are the smallest entity that can be described as living (excluding viruses). Often referred to as the building blocks of life, there are two main types of cell: prokaryotic and eukaryotic. The prokaryotic cell is the simpler of the two, with no nucleus or any other organelles. It only has a cytosol where most of the cell's biochemistry takes place, and a lipid membrane to separate this from the exterior. Prokaryotic cells are divided into two main classification domains: archaea and bacteria. The prokaryotic bacteria contain some distinct similarities to some of the key components of the eukaryotic cell including analogue cytoskeletal proteins. Eukaryotic cells are more complex, organised into much more complicated structures by internal lipid membranes which form functional apparatus including the nucleus, mitochondria, chloroplasts and Golgi (organelles) (Figure 1.1). The lipid

membranes in these systems are incredibly important for both compartmentalisation and signaling. Partitioning both the cell from the extra cellular environment and organelles from intra cellular environments, these semi-permeable boundaries allow for varying conditions, such as pH, ionic concentrations and protein concentrations, as well as separating moieties which could affect the regular functioning of the cell. The lipid bilayer's barrier properties not only isolate cellular environments but facilitate signaling, passage of materials and creation of ion gradients, vital to many processes and functions of the cell. To selectively regulate this transport, the plasma membrane is decorated with a vast assortment of membrane proteins, glycolipids and other components, which allow information, ions, nutrients, waste and cell products to be passed across the membrane in a number of ways.

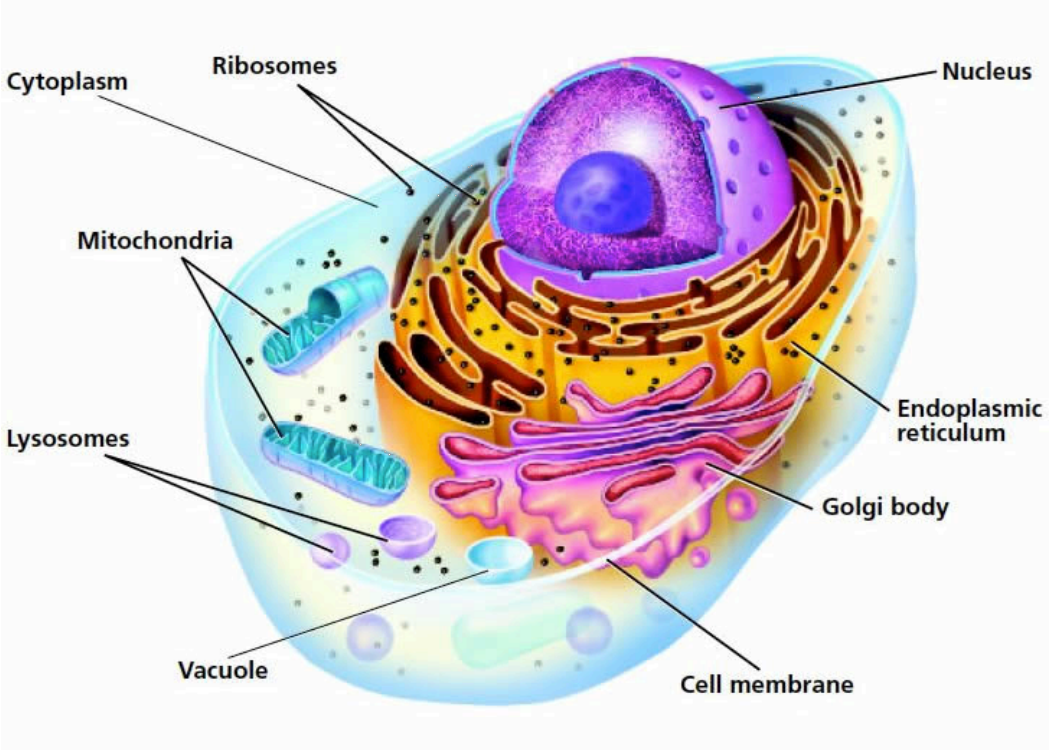

Figure 1.1: Schematic of the animal cell highlighting the membrane strutures found throughout, from the surrounding cell membrane to the many organelles and nucleus found within. Image from (http://www.stephsnature.com/lifescience/cellnotes.html).

1.3 Lipid Bilayers

Composed of two leaflets of oppositely facing lipid molecules, biological membranes, while at first appearing simple, are one of the most complex and important structures in the cell. The cellular membrane has thousands of different lipid molecules, almost as many different proteins, a dynamic supporting cytoskeleton on one side and an extra cellular matrix on the other (Figure 1.2). All these components work together to facilitate a huge number of processes centred around compartmentalising processes, allowing directed transport of matter, signalling and protein organisation.

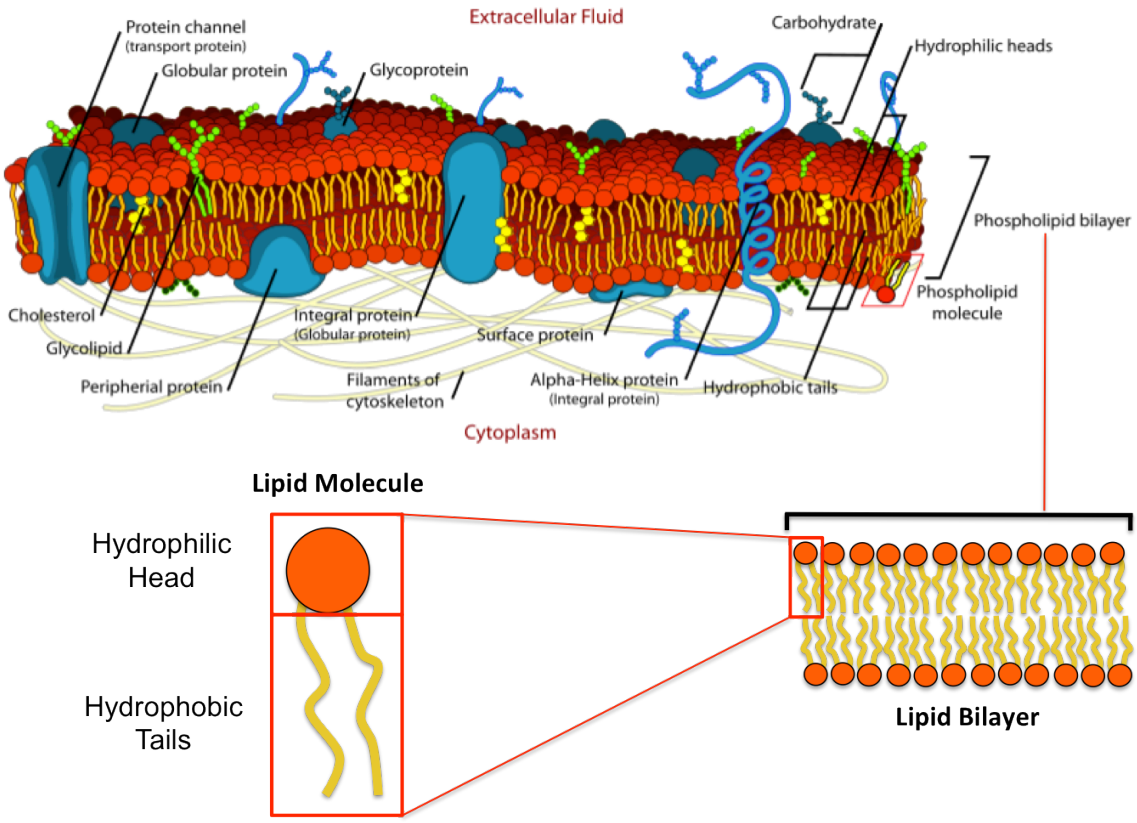

Figure 1.2: Schematic illustration showing the cellular membrane with lipids, various types of membrane proteins and an actin cytoskeleton. Additional illustrations show separated structures of a basic lipid bilayer and a single amphiphilic lipid molecule. Image adapted from (http://en.wikipedia.org/wiki/Cell_membrane).

1.3.1 Lipids

Lipid molecules make up the main component of the membrane. Phospholipid molecules have a polar hydrophilic head group and typically

two apolar hydrophobic fatty acid acyl chains (tails). The fatty acid tails can be various lengths, each being the same or different, saturated or unsaturated, giving different packing properties and phase transition temperatures (T_m). The lipid composition in a cellular membrane is usually leaflet asymmetric: while PE (phosphoethanolamine) and PS (phosphoserine) mainly face the interior (cytoplasm), PC (phosphocholine) and sphingomyelin (SM) mainly face the outside (extracellular).

The types of lipid used in this work are SM (chicken egg sphingomyelin), DPPC (1,2-dipalmitoyl-sn-glycero-3-phosphocholine), EDPPC (1,2-dipalmitoyl-sn-glycero-3-ethylphosphocholine), DOPC (1,2-dioleoyl-sn-glycero-3-phosphocholine), DOTAP (1,2-dioleoyl-3-trimethylammonium-propane) DOPE (1,2-dioleoyl-*sn*-glycero-3-phosphoethanolamine) and DOPE-biotin (Table 1.1). Sphingomyelin is a natural lipid mixture with mostly PC head groups and a range of tail chain lengths. The use of this natural lipid creates a membrane with properties closer to that of a cell membrane.

PC head group lipids (DOPC and DPPC) are a major constituent of cell membranes; they contain both a positive and negative charge and are said to be zwitterionic. Their primary role is to provide a structural framework for the membrane and maintain the permeability barrier. DOTAP and EDPPC are chelating lipids which have positively charged head groups upon the dissociation of a chloride ion. While cellular membranes contain very little positively charged lipid, they offer many uses in developing membrane based architectures [1]. Biotin-linked DOPE allows the binding of avidin proteins to DOPE and subsequently the binding of other biotin-linked proteins or lipids. Also used in this thesis is the sterol, cholesterol. Like phospholipids it is amphiphilic, however instead of the head-tail structure it has hydrophobic hydrocarbon rings and a hydrophilic 3β-hydroxyl group. In nature, cholesterol plays a vital role in mammalian cells, modulating membrane fluidity and reducing permeability, potentially having an important function in the formation of lipid rafts.

In addition to the lipids mentioned above, a number of fluorescently tagged lipids are also used throughout this work such as Texas Red-DHPE and Oregon Green-488 DHPE which allow lipids to be viewed with fluorescence techniques.

Lipid	3D	2D
DOPC	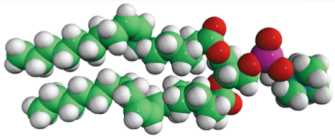	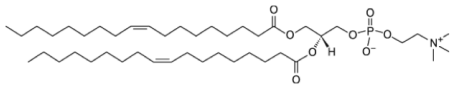
DOTAP	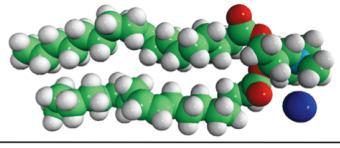	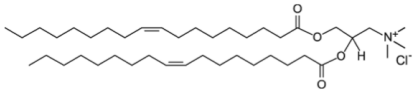
DPPC	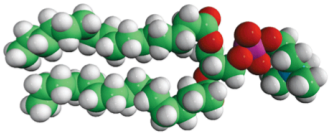	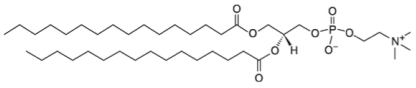
EDPPC	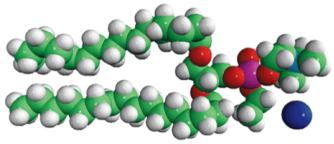	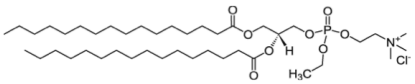
SM egg	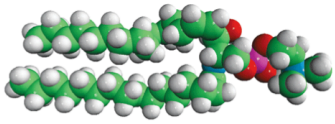	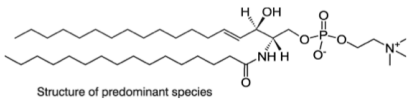 Structure of predominant species
Cholesterol	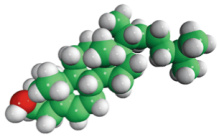	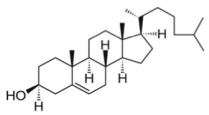
DOPE-biotin	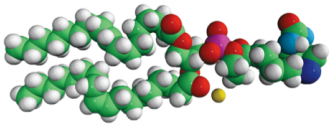	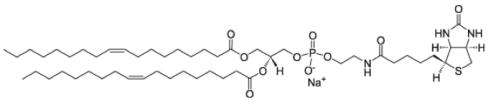

Table 1.1: The 2-D and 3-D structures of the lipids used for the work within this thesis. 2D and 3D Structures from (http://avantilipids.com)

1.3.2 Hydrophobic Interactions

The lipid bilayer self-assembles from amphiphilic lipid molecules which have a hydrophilic head and hydrophobic tails. In solution the hydrophobic interactions cause the molecules to pack together in order to hide their hydrophobic tails, by only exposing the head to the bulk water (Figure 1.3).

Hydrophobic forces have entropic origin, resulting from the entire system's statistical tendency to increase its entropy. Water is electrically polarized and is able to form hydrogen bonds internally, which leads to the minimisation of free energy. Since hydrophobic molecules are not polarized they are not able to form hydrogen bonds. Thus, when a hydrophobic molecule comes into contact with water, water repels it in favour of making bonds with itself and to minimize the free energy. In this way, hydrophobic tails of lipid molecules orient to each other and hydrophilic heads orient to the water. This effect not only leads to the formation of the lipid bilayer but a variety of other structures such as tubes, rods (hexagonal phases) and the three dimensional cubic phase. The resulting self-assembled structure formed depends on the lipid-water ratio, temperature, pressure, ionic strengths, pH and individual lipid shape i.e. conical or cylindrical.

1.3.3 Lipid Diffusion in the Bilayer

Due to the structure and forces which hold the bilayer together, lipid molecules can experience several types of molecular movements including 3D rotation of the whole lipid molecule, rotation of molecular segments, 2D diffusion in the plane of membrane and exchange to proximal membranes.

1.3.3.1 Lateral Diffusion

Lipids are free to move in the plane of the membrane in a 2D fluid. The rates of diffusion depend on the phase state of the bilayer (section 1.3.4) with diffusion constants from 10-20 $\mu m^2/s$ in fluid phases down to near static in more ordered phases. As described in section 2.2.2 the lateral diffusion of lipids in a bilayer can be determined via fluorescence recovery after photobleaching (FRAP). Lateral diffusion plays a vital role in cellular membranes, allowing proteins to interact.

1.3.3.2 Flip-Flop

Lipid flip-flop is the process whereby a lipid molecule flips from one leaflet of the bilayer to the other. It requires the translocation of the lipid head group through the hydrophobic interior of the membrane and thus is a rare

occurrence. Sum-Frequency Vibrational Spectroscopy work by Conboy et al has found half life rates of leaflet flip-flop ranging from 1 minute to several hours depending on the lipid and the temperature [2]. Flip-flop can also be increased by certain proteins such as flippases and translocases.

1.3.3.3 Molecular Exchange

In addition to translocation between leaflets, lipids can also be transferred between two bilayers. Like flip-flop, the molecular exchange process is very slow as it requires the transfer of the hydrophobic tails out of the bilayer.

1.3.4 Lipid Phase Behaviour

The phase behaviour of lipid bilayers is governed by the strength of the attractive Van der Waals (VdW) interactions between the adjacent carbon backbones of the lipid tails. The chains are not inherently straight, every bond can rotate. But because they can be straight under the right conditions, and they can then get close enough to VdW bond along the chain length. The extent of this interaction is in turn governed by how long the lipid tails are and how well they can pack together. Longer tailed lipids have more area over which to interact, increasing the strength of this interaction, thus decreasing the lipid mobility. For fully saturated chains, the chain length generally governs the temperature (T_m) below which a bilayer exists in a gel (L_β) phase, characterised by a high conformational order in the hydrocarbon chains and long-range 2D positional order. Above the transition temperature the bilayer will pass through a first-order melting transition to a disordered fluid phase (Ld) with a decrease in chain order and the loss of long-range correlations in lipid position. With a solid/gel phase the chains will tilt over 30 degrees to allow themselves to pack even more tightly.

An unsaturation in the lipid tail is a double bond, which forces a rigid bend into the chain, preventing it from straightening out and close-packing, and stopping the VdW attraction, hence lowering the melting temperature (eg. DOPC). Sterols such as cholesterol also get in the way of close packing and hence lower the transition temperature.

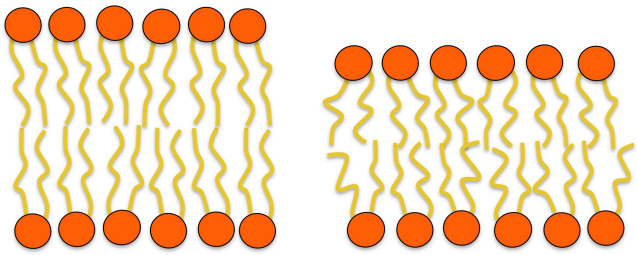

Figure 1.3: Illustrations of the gel and fluid bilayer phases. In the L_β or gel phase the hydrocarbon tails show a high order with dense lateral packing. At higher temperatures, beyond the transition temperature T_m, the gel phase melts to the L_α or liquid disordered (Ld) phase in which the tail groups become disordered.

For two component bilayers, with lipids possessing significantly different transitions temperatures, different phases may coexist. Figure 1.4 shows a generic example of a binary phase diagram. Phase diagrams show the expected nature of the thermodynamic phases existing in the membrane at a given temperature and composition.

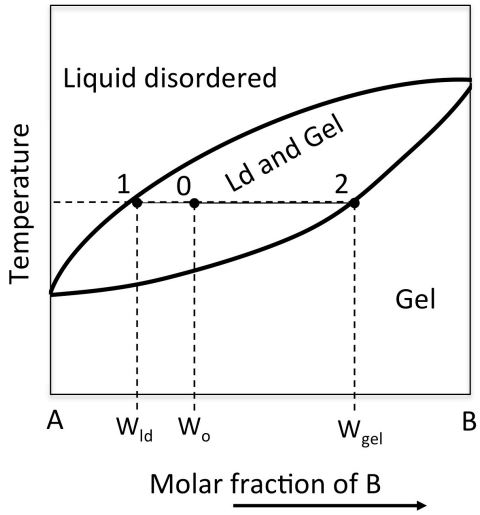

Figure 1.4: Representative phase diagram for hypothetical binary lipid mixtures for lipids with different transition temperatures. The diagram shows the regions of single liquid disordered, single gel and coexisting liquid disorded-gel phase.

An example of a binary lipid mixture which has a phase diagram akin to that in Figure 1.4 would be mixtures of DOPC (T_m = -17 ^oC) and DPPC (T_m = 41 ^oC), where the molar fraction B is the fraction of DPPC in the membrane. The converging points at B = 0 (100 % DOPC) and B = 1 (100% DPPC) are set by the different melting points of each component. The tie line drawn on the phase diagram, shown by the segment 1-0-2 in Figure 1.4, allows the determination of the molar fraction of each phase within the phase coexistence region. Briefly, the tie line is drawn horizontally at the composition's temperature from one phase to another (here from liquid to gel). The molar fraction of DOPC at the Ld boundary is given by W_{ld} and the molar fraction of DDPC at the gel boundary is given by W_{gel}. The fraction of each phase can then be calculated using lever rule equations (Eqn. 5.2) as described in section 5.1.2.

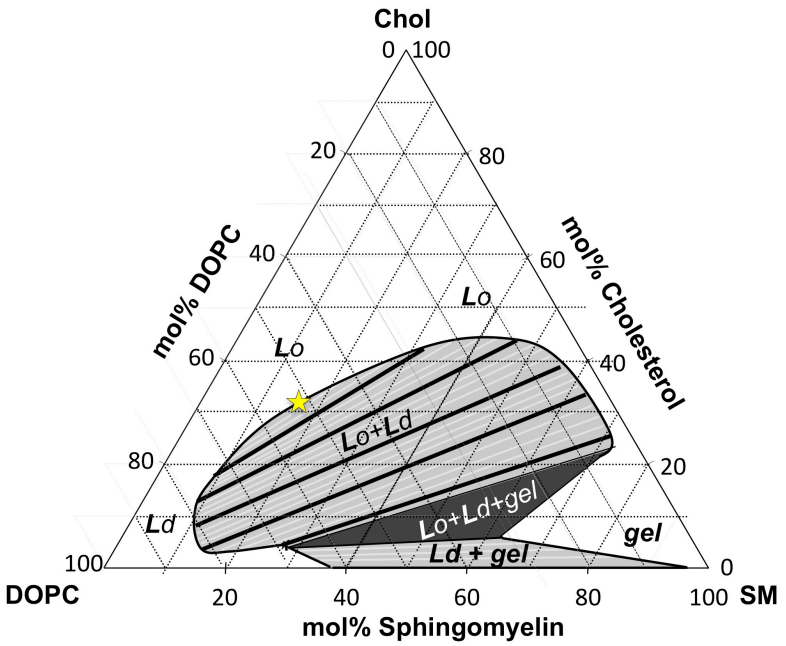

Figure 1.5: Ternary phase diagram for DOPC, sphingomyelin and cholesterol at room temperature. The diagram shows regions of single phase liquid ordered (Lo), liquid disordered (Ld) and gel, coexisting Lo + Ld, Ld + gel and Lo+Ld+gel. The star represents a critical point.

The inclusion of cholesterol into a binary phase separated bilayer takes the system a step towards the composition of mammalian cell membranes. The phase plot of three component mixtures can be represented by a Gibbs triangle, also known as a ternary phase diagram (Figure 1.5). This triangle

represents all possible compositions for the ternary mixture at one particular temperature. The region believed to be related to lipid rafts is the coexistence of liquid disordered and liquid ordered (Lo-Ld). In a Lo-Ld phase separated system, both phases are fluid but each phase has different packing and lipid and cholesterol content. The addition of cholesterol produces complicated effects due to it's small hydrophilic domain with adjacent rigid planar rings and a short single chain tail at the opposite end. The addition of cholesterol to a fluid phase bilayer decreases both lateral diffusion and permeability due to the added cholesterol intercalating between lipid molecules, filling in free space and decreasing the flexibility of surrounding lipid chains [3]. Whilst the addition of cholesterol to gel phase bilayers disrupts Van Der Waals interactions, decreasing order and increasing the diffusion coefficient [4]. Interactions of cholesterol with multi-component systems are even more complicated, resulting in complex phase diagrams (Figure 1.5).

1.3.4.2 Critical Points

Indicated by the star in the ternary phase diagram in Figure 1.5, a critical point is at a specific composition at a specific temperature at which the phase transition becomes second-order. The critical point is found at the point where the tie lines in the Lo-Ld coexistence region meet, as the composition of each become identical. Whilst to either side of the critical point, the coexisting phases undergo first-order transitions in which one phase slowly diminishes as the boundary to a single phase is crossed.

A critical point system undergoes large scale fluctuations between each phase as the energies associated with stabilising the phase separation diminish. Evidence is growing to show that some native biomembranes may tune their compositions to be near a critical point at a given temperature in order to exploit the delicate balance between phases [5]. A small change in composition (and hence a small amount of energy expended for the cell) can radically alter its chemical and mechanical properties. This idea is not new, but experimental evidence has only begun to emerge in recent years [6]. Critical fluctuations in phase separated lipid systems have been studied by

Keller and Veatch et al via numerous studies using NMR and fluorescence microscopy of giant unilamellar vesicles [6-9]. It has been proposed that critical fluctuations in both model and plasma membranes are what define lipid rafts. Out-of-equilibrium processes would govern domain sizes rather than the equilibrium structures [10].

One of the key attributes of critical behaviour is that it is universal, meaning that many properties can be understood without considering the details of the system. At a critical point, all systems that behave alike belong to the same ‘universality class’. For example, for any system in the Ising universality class, the properties depend only on the system's dimensionality and on thermodynamic variables such as temperature and pressure. This means that any system that belongs to the same class should exhibit the same critical behaviour and scale the same way with temperature, whether it is the spin in ferromagnets or liquid crystal orientations.

1.3.5 Biomimetic model membranes

To investigate the underlying biophysics of lipid and protein interactions a number of model lipid systems have been developed to simplify the complexity of the cell. By reducing the system down to a handful of different proteins and lipids, specific cellular processes can be constructed and probed in a controlled environment. Construction of protein membrane systems can also be used to create new technology by pulling out desired properties and tuning them to an application.

1.3.5.1 Supported Lipid Bilayers

Supported lipid bilayers are flat lipid bilayers lying on a substrate in an aqueous environment, with a gap between the bilayer and substrate thought to be typically ~1 nm. Supported lipid bilayers are one of the most commonly used model membrane, primarily due to their ease of use and the array of powerful surface analytical techniques which can be used to investigate them (AFM, QCM-D, Vibrational Sum Frequency, SPR and X-ray/Neutron Reflectivity). The main disadvantage of these supported bilayers is that the

lipids couple to the substrate, which causes a reduction in lipid diffusion (from ~15 $\mu m^2/s$ in free membranes down to 1-3 $\mu m^2/s$ for glass supported bilayers). In addition, if their extra-cellular domain extends out of the membrane, the close proximity of the substrate can cause transmembrane proteins to have hindered diffusion and for much larger proteins, denaturation through interaction with the substrate [11].

Supported bilayers are usually formed by vesicle fusion or Langmuir-Blodgett / Langmuir-Schaeffer methods. The vesicle fusion method relies on the rupture of uni-lamellar vesicles on the substrate and their subsequent fusion to form a continuous lipid bilayer (described in greater detail in Section 3.1.3). The process of supported bilayer formation can be affected by lipid and substrate chemistry, temperature, vesicle size and osmotic pressure [12]. Langmuir methods require passing the substrate through a lipid monolayer at a water/air interface to deposit one layer, then passing it back through to deposit the second layer. Although more difficult, the Langmuir methods have an advantage in that they allow asymmetric bilayers to be created. More novel techniques have also been employed to create supported lipid bilayers such as dip-pen nanolithography in which lipids are ‘drawn’ onto the substrate [13].

1.3.5.2 Small Uni-lamellar Vesicles

Also referred to as liposomes, small uni-lamellar vesicles (SUVs) are typically 25-400 nm in size with a single lipid bilayer shell. A typical self-assembly process triggered by hydrating dried lipid will not form vesicles with a single bilayer but multi-lamella vesicles (MLVs) which have multiple bilayer. To obtain SUVs from MLVs, tip sonication can be used to produce vesicles of ~ 25 nm size. Alternatively, extrusion through a membrane with a defined pore size can be used to tailor vesicle diameter (e.g. 400nm). The large majority of work performed on SUVs involves taking advantage of their compartmentalisation to encapsulate specific molecules such as dyes. This enables investigation of how molecules or proteins may attack a membrane through observing how the dye is released.

1.3.5.3 Giant Uni-lamellar Vesicles

In addition to SUVs it is possible to generate giant uni-lamellar vesicles (GUVs) with typical sizes of the order 0.5 - 30 μm. GUVs are possibly the model lipid system's closest to that of a cell in that they are a membrane closed environment of similar scale to cells and have no substrate interactions limiting lipid or protein diffusion. The most common method to produce GUVs is through an electroformation technique in which the GUVs swell from an initially dried lipid on one electrode towards another electrode a few millimetres away under a slow sinusoidal current [14]. The majority of studies carried out on GUVs are with fluorescence microscopy techniques using fluorescently labelled lipids and/or proteins.

1.3.5.4 Other Model Systems

Polymer cushioned bilayers have been developed to allow the incorporation of transmembrane proteins in an appropriate environment, such that they maintain their functionality. The inclusion of the polymer layer de-couples the membrane from the surface and still allows the use of surface analysis techniques. Many factors affect the suitability of the polymer layer including: hardness, hydrophobicity, charge density and degree of cross-linking [15]. Several types of polymer have been used including dextran, cellulose, chitosan, polyelectrolytes, lipopolymer tethers and pegylated lipids [16-18]

SAM modified supports used to create a 'hybrid' lipid bilayer are frequently generated by a pure alkane thiol. The system generated is a lipid monolayer on the hydrophobic surface generated by the SAM [19]. More complex hybrid bilayer membranes exist making use of a more lipoic SAM structure with a thiol head group modified for surface immobilisation [20]. The hybrid system has limitations, such as the incorporation of transmembrane components is difficult but can be achieved by incorporation of small ethylene oxide spacer units at the base of the alkane thiol [21]. One of the main advantages of SAM hybrid bilayers is the ability to use gold as a substrate, allowing electrical measurements to be taken.

Black lipid membranes are formed by painting a lipid solution in solvent over an aperture. As the solvent thins the bilayer is formed by a self-assembly process. Although highly unstable to perturbations, these systems allow transport across the membrane to be investigated with access to both sides of the free floating membrane [22].

1.3.6 Models of Lipid Organisation in Cellular Membranes

Although proteins add much of the functionality to the membrane, it is the 2D fluid nature of the lipid bilayer that gives these proteins a platform to move on/within and interact with each other. Not only does the lipid bilayer provide a barrier and platform for proteins but the lipids themselves play an active role in the 2D compartmentalisation, organisation and structure of proteins. The ideas about how lipids and proteins are organised in the cellular membrane have undergone a huge change over the last couple of decades and remain yet to be fully understood.

1.3.6.1 Fluid Mosaic Model

The Fluid Mosaic model was presented by Singer and Nicolson in 1972 as a hypothesis for the general structure and composition of cell membranes [23]. As shown in Figure 1.6A, the model is comprised of two monolayers of phospholipids, embedded with integral membrane proteins, peripheral membrane proteins, glycolipids and non-phospholipids (such as cholesterol). In this model, proteins and lipids are randomly distributed throughout the membrane, free to diffuse.

1.3.6.2 Original Raft Hypothesis

By 1974, studies on the effects of temperature on membrane behaviour gave of “clusters of lipids” in membranes [24]. The concept of lipid domains in membranes was formalized in 1982 by Karnovsky et al. [25], who observed heterogeneity in the lifetime decay of 1,6-diphenyl-1,3,5-hexatriene, indicating multiple phases in the lipid environment of the membrane. The term ‘lipid raft’ was formally described in 1997 by Simons and Ikonen, based on the dynamic clustering of sphingolipids and

cholesterol to form microdomains known as lipid rafts which can move within the fluid bilayer [26]. The saturated nature of the sphingolipid bonds causes these lipid rafts to be thicker than the rest of the membrane. This is energetically more favourable for some membrane proteins which have membrane spanning domains hydrophobically matched to thicker membranes and as such they accumulate in these regions (Figure 1.6 B). These rafts act to selectively sort the 2D distribution of proteins.

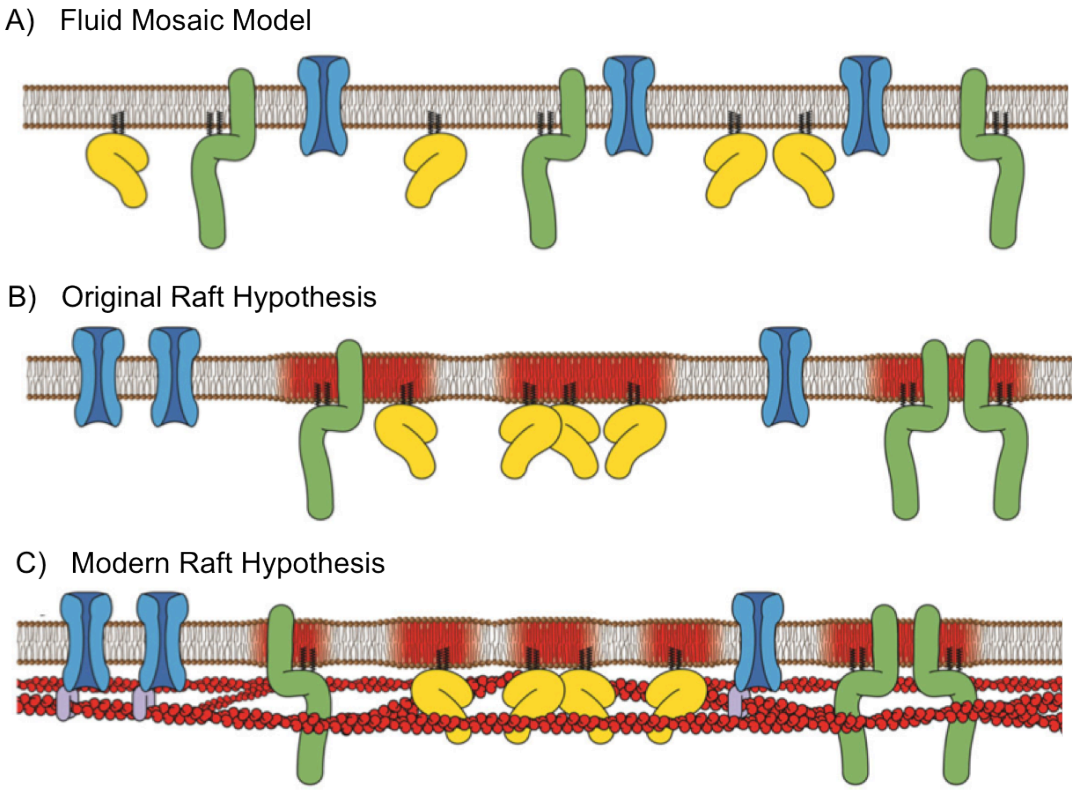

Figure 1.6: Models of lipid-protein organisation in the cell membrane. A) The fluid mosaic model (Singer and Nicolson, 1972) in which proteins are randomly distributed in a homogenous mixture of lipids. B) The raft hypothesis (Simons and Ikonen, 1997) with the clustering of sphingolipids and cholesterol into domains which act as clustering points for specific proteins. C) The current state of the raft hypothesis with highly dynamic and small lipid domains whose existence has an interaction with the actin cytoskeleton. Image from Owen et al [27].

In addition to hydrophobic matching of proteins, another method to locate to raft domains is through Glycosylphosphatidylinositol (GPI) anchoring. GPI anchored proteins have a lipid anchor with two saturated fatty acyl chains which preferentially insert into sphingolipid enriched domains. Doubly acylated, cholesterol-linked and palmitoylated proteins

have also been shown to partition into rafts. Through these various energetically favourable interactions, lipid rafts are proposed to create protein clustering points which are able to include/exclude certain proteins. This function plays an important role in many biological processes; for example in signal transduction, rafts form concentrating platforms for individual receptors activated by ligand binding. If receptor activation takes place in a lipid raft, the signalling complex is protected from non-raft enzymes such as membrane phosphatases that otherwise could affect the signalling process.

1.3.3.3 Modern Raft Hypothesis

The concept of lipid rafts in the cell membrane has evolved over recent years. At the 2006 Keystone Symposium of Lipid Rafts and Cell Function, lipid rafts were defined as "small (10-200nm), heterogeneous, highly dynamic, sterol- and sphingolipid-enriched domains that compartmentalise cellular processes. Small rafts can sometimes be stabilised to form larger platforms through protein-protein interactions". In addition, recent studies have shown increasing evidence that the cytoskeleton plays an important role in controlling raft formation [28-30]. Despite large amounts of *in vivo* and *vitro* work, the factors responsible for the formation of these domains are still not fully understood. The current consensus is that interactions between the plasma membrane lipids, proteins and the actin cytoskeleton are responsible (Figure 1.6 C), but to what degree and how each are responsible is unknown.

Direct evidence of rafts in living cells has remained elusive due to their proposed size (below the resolution limit of optical microscopy) and their apparently short lifetimes. However super resolution microscopy techniques such as photo-activated localisation microscopy (PALM), stimulated emission depletion (STED) microscopy [31] and structured illumination microscopy (SIM) [32] are allowing imaging of cells at length scales below 200nm [27] and may continue to shed further light on the *in vivo* complexity.

1.4 Membrane Proteins

Most membranes contain a similar mass ratio of lipid to protein [33] and as such, understanding protein-protein and lipid-protein interactions is vital to developing a better understanding of the cellular membrane as a whole. Membrane proteins are typically split into two categories: peripheral membrane proteins and integral membrane proteins (transmembrane). Peripheral membrane proteins either associate with particular lipids or transmembrane proteins, or partially insert into the lipid bilayer due to the presence of both hydrophilic and hydrophobic domains. The second type, transmembrane proteins, span the width of the membrane with hydrophilic domains appearing on one or both sides of the lipid bilayer. Typically the hydrophobic region is either α-helical or β-sheet in secondary structure.

Of the two membrane protein types, transmembrane proteins are the less stable type as they often require the surrounding lipids to maintain their structure, unfolding when outside their preferred environment. Transmembrane proteins play several roles in the function of the cell. One of the most important roles is communication as the protein is able to signal factors about the cell's environment e.g. mechanical forces, pH etc. [34]. Transport of ions and other small molecules across the cell membrane are also frequently undertaken by transmembrane proteins [35]. Whilst transmembrane proteins are key to so many functions within the cell, they remain the least understood group of proteins. The two membrane proteins studied in this thesis are the integral membrane protein M2, of the influenza virus that forms a pH sensitive proton channel and the actin binding protein ponticulin from *Dictyostelium discoideum.*

1.4.1 M2 Protein

The influenza-virus M2 protein is a 15 kDa [36] proton channel protein found in the viral lipid envelope. Upon endocytosis by a host cell, the channel opens due to the decreasing pH of the endosome, allowing protons to pass through the lipid envelope of the virus, facilitating uncoating of the viral RNA in preparation for transcription. The structure, as determined by NMR, of M2

is shown in Figure 1.7, the transmembrane portion has a four-helical bundle structure with amphipathic helices protruding out of the membrane. The proton channel is cytotoxic in heterologous expression systems and can be blocked with the antiviral drug rimantadine.

Along with M2's importance in the influenza life cycle, it also serves as a model proton-translocating channel due to its relative simplicity and small size. In addition M2 protein has been postulated to occupy the perimeter of the raft domain, formed when the virus buds out of the plasma membrane [37,38].

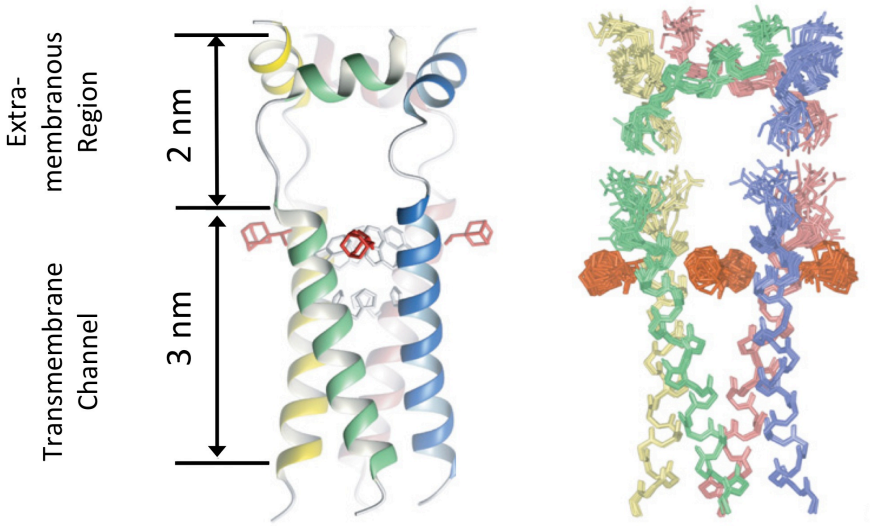

Figure 1.7: Structure of M2. (left) A ribbon representation of a typical structure from the NMR derived ensemble average, showing the left-handed packing of the transmembrane helices, right-handed packing of the amphipathic helices and the drug rimantadine (coloured in red). (Right) Ensemble of 15 low-energy structures derived from NMR restraints. Because residues 47–50 are unstructured, the transmembrane helices and the amphipathic helices (extra membranous region) are superimposed separately. Modified from Schnell et al [39].

1.4.1 Ponticulin

Within the soil living amoeba *Dictyostelium discoideum* it is estimated that there are ~300 ponticulins/μm^2 in the membrane and that ponticulin is responsible for 90-96 % of the high affinity actin binding in the cell [40]. Ponticulin is one of the few proteins known to provide a direct link between the cell membrane and the F-actin network [41]. Typically, binding of actin to

the membrane is obtained via multi-protein complexes. Ponticulin has also been shown to nucleate the growth of actin filaments [42], specifically showing greater growth rates when in its native membrane extract. It has been suggested that ponticulin binds actin oligomers not at the filament ends but to the filament side [43]. The binding of actin to ponticulin has been shown to be inhibited by 2 M sodium chloride indicating the interaction is primarily electrostatic [44]. It was also suggested that the binding of actin to the bilayer was clustered around specific membrane sites. Structural studies of ponticulin suggest it is a Type VI transmembrane protein, differing from other types of transmembrane proteins in that it has both a transmembrane domain and a GPI (Glycophosphatidylinositol) lipid anchor (Figure 1.8) [45].

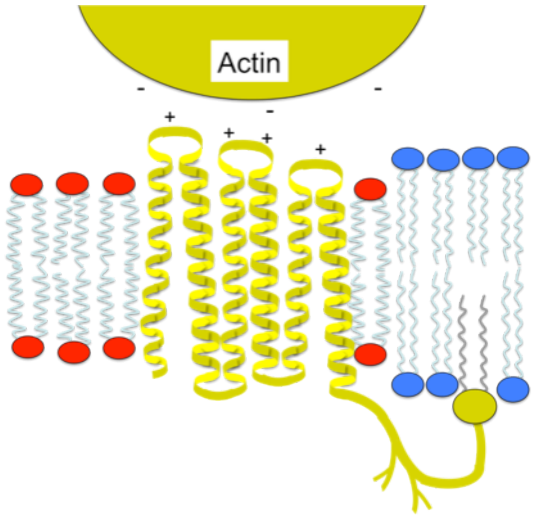

Figure 1.8: Schematic of the predicted structure of ponticulin [45] in a two phase lipid bilayer. In this image the GPI anchor is shown linking to a more ordered lipid phase with actin binding to the extra-membranous region at the opposing leaflet.

1.5 The Cytoskeleton

As with the human body the cellular membrane is not able to maintain its shape without a skeleton. In cells, this takes form of the highly dynamic and multifunctional cytoskeleton; complex networks of fibrous proteins - actin filaments, intermediate filaments and microtubules that help organise, structure and orient the cell (Figure 1.9). Since the cytoskeleton provides the structure that gives a cell its shape, when the cell moves, the cytoskeleton has to be broken down and deconstructed in one place and then be reconstructed in another. It is the reorganisation of the cytoskeleton that also allows cells to divide. In addition to the changes on a cellular level, the cytoskeleton also provides an intracellular transport network of tracks which cell components can be moved along, allowing for example, the movement of vesicles. These dynamic processes require a symphony of proteins working together, an intricate set of machinery which has the potential to be utilised for advanced bionanotechnology applications.

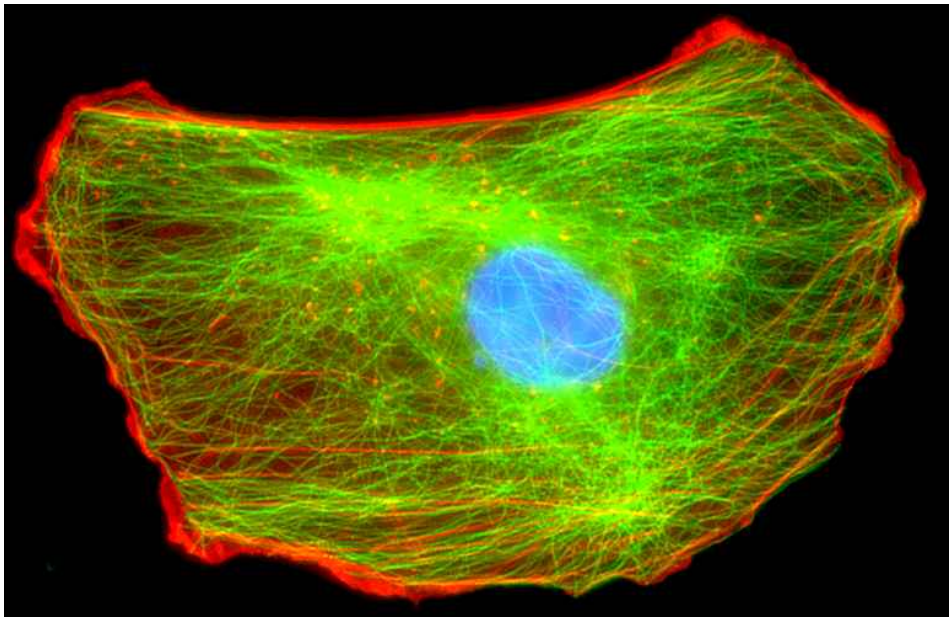

Figure 1.9: Fluoresence microscopy image of the cytoskeleton of a eukaryotic cell. The actin microfilaments are stained red, the microtubules made of tubulin are stained green and the nucleus is stained blue. Image from (http://bsp.med.harvard.edu/?q=node/60).

1.5.1 Microtubules

The largest of the cytoskeletal filaments are the microtubules which radiate away from the cell nucleus as hollow cylinders, 23 nm in diameter and typically up to 25 μm in length. The polymerisation of microtubules occurs via the end to end addition of dimers of alpha and beta tubulin which then form a cylindrical bundle of 13 protofilaments. During the polymerisation, each subunit undergoes GTP hydrolysis to GDP, taking the subunits from a stable to a less stable state. Depolymerisation occurs when the rate of hydrolysis is greater than the subunit addition. The orientation of subunit addition results in polarised filaments. It is this polarity that allows motor proteins such as kinesin and dynein to be controlled to move along the filament in opposing directions.

1.5.2 Intermediate Filaments

Intermediate filaments, so called as they have a diameter of 10 nm which is intermediate between actin filaments and microtubules, play a mostly structural role in the cell. There are about 70 different genes for coding different intermediate filaments but they can be sub-categorised into six types based on similarities in amino acid sequence. Able to assemble into a number of different structures, the central rod domains of two polypeptides wind around each other in a coiled-coil structure to form dimers. Dimers can then associate in a staggered antiparallel fashion to form tetramers. Tetramers can associate end to end to form protofilaments and laterally to form filaments. Unlike actin filaments and microtubules, intermediate filaments are apolar and thus have no plus/minus ends.

In cells intermediate filaments form an intricate network in the cytoplasm, extending from a ring surrounding the nucleus to the plasma membrane associating with the membrane, actin filaments and microtubules. Intermediate filaments thus provide a scaffold that integrates the components of the cytoskeleton and organises the internal structure of the cell.

1.5.3 Actin Filaments

Micro-filaments also known as actin filaments are one of the most abundant proteins found in the human body. They form the supporting scaffold beneath the cell membranes of eukaryotic cells and also the fibres upon which myosin motors pull on, in muscle cells. The filaments are 7 nm in diameter and can extend beyond 10 μm in length. As shown in Figure 1.9 actin filaments are found at highest density closest to the membrane, indicating their importance in maintaining local cellular shape. As well as providing mechanical support to the membrane, the use of actin as a scaffold in biology allows for a diverse range of dynamic processes to be utilised such as cell division, cell locomotion, muscle contraction and vesicle transportation. This diverse functionality is achieved through a huge range of actin binding proteins which can be used to: cap, cut, crosslink, bundle, branch and move actin filaments. This offers the potential to create an extremely varied range of structures (either mimicking biology or not) which can be tuned to the desired application.

1.5.3.1 Actin Structure and Polymerisation

Highly conserved throughout nature, actin can be found in species ranging from unicellular organisms to plants and animals. Recent studies have also shown actin analogues in bacteria [46]. The monomer form of actin, known as G-actin (globular), is a 42 kDa protein with dimensions of 55Å x 55Å x 35Å [47]. Split into four subunits, it has a central cleft to which ATP or ADP bind (Figure 1.10). G-actin has a single high affinity binding site at the cleft to which the binding of Mg^{2+} or Ca^{2+} occurs. It also has several lower affinity sites binding Ca^{2+}, Mg^{2+} and K^{+} [48]. Under high enough salt and actin concentrations, actin filaments grow by the reversible addition of G-actin monomers to both ends to produce a double helical filament form known as F-actin (filamentous). Typical F-actin filaments have a diameter between 7-10 nm and a full helical pitch of 72 nm.

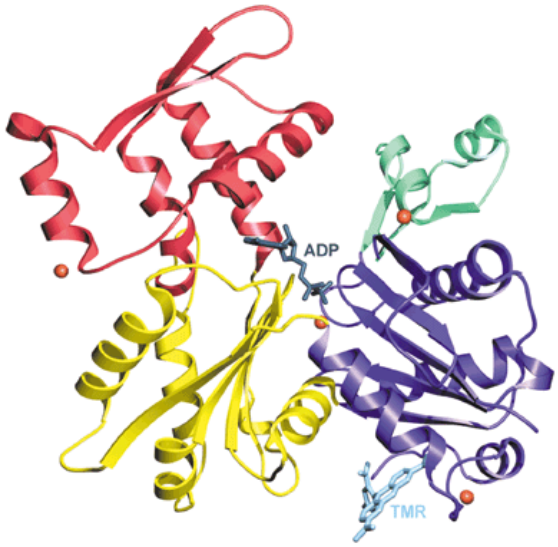

Figure 1.10 The structure of G-actin in the ADP state with the four subdomains highlighted by different colours, and ADP bound at the central cleft. Four Ca^{2+} ions are also shown bound to the actin monomer, represented as gold spheres. In this structure, tetramethylrhodamine-5-maleimide has been used to covalently attach a dye to a specific cysteine residue. Image from Otterbein et al [49]

The binding of G-actin to an actin complex greater than two monomers or an actin nucleating protein is much more favorable than two monomers binding to each other. This nucleation phase produces a period of slow polymerisation known as a lag phase. At the cleft, each actin is bound to ATP, which is hydrolyzed to ADP following filament assembly (Figure 1.11). Although ATP is not required for polymerisation, actin monomers to which ATP is bound polymerise much more readily than those to which ADP is bound. The preferential orientation of monomer-monomer binding during polymerisation produces polarized filaments, an important feature whereby all subunits in a filament point toward the same filament end. This creates filaments with which one end elongates 5-10 times quicker than the other. The different ends, known as the barbed (or plus) and pointed (or minus) end, allow growth to be directed during specific processes.

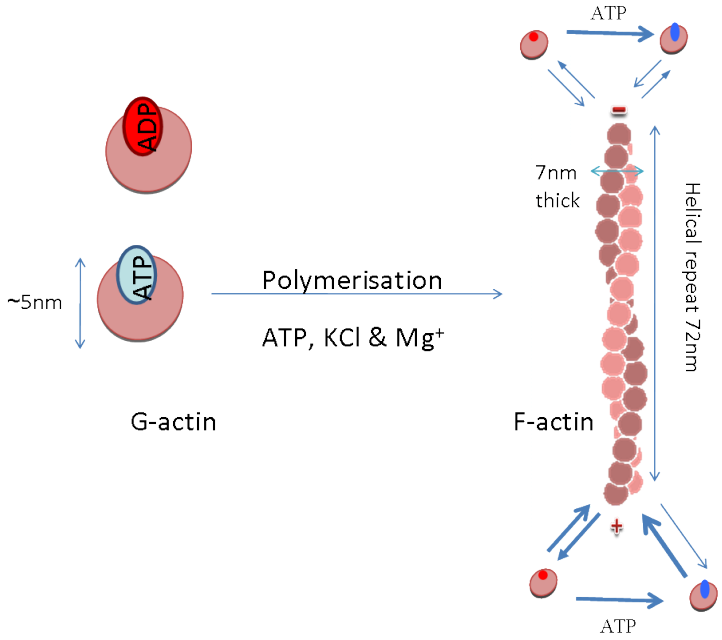

Figure 1.11: Illustration of G-actin and actin polymerisation dynamics. Arrow thicknesses give relative on/off rates of each configuration.

1.5.3.1 Actin Binding Proteins

In vivo actin length, polymerisation and networking are regulated by a large range of actin binding proteins. There are various actin proteins which can control filament length by capping, severing and/or promoting depolymerisation. Actin depolymerisation factor (ADF) Cofilin is a small protein (21 kDa) which binds cooperatively along the sides of actin filaments (1:1) and severs them at low binding densities. Gelsolin (95 kDa) is a calcium-dependent, strong fragmenter which also acts as a capping agent and a nucleation site [50,51]. Capping to the barbed end, gelsolin caps have half lives reported up to two hours which is much longer than the time scale of other cytoskeletal dynamics. Electron microscopy studies have shown that the number of actin filaments at a steady state is equal to the number of added gelsolin molecules. This is consistent with the interpretation that each gelsolin acts as a nucleus for the growth of an actin filament during polymerisation [52]. A good agreement between filament length and actin:gelsolin ratio allowed the approximate deduction of the following equation:

$$L = (370 \,.\, R_G)^{-1} \tag{1.1}$$

Where R_G = actin:gelsolin ratio and L is the filament length (μm). This equation is based on 370 actin monomers in a 1μm filament and the capping of one filament per gelsolin protein.

Filament networking gives actin filaments the structural cohesiveness required to perform larger processes with proteins that branch, cross-link and/or bundle. Arp2/3 complex is a branching protein which nucleates actin from the sides of mother filaments, exposing a new barbed end. An example of a flexible cross-link is filamin, abundant in the cell cortex. Filamin cross-links F-actin into orthogonal networks. Filamin-F-actin networks are compliant, weakly elastic solids; nevertheless they can support large shear stresses because of a pronounced nonlinear strain-stiffening [53].

A more flexible actin cross-linking protein is spectrin, a long fibrous protein which forms the primary component of the erythrocyte (red blood cell) cytoskeleton. 200 nm long and 3-6 nm across, the protein assembles via the association of two dimeric subunits of spectrin to form head-to-head tetramers [54]. In the red blood cell, the entire cytoskeleton is arranged in a spoke-and-hub network in which several spectrin tetramers (spokes) bind to the same 40 nm/14-subunit actin filament (hub). It is this network which allows a red blood cell to squeeze through narrow blood capillaries without rupturing its membrane and spontaneously return to its original shape.

1.6 Crossing the Membrane with Biomimetic Drug Delivery Carriers

The membrane and underlying cytoskeleton provide the cell with highly sophisticated machinery for numerous processes; however they also provide an important line of defense to prevent entry into the cell. While this is useful to protect against unwanted agents, it can offer problems for administering drugs free in solution. Other problem of free drugs include poor solubility, poor stability and/or unwanted toxicity. These issues have driven rapid growth in the research and development of drug delivery systems in the form of polymeric nano/microparticles, liposomes, micelles and microbubbles amongst others. The success of these systems relies on the selection of appropriate design parameters to overcome the biological obstacles in reaching the target; these are avoiding immune clearance and being able to specifically target and subsequently enter the cell. Gas filled microbubbles offer unique properties as combined carriers of therapeutic payloads and diagnostic agents. This thesis explores the use of lipid microbubbles and options to develop biomimetic shells to alter their physical properties.

1.6.1 Lipid Microbubbles

Ultrasound is one of the most commonly used medical imaging techniques, providing real-time images through the reflection of transmitted sound waves at tissue interfaces. Although blood cells are poor ultrasound scatterers, the gas-fluid interface found within a microbubble in solution offers a significant density change, still enabling visualisation of the blood pool. In addition to enhancing imaging capabilities, the use of microbubbles for targeted drug delivery is a hugely important and growing area of research. By targeting a microbubble, which has drugs loaded within the shell or in attached liposomes, to intravascular receptors, drugs can be released at high concentrations that would otherwise be harmful if administered to the whole body. Microbubbles have the advantage over other targeted drug delivery vehicles in that a variety of phenomena associated with their oscillations can be used to facilitate intercellular and extravascular transport of macromolecules [55-58]. Inertial cavitation is the expansion and contraction

as well as the collapse of bubbles, driven by the inertia of the surrounding fluid. It occurs when the acoustic pressure amplitude is above a threshold level [59]. In inertial cavitation, microbubbles first grow in volume, and then implode violently, resulting in fragmentation and microjetting. Evidence has indicated that nano- to micro scale pores generated on the cell membrane are the cause for increased membrane permeability, allowing transportation of drugs via these pores [60]. In addition to the increased permeability of the membrane, the fragmentation of bubble material offers a combined method to release its payload of drugs.

1.6.2 Microbubble Shell Properties

A typical ultrasound contrast agent is made up of microbubbles, composed of a gas core, coated by a thin shell of proteins, surfactants, lipopolymers and/or lipids. Until the 1990s, microbubbles were mostly used for right heart opacification and cardiac shunt diagnostics. This limited use was due to the large size and limited stability of the bubbles. The first microbubbles were large simple air bubbles with no shell, only lasting a few seconds in circulation and they were unable to pass through small capillaries due to their large size. Coating the gas cores with a shell produced a smaller size distribution (less than 10 μm in diameter) thus allowing passage through the lung capillaries. To further improve the lifetimes of these microbubbles, the gas used in the core was changed from air to a perfluorocarbon gas which has a high molecular weight, decreasing its solubility in water.

Whilst the microbubble lifetime is dominated by the solubility of the encapsulated gas and the resistance of the shell to gas permeation [61], the oscillatory behaviour in response to ultrasound is heavily influenced by the mechanical properties of the shell [62,63]. When interacting with ultrasound, microbubbles give rise to harmonic, superharmonic and subharmonic components in the scattered signal. The response of a bubble to an external pressure was originally described by Rayleigh [64] and modified by Plesset and Prosperetti [65] for the case of microbubbles. More recently de Jong et. al [62] modified this further for the case of encapsulated microbubbles deducing the following equation:

$$f_0 = \frac{1}{2\pi}\left(\frac{1}{\rho R_0^2}\left(\frac{3\gamma P_0 + 2(3\gamma - 1)\sigma_w}{R_0} + \frac{4\chi}{R_0}\right)\right)^{\frac{1}{2}} \qquad (1.2)$$

In this linear model the shell is assumed to be of constant thickness and perfectly elastic. The resonant frequency f_0, is dependent on the equilibrium radius R_0, the density of the surrounding medium ρ, the ambient pressure P_0, the surface tension of the bubble/water interface σ_W, the microbubble stiffness χ, and the isotropic constant γ.

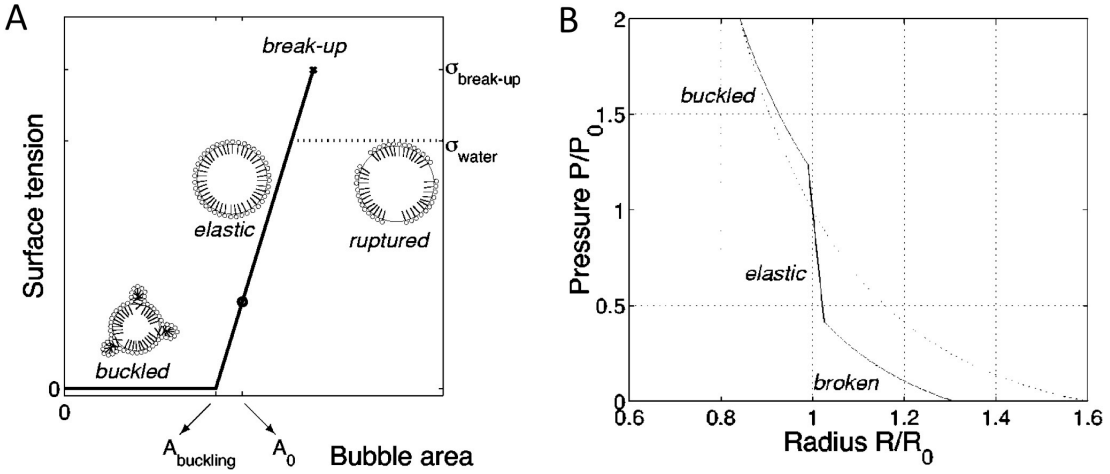

Figure 1.12: (A) Dynamic surface tension model for a lipid monolayer coated bubble (A_0 = area of monolayer at equilibrium). The model describes three regimes: buckled state (σ=0), elastic state ($\sigma = \chi(R^2/R^2_{buckling} - 1)$ and Ruptured state ($\sigma = \sigma_{water}$). (B) Implications of tension model for equilibrium radius response to ambient pressure variations at small frequencies compared to the resonance frequency. Figures taken from Marmottant et al [66].

Marmottant et. al. have more recently developed this model further to predict non-linear behaviour of phospholipid shells at large amplitude oscillations (termed compression-only). In this model, the non-linearity is induced by the buckling of the lipid monolayer (Figure 1.12). The non-linear 'compression only' behaviour i.e. easily compressing while only expanding slightly, gives rise to subharmonic ultrasound scattering (half the fundamental frequency) [67-69]. This non-linear scattering effect is not displayed by tissue and therefore allows greatly enhanced contrast between

blood from that of the surrounding tissue. This work was validated by experimental observations with a high-speed camera operated at several millions of frames per second [66]. Whilst there has been significant work to understand the subharmonic response of phospholipid coated microbubbles [70-72], there has been relatively little work on controlling the viscoelastic properties of the shell and the ‘compression only’ behaviour.

1.6.3 Microbubble Shell Compositions

1.6.2.1 Lipid Shells

Typically, two shell components are used to form stable microbubbles. The main component is saturated diacyl PC with a main phase transition temperature (T_m) from a gel to a fluid state above the working temperature. The low surface tension reached by the lipid monolayer stabilises the microbubble. The second component is typically a hydrophilic polymer, such as PEG with a lipid anchor. The purpose of PEG- lipid is to promote the self-assembly of the monolayer shell and to form a brush layer that shields the bubble against coalescence and immune cell interrogation. The lipid molecules are held together by weak physical forces, without chain entanglement, which makes the shell compliant to area expansion and compression during ultrasound imaging.

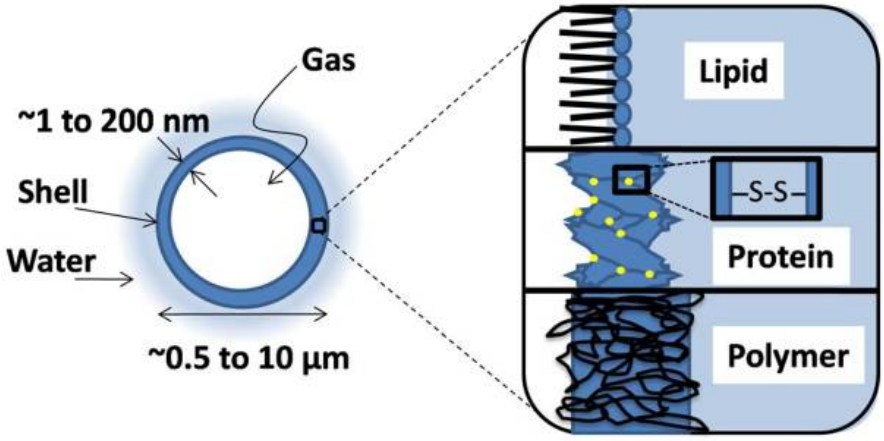

Figure 1.13: Schematic showing structure of a typical microbubble with different shell compositions. The gas core is a single chamber and makes up the majority of the total particle volume. The shell acts as a barrier between the encapsulated gas and the surrounding aqueous medium. Different shell materials may be used, including lipid (~ 3 nm thick), protein (15–20 nm thick) and polymer (100–200 nm thick). Image taken from [73].

1.6.2.2 Protein Shells

Albumin coated microbubbles were the earliest shells used in contrast ultrasound imaging. They are formed by sonication of a heated solution of human serum albumin in the presence of air. During sonication, microbubbles of air are formed, which become encapsulated within a 15-nm thick shell of aggregated albumin. Heating is necessary to denature the albumin prior to sonication and to facilitate encapsulation. Biochemical analysis suggested that the shell is a monomolecular layer of native and denatured albumin in multiple orientations [74]. Several proteins other than albumin have been used to coat microbubbles such as lysozyme which was found to be stable and retain its enzymatic activity for several months [75]. Korpanty et al. used a mixture of albumin and avidin to form microbubbles to allow biotin-mediated coupling of antibodies for targeting [76].

1.6.2.2 Polymer Shells

Several methods have been described to encapsulate gas in a polymer shell, one of which uses polymerisation at the air-liquid interface during agitation of an acidic medium, as described by Paradossi et al. [77]. Each of the methods has produced microbubbles with enhanced stability however, chain entanglement and covalent bonds inherent in the polymer shells have been shown to dampen the oscillation of the gas core until the shell is fractured by sufficient expansion [78].

1.6.2.2 Hybrid Shells

A new class of polymer-surfactant shell hybrids has been recently developed, composed of poly-electrolyte multilayer (PEM) shells on preformed microbubbles. The preformed microbubbles are coated with a charged surfactant or protein layer. Then a layer-by-layer assembly technique is used to adsorb oppositely charged polyions to the microbubble shell. Shchukin et al. were the first to report PEM deposition onto microbubbles [79]. They used the polymers poly(allylamine hydrochloride) (PAH) and poly(styrene sulfonate) (PSS) for the polyion pair. Borden et al. developed a PEM microbubble with phospholipid containing a cationic head-group (TAP) as the underlying shell ,with DNA and poly(L-lysine) (PLL) as the polyion pair [1]. Lentacker et al. described a multilayer microbubble in which albumin microbubbles were coated with DNA and PAH, where the latter layer served to bind and protect the DNA [80]. Also developed recently has been the use of biotin-linked lipids (10%) as an initial coating, allowing the adsorbtion of a streptavidin protein layer. This layer, which has been shown to crystallize on bilayers of the same biotin concentration, greatly increased bubble stiffness (~ 30 fold) and has the additional advantage of a system for the attachment a payload [81].

1.7 Thesis Aims

The work within this thesis is based on the construction of model cell membrane systems to develop better understandings of how their functions can be related to real cellular membranes and how they may be utilised for bio-nanotechnology applications.

In chapter 4, a new method for creating the smallest supported lipid membranes is developed. This work allows the effects of reduced dimensionality on lipid diffusion, protein diffusion and lipid packing to be studied. The differences observed due to the close proximity of the edges allows a limit of 25 nm, for the first time, on the extent to which the edge of a bilayer influences the bulk bilayer behaviour. These data create important implications for pore/defect formation in cell membranes, for the many processes that naturally occur in their vicinity and for drug delivery. Furthermore this work provides a model system for studying the role of dimensionality in biological processes including photosynthesis, catalytic processes at membranes, and the exchange of species between cells and their surroundings in which the dynamic behaviour of lipid membranes are key.

Chapter 5 looks at lipid mixtures in 2D dimensional membranes with the aim of understanding compositionally dependent shapes, sizes and dynamics of lipid domains. By mapping out the temperature dependent ternary diagram of DOPC, sphingomyelin and cholesterol mixtures, the critical points at different temperatures are tracked. The critical point behaviour is then shown to match that of a 2D Ising model. High speed AFM observations allow the detection of dynamic and size characteristics in agreement with the predicted ranges for lipid rafts hypothesised to exist in cellular membranes.

The work in chapter 6 begins to understand how membrane proteins interact with and partition into the various phases observed in chapter 5, taking the model phase system a step towards real cellular membranes by including proteins required to support an actin cytoskeleton. Using the actin

binding protein ponticulin, the studies show preferential localisation to the interface between phases, a property which may be crucial to the regulation of lipid raft like domains via the cytoskeleton.

It has been suggested that the enhanced nucleation activity of ponticulin is due to its positive charge. The ability of a cationic membrane to generate an F-actin network at the membrane is studied in chapter 7. The use of positively charged lipids allows the effects of lipid mobility, buffer conditions and overall membrane charge to be systematically investigated. The differing actin polymerisation characteristics under controlled conditions allows for the formulation of a detailed mathematical model, based on the diffusion of monomers from solution and in the plane of the bilayer, which elucidates the nature of charge induced polymerisation. The constructs produced give the next stepping stone in creating more complex mimics of the cellular membrane.

In the final results chapter 8, the phenomena of electrostatic induced actin polymerisation at cationic lipid surfaces (observed in chapter 7) is utilised to coat lipid microbubbles as combined ultrasound imaging and drug delivery vehicles. The use of actin in systems not only increases microbubble stability, elasticity and stiffness but also allows binding of liposomes as model drug carriers with the advantage of actin, only being polymerised at the bubble surface and not in solution. With the wealth of knowledge of actin in cells and an abundance of actin binding proteins that can further modify and tune desired properties, this coating gives a method to control the ultrasound response of microbubbles for medical use.

Chapter 2
Theory of Experimental Techniques

2.1 Atomic Force Microscopy

The Atomic force microscope (AFM) evolved out of the scanning probe microscope (SPM) classification of microscopes used for studying surface properties of materials from the atomic to the micron level. The AFM measures forces between a tip and the sample whilst scanning in a raster fashion across the surface to give a surface topography. Two vital components of an AFM are the probe and the scanner. The probe consists of a cantilever and a sharp tip (with tip radius of ~2 nm or greater), whereby forces between the sharp tip and sample cause a deflection in the typically ~ 100 μm long, soft cantilever to which it is bound. This deflection causes a change in cantilever angle which can be detected by a laser beam reflecting off the back of the cantilever end, onto a photodiode split into 4 quadrants. The scanner is controlled by voltages applied to separate elements of piezoelectric device which gives highly precise control of the tip or stage position both vertically and laterally. This combination allows the tip to be scanned over the sample, or the sample scanned under the tip, whilst measuring cantilever deflections which can then be interpreted by a computer to generate a map of surface topography.

The AFM can measure: forces at the pN scale, lateral distances at the nm scale and vertical distances at the sub angstrom scale. Coupled with the ability to operate under physiologically relevant, liquid environments this makes the AFM a great tool for the high resolution investigation of biological samples in a non-destructive manner.

2.1.1 Configuration

A common instrumental set up of an AFM is shown schematically in Figure 2.1, with the scanner moving the sample under the tip. Developments in each component have, and continue to allow advances in resolution, speed and function which will be discussed further in the following sections.

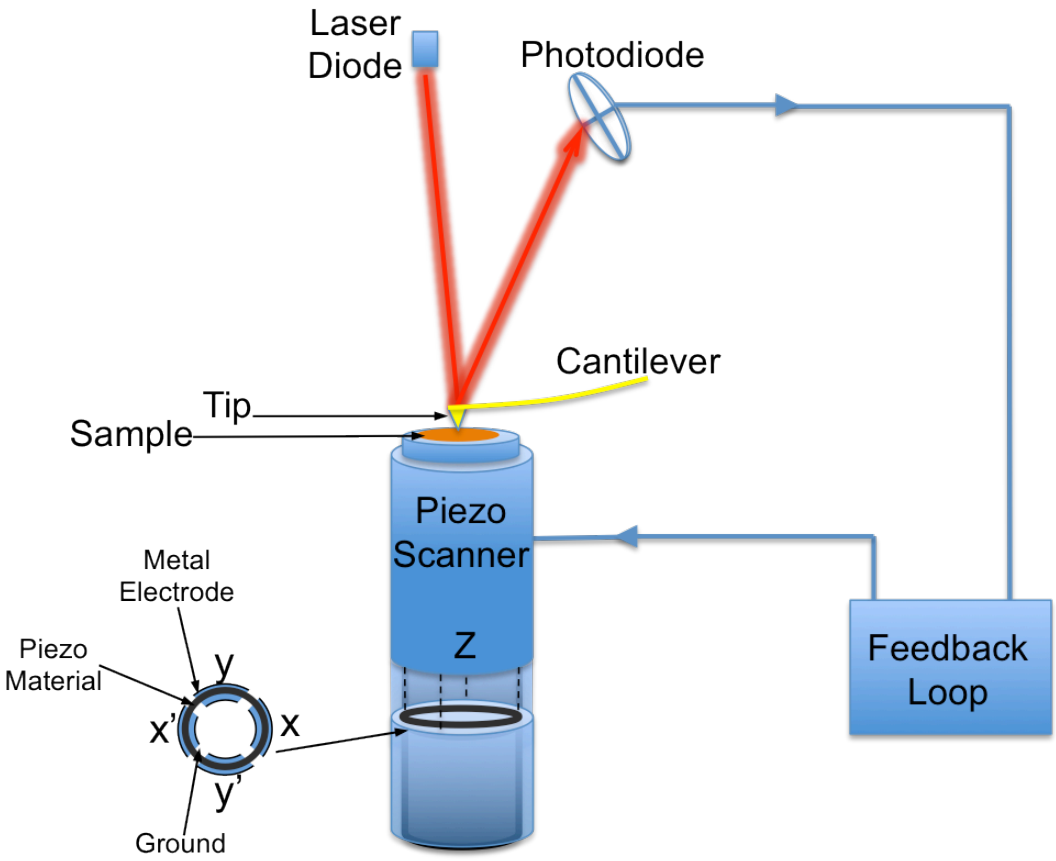

Figure 2.1: Schematic diagram showing the basic components of a tube scanner AFM.

2.1.1.1 Piezo Scanner

SPM Scanners are made from piezoelectric materials in such a configuration that provides precise positioning control. Piezoelectric materials contract or expand when a voltage is applied with a mechanical movement that is proportional to the voltage applied. The scanner has a combination of independently operated piezo electrodes for X, Y, and Z in a single tube, making a scanner that can manipulate samples and probes with high precision in three dimensions. AC voltages applied to the different electrodes

of the piezoelectric scanner produce a scanning raster motion in x and y. The scanner tube is made up of a cylinder divided length-ways into four sections of a piezoelectric crystal, there are two segments of the piezoelectric crystal for x (x' and x) and two for y (y' and y) (Figure 2.1).

2.1.1.2 Z Feedback Loop

To control the force applied by the tip to the sample a feedback loop is used to ensure the tip tracks the surface. The feedback circuit takes the tip deflection signal received from the photodiode and attempts to keep the cantilever deflection constant by changing the voltage applied to the scanner thus changing the tip sample separation. This not only regulates the applied force but also allows the force applied to be minimized reducing damage to both the tip and sample. In addition it is this feedback in height change which is used as the signal for generating an AFM height image.

The way in which the feedback loop responds to the tip forces can be controlled by settings known as the integral and proportional gains, correcting cumulative height errors and changing the height in proportion to tip deflection respectively. Scanning can also be performed with the z feedback turned off allowing faster scanning but only providing useful measurement for very flat regular surfaces with which tip z position remains relatively constant.

2.1.1.3 Probes

The probes used in AFM typically consists of a triangular or straight silicon nitride cantilever, 100–200 μm in length, 20 μm in width, with an pyramidal probe tip (Figure 2.2). There are a huge variety of different probes varying in cantilever stiffness, tip geometry and material. The assortment probes is born out of the need to study a continually expanding number of properties/applications using AFM such as high resolution, soft matterials, magnetic properties, electric properties and mechanical properties.

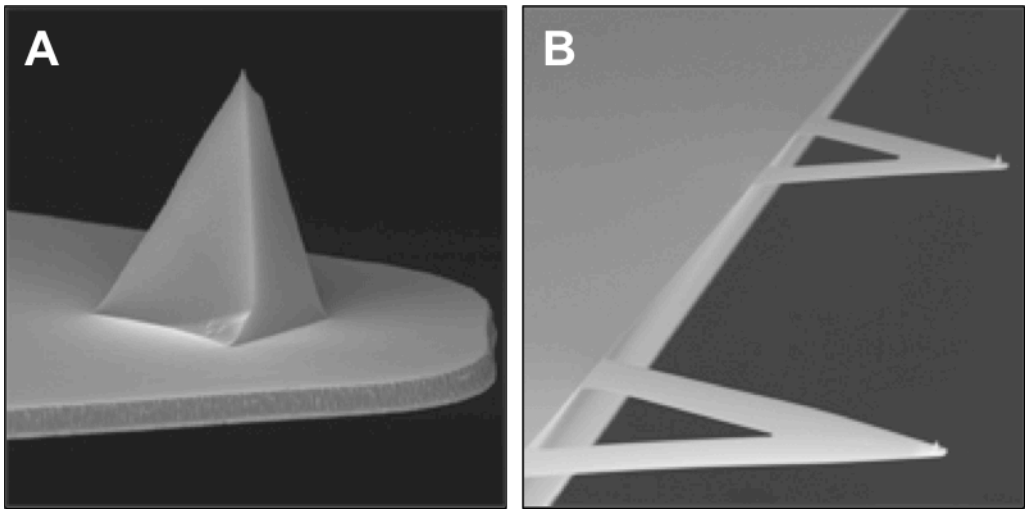

Figure 2.2: Electron micrographs of typical silicon nitride tips (A) and cantilevers (B) used in contact mode and fluid tapping mode imaging.

Cantilevers typically have a spring constant between 0.01 and 100 N/m and hence some are very soft and fragile. The spring constants of softer cantilevers allow a force resolution of pN. Although soft, the cantilever needs to be able to respond quickly to any force and to resonate at high frequencies for tapping imaging modes. This is achieved by having cantilevers with low mass, which has had to be further lowered for tips being used in fast scan AFMs which require even higher resonant frequencies.

The vertical deflection of the cantilever can be detected to within an Angstrom. This extremely high resolution is achieved though the optical lever method [82] in which a tilt in the cantilever of angle θ leads to a change in the incident laser beam of 2θ. The beam is reflected from the back of the cantilever onto a split photodiode (~ 3 cm away). Zero deflection is generally set such that each diode receives equal signal thus any deflection causes an imbalance of light hitting diodes therefore giving the deflection signal. Another method to detect deflection is to use optical interferometry which has been recently developed to be highly sensitive even in aqueous environments [83].

2.1.2 Tip Forces

As the tip interacts with the surface it can experience a number of different forces resulting in both repulsion and attraction. Both attractive and repulsive forces can be expressed mathematically using “Lennard-Jones function” as:

$$U(r) = 4\varepsilon\left(\left(\frac{\sigma}{r}\right)^{12} - \left(\frac{\sigma}{r}\right)^{6}\right) \tag{2.1}$$

Where the potential energy U(r) between two particles (tip and the surface) depends on their distance r. ε and σ correspond to the depth of the potential well and the separation at which the potential is zero respectively.

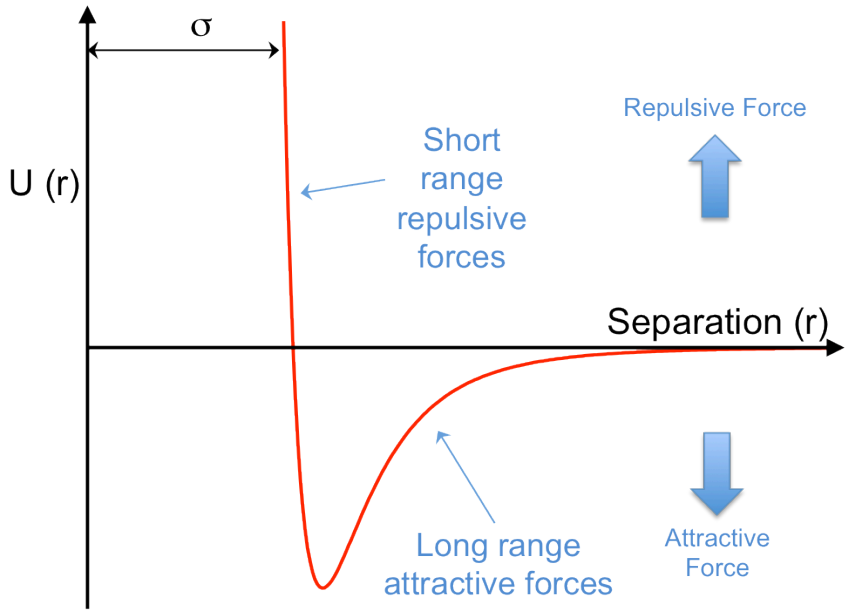

Figure 2.3: Plot of potential U(r) against distance depicting the Lennard-Jones potential. This graphs shows the combination of attractive and repulsive forces.

The Lennard-Jones potential is made up of two functions: the long range $(1/r)^6$ attractive term and the steep $(1/r)^{12}$ repulsive term. The attractive term arises from Van Der Waals interactions which are caused by fluctuations of the electron cloud surrounding the atomic nucleus creating instantaneous dipoles that can become correlated thus providing an attraction. These forces are relatively weak but long-ranged and can arise from 3 different circumstances: force between two permanent dipoles (Keesom force), force

between a permanent dipole and a corresponding induced dipole (Debye force) and the force between two instantaneously induced dipoles (London dispersion force).

The strong short range repulsive force comes from the Pauli exclusion principle that two electrons cannot occupy the same quantum state. Two particles at inter-atomic separation will begin to experience a repulsive force as their separation is decreased. The distance of closest approach is known as the hard sphere limit in which any further approach would lead to the overlapping of electron orbitals, and the sharing of a quantum state.

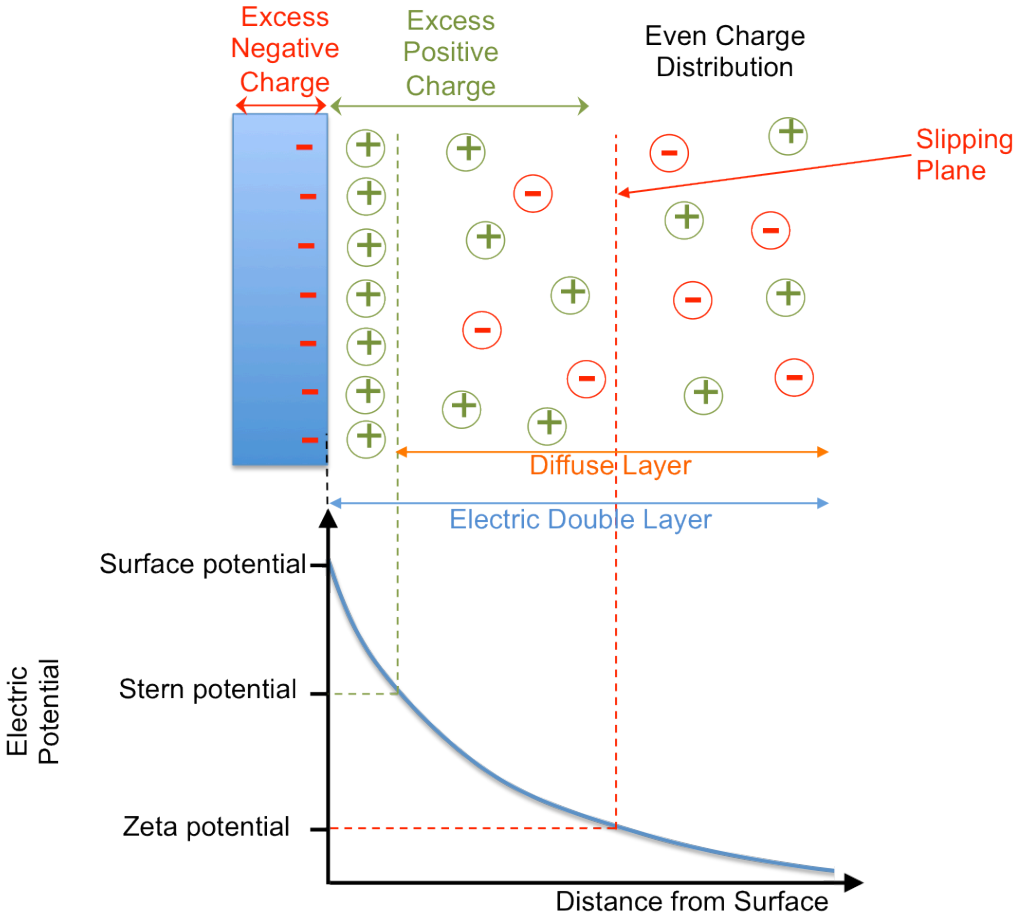

Figure 2.4 Illustration of an electric double layer at a negatively charged surface with plot showing electric potential as a function of distance from the surface.

When imaging with AFM in liquid conditions the Van Der Waals forces are effectively screened, however in addition to the above forces are electric

double layer forces. The electric double layer arises at charged surfaces in disperse environments due to the ions in solution acting to neutralise the net exposed charge. The electric double layer consists of three parts: the surface charge, the stern layer (counterions attached to the surface charge by its electrostatic force) and the diffuse layer containing free ions with a higher concentration of counterions (Figure 2.4).

The combination of Van Der Waals forces (U_A) and electric double layer forces (U_R) form the basis of Derjaguin-Landau-Verwey-Overbeek (DVLO) theory for interacting charged objects in an aqueous medium.

$$U_T = U_A + U_R \tag{2.2}$$

For a sphere (tip) interacting with a flat surface the Van Der Waals interaction is described as:

$$U_A = -\frac{AR}{6r} \tag{2.3}$$

Where A correspond to the Hamaker constant, R is the tip radius and r is the tip-sample separation. The thickness of the diffuse electric double layer is known as the Debye screening length, δ, the characteristic length over which the potential of a charged body is reduced by surrounding ions, i, of concentration, c and valance, z.

$$\delta = \frac{1}{\kappa} = \sqrt{\frac{\varepsilon k_b T}{e^2 \sum_i c_i z_i^2}} \tag{2.4}$$

Taking the Derjaguin approximation the potential of the electric double layer can be described as:

$$U_R = 64\pi R\varepsilon\gamma_1\gamma_2 \left(\frac{k_b T}{ze}\right)^2 \exp(-\kappa r) \tag{2.5}$$

Where γ is given by:

$$\gamma_i = \tanh(\frac{z_i e\psi}{4k_b T}) \quad (2.6)$$

Where ψ is the electrostatic potential.

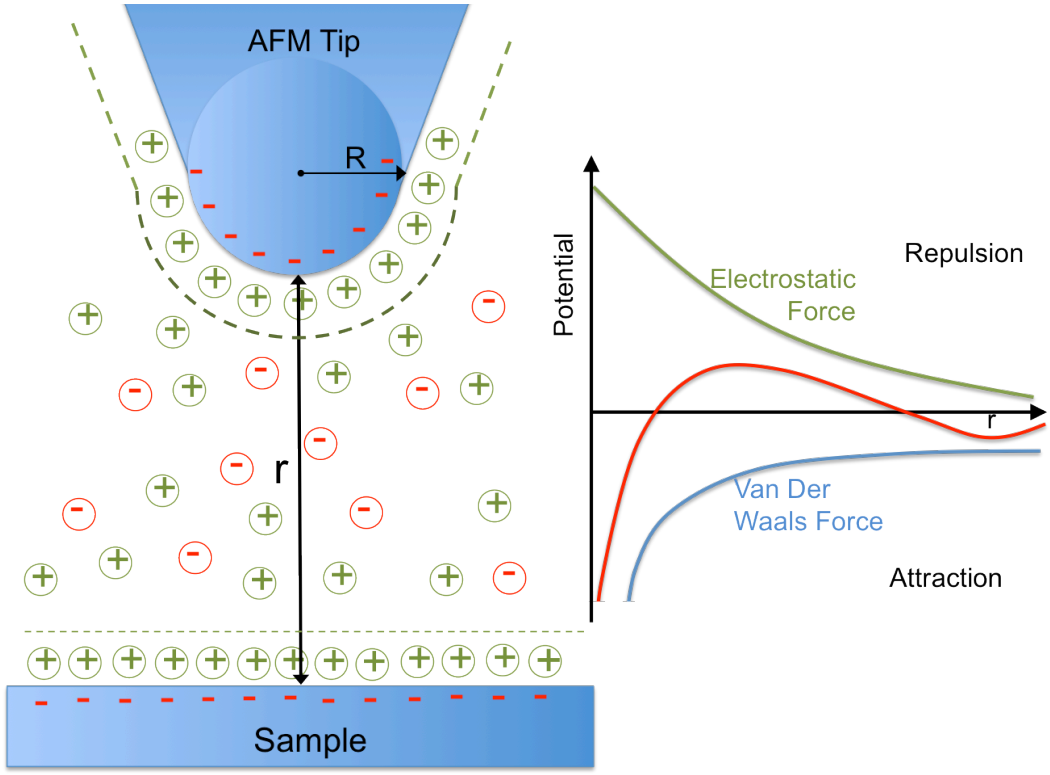

Figure 2.5: Illustration of ion distribution for a negatively charged tip interacting with a negatively charged sample in an aqueous medium. Plot shows the potential as a function of separation at physiological ionic strength.

At physiological ionic strengths the sum of Van Der Waals forces and electrostatic forces leads to a primary attractive force at longer distances which turns to repulsive as the electrostatics dominate, finally reverting to attraction at closer separations (Figure 2.5). Changes in ionic strength can transform the balance of forces leading to reduced repulsion or attraction. DLVO theory fails to describe forces when the separation becomes less than a few nanometers at which the structuring of the water molecules becomes important. Solvation/hydration forces arise due to changes in the semi ordered layers of water molecules leading to an oscillating

repulsive/attractive regime as separation is decreased. The ordering of molecules depends primarily on the surface chemistry.

2.1.3 Modes of Operation

The AFM has a large range of imaging modes based on different ways of interacting the tip with the sample. Each mode can be suitable for different kinds of sample and can be employed depending on the information required from those samples. In this section, a brief description of some of the modes used in this work are introduced, highlighting the advantages and disadvantages of each.

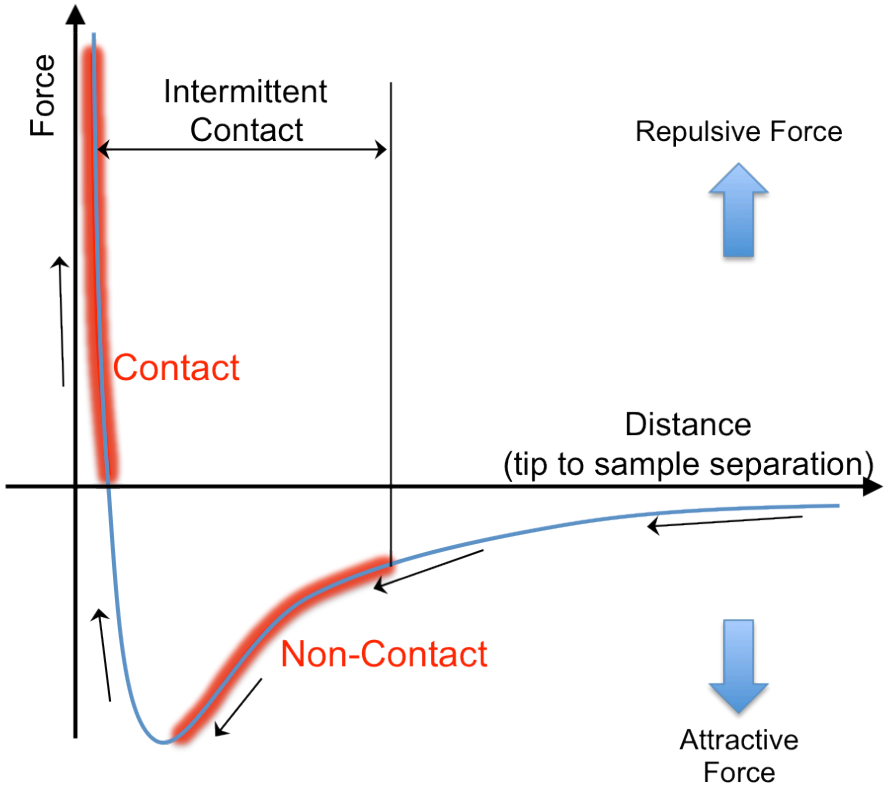

Figure 2.6: A plot showing the forces between tip and sample in air. The typical imaging modes are shaded for clarity.

2.1.3.1 Contact mode

The original mode of AFM operation is Contact mode (CM) in which the tip stays in close contact with the sample while scanning. The two different methods of applying contact mode are either by holding the tip at constant force or by holding it at constant height. During constant force the feedback

loop maintains constant tip sample force by controlling the z-piezo. In this mode the position of the z-piezo replicates the topography. In constant height mode no feedback loop is used and the cantilever is held at a constant level in relation to the surface. An image is then created from the cantilever deflection giving greater vertical sensitivity but at the expense of potentially large forces to samples which are not very flat. In contact mode, the tip is always in contact with the surface and can thus create high shear forces that could damage and deform the surface, and in some cases sweep the sample off the surface. The large force applied on the surface can make contact mode unsuitable to image some sensitive, soft biological samples such as dispersed proteins. Contact mode is however very useful for imaging supported lipid bilayers which are very flat and laterally stabilised by hydrophobic forces.

2.1.3.2 Tapping mode

A less invasive mode of AFM, key for biological samples, is tapping mode (also known as intermittent contact mode). In this mode the tip is oscillated in the z direction whilst still being raster scanned across the surface, this greatly reduces shear forces and sample damage. Driven by a sinusoidal voltage applied to the piezo the tip is oscillated at a resonant frequency, typically 9 kHz in fluid. The piezo motion causes the cantilever to oscillate with a high amplitude (~ 20 nm) when the tip is not in contact with the surface. The oscillating tip is moved towards the surface until it begins to lightly touch or tap the surface. During scanning, the vertically oscillating tip alternately contacts the surface and lifts off. As the oscillating cantilever begins to intermittently contact the surface, the cantilever oscillation is reduced due to energy loss. The reduction in oscillation amplitude is used to identify and measure the surface features. During tapping mode operation, the cantilever oscillation amplitude is maintained constant by a feedback loop as in contact mode. If the oscillating tip approaches a bump, the oscillation of the cantilever is damped, and this results in the feedback loop moving the cantilever further away from the surface, so that the oscillation amplitude and tapping mode imaging force are maintained. As with constant

force contact mode, the feedback loop controlled vertical positioning of the cantilever is used to generate the topographical images of the sample.

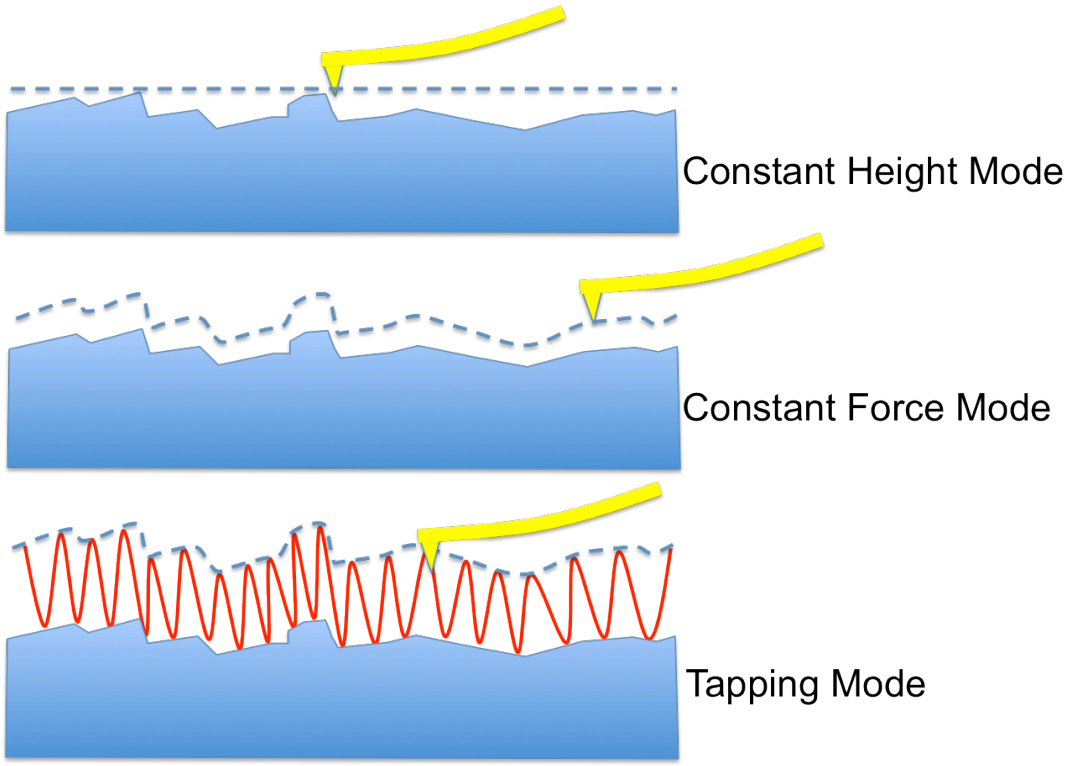

Figure 2.7: General imaging modes in AFM. Constant height mode (top) in which no feedback loop is used. Constant force mode (middle) whereby the feedback loop keeps the tip at a constant height from the surface. Tapping mode (bottom) where the tip is oscilated at/near a resonant frequency interacting with the surace with each cycle while the feedback loop acts to maintain a constant height away from the surface topology.

In addition to detecting the change in tip amplitude during scanning, referred to as amplitude modulation AFM (AM AFM), the change in resonant frequency can also be used to image the surface in frequency modulation AFM (FM AFM). FM AFM has recently been developed to be compatible in liquid environments allows atomic resolution to be obtained. An additional signal available during tapping mode is the phase difference resulting from the lag between the phase of the piezo driving frequency the tip and resulting phase of the motion of tip as measured by the deflection system. Although the phase lag is unable to obtain quantitative data, it does give qualitative information on the energy dissipated by the tip on the sample allowing contrast between areas of a sample which may be softer or more

adhesive. Phase imaging can also in some cases allow greater resolution to be obtained and allow for faster scan rates.

2.1.3.3 Force Spectroscopy

Although AFM was originally developed to image surfaces it can also be used to probe the mechanical properties of a surface or body with extremely high precision. In force spectroscopy mode the tip is moved in z direction only, pressing down on a sample at a single point then pulling away collecting deflection-distance plots (force curves), which can be converted to force-distance plots.

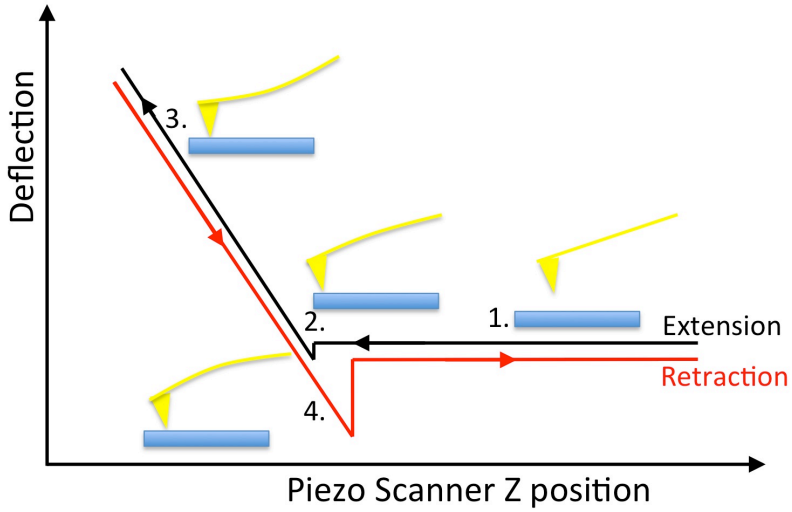

Figure 2.8 Typical deflection-separation force curve with both extension and retraction curves for a tip interacting with a hard surface with illustrations showing tip deflection in each step.

A typical force curve is shown in Figure 2.8**,** initially in position 1. the tip is approaching the sample. At position 2, the tip jumps into contact with the surface due to small attractive forces (usually attributed to capillary forces in air). From 2, the cantilever is deflected upwards as the z-piezo continues to approach applying a force to the sample until pre-set maximum deflection is reached at 3. On a hard sample, the deflection curve is linear with a gradient corresponding to the cantilever deflection sensitivity. On soft surfaces, the tip will indent the sample, leading to a non-linear region, the slope of which gives information about relative stiffness of the sample. The tip is then retracted, withdrawing the tip towards position 4, at which the tip is held by

the sample by adhesive forces. The tip then leaves the surface when the force of adhesion is overcome returning to zero deflection at position 1.

Force volume mapping combines force spectroscopy with low resolution imaging by taking a 2D array of force curves and height data at points in a specified square area (typically 32 x 32). This allows the mechanical properties to be mapped spatially in x-y but with limited resolution. In addition to investigating the mechanical properties of surfaces, tips can be functionalised so that force spectroscopy can be used to study the unfolding proteins to obtain their substructure and to probe adhesion between molecules.

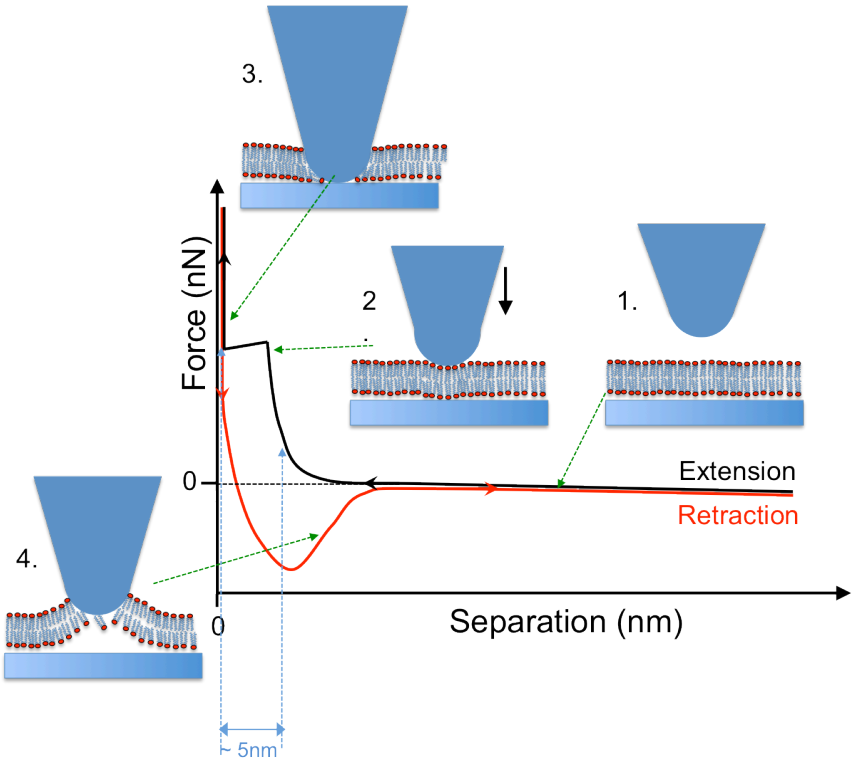

Figure 2.9 Typical Force-Separation plot obtained from punching through a supported lipid bilayer.

Force Spectroscopy is an important tool for determining the existence of a featureless smooth bilayer as the tip can be forced to penetrate the bilayer producing a distinctive break through event in the Force-indentation profile. Measurements on large delicate objects such as cells, microbubbles and liposomes can be done using tipless cantilevers providing more global stiffness information.

2.1.3.4 Peak Force Tapping mode

Peak Force Tapping mode is a newly developed imaging mode allowing quantitative nanomechanical mapping of surfaces by effectively combining high resolution tapping mode with force spectroscopy. In peak force tapping mode the cantilever is oscillated (typically at 2 kHz) but well below resonance resulting in a continuous series of force-distance curves. By performing force-distances curves at each pixel the force can be kept constant by keeping the peak applied force constant. In addition, real time analysis of each force curve allows material properties to be extracted and quantified within an image, such as modulus, adhesion force, and deformation depth. As shown in Figure 2.10 the deformation is calculated from the tips travel beyond contact, the adhesion force is obtained from the maximum retraction force, the energy dissipation is calculated from the total area between the extension and retraction curve and the Young's modulus is derived from the gradient of the retraction curve.

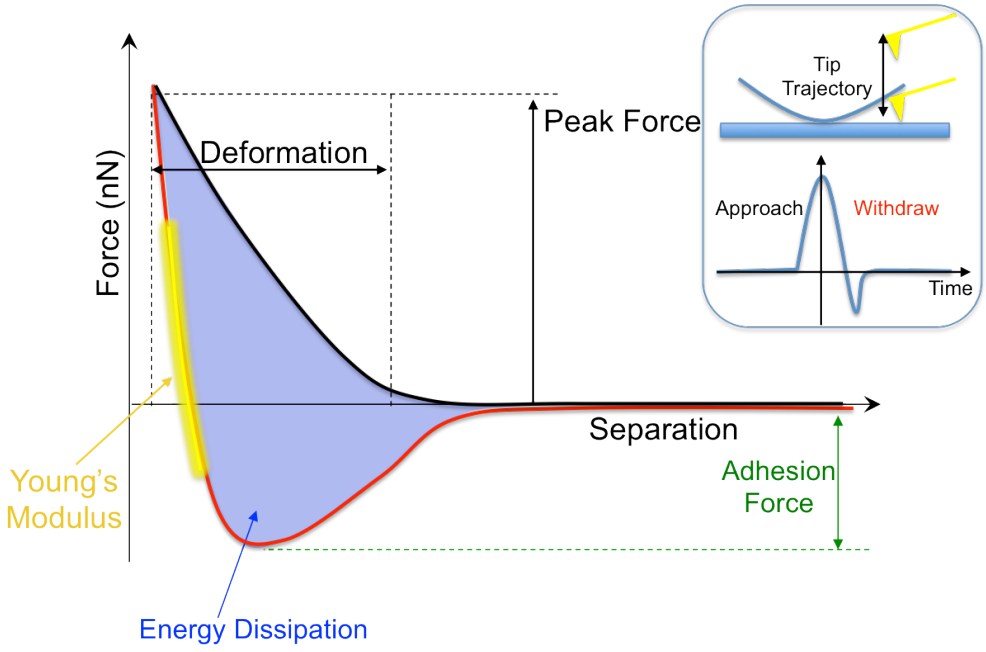

Figure 2.10 Quantitative nanomechial mapping (QNM) in peak force tapping mode. Force-Separation plot with highlighted values used to calculate different mechanical properties at each point. Image shows the tip trajectory for each pixel during peak force tapping mode with a plot of force versus time.

The automatic control over applied force allows peak force tapping mode to be automated for given probes in a mode named ScanAsyst mode, aiming to make AFM imaging more accessible to users with less experience. In ScanAsyst mode, feedback gain, tip setpoint, scan speed and z limit are all continually automatically adjusted by the software to optimize imaging.

2.1.4 High Speed AFM

The recent arrival of high speed AFM (HS-AFM) opens up new territory in which the fast dynamics of biological systems can now be visualised with both high temporal and spatial resolution. Typical AFM image scan rates are of the order 1-5 minutes per image while currently HS-AFM allows imagining at millisecond frame rates, it is at these time scales that proteins typically operate. This leap in imaging speed is achieved by a number of advances in AFM technology allowing the time delay in measurement/feedback loop to be drastically reduced (Figure 2.11). Operating in tapping mode the main factors responsible for time delays are: the response time of the oscillating cantilever, the time required for measuring the cantilever oscillation amplitude, the time of integrating the error signal with a feedback controller, the response time of the *z*-scanner and the 'parachuting' time (cantilever encountering a steeply declining region causing the tip detach from the sample surface and landing on the surface again).

The cantilever response time is reduced by using smaller cantilevers which consequently increases the cantilever resonant frequency (in liquid from ~10 kHz up to >100 kHz). Tapping at higher frequencies allows the sample to be probed more in a given time period and reduces the noise. To achieve higher scan rates the x, y and z piezo scanners must work at higher frequencies, at these frequencies unwanted vibrations and resonant frequencies become problematic. To combat these vibrations counteracting piezoactuators can be placed in a supporting base to displace simultaneously and in the opposite direction. To keep up with the faster required feedback, higher bandwidth electronics are used in the controller.

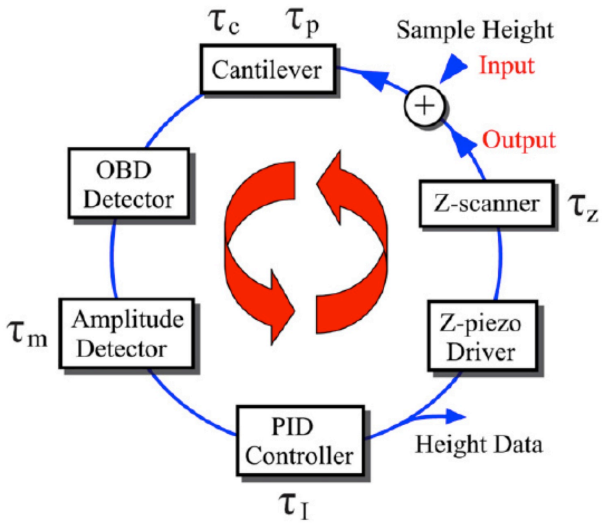

Figure 2.11: Feedback loop of tapping mode AFM and main time delays. The input to the feedback loop is the variation of sample surface height and the output is the displacement of the **z**-scanner. The time delay in the loop is mainly produced by the cantilever response time (τ_c), the parachuting time (τ_p), the time required to measure the cantilever oscillation amplitude (τ_m), the integral time of error signal at the PID (proportional-integral-derivative) controller (τ_I) and the **z**-scanner response time (τ_z). The OBD (optical beam deflection) detector has negligible associated time delay however it must be able to detect reflected signal from the back of much smaller cantilevers. Figure from Ando et al [84].

The development of high-speed began in the early 1990s, only a few years after the invention of AFM with the aim of fast inspection and lithography of a wide area of hard material surfaces using AFM [85]. Cantilevers and cantilever arrays were developed with integrated sensors and/or actuators [86,87]. Whilst simplifying the configuration of AFM, the fabrication of these cantilevers was only possible in relatively large dimensions, resulting in low resonant frequencies and large spring constants, this approach was too invasive for biological research. Increasing the scan speed of AFM was subsequently taken over by the groups of Hansma and Ando, both working towards increasing the feedback bandwidth by developing fast-response devices. Both groups developed small cantilevers and optical beam deflection (OBD) detectors for small cantilevers with Ando's group additionally developing a fast scanner and a fast amplitude detector [88]. In 1999 Hansma's group reported imaging of DNA at 0.6 frames per second [89]. Whilst the high-speed AFM developed by Ando's group in 2001 enabled filming of the Brownian motion of myosin V on

mica surfaces at 12.5 fps [88]. However, the feedback bandwidth in both of these system was not high enough to have a capability of low invasiveness to fragile proteins.

Subsequently in 2005 and 2006 improvements were made via the invention of an active damping technique for the z-scanner and a dynamic proportional–integral-derivative controller [90,91]. In addition smaller cantilevers with a resonant frequency of 1.2 MHz in water with a small spring constant of 0.2 N/m were developed by Olympus. As a result, the feedback bandwidth was significantly increased up to 100 kHz. By 2008, Ando's group finalised the development of high-speed AFM suitable for observing dynamic structural changes of biological molecules [92].

Since the development of this system Ando's group and others have published studies on the dynamics of numerous biological systems: from the walking of myosin V on actin filaments [93], the diffusion of point defects in streptavidin crystals bound to membranes [94], to the structural changes of single membrane proteins in response to the adsorption of light [95].

2.1.5 Nanolithography and Nanoscratching

Nanolithography is an AFM technique which allows nanometer-scale patterns to be drawn on a sample surface using the tip. This can be done by coating the AFM tip with a material to be deposited then scanning the tip in a pre-defined manner to create the pattern. Patterns can also be created by mechanically etching the surface by applying excessive force with the tip. Typical nanolithography software allows the user to create programs that control tip movements to draw a pre-defined pattern using bitmap images or vector based graphic objects imported into the software.

2.1.5 Tip Artefacts

The two aspects of an AFM tip that affect the image are its tip sidewall angles and its radius of curvature. For the work contained in this thesis the objects being imaged have heights similar to the tip radius and thus sidewall

angle does not play any significant role in the images produced. The smaller the radius of curvature, the smaller the feature that can be resolved laterally. The accumulation of debris on the end of the tip can dull the tip and result in image distortion. A dull or dirty tip may not affect the measurement of the vertical dimensions of samples however the features in the image may all have the same shape. What is really being imaged is the worn shape of the tip or the shape of the debris, not the morphology of the surface features. Double or multiple tip images are formed with a tip with two or more end points that contact the sample while imaging. Loose debris on the sample surface can also cause loss of image resolution and produce streaking/skips in the image. The debris can sometimes be detached from the tip to restore image resolution/quality whilst loose debris on the sample surface can be swept out of the image area after a few scans, making it possible to acquire a relatively clean image.

Feedback parameters not being adjusted properly can cause poor tracking of the surface such that the tip will not trace down the back side of the features producing tails on objects. This can normally be corrected for by imaging with a lower setpoint voltage, increased gains, and slower scan rates. The primary limiting factor in the highest obtainable vertical resolution is generally down to the overall system noise as a result of combined effects from electrical, mechanical, and acoustic noise sources.

2.2 Fluorescence Microscopy

2.2.1 Fluorescence

Fluorescence is an optical phenomenon in which molecular excitation by a photon triggers fluorescent molecules, called fluorophores, resulting in the emission of a photon of longer wavelength within nanoseconds of the excitation. As shown in Figure 2.12 by the Jablonski diagram, excitation light is absorbed by an electron of a fluorescent particle raising the energy level of the electron to an excited state. During the short excitation period, a fraction of the energy is dissipated by molecular collisions or transferred to a proximal molecule, the remaining energy is emitted as a photon to relax the electron back to the ground state. The emitted photon usually carries less energy than the excitation photon and therefore has a longer wavelength, this difference is known as the stokes shift. If the stokes shift is great enough the emitted fluorescence can be distinguished from the excitation light through filtration of the exciting light allowing the visualisation of single fluorescent molecules. The excitation and photon emission process can be repeated until the fluorophore is irreversibly damaged (Photobleached).

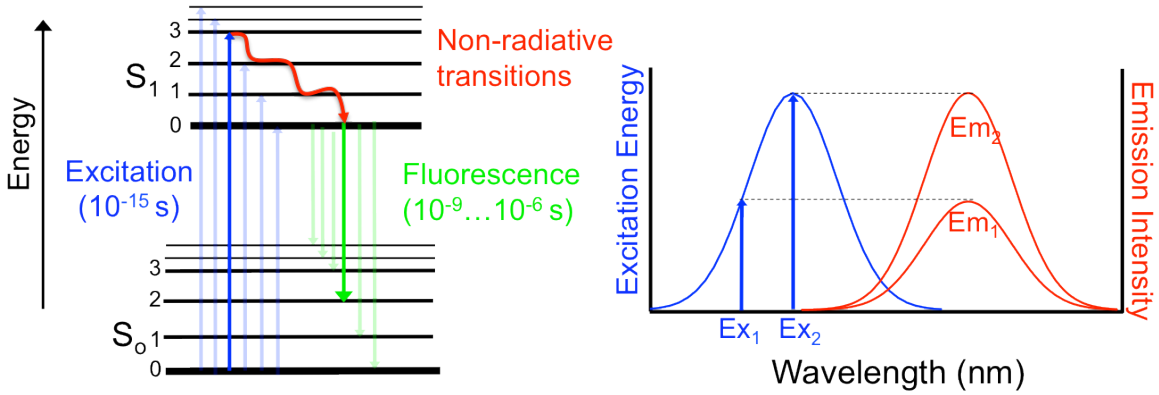

Figure 2.12: Jablonski diagram depicting the different energy states and the relevant pathways for photon excitation/emission (left). Plot showing a typical excitation and emission spectra with energies and corresponding emission intensities (right).

2.2.2 Fluorescence Recovery After Photobleaching

The diffusion of fluorescently labeled molecules (typically in 2D) can be determined using Fluorescence Recovery After Photobleaching (FRAP). The technique works by photobleaching a small area, then monitoring recovery as surrounding non bleached molecules diffuse into the bleached area and bleached molecules diffuse out via Brownian motion. In this work the bleached area was obtained by minimising the aperture of the microscope, removing all neutral density filters and illuminating the area with white light for a given period of time (typically 10 seconds). Photobleaching can also be performed using a laser spot. During bleaching the fluorophores receive a high intensity illumination and their fluorescent lifetime quickly elapses. Images obtained during a typical FRAP experiment initially show a dark region (bleached area) which then recovers to the surrounding intensity over time. Multiple images are captured during the time course of this process and analysed to obtain a measure of both the lipid diffusion coefficient and the bilayer mobility fraction. Background can be corrected for by obtaining a background image of the sample before photobleaching. Photobleaching of the non-bleached area and bleached area during recovery can also be corrected during image analysis.

There are number of different methods in which FRAP data can be analysed, in this thesis the Soumpasis [96] solution to Axelrod et al. [97] equations was used. Images were initially analysed using ImageJ (Freeware by NIH), the average intensity of the photobleached spot and a reference spot away from the photobleached area were measured. The first step in the analysis process is to correct for the background photobleaching due to image acquisition and photobleach spot generation.

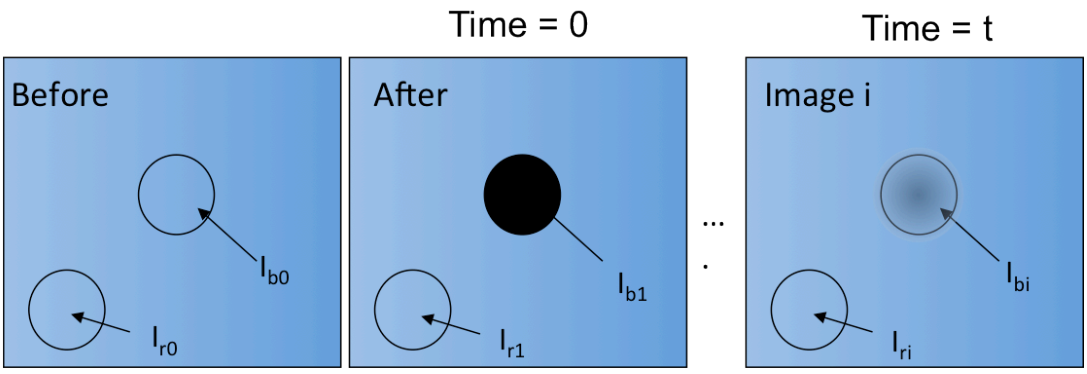

Figure 2.13: Diagram showing the measurements taken during the analysis of a FRAP image set. An image is taken before bleaching followed by an image straight after bleaching for time = 0. A series of images (i) are then taken over time, t showing the recovery of the bleached area and the diffusion of the bleached molecules. In each image intensities at a reference area I_r and within the bleach area I_b area are analysed.

In the analysis the background change in intensity due to photobleaching is corrected for using

$$I_{b2}^{*} = I_{b2} + (I_{r1} - I_{r2}) \tag{2.7}$$

$$I_{bi}^{*} = I_{bi} + \left(I_{r(i-1)} - I_{ri}\right) \tag{2.8}$$

Where i represents image number. The background corrected intensities are then normalised:

$$f(t) = \frac{(I_{bi}^{*} - I_{b1})}{(I_{bo}^{*} - I_{b1})} \tag{2.9}$$

Normalised intensities are then plotted with time and fitted using a Box Lucas model for the exponential recovery:

$$y(t) = A\,(1 - e^{\tau T}) \tag{2.10}$$

where A is the mobile fraction and τ is the decay constant. From the decay constant it is possible to calculate the half life:

$$t_{half} = \frac{ln\ 0.5}{-\tau} \tag{2.11}$$

The diffusion coefficient can then be determined from a knowledge of the half life and an accurate measure of the radius of the photobleach area using the equation:

$$D = \frac{0.22r^2}{t_{half}} \tag{2.12}$$

2.2.3 Epi Fluorescent Microscope Configuration

One of the most widely used techniques for fluorescence imaging is the epi-fluorescence microscope. As shown in Figure 2.14 rather than in a typical microscope where light is used in a transmission mode, in the epi fluorescent microscope both the excitation and emission are passed through the objective. The excitation and emission lights are split by a dichroic mirror (typically mounted at 45°) reflecting shorter wavelengths onto the sample and transmitting longer wavelengths into the eyepiece or camera. Excitation filter blocks are used to select a desired relatively narrow range of wavelengths with which to excite the fluorescent molecules. Selecting multiple filters matched to the excitation of different fluorophores (with minimal overlap) allows the imaging of different molecules simultaneously.

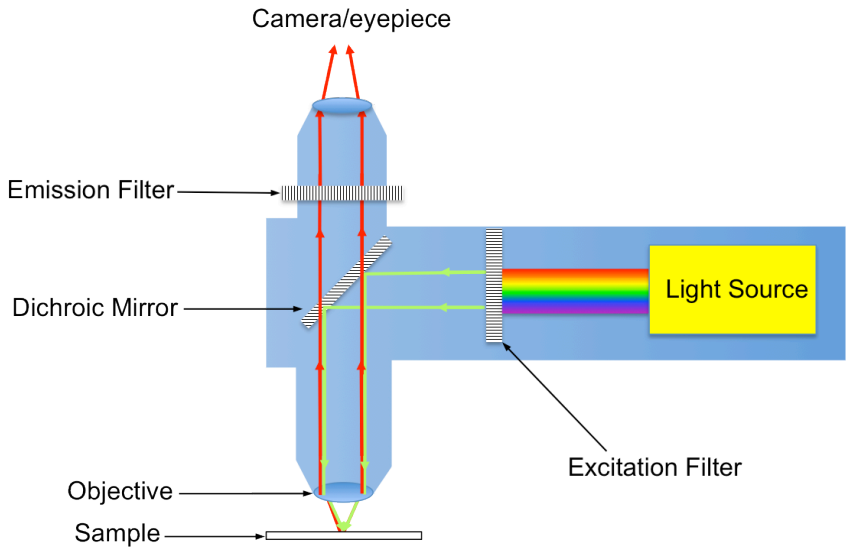

Figure 2.14: Basic configuration of an epi-fluorescence microscope with light path for epi-fluorescence mode.

2.2.4 Total Internal Reflection Fluorescence Microscopy

Total Internal Reflection Fluorescence (TIRF) Microscopy is a fluorescence technique used to minimise the excitation and detection of fluorophores to a thin region of the specimen by exploiting the exponentially decaying evanescent wave generated when light is totally internally reflected. By drastically reducing the background fluorescence from outside the focal plane the signal-to-noise ratio, and therefore spatial resolution of the sample is improved.

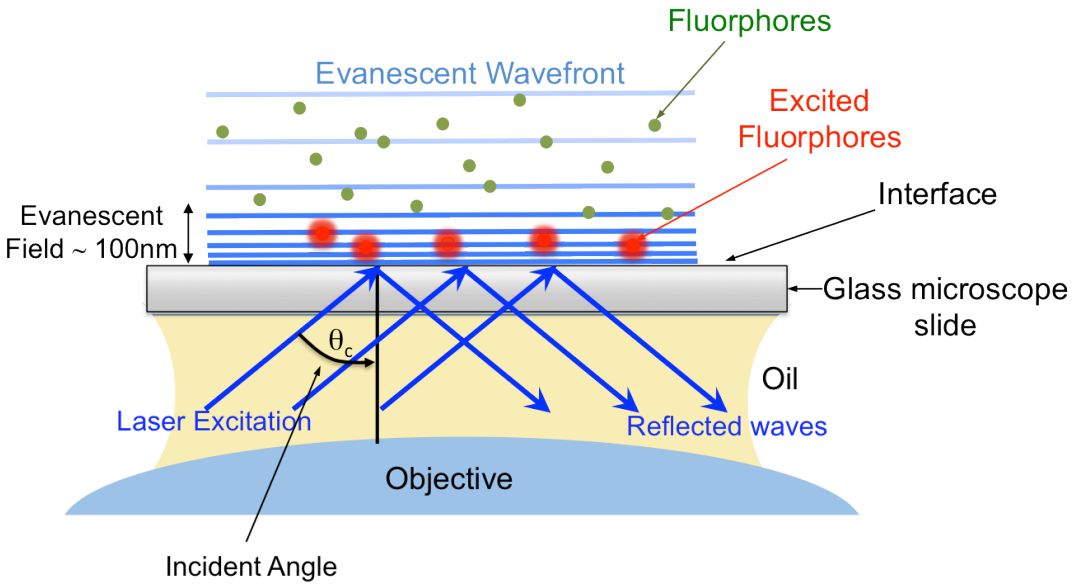

Figure 2.15: Schematic Illustration of the sample illumination of a total internal reflection fluorescence microscope in which fluorescent molecules nearest the glass are being excited.

To achieve total internal reflection the refractive index of the sample substrate must be greater than the that of the sample of interest, for the general setup of glass cover slip with an aqueous medium this condition is met. As light strikes the interface of the two materials it will be refracted at a an angle less than the angle of incidence, decreasing the angle further until it reaches parallel to the interface causes the beam to be reflected entirely back into the first medium, at an angle termed the critical angle (θ_c). When light is incident at angles greater than the critical angle, the reflected light generates electromagnetic field adjacent to the interface, in the lower-index medium. This evanescent field has the same frequency to the incident light,

and because it decays exponentially in intensity with distance from the interface, the excitation of fluorophores is limited to an area typically less than 100 nm in thickness.

2.3 Combined AFM-Fluorescence Microscopy

Fluorescence microscopy frequently has a number of drawbacks including lower spatial resolution and complex sample preparation. Another limitation of this microscopy is that the molecule must be bound to the fluorophore, which in turn, can alter the state of the molecule. On the other hand, AFM is a measurement made with a probe that is scanned cross the surface. It provides three dimensional molecular resolution of biological molecules with no additional contrasting agent (such as fluorophores, dyes, etc.) or compromise to the sample. The combination of these two techniques gives a full range of resolution from the mm down to the nm whilst allowing selected species recognition from the fluorescence with topography from the AFM.

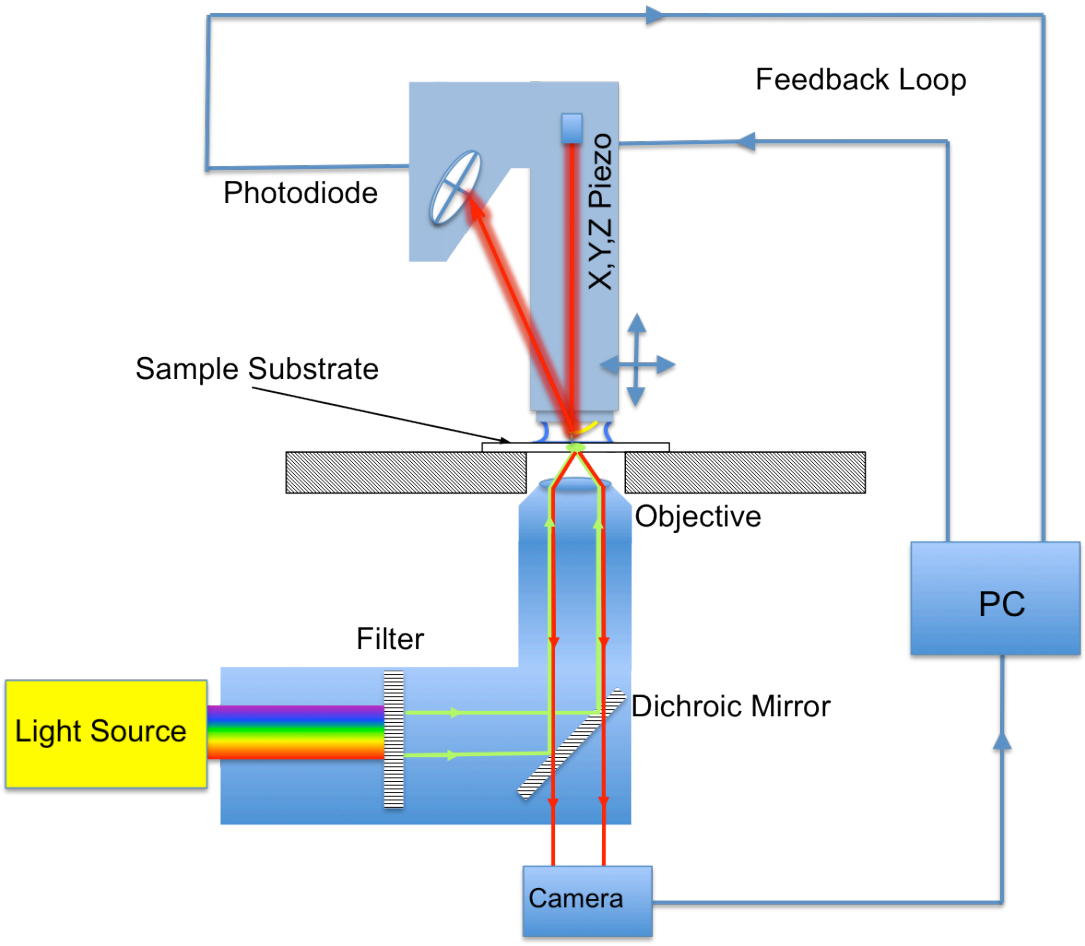

Figure 2.16: Schematic depiction of the Bioscope AFM. The sample is prepared on a transparent substrate from which fluoresence microscopy passes through from below whilst the AFM head assembly scans from above.

Successful simultaneous AFM and fluorescence measurements require specific configurations of both instruments. Firstly, the AFM must not interfere with fluorescence microcopy measurement. In addition, both measurements have potentially conflicting spatial constraints. The fluorescence microscope requires that the sample be close to the inverted microscope objectives. For the AFM, the cantilever must also reside close to the sample for imaging. Designed specifically so that the sample can be accessed both by the inverted optical microscope and the scanning stage of the AFM a typical setup is shown in Figure 2.16. In this assembly the AFM head contains the x,y and z piezos as well as the tip holder and photodetector.

2.4 Quartz Crystal Microbalance with Dissipation

The main component of a Quartz Crystal Microbalance (QCM) is the thin quartz disc between a pair of electrodes. The piezoelectric properties of quartz mean that applying electric fields to it results in mechanical strain, thus it is possible to excite the crystal to oscillation by applying an AC voltage across its electrodes. By oscillating the crystal at resonant frequencies (MHz) the sensor is highly sensitive to any additional mass adsorbed, causing a shift in these frequencies.

The resonant frequency (f) of the sensor depends on the total oscillating mass, including water coupled to the oscillation. When a thin film is attached to the sensor, the frequency decreases. If the film is thin and rigid the decrease in frequency is proportional to the mass of the film. In this way, QCMs operate as a very sensitive balance. In Quartz Crystal Microbalance with dissipation (QCM-D) not only is the frequency monitored with each oscillation cycle but the energy dissipation (damping) is also measured every time the drive generator output is stopped and the sensor oscillation starts to decay exponentially. The Dissipation factor D is inversely proportional to the decay time constant τ:

$$D = \frac{1}{\pi f \tau} \tag{2.13}$$

For a soft film attached to the quartz crystal the oscillations decay rapidly (high dissipation). In contrast, a rigid material gives low dissipation.

2.4.2 Sauerbrey Relationship

For a non-dissipative adsorbed masses ($D < 1\times10^{-6}$) the Sauerbrey relationship describes an accurate linear relation between the frequency change and the adsorbed mass [98]. The additional mass is assumed to be an extension of the existing crystal and therefore for the relation to prove accurate, the added mass Δm must be evenly distributed, relatively small (compared to the weight of the crystal) and rigid (Dissipation $< 1\times10^{-6}$). In

this case, the relationship between frequency and mass follows the Sauerbrey relationship:

$$\Delta f = -\frac{f_0}{\rho_q h_q}\Delta m = -n\frac{1}{C}\Delta m \quad (2.14)$$

Where ρ_q and h_q are the density and thickness of the quartz layer respectively and thus c is a property of the quartz crystal. n corresponds to the frequency harmonic (n = 1, 3, 5, 7...). For the 5 MHz quartz crystals used in this thesis c = 17.7 ng cm^{-2} Hz^{-1}. In an aqueous medium, changes in the resonant frequency of <0.2 Hz can be detected corresponding to a 0.5 ng/cm^2 mass sensitivity.

2.4.2 Voigt Model

Investigating protein adsorption with QCM-D often leads to dissipative systems for which Sauerbrey relation does not apply. The dissipative losses within the system can be described in terms of the energy lost during one oscillation $E_{dissipated}$ and the energy stored in the oscillating system E_{stored} leading to a unitless value for dissipation (D):

$$D = \frac{E_{\text{dissipated}}}{2\pi E_{stored}} \quad (2.15)$$

Energy loss in a system indicates the mechanical properties are viscoelastic. Viscoelastic materials can be related to energy storage and dissipation processes, resulting from the balance between applied stress and subsequent relaxation in the material. The Voigt model describes viscoelastic materials as a purely elastic spring in parallel with a viscous damper as shown in Figure 2.17.

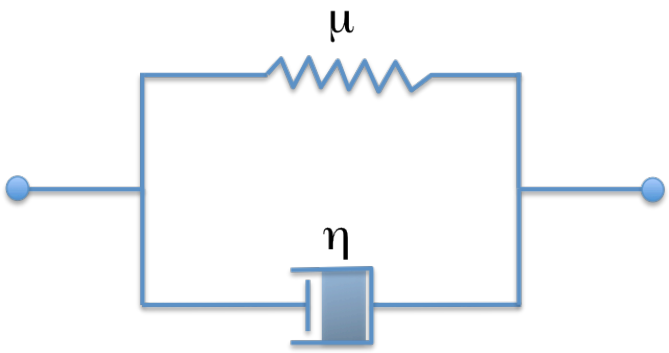

Figure 2.17: Schematic of the Voigt Model showing the parallel arrangement of a elastic spring of elastic modulus μ and a viscous dashpot of viscosity η.

The force on the sample is parallel to the substrate and thus shear viscosity coefficient η and a shear elasticity modulus μ are used model QCM-D data. The complex shear modulus allows one to cover both the elastic portion through the storage modulus and the viscous portion through the loss modulus.

$$\mu^* = \mu + i\omega\eta \tag{2.16}$$

The wave equation for the bulk shear waves propagating in a viscoelastic medium can be described by:

$$\mu^* \frac{\partial^2 u_x(y,t)}{\partial y^2} = \rho\omega^2 u_x(y,t) \tag{2.17}$$

Where u_x is the displacement. Considering the case of two viscoelastic layers covering the surface of a piezo-electric plate oscillating in a pure shear mode in bulk liquid shown in Figure 2.18, a general solution for the wave equation (Eqn. 2.17) can be found by applying ”no-slip” boundary conditions to the interfaces between the quartz and both viscoelastic Voigt elements [99].

$$\Delta f \approx -1/(2\pi\rho_0 h_0 \left\{\frac{\eta_3}{\delta_3} + \sum_{j=1,2}\left[h_j\rho_j\omega - 2h_j\left(\frac{\eta_3}{\delta_3}\right)^2 \frac{\eta_j\omega^2}{\mu_j^2+\omega^2\eta_j^2}\right]\right\} \tag{2.18}$$

$$\Delta D \approx -1/(2\pi\rho_0 h_0 \left\{\frac{\eta_3}{\delta_3} + \sum_{j=1,2}\left[2h_j\left(\frac{\eta_3}{\delta_3}\right)^2 \frac{\eta_j\omega}{\mu_j^2+\omega^2\eta_j^2}\right]\right\} \quad (2.19)$$

Where constants and variables are shown in Figure 2.18. From Eqn.s 2.18 and 2.19 it follows that a thin layer with a finite thickness will demonstate a different accustic response depending on the ratio between the viscosity and elasticity of the film.

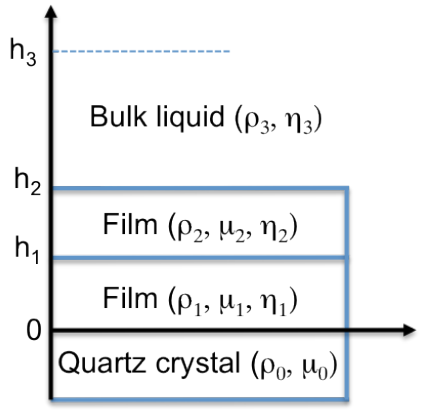

Figure 2.18: Schematic showing the geometry (and associated variables) of a quartz crystal microbalance covered by a double layer viscoelastic film oscillating in a bulk liquid.

2.4.3 QCM-D Data

The Voigt modelling of QCM-D data obtained in this thesis was undertaken using QTools software (QSense, Sweden). Data from actin layers bound to membranes found in this thesis required two layer modelling; to achieve a more accurate model the first layer is modelled on its own and then the values for this layer are fixed for the modelling of the second layer. Each layer was fitted using a fixed density (1050 kg m^{-3} for bilayer and 1200 kg m^{-3} for actin) whilst varying the viscosity (1x10^{-6} to 0.1 kg m^{-1} s^{-1}), shear (1000 to 1x10^{8} Pa) and thickness (1x10^{-12} to 1x10^{-6} m) between two specific broad limits. The model grid fits these values optimally to the experimental data. This is undertaken using logarithmic steps to increase the speed of the fitting process. The overtones required for fitting are then selected, a minimum of two are required but, within this thesis, at least three were always used (typically more). The standard deviation of each overtone

is then calculated, to measure the variance of each of the overtones with respect to fitting the model data. The final stage is to define the modelling process; this involves selecting the specific section of data requiring modelling, i.e. bilayer formation for layer one. The last stage is to define the vector parameters, which relate to how the model progressively fits the data points. At the start of the experiment, when dissipation is close to zero, the results of modelling can be found to vary greatly, thus it is essential that the modelling be undertaken in reverse to eliminate any problems due to the model initialising on an inaccurate description of the system.

Chapter 3
Experimental Protocols

This chapter documents the experimental procedures used and developed within this thesis, giving the details of the sample and substrate preparation methods used.

3.1 General Protocols

3.1.1 Substrate Preparation

3.1.1.1 Mica

The mica was punched to generate 1 cm diameter circles and then glued to magnetic AFM stubs with water resistant epoxy. The glue was allowed to cure for at least 24hr before use. All mica was freshly cleaved prior to use using adhesive tape to remove the top few layers.

3.1.1.2 Glass Cleaning

Piranha cleaning is used to ensure that glassware is free of organic contaminants and that the surface is suitably hydrophilic. Before undertaking piranha cleaning, substrates are cleaned using a less intensive protocol to reduce any excessive reaction to the substrate upon addition to the piranha solution. The pre-piranha process for cleaning glass is to wipe glass with a lens tissue that has been soaked in 10 % Decon90 and then rinsed. The glass is then thoroughly rinsed with de-ionised water. The glass is then sequentially sonicated in 10 % Decon90, MilliQ de-ionised water, iso-propanol and MilliQ de-ionised water with rinsing between each stage.

Piranha solution is a mixture of sulphuric acid H_2SO_4 and hydrogen peroxide H_2O_2 in a 3:1 ratio. Great care should be taken in the handling of piranha solution, as it is a highly reactive mixture. It is a strong oxidiser and will remove most organic matter whilst also hydroxylating the surface. The sulphuric acid was added to the Pyrex glass beaker first, followed by the

hydrogen peroxide. The reaction is exothermic and a thermometer must be used to monitor solution temperature and thus be used as a guide for mixing rate. Ideally the temperature should be kept lower than 100°C for safety reasons.

For the work contained in this thesis and specifically coverslip cleaning the piranha solution was made and allowed to cool to 90°C before adding the coverslips. The coverslips were then immersed for 5 min. This decreased the surface etching and was found to reduce the brittleness of the glass when being clamped into the required flow cell. After the 5 min immersion in the piranha solution all glassware was thoroughly rinsed in MilliQ de-ionised water. The remaining piranha solution must be neutralised with soda ash and diluted by a large volume of water. Piranha cleaned substrates were used on the day of cleaning, if not being used immediately on the day of cleaning they were stored in a beaker of de-ionised water.

3.1.1.3 Cleaning of QCM-D Crystals

Due to the nature of measurement made with QCM-D crystals they are very sensitive to any contaminants and their addition or loss. Therefore it was imperative that a good cleaning methodology was developed for the work being undertaken.

Silicon coated crystals were cleaned in a specially designed Teflon crystal holder that allowed good solvent access to the crystal faces and also protected the very delicate crystals. The crystals were first bath sonicated in 4 % sodium dodecyl sulfate (SDS) detergent for 15 min, then thoroughly rinsed in de-ionised water ensuring that the detergent was thoroughly diluted and that the crystals did not pass through the air water interface. The crystals were then sonicated in de-ionised water for a further 15 min followed by sonication in methanol for 5 min and then sonication in de-ionised water for 5 min. The crystals are then dried under a N_2 stream and put into the UV-Ozone cleaner for 30 min. After the UV-Ozone cleaner they were rinsed again with de-ionised water and dried under a N_2 stream. The crystals were

then used immediately, placing them into the QCM-D crystal holders and beginning the experiment.

3.1.2 Vesicle Formation

3.1.2.1 Tip Sonication

Tip sonication was used in lipid solutions which contained no protein as an alternative to extrusion. Tip sonication is used to generate lipid vesicles with a typical size ranging from 40-60 nm [100]. Dried lipids were solubilised in the required buffer and vortexed. In this current state the sample is a solution of multi-laminar vesicles (MLVs). The lipid suspensions were then tip sonicated (blasted using a pulsing ultrasound probe) for 30 min on a low power setting or until the solution became clear, creating a solution of small uni-lamellar vesicles (SUVs). The smaller size makes them ideal for the formation of lipid bilayers by the vesicle rupture process. During sonication the solution was kept cooled and nitrogen was blown over the top of the sonication vial to prevent oxidation. The resulting solution was micro centrifuged for 1 min at 13,000 rpm, to remove Ti particles broken away from the tip during sonication.

3.1.2.2 Extrusion

This method was used to homogenise vesicle sizes of lipid samples primarily with samples containing protein, aiding planar bilayer formation without damaging the proteins. Before use, the Avanti Polar Lipids mini extruder was cleaned by sonication of all sample facing parts in water then methanol. It was then thoroughly dried in a heated environment. The two syringes were thoroughly cleaned by passages with chloroform followed by de-ionised water or buffer. The extruder was then constructed as per the instructions (Figure 3.1), 'O' rings were inserted into both halves of the cell, two support filters were placed on each half over the small pore with a small droplet of buffer to increase adhesion. The filter of desired pore size (typically 50-400 nm) was then placed on the support and the two halves were brought together and secured in the metal mount. The lipid solution was pushed between the two syringes, back and forth through the filter, 11 times so that

removal of the extruded lipid solution occurs in the opposing syringe. The extruded lipid was then in the form of uni-lamellar vesicles, suitable for planar lipid bilayer formation. After use, the syringes were cleaned in the reverse order as previously described and facing parts are cleaned as before.

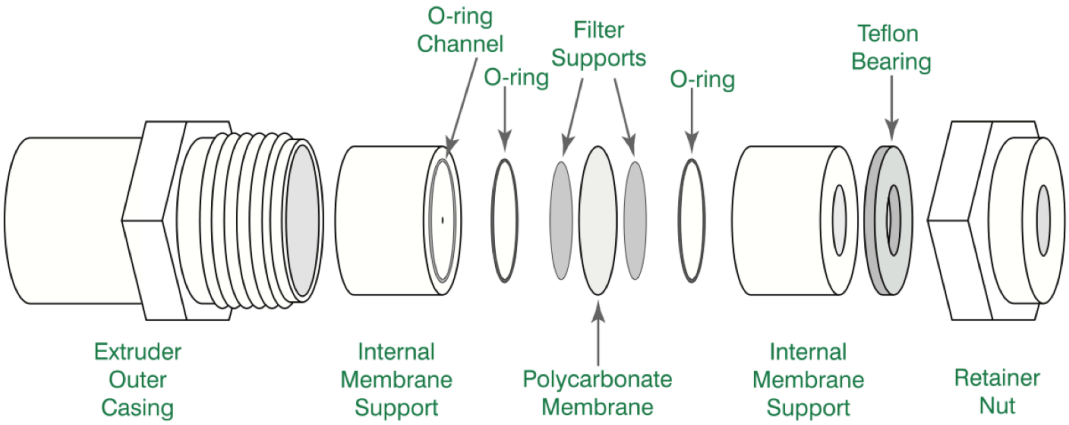

Figure 3.1: Schematic depiction of the Avanti Lipids mini extruder and its required construction layout for lipid vesicle extrusion.

3.1.3 Supported Lipid Bilayer Formation

Unless otherwise stated lipid bilayers were formed via adsorption and rupture from a vesicle solution (Figure 3.2). Tip sonicated or extruded vesicles were incubated with a substrate at a typical concentration of 0.1-1 mg/ml. Depending on the lipid composition and substrate the incubation conditions and incubation times were matched to aid bilayer formation. Typically untreated clean mica and glass have a net negative surface charge and therefore electrostatics play an important role in the vesicle rupture process. For vesicles containing any positively lipids such as DOTAP the electrostatic interaction between the substrate and vesicle is attractive and thus vesicles rupture on impact in de-ionised water (Figure 3.2a) [101]. Bilayer formation with neutral vesicles, for example DOPC, also occurred in de-ionised water conditions following the critical surface concentration of vesicles (Figure 3.2b). When using vesicles containing negatively charged lipids divalent cations such as Mg^{2+} were required in solution to screen the electrostatic repulsion. Typically negatively charged vesicles were incubated

with the substrate in 2 mM $MgCl_2$. After incubation for 30 min, the required sample buffer was exchanged at least 10 times to remove vesicles from the bulk solution and also any vesicles non-specifically bound to the bilayer surface.

When forming bilayers with lipids which have lipid fluid transition temperatures above room temperature (eg. DPPC has a of T_m = 41 ^oC) or which are expected to phase separate at room temperature, vesicles were incubated in an oven at 55 ^oC for 15-30 min. After incubation the sample was immediately rinsed with buffer which has also been heated at the same temperature, exchanging at least 10 times to remove vesicles before cooling.

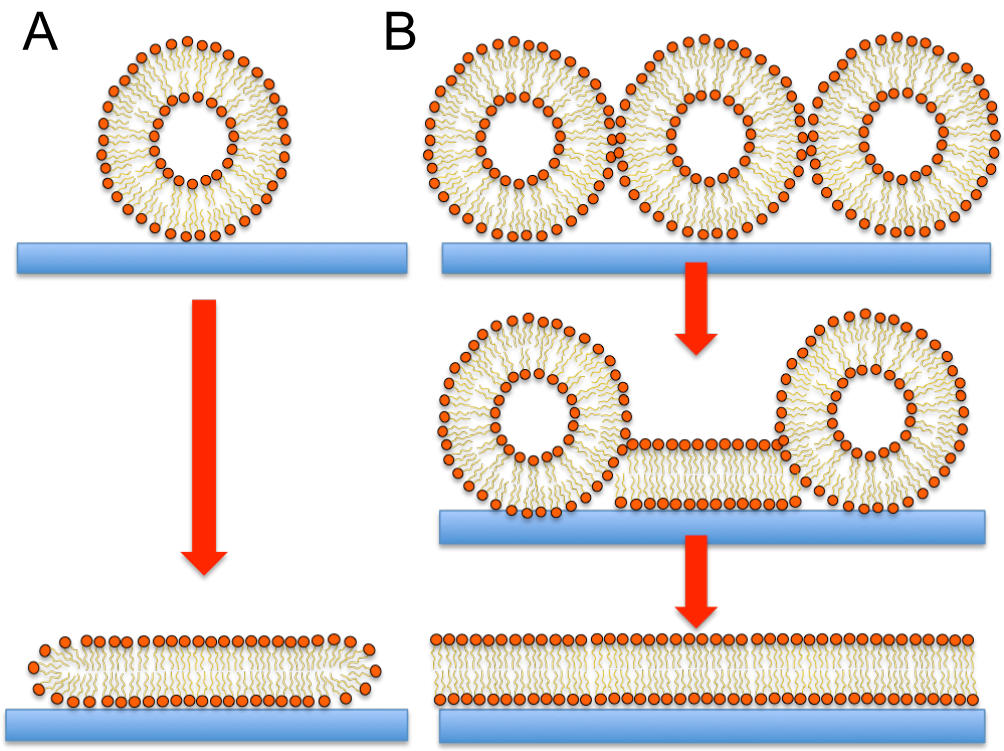

Figure 3.2: Schematic representation of the different routes for vesicle rupture and fusion leading to the formation of a planar supported lipid bilayer. The mechanisms shown are: (A) vesicle rupture induced by interaction with substrate, (B) vesicles rupture at a critical surface concentration and then leading edge induces rupture of surrounding vesicles [101].

3.2 Formation and Characterisation of Low Dimensional Supported Lipid Bilayers Protocols

3.2.1 Lipid deposition from AFM tips

Clean silicon nitride NP-S tips (Bruker) with typical spring constants ranging from 0.12 to 0.32 N/m were placed on glass cover slips with tip facing away from the glass. 10 µl of 5 mg/ml lipid in chloroform was then pipetted using a glass 50 µl syringe (Hamilton, Bonaduz) onto the back on the cantilever overflowing to the surrounding glass. The chloroform-lipid mix was then dried either under vacuum for 1-2 hr or under a stream of nitrogen for 10 min with no observable difference between either technique. Washing of excess lipid was performed by soaking the lipid coated tip in 200 µl of ultra pure water for 5 min followed by 5 x 200 µl rinses. Tips were then loaded into the AFM cantilever holder of either: a Bioscope with Nanoscope III controller, a Multimode 8 on a NanoScope V controller or a Dimension Fast-Scan Bio AFM (Bruker). Ultra pure water was added to freshly cleaved mica and the AFM-tip assembly was submerged before imaging. Unless otherwise stated writing of bilayers was performed by scanning the surface in contact mode and at room temperature (22 ^{o}C). To create lipid bilayer channels the mica surface was imaged for half a scan in contact mode with typical imaging gains and set points. The lines per scan were varied depending on the scan size and expected line width to maximize line density whilst minimizing overlap of written bilayers, for example a 30 µm area would be scanned with a tip velocity greater than 15 µm/s with 256 lines to give line separation of 120 nm.

3.2.2 High-speed atomic force microscopy (HS-AFM) of M2 Diffusion

HS-AFM observations were performed in tapping mode using a Dimension FastScan Bio AFM with Fast Scan Dx probes (Bruker), Short cantilevers designed for HS-AFM with a 15 µm length, a spring constant of ~ 0.25 N/m and a resonance frequency of 110 kHz. The force applied by the tip on the sample was minimised by maximising the set-point whilst maintaining

tracking of the surface. Under excessive forces the membrane channels were observed to be irreversibly damaged. Influenza M2 protein was stored in 4% methanol solution at 20 µg/ml, the protein was allowed to insert into the bilayer channels by addition to the solution at 5%, giving a final concentration of 1 µg/ml in 0.2% methanol.

3.2.3 Finite Element Analysis Modelling

Finite element calculations were carried out by solving the Nernst-Planck equation in COMSOL Multiphysics using the Chemical Reaction Engineering Module. The patterns were modelled as straight stripes of the same length and width as obtained in the experiment. Fluorescence recovery after photo bleaching (FRAP) was simulated by setting the concentration of one component in a round bleach spot region of the same size as in the experiment to zero while the rest of the pattern was modelled with a concentration of 1. The change of concentration in the bleach spot region was taken as the recovery curve of the bleach spot.

3.3 Lipid Domain Dynamics in Phase Separated Model Membranes Protocols

3.3.1 Bilayer Formation

Supported lipid bilayers were formed using the vesicle rupture method. The stock solutions of each lipid component (at 5 mM in chloroform, supplied by Avanti either dry or in a sealed vial dissolved in chloroform) were mixed in a small vial to the correct molar proportion. The chloroform was removed first by drying under a gentle stream of N_2 and then for at least a couple of hours under vacuum, before being hydrated with water to a final lipid concentration of 1 mg ml^{-1} and vortexed. This suspension was tip sonicated until clear, usually for 10 min, indicating the formation of small unilamellar vesicles (SUVs). 100 ml of this solution was introduced to a freshly cleaved mica substrate and incubated in a sealed humid chamber within an oven at 55 ^oC for 30 min. The bilayers were then rinsed across the top with de-ionized water at 55 ^oC to remove the remaining unruptured vesicles still weakly attached to the substrate, together with suspended vesicles, before allowing to cool to room temperature over 30 min. Rinsing is performed approximately 10 times with 200 mL fairly vigorous jets from a Gilson pipette, the wash directed parallel across the top surface of the bilayer.

3.3.2 AFM Imaging

AFM experiments at standard imaging speeds (2Hz line scan rate) at room temperature and above were performed using a Bruker Multimode AFM on a Nanoscope IV controller. Bruker NP probes were used, the shorter 0.12 N m^{-1} probe in preference. HS-AFM observations were performed in tapping mode using a Dimension FastScan Bio AFM with Fast Scan Dx probes (Bruker), with a spring constant of ~ 0.25 N/m and a resonance frequency of 110 kHz. The force applied by the tip on the sample was minimised by maximising the set point whilst maintaining tracking of the surface.

Temperature control was achieved on the Multimode AFM using a feedback controlled Bruker heater stage. The internal thermocouple in the

heater cap was disconnected, and the feedback controller was connected to a very fine thermocouple inserted in the AFM fluid cell and rested on the mica surface about 2 mm to one side of the probe, immersed in the liquid. A similar setup was used on the Dimension FastScan Bio AFM, utilising the built heat stage and connected temperature controller. A fine thermocouple was also inserted into the sample on the fast scan system to obtain a second measure of temperature.

3.4 Actin Binding Transmembrane Proteins in Phase Separated Lipid Bilayers

3.4.1 Actin Purification

Rabbit skeletal muscle actin was purified from rabbit skeletal muscle acetone powder following the method of Pardee and Spudich [102]. Briefly this process involves the immediate removal (following death) of the back and hind leg muscles of a rabbit in a cold room, the muscle is minced and mixed sequentially with buffers and filtered using cheesecloth after each step (whilst remaining in the cold room). The mince is then mixed with pre-chilled acetone and allowed to dry in a cold environment; this leaves rabbit skeletal muscle acetone powder at which point it is stored at -80^{o}C. After this a re-suspension buffer is used and then a filtration step through glass wool. Then the actin undergoes polymerisation and subsequent depolymerisation cycles with centrifugation steps to remove the α-actinin and tropomyosin, leading to a final step of dialysis to leave the actin in monomeric form. It is then snap frozen in small aliquots prior to storage at -80°C. Actin purity is tested by SDS-PAGE (Figure 3.3) and concentration determined by BCA.

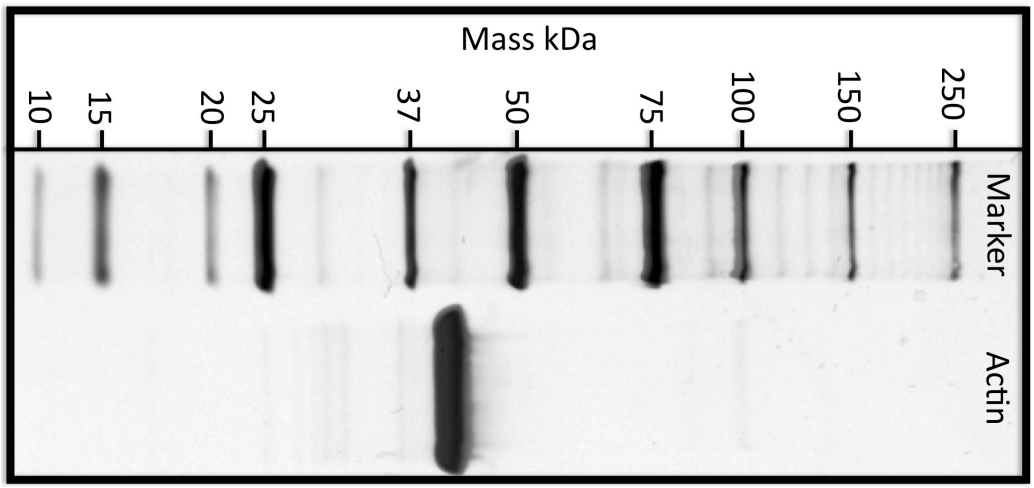

Figure 3.3: SDS-PAGE showing the purity of the final actin stock after the purification following the method of Pardee and Spudich [102].

3.4.2 Ponticulin Purification

D. discoideum strain AX3-K, was grown axenically to a concentration of $1x10^7$ cells/ml. Ponticulin was purified from the harvested cells according to the method of Chia et al [40]. However, during routine testing for activity, after the F-actin affinity column purification stage, it was noticed that a high-speed spin sedimented most of the contaminating protein in the extract [103]. Thus, instead of using the final steps of the Chia method (gel filtration), a high-speed ultracentrifugation step (300,000 g, 4 °C, 1 h) was used. As can be seen in Figure 3.4, the pellet from the high speed ultracentrifugation step contains virtually all the contaminating protein from the sample. While a small amount of ponticulin (at 17 kDa) can also be seen, this is only a small fraction as compared to the total ponticulin present in the supernatant. Densiometric analysis of the supernatant shows that ponticulin is 97 % pure and that only 0.2 % of the ponticulin is lost in the ultracentrifugation process.

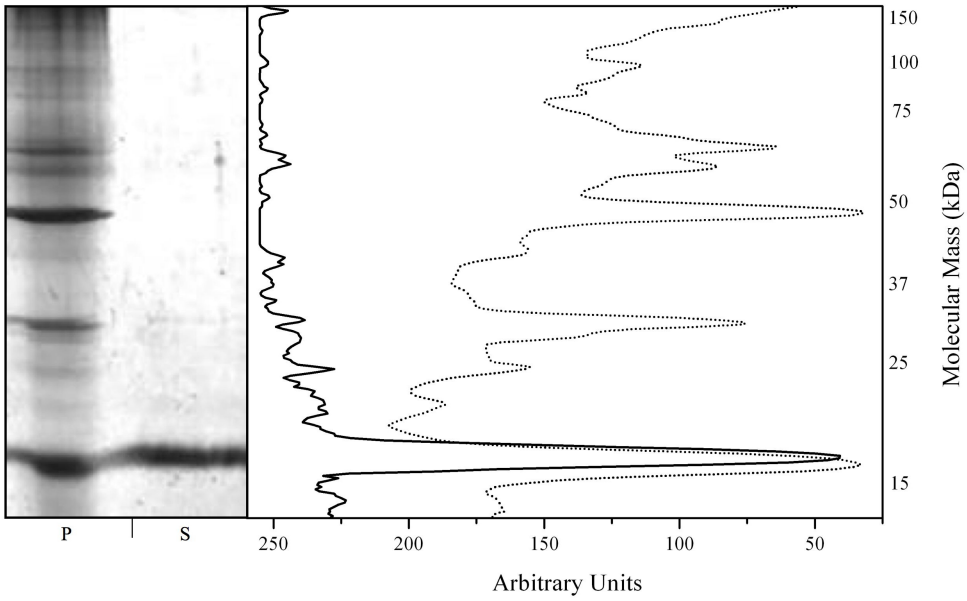

Figure 3.4: SDS-PAGE showing the purity of the final ponticulin stock after the modification of the original method by Chia et al. [40] to an ultra-high speed centrifugation step rather than the previously described HIC or gel filtration step. Where P is the pellet lane and S is the supernatant lane and the full pellet is run alongside 0.002 % of the supernatant. The gel shows the removal of nearly all proteins that are not the same mass as pontiuclin.

3.4.3 Detergent solubilisation and rapid dilution

This procedure was used to incorporate the transmembrane protein ponticulin within vesicle membranes. The desired lipid mix was dried from a 1:1 methanol/chloroform solution, under nitrogen for 15 min. This was then dried further in a vacuum desiccator for a minimum of 2 hr, preferably overnight. The dried lipid was stored under argon at -25 ^{o}C until use. The lipid was re-suspended in 1.37% (w/v) octyl-β-D-glucopyranoside, added incrementally until the solution became optically transparent upon vortexing [104]. When ponticulin was included, in a 0.6% (w/w) ratio with the lipid, the amount of detergent required was reduced to compensate for that present in the ponticulin stock solution. The re-suspended solutions were then allowed to equilibrate at 4 ^{o}C for 15 min. A rapid dilution was performed by adding the detergent to a large volume of 10mM Tris buffer (pH 7.5) such that it was diluted below its critical micelle concentration (0.7% w/v) [105]. The detergent based solution was pipetted into the centre of the buffer solution obtaining an octyl-β-D-glucopyranoside concentration below 0.01%. The solution was then centrifuged at 370,000 g, at 4 ^{o}C for 1 hr, to pellet out the vesicles from the solution, using a Beckman Ultracentrifuge and a 70 Ti rotor. The supernatant containing the detergent was removed and the pellet was resuspended with a small volume, typically 500µl, by vortexing with buffer. To further remove detergent in the solution the rapid dilution, centrifugation and re-suspension of the pellet step was repeated.

The resuspended vesicle solution was subsequently extruded using the method described in section 3.1.2.2. Vesicles were incubated with mica at 40 ^{o}C for 30 min in 2 mM $MgCl_2$, 10 mM Tris pH 7.5 buffer following which rinsing was performed with 10 mM Tris pH 7.5 buffer.

3.4.4 G-Actin Binding

Before use, the G-actin solution was allowed to thaw and equilibrate on ice for 30 min. The G-actin solution was then diluted to the desired working concentration of 0.4 mg/mL in G-buffer (5 mM Tris-HCl at pH 8, 0.02 mM $CaCl_2$, 1 mM DTT, and 0.2 mM ATP). The diluted actin was then centrifuged

(100 000*g*, 4 °C, 1 h) to remove any large actin crystals generated by the snap freezing process. The supernatant was collected and used the same day. When required the respective bilayers were incubated with G-actin at a concentration of 1 μM.

3.5 Actin Polymerisation at Cationic Lipid Bilayers Protocols

3.5.1 Supported Lipid Bilayer Formation

Lipid vesicles of various compositions were tip sonicated and incubated with mica, glass or silicon coated QCM-D crystals in de-ionised water (for cleaning protocols see section 3.1.1). If the samples contained lipids with phase transition temperatures above 25 ºC they were incubated in a sealed humid chamber within an oven at 50 ºC for 20 minutes. Other lipid mixtures were incubated at room temperature. Rinsing was performed with a pipette as described in section 3.1.3.

3.5.2 Actin Treatment

Rabbit skeletal muscle actin was purified as described in section 3.4.1. After a 30 min thaw at 4 ^{o}C the diluted actin was then centrifuged (100 000g, 4 °C, 1 h) to remove any large actin crystals generated by the snap freezing process. The G-actin solution was diluted to the desired working concentration of 0.04mg/ml in G-buffer (5 mM Tris-HCl pH 7.5, 0.02 mM CaCl2, 0.2 mM ATP and 0.5 mM DTT).

3.5.3 AFM Imaging & Analysis

AFM experiments were performed at room temperature (22ºC) using a Bruker Multimode 8 AFM on a Nanoscope V controller. Oxide sharpened silicon nitride tips (Bruker) with typical spring constants of 0.32N/m were used in either tapping mode or peak-force tapping mode. All images were performed on mica substrates mounted on Teflon discs in G-buffer conditions. Filament surface coverage was calculated using a bearing analysis. To avoid miscalculation caused by tip convolution filament density and filament packing fraction were determined by importing images into imageJ and manually tracing individual filaments with segmented lines. Summed lengths of all filaments were converted to an area or packing fraction by assuming a constant filament thickness of 7.5nm.

3.5.4 QCM-D Measurements

QCM-D measurements were performed using a QSense E4 multifrequency QCM-D instrument (Q-Sense, Gothenburg, Sweden) in a flow through cell of 40 µL volume. Data from 15, 25, 35, 45, 55, and 65 MHz overtones (3^{rd}, 5^{th}, 7^{th}, 9^{th}, 11th, and 13th, respectively) were collected. Before use, all SiO_2 crystals were cleaned by ultrasonication in 0.4% SDS for 15 min followed by copious rinsing and ultrasonication in de-ionised water for 15 min. The crystals were then dried under nitrogen and UV-ozone cleaned for 30 min. After UV-ozone treatment, they were rinsed with de-ionised water, dried under nitrogen, and used immediately. Initially, the system was filled with buffer such that the resonant frequencies of the overtone to be used could be found. The vesicle solution was injected, under a constant flow of 40 µL/min, at a concentration of 0.1 mg/mL. Frequency and dissipation changed in a manner characteristic of vesicle adsorption and then rupture, to form a planar bilayer. Upon reduction of the dissipation peak to a minimum, indicating complete bilayer formation, the bilayer was rinsed first with de-ionised water and then with buffer to removed adhering vesicles. After bilayer formation, G-actin was added at 14 mL/min and the change in frequency and dissipation were monitored. The actin layer was modelled using the QTools software (QSense AB, Gothenberg, Sweden) with a Kelvin−Voigt model and a minimum of three overtones.

3.6 Self Assembled Actin Coated Lipid Microbubbles Protocols

3.6.1 Microbubble Formation and Coating

To form lipid microbubbles, lipids were pre-mixed in chloroform then dried under nitrogen gas followed by vacuum desiccation. The solution was then resuspended and vortexed in 5 mM Tris pH 7.5 before being bath sonicated for 1 hr. C_3F_8 gas was then bubbled through the lipid liquid for 5 min saturating the solution and vial headspace. A mechanical shaker was then used to rapidly shake the solution for 10 s to form the microbubbles. Rabbit skeletal muscle actin was purified as described in section 3.4.1. Actin coated microbubbles were produced by incubating the lipid coated microbubbles with 10% volume actin at 0.4mg/ml for 30min in appropriate buffer. Before use, the G-actin solution was allowed to thaw and equilibrate on ice for 30 min. The G-actin solution was then diluted to the desired working concentration of 0.4 mg/mL in G-buffer (5 mM Tris-HCl at pH 7.5, 0.02 mM $CaCl_2$, 1mM DTT, and 0.2mM ATP). The diluted actin was then centrifuged (100 000*g*, 4 °C, 1 h) to remove any large actin crystals generated by the snap freezing process. The supernatant was collected and ready for use in G-actin experiments. To form F-actin filaments, P-buffer (500 mM KCl, 50 mM $MgCl_2$, and 10 mM ATP) was added 10% by volume. Actin was then allowed to polymerise at room temperature for 45 min. Phalloidin (Invitrogen, OR, USA) was added at an equimolar concentration to prevent depolymerisation of the F-actin and was allowed to bind for 15 min. In the case of gelsolin cut filaments, gelsolin (Cytoskeleton Inc. CO, USA) was added before polymerisation with 10% 500 mM KCl, 50 mM $MgCl_2$, 10 mM ATP, 2mM $CaCl_2$ buffer by volume and allowed to polymerise for the same time. When required, rhodamine or biotinylated actin (Cytoskeleton Inc. CO, USA) were diluted to working concentrations of 0.4 mg/ml by G-buffer and added to unlabeled actin at a ratio of 1:9 (w/w), to provide a sufficient fluorescence signal for fluorescence microscopy or binding to neutravidin surfaces.

3.6.2 Fluorescence Microscopy

Fluorescence microscopy images were taken on either a Nikon Eclipse E600 epi-fluorescence microscope or Nikon 90i. Images were obtained using either a 40x objective or a 100x oil immersion objective, imaging through cleaned glass coverslips.

3.6.3 Microbubble Dissolution

Microbubbles were held in a 50 μm deep fluid cell with fluid inlet and outlet ports and replaceable glass slide top. 500 ml of buffer (5 mM Tris pH 7.5) was degassed by stirring the solution under vacuum at pressure of 20 mbar. The degassed solution was then flowed through the fluid cell containing the microbubbles under a flow rate of 2 ml min^{-1} such that several chamber full volumes were passed through an inlet. The change in bubble radius was then imaged over time with light microscopy.

3.6.4 Force Spectroscopy

Microbubble force spectroscopy was performed with cantilevers without tips allowing the bubbles to be compressed effectively by two opposing flat plates.

3.6.4.1 Substrates for the attachment of microbubbles

The microbubbles to be studied were immobilised on a gold-coated self-assembled monolayer functionalised substrate containing a biotinylated thiol (Asemblon, WA, USA). To obtain a thin gold coating on glass cover slips, thermal evaporation (Auto 306, Edwards) was used. To obtain a high quality gold layer it was important that the initial surface was thoroughly cleaned. This was undertaken by sonication in: Decon90 at 2 % for 15 mins, rinsing with de-ionised water to ensure removal of detergent, sonication in de-ionised water, another rinsing step, then sonication in propanol, rinsed with propanol and then drying under a N_2 stream.

Once cleaned, the substrates were mounted onto a rotating plate inside the thermal evaporation chamber. Gold and chromium are loaded into the boat behind the evaporation shutter, the evaporation chamber is then sealed and pumped down to a pressure less than 1 x 10^{-6} mbar (cooled by liquid nitrogen to obtain this pressure). After reaching the desired pressure the gold is melted by slowly increasing the current being passed through the boat to 36 A thus melting the chromium/gold and out gassing the contaminants, the current being passed is then reduced to 32 A and the shutter is opened. The current is adjusted to ensure an evaporation rate that remains between 0.12 and 0.16 nm s^{-1}. Initially a 2 nm layer of chromium is evaporated onto the surface followed by 20 nm layer of gold. The chamber is then allowed to cool under pressure until it reaches room temperature.

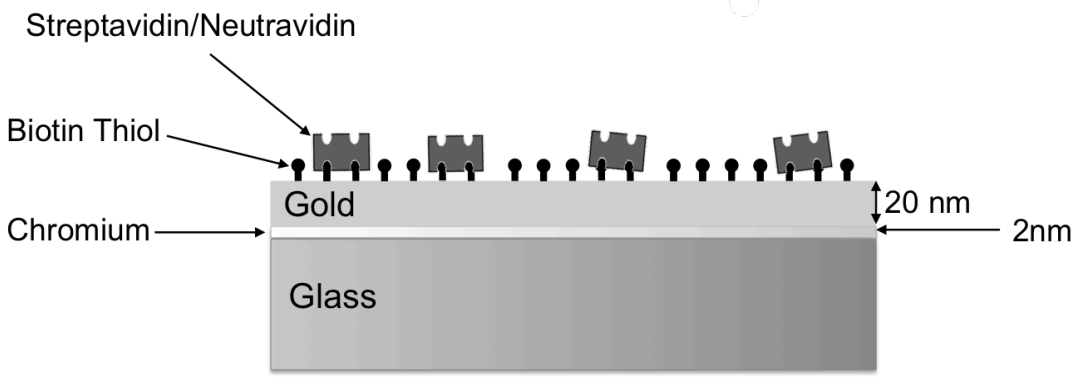

Figure 3.5: Illustration showing substrates used to attach microbubbles to a surface before performing force spectroscopy measurments. 2 nm of chromium followed by a 20 nm layer of gold were evaporated onto a glass cover slip. This allowed the formation of a biotin thiol SAM and the subsequent binding of streptavidin or neutravidin proteins with available binding sites for biotin linked actin and lipids.

The SAMs were formed by incubation for 12 h in a 15 mM methanolic solution containing a mixture (90:10 mol.%) of 6-mercaptohexanol (Sigma-Aldrich, Poole, UK) and a biotinylated thiol (Asemblon, WA, USA).

For the attachment of the lipid coated bubbles the substrate was then incubated for 1 h in a 0.1 mg ml^{-1} solution of neutravidin before being placed in contact with the microbubble solution overturned for 1 hr assisting the attachment of floating microbubbles via biotin–neutravidin links. In the case of the actin coated bubbles, 10% biotinylated actin was included in the actin mix and the bubbles were incubated with the substrate for a period of 2 h, then rinsed under flow with excess (5 mM Tris pH 7.5).

3.6.4.2 Cantilever Calibration

To obtain microbubble stiffness data it is essential to accurately quantify the spring constant (K_c) of the cantilever to enable the force applied by the AFM cantilever to be measured, whose deflection is already accurately determined. At experimental deflections the cantilevers follow Hooke's law such that the applied force (F) is equal to the cantilever deflection (Z_C) multiplied by the spring constant of the cantilever (K_C)

Depending on this relation, and by considering the cantilever geometry, a formula is given (Eqn. 3.1) that can calculate the spring constant of rectangular cantilever using its geometry, where, E is the elastic modulus of the cantilever material, and (w),(L), and (t_C) are the width, length, and thickness of the cantilever respectively [106,107].

$$K_C = \frac{F}{Z_C} = \frac{EWt_c^3}{4L^3} \qquad (3.1)$$

However a more accurate method is the called the thermal tune method [108]. This considers the cantilever as a harmonic oscillator in equilibrium with the surroundings, measuring the mechanical response of the cantilever due to the thermal fluctuations (when the tip far from the surface to prevent hydrodynamic damping) and is represented as:

$$H = \frac{P^2}{2m} + \frac{1}{2} m\omega_0^2 q^2 \qquad (3.2)$$

Giving (q) as the oscillator displacement, (p) is the momentum; (m) mass of oscillating body, ω_0 represents the resonant angular frequency. The equipartition theory presents the quadratic term of the equation as:

$$\left\langle \frac{1}{2} m\omega_0^2 q^2 \right\rangle = \frac{1}{2} K_B T \qquad (3.3)$$

Where K_B is Boltzman constant = 1.38 x 10^{-23}, (T) is the temperature in Kelvin. As $\omega_0^2 = \frac{K}{m}$ with K as the spring constant of the cantilever, equation 3.3 is converted to:

$$K_C = \frac{k_B T}{\langle q^2 \rangle} \qquad (3.4)$$

This method is the most popular in use for its accurate results and ease of application. The spring constants of cantilevers used in this study were measured using the automated thermal tune function within the Asylum Research software with the cantilever in solution.

3.6.4.2 Microbubble Measurements

The mechanical properties of the microbubbles were determined using an MFP-3D AFM (Asylum Research, Santa Barbara, CA, USA) combined with tipless silicon cantilevers (Nanosensors, UK) with a spring constant range of kc = 0.05-0.1 mN m^{-1}. All fluid force–indentation measurements were made in the closed z loop mode, which eliminates any non-linear piezo hysteresis effects. Before each experiment the spring constant of each cantilever was calibrated using the thermal tuning method and the laser sensitivity was measured by pressing the cantilever end down onto a hard surface assuming no deformation. Using the optics within the AFM system, the cantilever is located above the pole of the microbubble and 50 force curves are taken with a constant loading rate of 2 μm s^{-1}.

Chapter 4

Formation and Characterisation of Low Dimensional Supported Lipid Bilayers

This chapter focuses on developing lipid nanolithography methods to produce membranes, under liquid, with resolution down to sub 10 nm scales. Fine control over the written bilayer dimensions was achieved through varying the scanning tip velocity. The diffusion of the lipids in these systems was characterised using FRAP to show as the widths of the bilayers are reduced the diffusion of lipids also reduces, implying closer packing of lipids in the vicinity of membrane boundaries. High-speed AFM was used to study the diffusion of the membrane protein M2 in these channels. This chapter also presents preliminary work on using the deposition technique to pattern membranes at reduced scales.

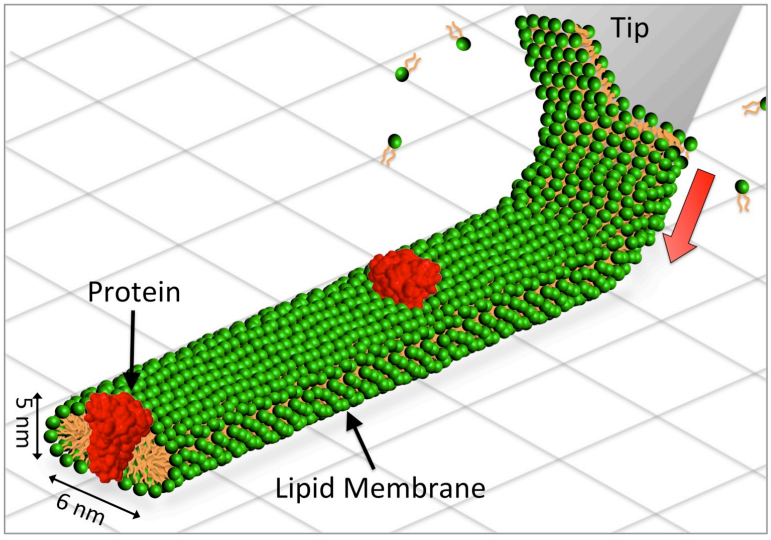

Figure 4.1: Illustration showing the deposition of lipid from the AFM tip onto a surface. The tip is traveling in the opposing direction to the deposition. Included in the membrane are two M2 proteins which are added separately after lipid deposition.

4.1 Deposition of Lipid Bilayers

Spatial control over supported lipid bilayers has been a widely pursued goal in bioanalytical chemistry. In the past microcontact printing has been a widely used method to pattern bilayers at the micron to much larger scale. The method is analogous to potato printing in that it uses a master polydimethylsiloxane (PDMS) stamp with recesses defining the pattern, the stamp is inked by placing the PDMS in contact with the desired material to be deposited and then placing it in contact with the substrate. For lipid membrane microcontact printing, typical inks used are fibronectin or BSA. Printing of these prevents the adsorption and rupture of lipid vesicles thus allowing bilayers to be exclusively formed in the non-printed areas [109,110]. It has also been shown that the stamp can be used to directly print the bilayer onto the surface [110].

A photolithographically patterned polymer lift-off technique was demonstrated by Orth et al in which bilayers bound to a patterned polymer are mechanically peeled away. The peeled away membrane leaves patterned bilayers in silicon dioxide areas of the substrate which have not been coated with polymer. This method was able to achieve bilayer resolution down to 1 μm [111].

The application of scanning probe lithography has been previously used to both remove and deposit lipid membranes. Jackson and Groves used AFM to completely remove lipid membranes in pre-patterned 1 × 1 μm chromium arrays and then backfilled these regions with new lipid components [112]. A similar method was used by Cremer at al to create the supported bilayer by etching 55 nm gaps into a BSA layer with an AFM tip and forming lipid bilayers by back-filling these etched regions via vesicle fusion [113]. Attempts by this study to form lipid structures with dimensions less than 55 nm were unsuccessful leading to the suggestion that they may have found the limit at which the smallest supported membranes could be produced, determined by the interplay between line tension and the work of adhesion [113]. Additionally it was suggested that BSA may influence the edge structure of the membrane.

Dip-pen nanolithography methods for patterning bilayer and multi-bilayers were initially developed by Lenhert *et al.* who were able to "write" bilayer patterns with feature sizes down to 100 nm under carefully controlled humidity [13,114,115]. Dip-pen nanolithography was carried out on commercial instruments equipped with environmental chambers and inkwells. The tips were "inked" by bringing the tip into contact with a lipid inkwell and increasing the humidity to 70% for at least 5 min. Tips were then placed in contact with the surface at 70% humidity before depositing lipid either in air at various humidity conditions or being completely immersed in solution [114]. This method was also used to show simultaneous deposition of multiple functional lipids, including biotinylated and nickel chelating lipids, allowing the binding of cells after lipid deposition [116,117]

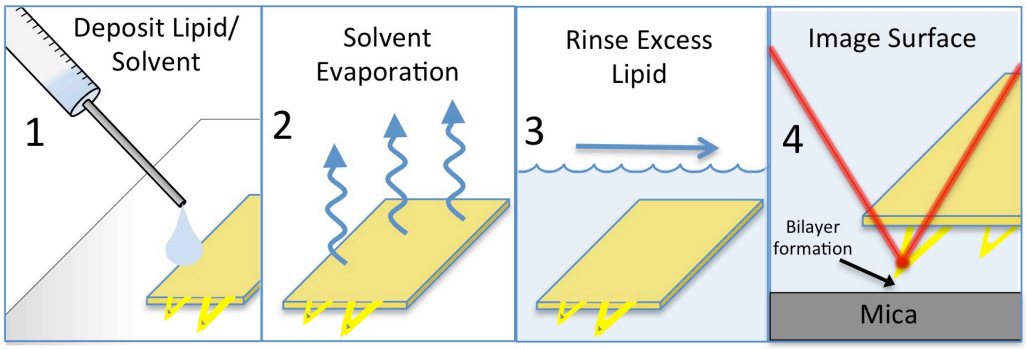

Figure 4.2: Schematic of technique used to create 1D lipid bilayers: (1) lipid is deposited with a 5 µl droplet of lipid in chloroform (5 mg/ml) onto the probe with the tips facing up (away from a glass substrate), (2) the solvent is allowed to evaporate under vacuum for 10 min, (3) excess lipid is removed from the back of the cantilever by submerging in water for 5 min, (4) to write the lipid the surface is imaged under aqueous liquid conditions using contact mode or tapping mode.

In the work within this thesis, to deposit lipid onto the mica, AFM tips were initially primed with a lipid coating (Figure 4.2), by pipetting 10 µl of lipid solution, in chloroform at a concentration of 5 mg/ml, onto the back of the cantilever with tips lying face up on a clean glass cover slip. The lipid was then allowed to dry under vacuum or a stream of nitrogen. The dry lipid coated tips were found to be stable for several days. To then deposit lipid onto the mica surface, the cantilever was first immersed in 200 µl de-ionised water for 5 min and then rinsed with 5 repeated 200 µl pipetted injections of

water across the top of the tip to remove excess lipid. The cantilever was then loaded into the AFM and used to scan the surface under aqueous fluid conditions. The lipid spreads from the tip as it scanned as depicted in Figure 4.1. An alternative method used to coat the tip was performed by taking a clean tip, loading it into the AFM head and then scanning a clean piece of mica in air. With the tip in contact with the surface, 50 μl of 5 mg/ml lipid solution in chloroform was added to the mica therefore coating the mica, tip and tip holder through capillary action. The tip was then removed from the AFM and allowed to dry under vacuum. Once dried of solvent, the excess lipid was removed from the tip through 5 min immersion in water and repeated pipetting. The AFM tip holder was cleaned of lipid using a methanol rinse and the mica was cleaved. The fresh mica surface was then imaged with the lipid coated tip under fluid condition to deposit a bilayer. Although proving a successful method to deposit bilayers, throughout this chapter this 2nd method wasn't used as it required more cleaning and produced no noticeable difference in lipid deposition. Both these methods differ from previous dip pen lipid work by Lenhert et. al. in that it can be done without humidity control or dedicated dip-pen lithography systems.

4.1.1 Single Phase Bilayer Deposition

Using the technique shown in Figure 4.2 lipid deposition was found to occur with both common imaging modes i.e. contact mode and tapping mode. Figure 4.3 shows an AFM image comparing deposition for both contact mode (right) and tapping mode (left). Height profiles of the deposited lipid on the surface give a height of 4.2 nm, consistent with a single bilayer. The lipid patches created in contact mode show much greater deposition of lipid, implying the lipid flow from the tip is faster in contact mode. This may be expected since by the very nature of the imaging mode the tip spends less time in contact with the surface in tapping mode.

Whilst all imaging was with aspect ratios which scan in the x direction i.e producing squares or horizontal lines, vertical lines can also be seen linking separate scans (Figure 4.3). These lines are created by the tip remaining in contact during a change in scanning position whilst changing

the scanning offsets. The features created in Figure 4.3 show the ability of this technique to create small patterned membrane via basic scanning commands i.e. without lithography software.

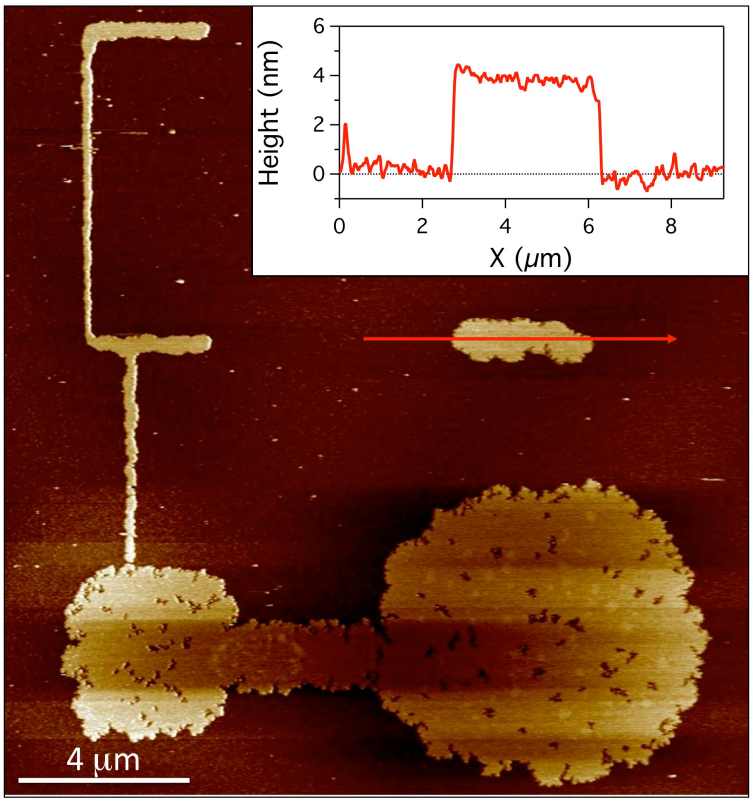

Figure 4.3: AFM image of DOPC bilayers deposited via continuous scanning. The large patch to the bottom right and strip above were created in contact mode using 4 scans with 3 μm area with aspect ratios of 1:1 and 30:1 respectively. Lipid patches to the left were created with the same scan settings but in tapping mode. The inset height profile shows the height along the red arrow in the AFM image.

Capturing images *in-situ*, during lipid deposition in tapping mode allowed the lipid deposition to be observed over time in (Figure 4.4). For this 6 x 6 μm area, at a tip velocity of 100 μm/s, it takes 9 scans to create a DOPC bilayer with small defects. Height analysis of the defects and bilayer patches is consistent with a single bilayer (5-5.5 nm). Figure 4.5A shows the resulting patch of lipid (after scanning the 6 μm area in Figure 4.4) with dimensions greater than 9 μm, this indicates a 3 μm spreading of lipid away from the target area. In addition to contact and tapping mode, peak force tapping mode also showed bilayer deposition at similar rates to contact mode, typically only requiring 1-2 scans.

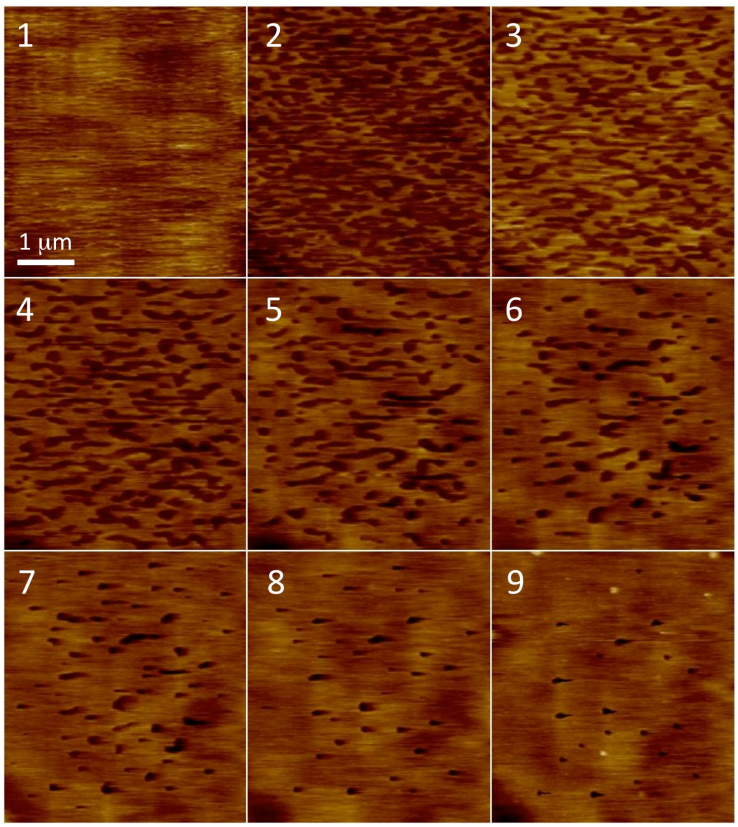

Figure 4.4: Formation of DOPC bilayer from a lipid coated AFM tip in tapping mode. The 6 μm area was scanned at 15 seconds per frame with 256 lines at a tip velocity of 100 μm/s.

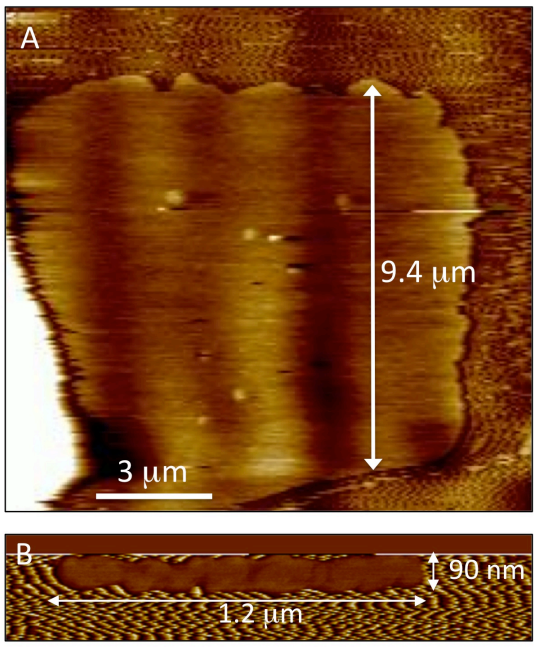

Figure 4.5: AFM images of bilayers created with lipid coated tips in tapping mode. (A) The DOPC patch created via in-situ tapping mode deposition in Figure 4.4. (B) Sphingomyelin lipid bilayer created multiple tapping mode scans of a 1 μm area with an aspect ratio of 30:1.

Despite the reduced mobility of gel-phase lipids it was found sphingomyelin bilayers, which have a Tm of 41 ^{o}C, could also be deposited onto the mica via the tip, as shown by Figure 4.5. This opens up the possibility of patterning gel phase bilayers and backfilling with fluid lipids using the gel phase as a barrier.

4.1.2 Multi-Phase Bilayer Deposition

The tip deposition method also allows the preparation of multi-phase bilayers to be written at room temperature. The formation over multiple scans of a biomimetic two-phase bilayer system from DOPC-Sphingomyelin-Cholesterol (25-40-35) coated tip in tapping mode is shown in Figure 4.6.

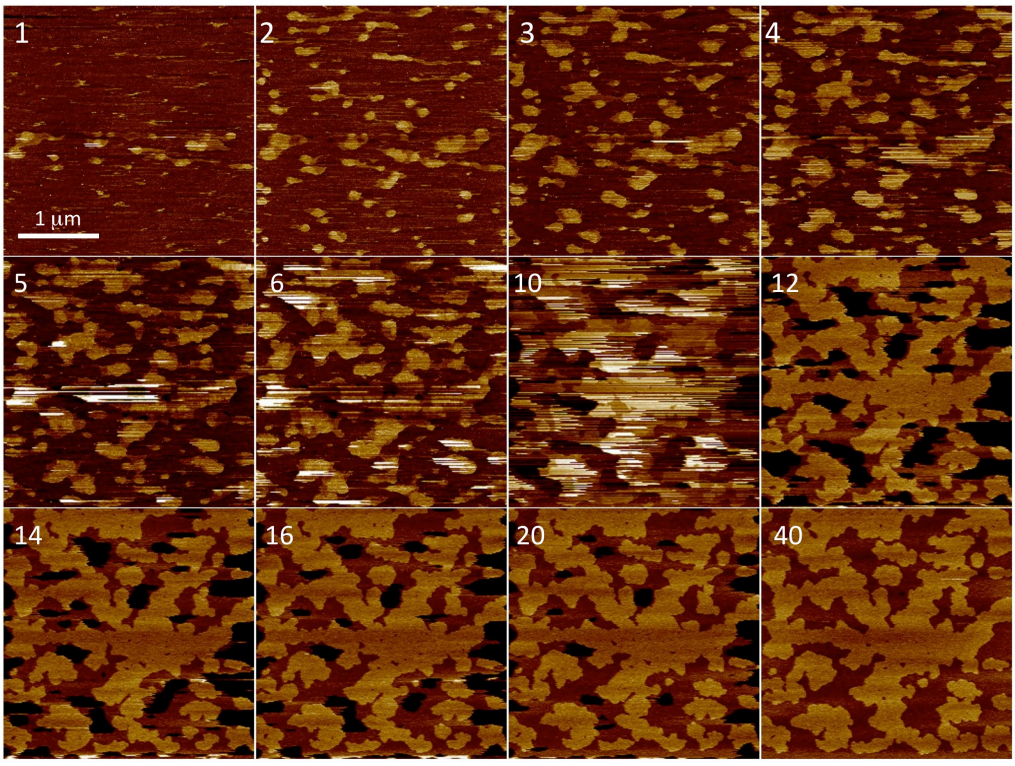

Figure 4.6: Formation of phase separated bilayers from a DOPC:Spingomyelin:Cholesterol coated tip in tapping mode. Images taken at rate of 46 s/frame (full image size 3µm).

Initially the more ordered phase is deposited in predominantly circular patches which grow in size and allow the deposition of the more fluid phase to the inter-regions eventually filling the 3 μm scan area. The number of scans taken to create a complete bilayer is greater than with DOPC alone, this may be due to a slower flow rate of lipid off the tip for lipids with lower mobility.

The phase separation of a DOPC:Sphingomyelin:Cholesterol (50%-30%-20%) created in contact mode at room temperature shows comparable liquid ordered and liquid disordered domains to that observed for the same composition formed via vesicle fusion (Figure 4.7). The area fraction of Liquid ordered domain was measured to be 23% for the vesicle fusion method and 30% for the tip deposition technique. Although these areas fractions are comparable, further studies of deposition at temperatures above the transition temperature of the two phases may produce more reliable and more consistent phase behaviour. The preparation of bilayers via vesicle fusion requires drying of lipids, tip sonication followed by vesicle fusion taking a typically taking minimum of 2 hr, whilst this tip method can completed within 30 min, reducing preparation times by a factor of 4.

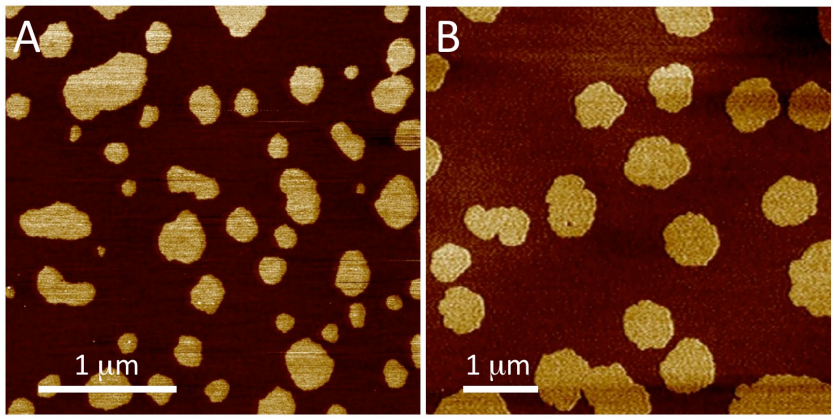

Figure 4.7: Comparison between phase behaviour of DOPC:Spingomyelin:Cholesterol (50%-30%-20%) mixtures for bilayer formed by vesicle fusion (left) and tip deposition (right) methods. Bilayers were deposited and imaged at room temperature. Full image size 3 μm; z-color scale 2 nm.

4.2 Controlled Bilayer Deposition

The deposition of lipid on the surface requires the transfer of material from the tip to the substrate, it is expected that the amount of material transferred should be governed by the material-surface adhesion, the spreading characteristics of the lipid and the amount of time spent in contact. This section describes the deposition characteristics of DOPC on mica in contact mode, and its dependence on tip velocity. When imaging the surface the AFM tip performs a raster scan, in which one continuous line zigzags in the scan direction. This raster is most evident when depositing lipid in contact mode using a low number of scan lines with a relatively large area so that the deposition lines do not overlap (Figure 4.8).

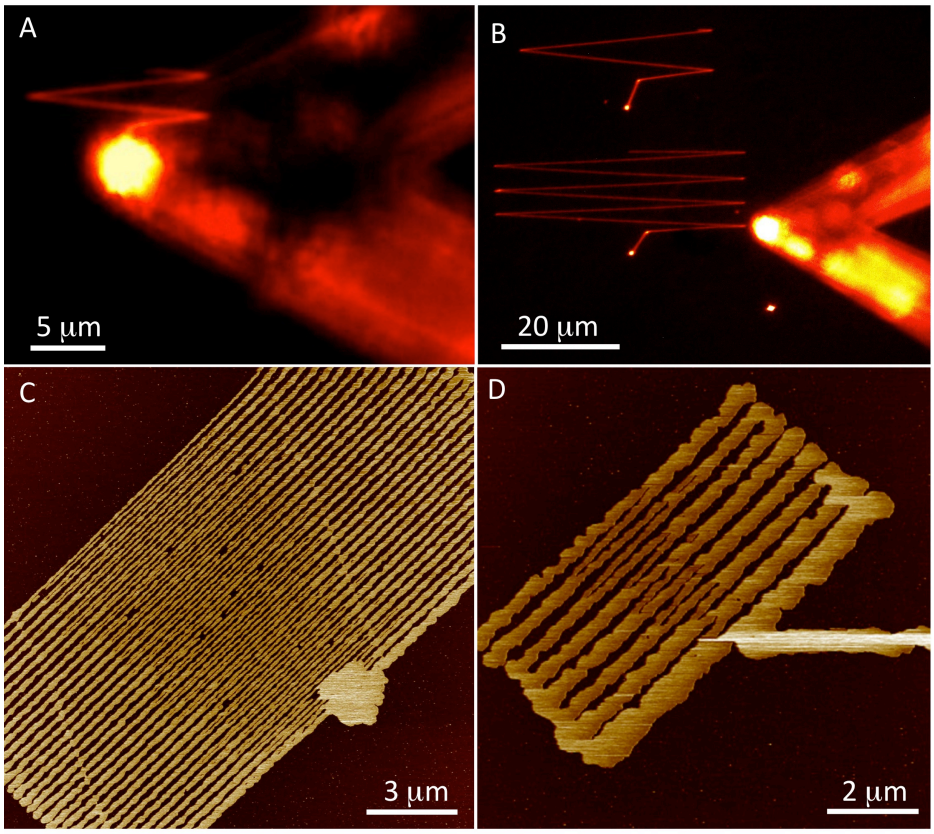

Figure 4.8: Single line deposition of lipid created by performing half a scan in contact mode with lipid coated tips. (A,B) False coloured fluorescence images of *in situ* writing of DOPC- 2%Texas red DHPE lipid on mica. AFM images of DOPC bilayers written at tip velcoities of 10 μm/s (C) and 2 μm/s (D).

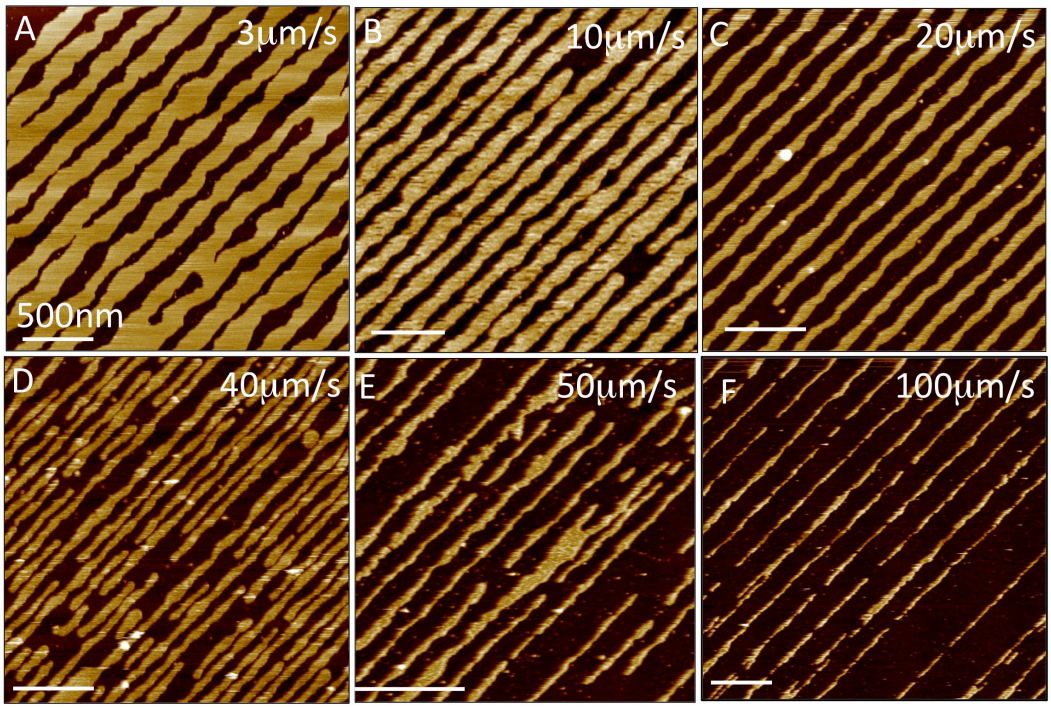

Figure 4.9: Effect of tip velocity on written bilayer line width with DOPC lipid coated tips. (A-F) AFM images of bilayer lines written by single tip traces per line at 3,10, 20, 40, 50 and 100 μm/s (scale bars = 500 nm).

Inclusion of 2% Texas-red-DHPE lipid in the lipid mix allowed visualisation of the deposition process using fluorescence. Figure 4.8A clearly illustrates this raster nature, in which a 10 μm area is scanned with 4 lines using a DOPC-2% tx-red-DHPE lipid coated tip. Using an increased number of lines in Figure 4.5B, the initial contact point can been seen at the bottom of the zigzag with a high intensity single point, the tip then begins tracing (left to right) and retracing the surface (right to left) before reaching the top of the scan area at which point the tip is manually retracted. The fluorescence images also show the coating of lipid at very high concentrations at the tip apex with less lipid coating the flexible cantilever. Although it is possible to image the deposited lipid with the same tip used to write, the continual deposition of lipid fills any patterning, however the same tip can easily be used if removed from the AFM and rinsed with methanol to remove lipid bound to the tip. AFM imaging (Figure 4.5 C,D) shows how the zigzags can become merged at the raster apexes, as the lipid lines overlap.

Lines created by a single traverse of the tip can only be observed in the central regions of these images.

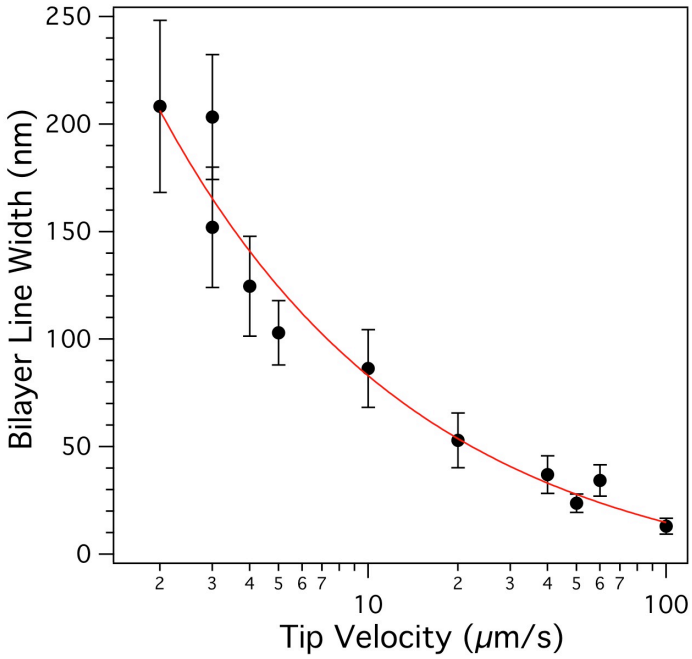

Figure 4.10: Plot of bilayer width against tip velocity used during deposition. The data is fit to $w = 315/v^{½}$ where, w, is the bilayer width and, v, is the tip velocity.

By systematically varying tip velocity, Figure 4.9, shows that as tip speed, *v*, is increased less lipids was deposited and the resulting bilayer stripes were narrower, providing fine control over stripe width (*w*) between 10 nm and 200 nm. At higher velocities the number of line defects increased, this could be due to either noise, improper tracking of the surface or an inherent characteristic of the lipid spreading. The relationship between *w* and *v* follows an inverse-square-root relation: $w = A/\sqrt{v}$, where A is a constant (Figure 4.10). This behaviour suggests that the stripe width is kinetically controlled, i.e. governed the spreading of the bilayer on the surface. The spreading of lipid on planar surfaces has previously been shown to exhibit square-root-of-time dependence due to competition between a spreading power S and a resistive drag γ_s [118-120]:

$$w(t) = \sqrt{\frac{St}{2\gamma_s}} = \sqrt{\beta t} \qquad (4.1)$$

Taking a contact time of d/v, where d is the tip diameter, the spreading coefficient β can be determined from the fit in Figure 4.10 to give a value of 6 $\mu m^2/s$ which is in reasonable agreement for PC lipids on mica which have been shown to have values of ~ 40$\mu m^2/s$.[118]

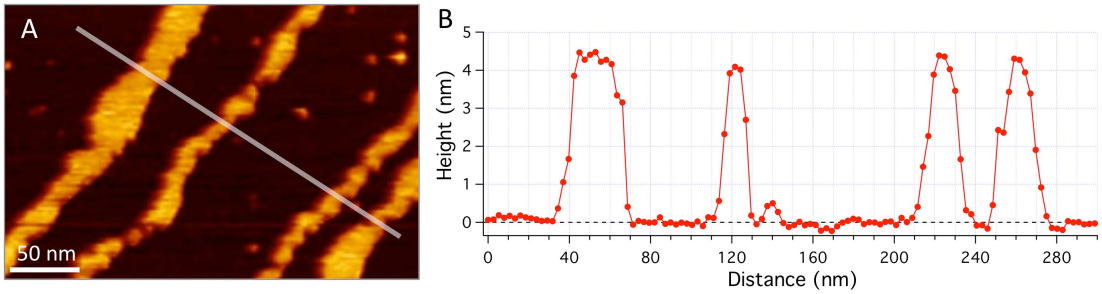

Figure 4.11. (A) High resolution AFM of DOPC bilayers written at 100 µm/s with height profile (B) along the white line showing widths of 20 nm, 8 nm, 10.5, and 11 nm (± 2.5 nm).

The average minimum continuous bilayer widths observed were 10 ± 2.5 nm wide (Figure 4.11 A,B) as measured through the full-width-half-maximum. However removing the tip convolution created by a 4-8 nm radius tip gives an average width of 6 ± 2.5 nm. The hydrophobic penalty associated with exposing the hydrophobic tails at the edges of the bilayer to water causes the bilayer to remodel into a hemi-micellar configuration (Figure 4.12) [121]. For a 6-10 nm wide bilayer with ~ 2.5 nm of lipid on either side taken up by the edges leaves only 1-5 nm wide regions of planar lipid, thus these systems are in the regime of tens of lipid molecules, or single membrane proteins, wide. Since a significant portion of the lipids are located in edge regions in these systems, this makes them ideal for studying lipid behaviour at bilayer boundaries, which is crucial for understanding transient defects formed in cell membranes and hence for a range of important biological processes such as membrane fusion, endocytosis, viral infections, and budding [122].

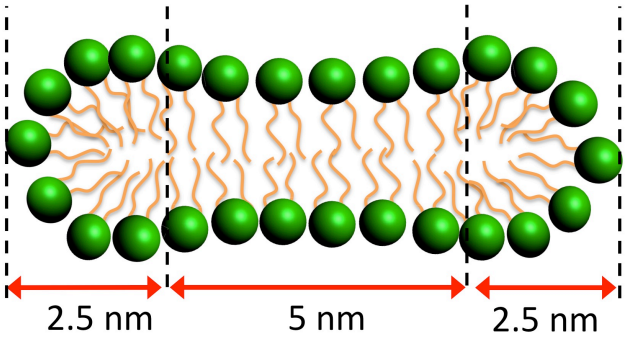

Figure 4.12: Illustration showing the cross-section of a 10 nm wide bilayer with hemi-micellar caps preventing exposure of the hydrophilic tail groups to water.

The energy cost per unit length for reorganising the lipids at the edge takes the form of edge tension (γ) whilst the interaction between the bilayer and the surface is given by the adhesion energy (W_A) which should more than counteract the penalty due to the line tension for the bilayer to be stable (Figure 4.13)[123]. The total energies of a patch of bilayer can then be described by the following pair of equations:

$$E_{edge} = \gamma \, . perimeter \tag{4.2}$$

$$E_{Surface} = W_A \, . Area \tag{4.3}$$

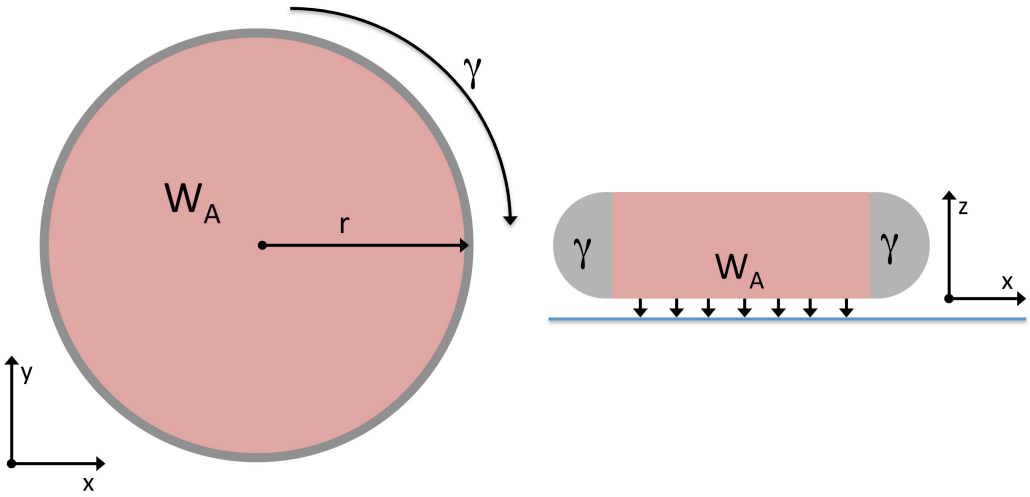

Figure 4.13 Schematics (left, top view and right, side view) showing the energies associated with a circular lipid bilayer disc. The bilayer is held to the surface by an adhesion energy (W_A) dependent on the bilayer area while the unfavourable line tension (γ) acts around the perimeter.

For a bilayer to be energetically stable the surface adhesion energy (Eqn. 4.3) must be greater than or equal to the edge energy (Eqn. 4.2) in order for a stable SLB to form. To find the minimum stable dimensions of a bilayer the energies can be equated. For a circular bilayer disc (Figure 4.13) this gives a minimum stable radius, r, of:

$$r = 2\frac{\gamma}{W_A} \tag{4.4}$$

Taking W_A to be 3.5×10^{-3} J/m^2 for PC vesicles adhering to mica[124] and γ to be 27.7 ± 2.5 pN [125], Eqn 4.4 gives an minimum disc radius of 16 nm. For the bilayer channels observed in this thesis the dimensions are width, *w,* and length, *l,* and thus the minimum stable bilayer dimensions becomes [113]:

$$W_A \times w \times l = \gamma \times 2(w + l) \tag{4.5}$$

For *l* > 1 μm Eqn 4.5 predicts a minimum for the value for *w,* for a stable DOPC bilayer bound to mica, to be around ~ 15 nm, which is reasonably consistent with the observations within this work. These theoretical arguments also suggest that the stability of the smallest membranes maybe be increased by increasing the adhesion to the substrate via substrate-lipid interaction or by reducing the line tension through edge active lipids/molecules.

Measurements of the bilayer height for different widths of bilayers show a sudden decrease as bilayer width is reduced below 50 nm (Figure 4.14). This suggests a change in the lipid packing in these low dimensional systems.

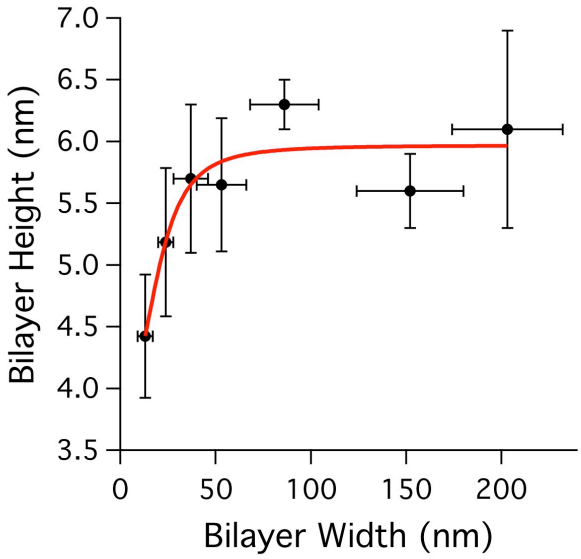

Figure 4.14: Measured bilayer height for varying bilayer channel width.

4.3 Lipid Diffusion

4.3.1 Experimental FRAP

Lipid membranes are highly dynamic structures and to function properly the lipids must be able to diffuse freely. Lipid mobility was determined using FRAP (fluorescence recovery after photo-bleaching, section 2.2.2) for lipid bilayer stripes of varying width. Figure 4.15A shows an example of images taken 10 s, 11 min and 24 min after bleaching an area of nanopatterned bilayer stripes (37 nm wide). The organisation of the bilayer stripes is a 100 x 50 μm raster pattern, as shown schematically in Figure 4.15B, the bleaching was performed with a circular spot size of 48 μm diameter. Over 24 min the bleached area is almost completely recovered indicating that the lipids in these thin channels are mobile.

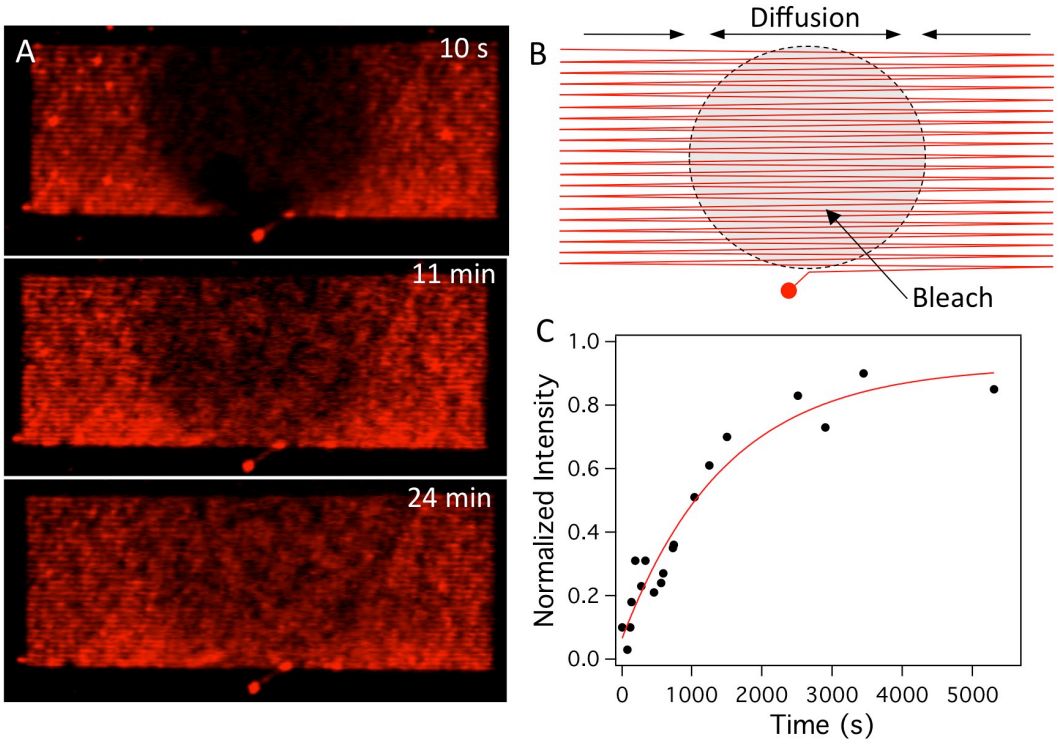

Figure 4.15. Diffusion behaviour of lipids in nanoscopic bilayers. (A) FRAP images of multiple 2.0 mol % Texas red DHPE/DOPC bilayer stripes as a function of time with stripe widths of 37 ± 9 nm. The bleached bilayer spot is shown immediately after, at 11 min and at 24 min after bleaching (bleach spot radius = 24.1 μm). (B) Schematic of the bleaching of zig-zag bilayer stripes shown in (A). (C) Plot of normalised fluorescence intensity change of a bleached area, lines show fit used to determine diffusion constants and mobile fractions.

Analysis of the normalised fluorescence intensity curve vs. time (Figure 4.15C) allows determination of the lipid diffusion coefficient and mobile fractions using the method outlined in 2.2.2 [97]. For the 37 nm wide lines in Figure 4.15 the diffusion constant was calculated at 0.32 ± 0.08 $\mu m^2/s$ with a mobile fraction of 0.92.

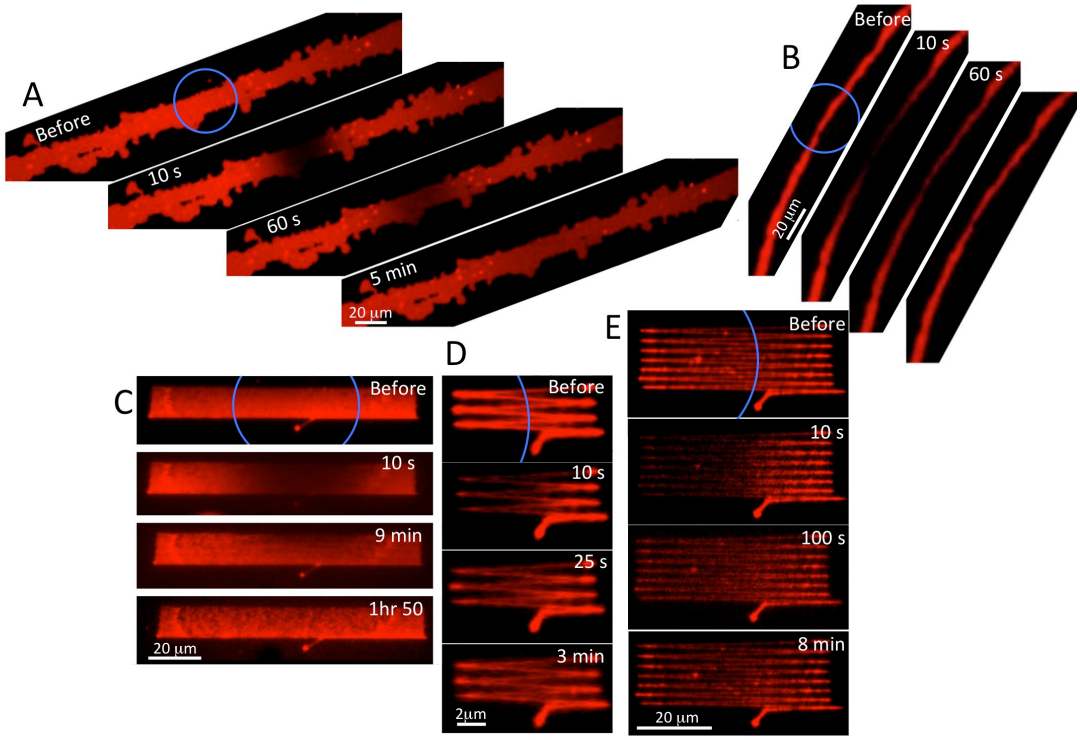

Figure 4.16: FRAP images of DOPC bilayer lines with 2.0 % Texas red DHPE as a function of time with lines widths of (A) 14 µm, (B) 1.8 µm, (C) 52 nm, (D) 120 and (E) 86 nm. The images show the bilayer before bleaching (with blue circular line highlighting region to be bleached), immediately after bleaching, and at 2 more time intervals later.

Lipid lines greater than 200 nm in width were created via contact with between the lipid coated cantilever chip and substrate by binging a chip without cantilevers into contact with the substrate. This allowed the diffusion constant to be investigated for bilayer stripes at widths ranging from 14 µm down to 37 nm (as created by the tip). Figure 4.16 shows a selection of the resulting bilayers formed with images of before and at intervals after bleaching, the corresponding plots of normalised fluorescence intensity change with time are shown in Figure 4.17A.

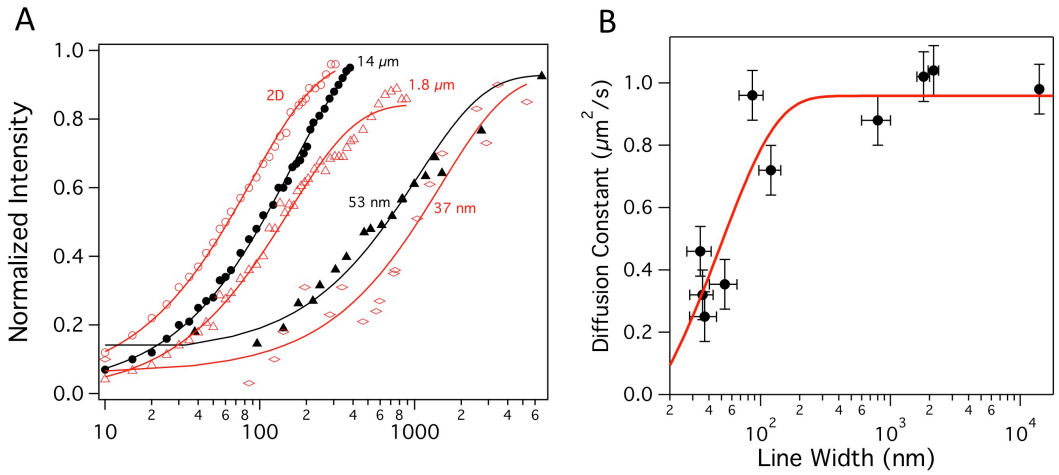

Figure 4.17. (A) Plots of normalised fluorescence intensity change of a bleached area, lines show fits used to determine diffusion constants and mobile fractions. (B) Diffusion constant as determined by 1D diffusion equation as a function of bilayer line width.

Lipid molecules in stripes wider than 100 nm had an average diffusion coefficient of 0.95 ± 0.06 $\mu m^2/s$ (Figure 4.17B), in agreement with measurements of macroscopic 2D DOPC lipid bilayers created by vesicle fusion on mica (0.90 ± 0.10 $\mu m^2/s$). As the stripe width was decreased below 100 nm the lipid mobility decreases sharply to values around 0.3 ± 0.1 $\mu m^2/s$ for bilayer with widths ~ 35 nm. The mobile fraction varied in the range from 0.86 to 0.98 but showed no correlation with stripe width.

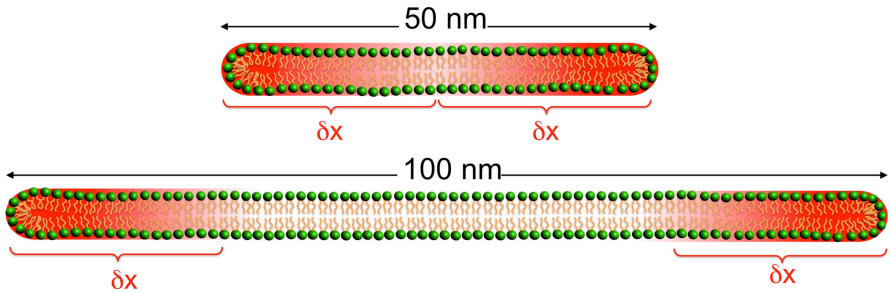

Figure 4.18: Schematic representation showing the reduced mobility propagating a distance δx (~25 nm) from the bilayer edges leading to the decrease in diffusion constants observed below 100 nm.

The decrease in diffusion coefficient with stripe width likely reflects the increase in bilayer fraction taken up by lipids, in the micellar caps, plus small fluctuations in bilayer width. The literature, based on both experiment and simulation, has been split over whether the lipid should be more “ordered” or “disordered” in these micellar caps, with perhaps a growing evidence that the presence of a membrane edge leads to higher density and reduced mobility [121,126,127][128]. How far this region of reduced mobility propagates into the bilayer has not previously been determined. If the region of reduced mobility propagates a distance δx from the bilayer edge then one would expect a dramatic reduction in mobility when the bilayer stripe width approaches 2δx (shown schematically in Figure 4.18). The results, Figure 4.17, show that this reduced lipid mobility occurs for stripe widths less than 50 nm implying that the influence of the reduced mobility region extends for up to 25 nm from the bilayer edge. The measurements of lipid bilayer height showed for decreasing bilayer width the height also decreases for widths less than 50 nm (Figure 4.14). This decrease in height suggests conformational changes in lipid packing, however, bilayers typically increase in thickness with increased order and thus the data on decreasing height may suggest a tilted phase is induced at bilayer edges.

4.3.2 Finite Element Analysis

To investigate the effect of confinement in a model uniform system, finite element calculations were performed by solving the Nernst-Planck equation in COMSOL Multiphysics. The patterns were modelled as straight stripes of the same length and width (Figure 4.19A). Experimental values of the 2D diffusion of DOPC bilayers were used for lipid mobility values in the model. FRAP was simulated by setting the concentration of one component in a round bleach spot region (of the same size as in the experiment) to zero while the rest of the pattern was modelled with a concentration of 1. The change of concentration in the bleach spot region was taken as the recovery curve of the bleach spot. Analysis of bilayer recovery (Figure 4.19B) using the 2D diffusion equation showed good agreement with the experimental values for bilayer widths between 100 nm and 10 μm. However the simulations did not show any change in diffusion behaviour for bilayer widths

below 100 nm. In addition the results showed the application of the 1D diffusion equation is only valid when the bleach spot radius is significantly greater than the width of the bilayer stripe.

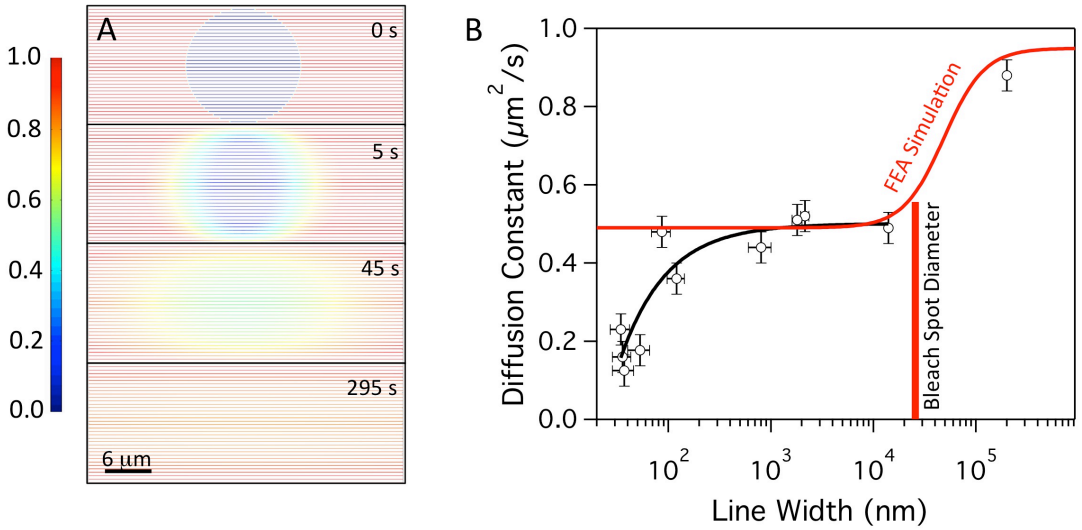

Figure 4.19: Finite element analysis modelled diffusion of in varying line widths. (A) Simulated FRAP experiment on 36 lines, 53 nm wide and 100 µm long model 2D channels. Colour bar represents relative concentration. (B) Comparison of finite elements analysis results to measured lipid diffusion (all analysed using the 2D diffusion equation) with bleach spot radius indicated on graph.

4.4 Protein Diffusion

The controlled formation of bilayer stripes whose widths are sub 100 nm allows the investigation into effects of confinement on protein-lipid and protein-protein interactions, for integral and or peripheral membrane proteins. As a first demonstration this section reports on the insertion of the integral membrane protein M2, of influenza virus that forms a pH sensitive proton channel in the viral lipid membrane and is essential for viral replication. After addition to the solution above the bilayer, small objects were found to appear in the bilayer stripes, AFM height measurements show an average protrusion of 1-2 nm (Figure 4.20) consistent with previous AFM measurements[129] and structural data of M2[39].

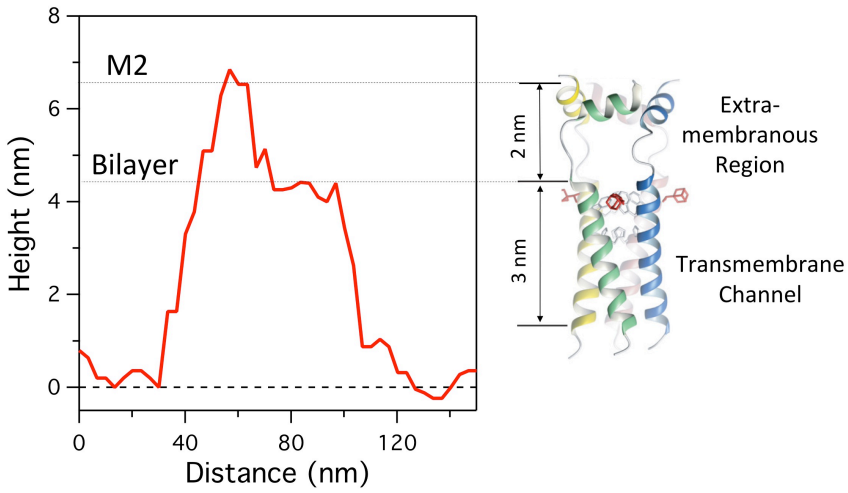

Figure 4.20: AFM height profile perpendicular to channel direction of M2 in a 60 nm wide channel. The structure of the M2 channel is shown with the four transmembrane helices embedded in the membrane and the amphipathic helices which protrude 2 nm out of the membrane.

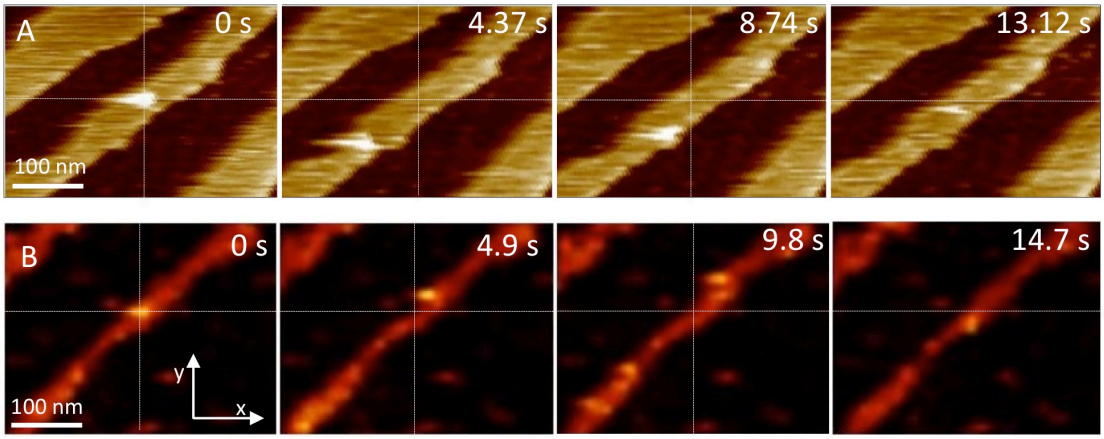

Figure 4.21: One-dimensional diffusion of the integral membrane protein M2 of influenza virus in 1D lipid bilayers. High-speed AFM image time sequences of M2 diffusion in 60 nm (A) and 30 nm (B) wide bilayer tracks.

High speed AFM scanning, at 0.20-0.23 frames per second, shows protein diffusion in bilayers of varying widths (Figure 4.21 A,B). The images in Figure 4.21 are taken from sequences of 43 and 49 images for A and B respectively. Throughout imaging the M2 protein is only observed in the membrane channel. The typical step distance of the protein between frames ranged from 0 to 150 nm with little net motion in either direction along the channel. The x-y displacement plots with time (Figure 4.22) for the examples given in Figure 4.21 show that the M2 diffuses non-biasedly along the thin bilayer stripes. The scan direction was continually from top to bottom but produced no net motion of the protein in either direction suggesting no significant motion due to tip forces. The diffusion constant, D, of a single particle can be determined via it's mean squared displacement, $\langle x^2 \rangle$, for a given time interval between displacement measurements, t:

$$< x^2 > = q_i D t \qquad (4.6)$$

Where q_i is a numerical constant which depends on dimensionality: q_i = 2, 4, or 6, for 1, 2, or 3 dimensional diffusion. Analysis of the mean squared displacement with time of the proteins gives 1D diffusion constants via Eqn 4.6 (using q_i = 2) of 300 and 260 ± 30 nm^2/s for the 30 and 55 nm channels respectively. The maximum velocities of the M2 protein, at 34

nm/s, are consistent with high-speed AFM data of outer membrane protein F (OmpF) in 2D membranes [130].

Despite little difference in protein diffusion constant in the two different channel widths, Figure 4.22A suggests that diffusion may be confined within the central region of the bilayer stripes, supporting the idea that the lipid is more densely packed at the bilayer edge.

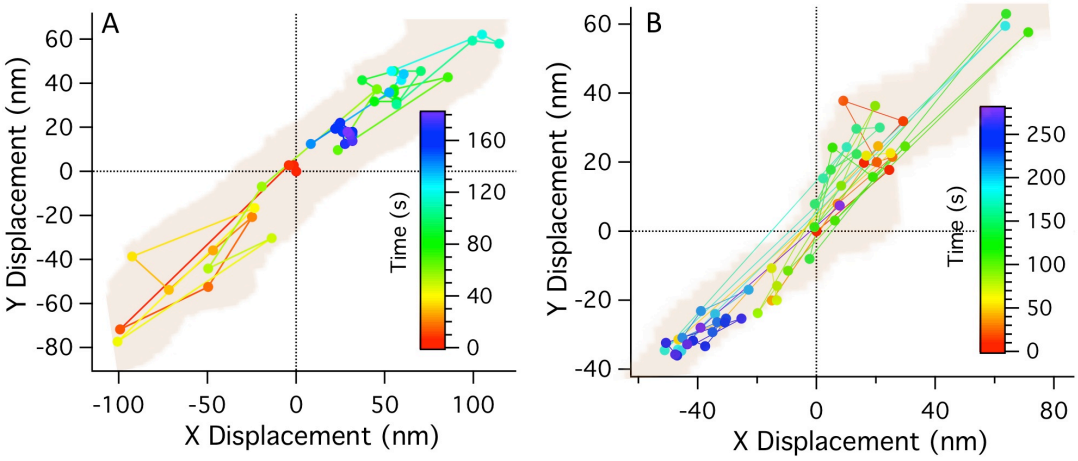

Figure 4.22: Displacement traces of M2 protein in x and y relative to starting position analyzed from Figure 4.13 (A) and (B) respectively.

Plots of displacement probability for a 1D random walk for purely random systems have a Gaussian profile about zero. Figure 4.23 show the displacement frequency along the channel axis. In the wider of the two channels (Figure 4.23A) the highest residency time is found in the widest parts of the channel. In the narrower channel (Figure 4.23B) we find a double peaked distribution caused by protein to becoming trapped in the narrowest region of the channel at -50 nm displacement. Figure 4.23B also shows the protein spends a large amount of time in the widest region of the channel due to lateral diffusion not in the channel direction. However more data is required to make firm conclusions about the trapping in narrow regions and preference to diffuse in the centre of the channel.

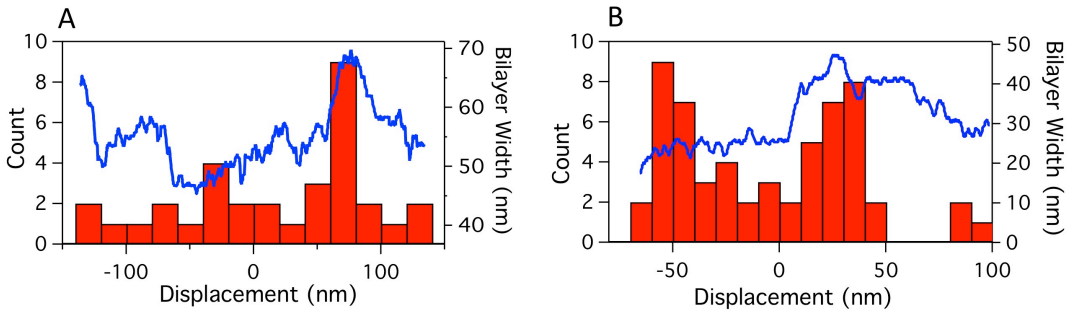

Figure 4.23: (A) and (B) histograms of protein displacement and line plot of bilayer width along the channel axis for the 60 nm and 30 nm channels respectively.

4.5 Nanoscale patterning of Lipid Bilayers

The lipid deposition method discussed in this chapter potentially offers a new and simple way to create the smallest achieved patterned supported lipid bilayers when utilised with nanolithography software. Patterning at these scales opens the possibility of creating nano-corrals for studying membrane proteins at the single molecule level, protein-protein and protein-lipid interactions as well as for studying processes that rely on diffusion in more systematic ways. To study lipid bilayer patterning using this technique the following sections begin to look at three input methods used by a nanolithography software and the advantages/disadvantages of each. All patterning modes can be run in either tapping mode or contact mode. For this study only contact mode is investigated since the tip velocity-deposition rate has already been well characterised for this mode (section 4.2).

4.5.1 Path Patterning

Path mode allows the user to draw straight line segments and polygons of a specified number of sides and sweep angle in the lithography software (NanoMan VS, Nanolithography 7, Bruker). The tip can then be made to traverse a recorded path according to XY velocity, tip voltage, tip voltage ramp and amplitude set point, all of which can be varied by the user. Figure 4.24A shows a typical path created using the NanoMan-Nanolithography software using 10 polygons of 16 nodes,180^{o} sweep angle and decreasing radii. For the tip to perform this path it must first be brought into contact with the surface, once scanning, the path can be selected to be followed by the tip at any time. Figure 4.24B shows an AFM image of the resulting pattern created by performing the path at an inputted tip velocity of 20 μm/s. The vertical line leading to the top of the image and top fraction of deposited bilayer are a result of the initial tip contact and automatic scanning from the image top to bottom. The spiral bilayer pattern shows a bilayer with line width starting at 250 nm which then increases with decreasing spiral arm radius (Figure 4.24 B,C) suggesting that the tip velocity reduces as the feature size decreases. Previous results (section 4.2) show for a tip velocity of 20 μm/s, line widths of ~ 50 nm are drawn, 5 fold thinner than the thinnest

obtained in the spiral pattern. Using the fitted function derived in section 4.2, width = 315/(tip velocity)$^{1/2}$, the line widths obtained in the spiral patterned bilayer can be back calculated to an expected tip velocity. These calculations predict the tip is traveling at velocities between 0.1 and 0.8 μm/s. Plotting the derived tip velocity against the distance between nodes in the drawn path (Figure 4.24A) shows a linear relation that as node separation is decreased so too is tip velocity (Figure 4.24D). This relation indicates a pausing/slowing of the tip by the nodes.

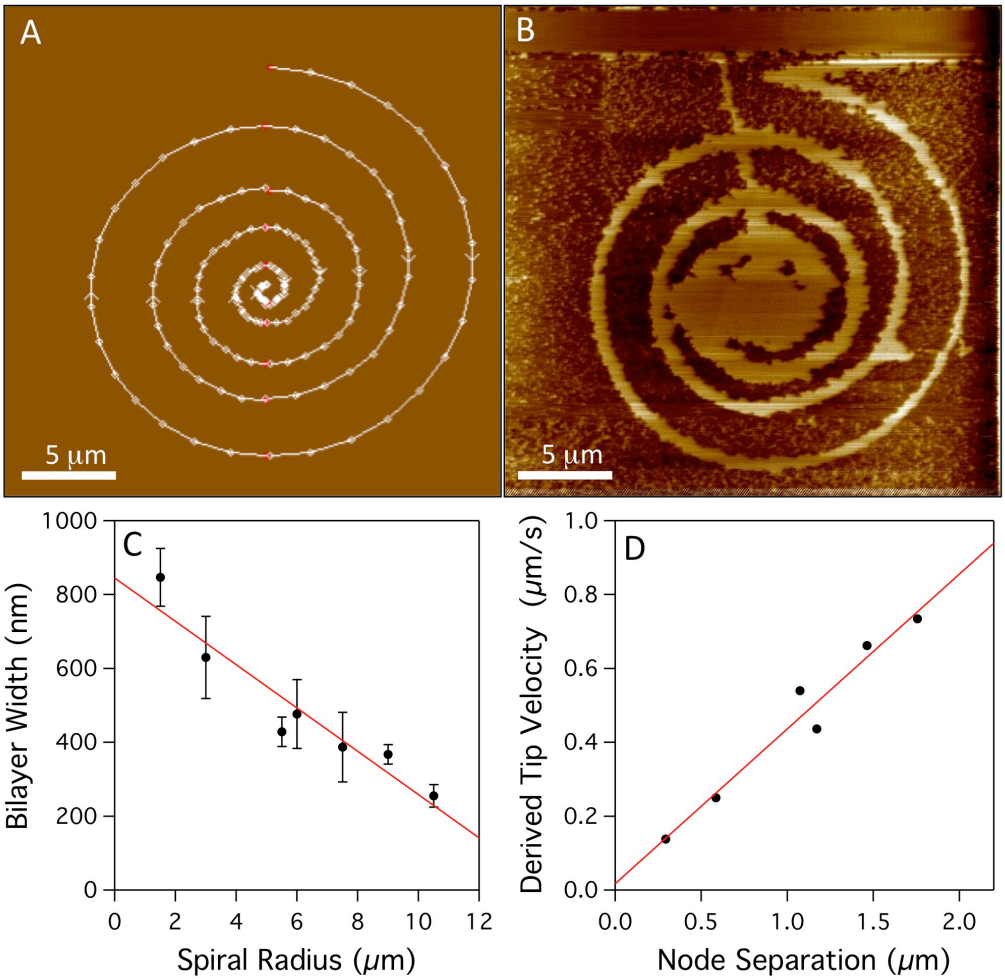

Figure 4.24: Patterning of DOPC lipid bilayers on mica using path mode in contact mode. (A) Image of the spiral path drawn using 10 polygon of 16 nodes,180° sweep angle and radii decreasing from 10.5 μm. (B) AFM image of lipid bilayer created by performing path in (A) at a inputted tip velocity of 20 μm/s. (C) Bilayer line width as a function of spiral arm radius. (D) Expected tip velocity using function derived in section 7.2 as a function of node separation.

To further investigate the effect of nodes in path mode, concentric DOPC pentagons were patterned at 20 and 35 μm/s. The bilayer line widths for the different velocities were measured to be 200 nm and 120 nm respectively, as with the spiral pattern these widths are much greater than expected. Figure 4.25 shows at each vertex there is an increased lipid deposition. The fact that these nodes are much more visible than in the spiral pattern may be an indication that the pause time is dependant on the angular change in direction.

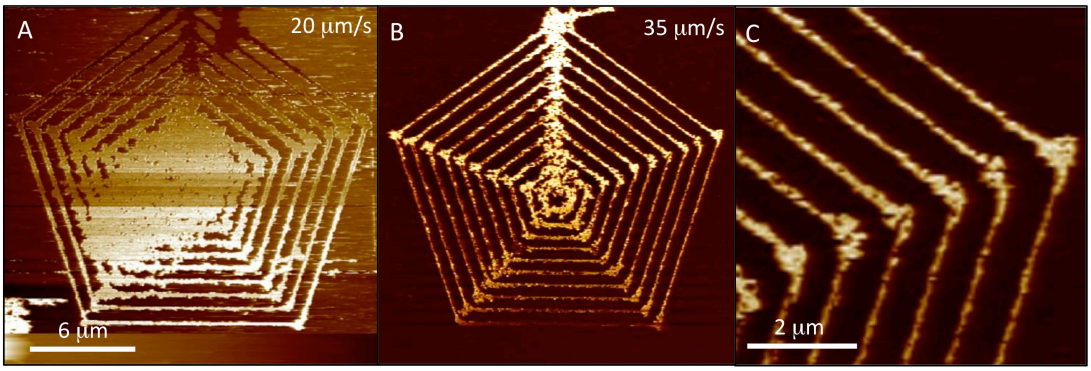

Figure 4.25: Patterning of DOPC lipid bilayers on mica using path mode drawn concentric penagons with tip velocities of (A) 20 μm/s and (B) 35 μm/s. (C) Higher magnification image of (B).

4.5.2 Vector File Patterning

Vector file importing allows the use of more complicated 3rd party software created images supported by programs such as Microsoft PowerPoint. Vector files store the lines that make up a graphic as formulae and thus the images are resolution independent. Upon import of a vector file into the Nanolithography software a minimum vertex spacing must be selected, this sets the “resolution” of the vectors by forcing a minimum length for any straight line segment. If a line segment is shorter than the minimum vertex spacing then the segment will be merged with the adjoining segment by the connecting head of the first segment. Unlike the path drawing tool, vector import allows the dimensions of the pattern to be altered after drawing.

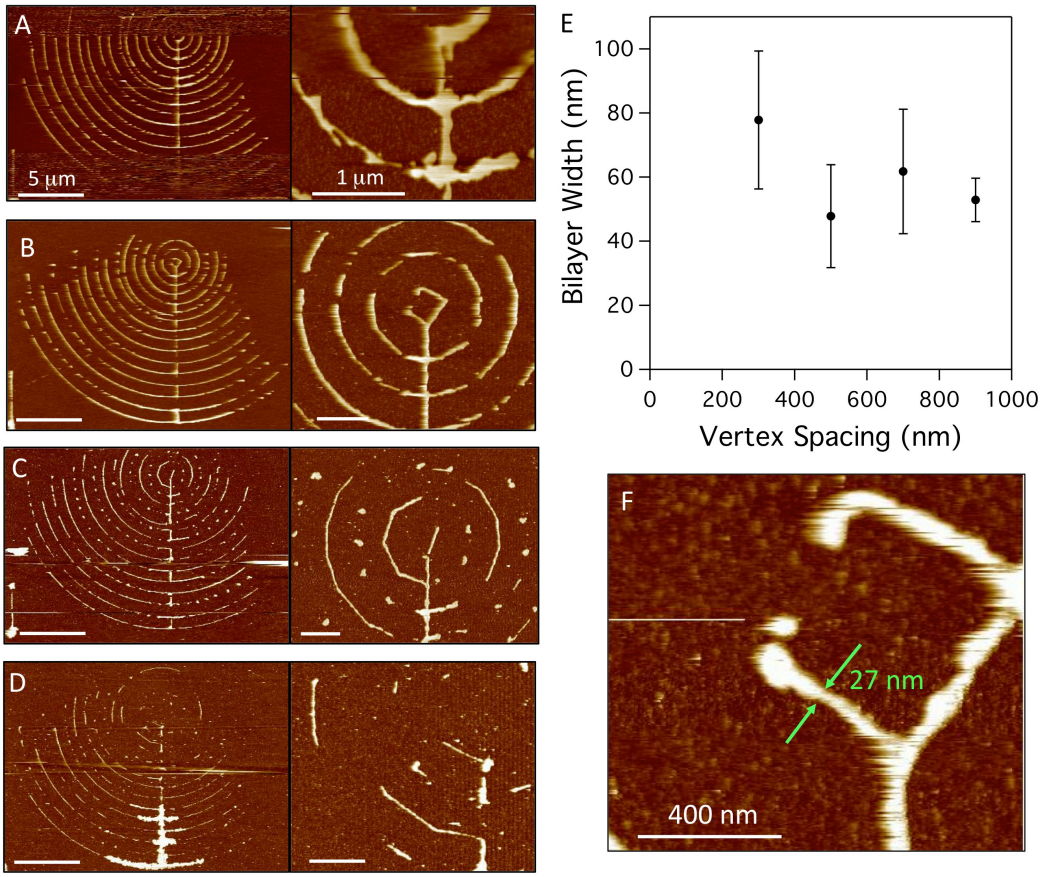

Figure 4.26: Vertex patterning of DOPC lipid bilayers on mica using concentric circles drawn in Microsoft PowerPoint. AFM images show the resulting patterned bilayers for varying vertex spacing of (A) 300 nm, (B) 500 nm, (C) 700 nm and (D) 900 nm (left images – large area scans, right images – higher resolution scans). (E) Plot bilayer line width for varying vertex spacing. (F) Higher resolution scan of centre of (B) showing the smallest patterned bilayer. All patterning was performed at a tip velocity of 100 μm/s.

Figure 4.26 shows the patterning of DOPC bilayers on mica using the vertex import of concentric circles for varying vertex spacing at a tip velocity of 100 μm/s. The lithography appears to have only written the lower half of the pattern this could be due to a z range issue or possibly irregular coating of lipid on the tip. As vertex spacing is increased the circles become n sided objects according to $n = 2\pi r/V_s$ where r is the radius and V_s is the vector spacing. For V_s = 300 nm, the majority of the pattern is intact, however as V_s is increased the patterns become more and more disconnected, with some lines appear as dots spaced at the expected vertex spacing. The effect of increasing V_s appears to have a negligible effect on bilayer line width (Figure 4.26 E). The smallest patterned feature created using this method is shown

in Figure 4.26F, a 500 x 500 nm square made up of bilayer with line widths down to 27 nm.

4.5.3 Bitmap Image Patterning

Bitmap image mode allows images to be imported and patterned either as binary or greyscale images. The nanolithography is done by associating the shade of the grey scale (on a defined max/min scale) with either: tip velocity, tip voltage or setpoint. When using binary images the scale becomes either maximum or minimum set values. Unlike in path or vector mode, the patterning is done in a raster fashion with defined scan line spacing. For this study binary images were used (Figure 4.27A) and the setpoint was used as the control such that the tip was either brought into contact for areas shaded black and out of contact for white areas.

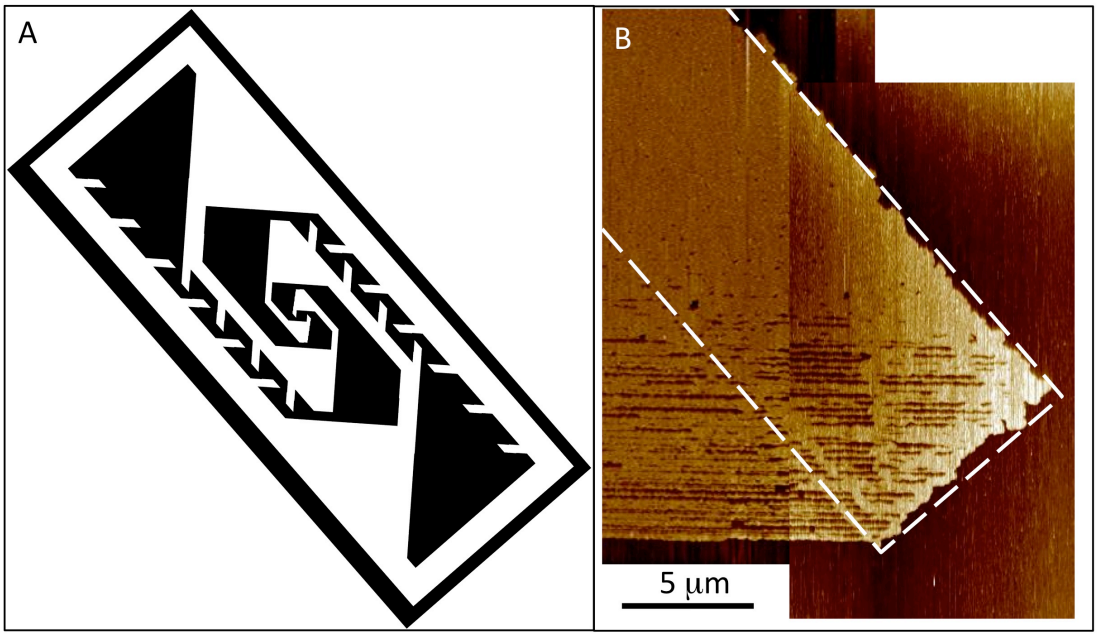

Figure 4.27: Bitmap patterning of DOPC lipid bilayers on mica. (A) Bitmap image imported into software. (B) Resulting AFM images of pattern (A) written with a 20 μm x 20μm total size, 120nm line spacing, 100 μm/s tip velocity and 300nm/s z lift off velocity.

Figure 4.27B shows the result of patterning the image shown in Figure 4.27A, using a 20 μm x 20μm total size, 120nm line spacing, 100 μm/s tip velocity and 300nm/s lift off z lift off velocity. The area highlighted by the white dashed line shows outline of the bitmap pattern. It is clear that the patterning didn't work as intended and lipid was deposited in areas the setpoint should have brought the tip off the surface, however some features of the pattern can be seen in the lower portion of the image. Further study is required to determine the optimum parameters to pattern bilayers using this method potentially utilising the tip velocity function to write with lower velocity and not write with velocities too high to deposit the lipid. Higher spring constant cantilevers may also permit better switching between contact and non-contact states required for patterning.

4.6 Conclusions

In conclusion, this chapter has shown a simple method forming stable patterned lipid membranes at length scales significantly less than previously observed and at the theoretically predicted limit for supported membrane stability. By measuring lipid diffusion in such patterned bilayers it has been shown that the lipid molecules undergo a sharp transition from 2D to 1D behaviour as the pattern width reduces below 50 nm, suggesting that lipid ordering is different close to the edges of the bilayer patterns and that this ordering has an influence up to 25 nm from the bilayer edge. This has potential implications for pore/defect formation in membranes, processes that naturally occur in their vicinity and for enhance drug delivery using membrane poration techniques. The data suggests that in the vicinity of the membrane edges the otherwise disordered lipids are in a more ordered possibly tilted phase. Observation of the diffusion of the transmembrane protein, M2, in these nanopatterned bilayer stripes suggests there may be an optimum width of the mobile lipid region for enhanced diffusion. In 2D membranes (stripe width > 100 nm) and in membranes of very restricted dimension (< 25 nm) the directional diffusion of the protein is restricted for different reasons, either due to the dimensionality or due to the change in physical behaviour of the lipids. Nanolithography of bilayers using this technique shows that it is possible to create nanopatterned supported lipid bilayers at scales smaller than ever previously achieved. This work opens the way to watching biological processes on the scale of individual molecules, including conformation, chemistry, and organisation. It also provides a model system for studying the role of dimensionality in biological processes, including photosynthesis, catalytic processes at membranes, and exchange of species between cells and their surroundings, in which the dynamic behaviour of lipid membranes are key.

Chapter 5
Lipid Domain Dynamics in Phase Separated Model Cell Membranes

This chapter investigates phase separation in multi-component supported lipid bilayers (DOPC - sphingomyelin - Cholesterol) with a focus on understanding the critical phenomena associated with systems near critical points. These lipid systems are aimed to mimic lipid raft behaviour in cellular membranes in order to develop our understanding of the mechanisms behind their structure and dynamics. The regions of criticality were determined by accurately measuring and calculating phase diagrams for the 2 phase Liquid disordered (L_d) – liquid ordered (L_o) region, and tracking how it moves with temperature, then increasing the sampling density around the estimated critical regions. High-speed AFM was then used to study a critical composition below the critical temperature (T_c), crossing T_c and above T_c. Domain boundary fluctuations were observed below T_c and characterised using line tension measurements whilst above T_c compositional fluctuations were observed and characterised using spatial correlation functions. From this analysis, the phase transition was found to be most closely described by the 2D Ising model, showing it is a critical transition. The nucleation and dissolution of domains, with lifetimes detected as low as 2 seconds, were observed around and above T_c, showing lifetime decreasing with increasing temperature. A region of critically fluctuating 10–100 nm nanodomains was found to extend a considerable distance above T_c to temperatures within the biological range, and seem to be an ideal candidate for the actual structure of lipid rafts in cell membranes. Although evidence for this idea has recently emerged, this is the first direct visualisation of nanoscale domains with short lifetimes in the critical region.

Much research has gone into the study of lipid domains, mainly using techniques such as NMR [131] or neutron scattering of multiple ordered layers [132] and fluorescence microscopy [133] or FRET of giant/large unilamellar vesicles [134]. These techniques work on different length scales,

and there are often discrepancies between them that must be resolved. For instance, for certain types of lipid mixture the GUVs appear to be in a continuous single phase where one would expect phase separation to occur according to the established phase diagrams. FRET measurements, limited to distances of up to 50 nm, indicate that there are indeed separate co-existing phases, so the domains must be much smaller than the resolution limit of optical microscopy (approximately 300 nm). AFM can cover this length scale, ranging from 10's of microns down to the nanometre level. Up until recently the main limitation of AFM was the low time resolution, but high-speed AFM overcomes this, allowing the dynamics to be resolved at time scales of seconds.

The work in this chapter seeks to understand what are the compositionally dependent shape and size of domains present (if any), on a nanometrer or micron scale; are they discrete domains or a continuous network (nucleated or spinodal); are they stable or transient? Once all these questions have been answered, then understanding how membrane proteins interact with and partition into the various phases can be developed, and how model membranes relate to the properties of more complex and compositionally heterogeneous biological cell membranes.

5.1 Determination of Phase Diagram

5.1.1 Room Temperature Measurements

The DOPC, sphingomyelin (SM) and cholesterol (Chol) mixture has been widely studied over the years as it is thought to be a good analogue of cell membranes. The heterogeneity of the naturally derived egg-SM introduces a controlled element of lipid complexity to the model with a fatty acid distribution of 86% 16:0 (chain length:unsaturated bonds), 6% 18:0, 3% 22:0, 3% 24:1 and 2% unknown. Initially a large number of sample compositions were chosen across the phase diagram with cholesterol concentrations near animal cell plasma membranes and imaged at a room temperature. Typical AFM images of a bilayer displaying phase separation are shown in Figure 5.1. The lateral packing density of the liquid ordered phase is greater than the liquid disordered and leads to an increased bilayer thickness of approximately 0.8 nm.

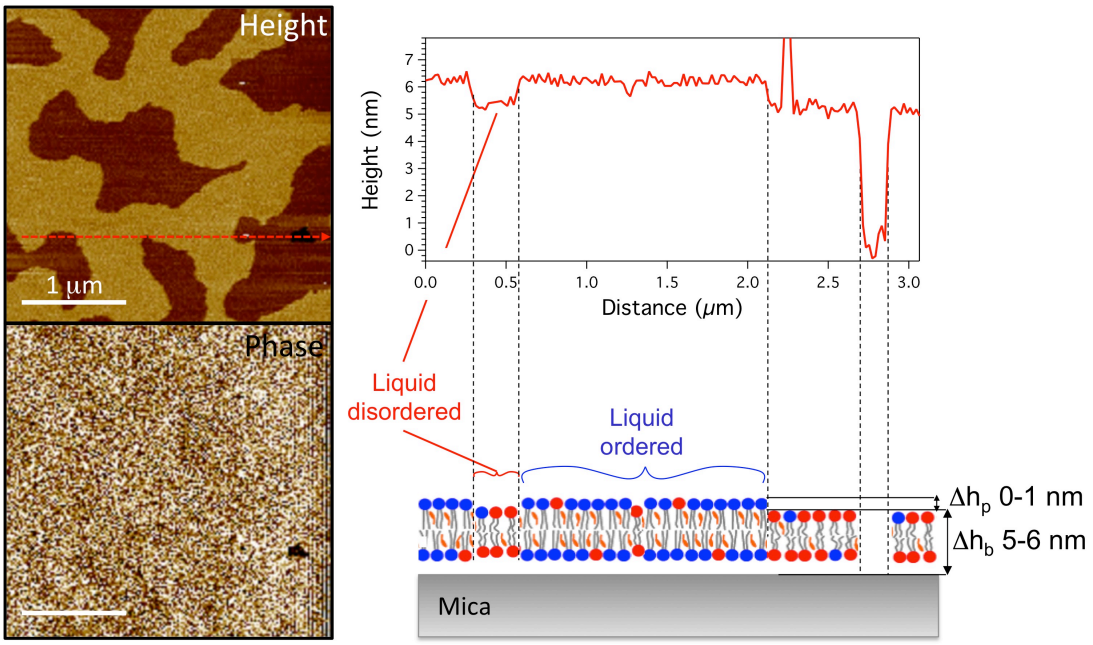

Figure 5.1: Tapping mode AFM height (top) and phase (bottom) images of a 28% DOPC, 35% SM, 27% chol bilayer displaying liquid ordered-liquid disordered phase separation. The plot of height versus distance shows the height profile of the dashed red arrow across the height AFM image traversing the different phases, a vesicle and a bilayer defect. The illustration highlights the height and compositional differences between each phase (Δh_p) and between the bilayer and mica (Δh_b).

Phase imaging of the bilayer showed negligible difference between the L_o and L_d phases however a clear difference was observed between the bilayer and the mica. The height profile crossing the bilayer defect allowed a bilayer thickness of 5.4 ± 0.4 nm to be measured, this thickness is consistent with previous work.

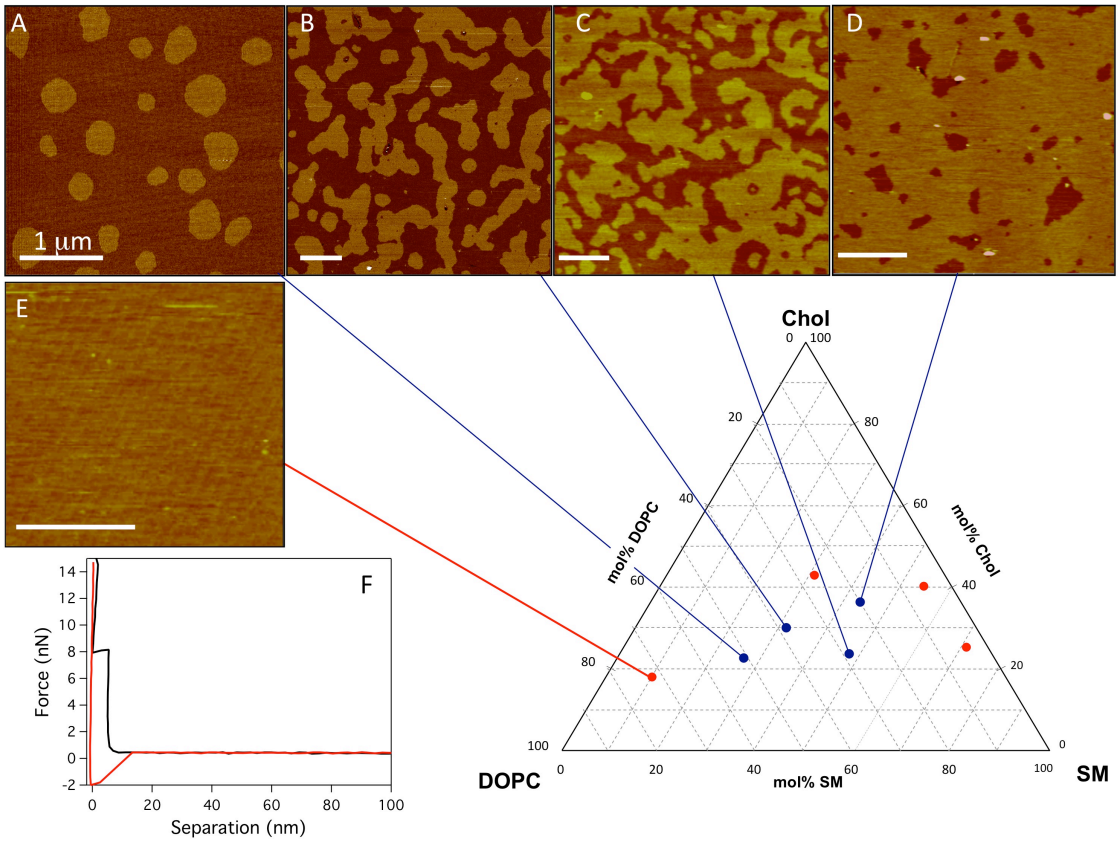

Figure 5.2: AFM images of various DOPC-SM-Cholesterol compositions (A: 51-22-27, B: 38-32-30, C: 28-48-24, D: 20-43-37, E: 72-10-18) at room temperature as labeled on the ternary diagram (scale bars = 1 μm). Red points on the phase diagram show compositions with which no phase separation was observed, force spectroscopy measurments (F) were used to determine the existance of a lipid bilayer since the AFM images appear featurless (E).

In the absence of cholesterol, gel phase domains have been observed while at high cholesterol content (>40%) the bilayer orders into a single *Lo* phase [135]. Lo-Ld phase separation can be differentiated from Gel-liquid separation by the smoother domain edges, different bilayer thickness (Gel-liquid height difference is generally 1.2 nm) and mechanical properties via force spectroscopy [136].

By systematically varying the DOPC, sphingomyelin and cholesterol concentrations close to the equimolar regions, the L_o-L_d phase boundary at room temperature can be mapped out in a ternary phase diagram (Figure 1.5). At high DOPC concentrations Figure 5.2 A shows most of the area is taken up by Ld phase with a small fraction of nucleated circular Lo domains. As the SM concentration was increased the phase separation displays a more spinodal structure, no longer with single domains but continuous linked phases taking up similar area fractions (Figure 5.2 B,C). These two different types of structure observed illustrate the differences between nucleation and spinodal decomposition. In general phase separated systems, nucleation is associated with metastability, i.e. the existence of an energy barrier and the occurrence of a rare but large energy fluctuation. Spinodal decomposition however refers to phase separation in an initially unstable system in which even the smallest fluctuations will grow because the energy barrier is negligible or zero. To reach the spinodal region of the phase diagram, a transition must take the material through the binodal region (phase coexistence boundary) or the critical point. Often phase separation will occur via nucleation as the system passes through the binodal, and spinodal decomposition will not be observed unless the system is quenched for example via a very fast transition in temperature. The observation of spinodal structures in Figure 5.2 implies that during the cooling of the bilayer the system passes through/near a critical region.

At even higher cholesterol/SM concentrations the inverse of the high DOPC composition was observed with mostly Lo and small Ld domains (Figure 5.2D). Several compositions were in the single phase region appearing as a single flat surface (Figure 5.1 E), shown as red markers on the phase diagram in Figure 5.2. For such compositions force spectroscopy measurements (Figure 5.2 F) were used to confirm the presence of a lipid bilayer as opposed to the flat surface of the underlying mica. The force curves showed the characteristic 5-6 nm break-though jump to the surface after applying ~ 8nN of force to the bilayer.

5.1.2 Phase Diagram Construction Method

Construction of the phase boundaries and tie lines in the phase diagram requires the conversion from domain area fraction (as acquired by AFM imaging) to phase molar fraction. For a given phase separated system of two species A and B, lipid A is apportioned between the two phases 1 and 2 according to:

$$\bar{c} = \alpha c_1 + (1 - \alpha) c_2 \tag{5.1}$$

where $\bar{c}$ is the average mole fraction of lipid A in the system (i.e., the starting composition), α is the mole fraction of phase 1 in the system, and c_1 and c_2 are the mole fractions of lipid A in phases 1 and 2. The relative deviations of the phase 1 and 2 compositions from the mean composition are thus given by the lever rule:

$$\frac{c_1 - \bar{c}}{\bar{c} - c_2} = \frac{1 - \alpha}{\alpha} \tag{5.2}$$

That is, the ratio of the molar fractions of material in the two phases is equal to the ratio of the distances along the tie lines from the average lipid composition to the boundaries of the two-phase region. In a ternary mixture there are two equations: one for $\bar{c}_A$ and one for $\bar{c}_B$. However, the observed area fraction of phase 1 in the AFM images α' is not the molar fraction α, which must be calculated by considering the average surface area per lipid. Thus α is related to the observed area fraction of phase 1 by:

$$\alpha = \frac{\alpha'}{\alpha'(1 - \alpha')\frac{a_1}{a_2}} \tag{5.3}$$

where a_1 and a_2 are the average area per molecule (averaged over all species) in phases 1 and 2. In certain instances, where more than one starting composition lie along the same tie line (e.g., any binary system), we

can express the tie line ratio as an equation for each composition, and then solve the simultaneous equations to determine the exact boundary location. If we substitute Eqn. (5.3) into Eqn. (5.1) we find a useful form:

$$\bar{c} = \frac{\alpha'}{\alpha' + (1 - \alpha')\frac{\alpha_1}{\alpha_2}}\, c_1 + \frac{(1 - \alpha')}{\alpha' + (1 - \alpha')}\, c_2 \qquad (5.4)$$

The straightening of the acyl chains by cholesterol i.e. the very process which causes the difference between Lo and Ld phases, means that the molecular areas are Chol dependent. The area per molecule of DOPC and SM in lipid bilayers in the presence of Chol over a wide range of concentrations is not available in the literature, but there have been extensive studies of the pure components by X-ray crystallography, small angle neutron scattering (SANS) and NMR spectroscopy in bilayers, and of binary and ternary mixtures in monolayers as a function of surface pressure by the Langmuir–Blodgett (LB) technique. From these data the molecular areas of DOPC and SM in the presence of Chol can be inferred as shown in Table 5.1. Although these variations of molecular area as a function of composition are estimates, the iterative procedure used to generate phase diagrams must produce a self-consistent result for all the compositions studied: self consistency could only be achieved by correcting for the surface area using the values in Table 5.1, indicating that they are reliable estimates.

In a phase separated region, the main quantitative information we have is the relative distance from the starting composition to each phase boundary along the straight tie line. For example, in a 63.75 mol % DOPC: 21.25% SM: 15.0% Chol mixture, the AFM data indicated that the sample is 12.7% L_o phase and 87.3% L_d, which gives a tie-line ratio of 0.239 (0.239 being the relative distance to the L_d phase boundary and 1 being the relative distance to the L_o phase boundary). However, these are not absolute distances, so can not be used in isolation to locate the exact orientation or length of the tie lines. To determine the position of the two-phase boundary several thermodynamic rules and assumptions are used:

a) Tie-lines can never cross one another.
b) The orientation of tie-lines close to one another will not vary greatly.
c) A composition must lie within the bounds of the ternary phase diagram.
d) The two-phase boundary is relatively smooth and has no discontinuities.

Lipid	Surface Area per molecule (Å^{-2})	Source
DOPC	67	[137]
SM	41	[138]
Chol	36	[139]
DOPC/Chol	$67 + \frac{52-67}{0.5}x, \quad x \in [0, 0.5]$ $52.5 + \frac{36-52}{0.2}(x-0.5), \quad x \in [0.5, 07]$ $36, \quad x > 0.7$ Where *x* is the mole fraction of cholesterol	[139]
SM/Chol	$41 + \frac{40-41}{0.1}x, \quad x \in [0, 0.1]$ $40, \quad x \in [0.1, 0.25]$ $40 + \frac{38-40}{0.15}(x-0.25), \quad x \in [0.25, 0.4]$ $38 + \frac{44-38}{0.1}(x-0.4), \quad x \in [0.4, 0.5]$ $44, \quad x > 0.5$ Where *x* is the mole fraction of cholesterol	[140,141]
DOPC/SM	$67 + (51-67)x, \quad x \in [0, 1]$ Where *x* is the mole fraction of SM	[141]

Table 5.1 Estimated surface area per molecule of the pure lipids and binary mixtures used in the derivation of the phase diagram in Figure 5.3, which takes into account the condensing effect of cholesterol. Values were available for hydrated bilayers or estimated from Langmuir–Blodgett studies of monolayers. Studies were performed at room temperature. For our analysis, we assumed linear expansion upon heating.

By increasing the temperature of the samples, the point at which each composition crosses a boundary gives single precise locations in the temperature-phase space (marked with stars in the phase plots in Figure 5.5), from which a rough indication of the position of the boundary can be plotted, together with an estimation of its progress with temperature. An additional piece of information for determining the tie line end points is the measurement of the height difference between the two phases. This measurement is analogous to the quadrupole splitting spectra measured by Veatch et al.[133] in their NMR measurements of deuterium labelled lipid bilayers. The further around the boundary one travels in each direction away from the critical point, the greater the height difference. Of particular importance is the fact that two compositions, which lie along the same tie line, will have domains with an identical composition (at different area ratios according to the lever rule), so they will have an identical L_d–L_o height difference (providing the bilayer normal force exerted by the AFM is identical as the bilayer is compressible, with different phases having a different compressibility).

5.1.3 Temperature Dependant Measurements

To locate the precise position of the critical point, and to track how it moves with temperature, compositions were prepared across a narrow range within the interior of the measured two-phase region (determined at room temperature), with a higher concentration around the estimated critical region. Imaging of the bilayer morphology was performed as a function of temperature. The temperature was increased until all trace of the domain structure had disappeared. Figure 5.3 shows a typical selection of images of various compositions selected to highlight the general trends, with the samples A, B, C, D as a linear transect across the critical region from left to right. Samples A and B (A: 48-25-27, B: 40-30-30 DOPC-SM-Chol) are clearly to the left of the critical point, with isolated domains of L_o surrounded by the L_d phase. Sample A is closer to the phase boundary, with the L_o phase disappearing at 26 ^oC, 3.5 degrees before those in sample B. It is interesting to note the non-circular domain boundary in comparison to the

rounder domains in Figure 5.2A, which derive from compositions far to the left of the critical region. Even though here the crossing of the boundary is a first order transition, the line tension in the domains is considerably reduced, shown qualitatively by the smaller domain sizes and increased circumference to area ratio. On the other side of the critical region, composition D (23-40-37 DOPC-SM-Chol) exhibits a continuous L_o phase with small islands of L_d phase. As the temperature increases, these final L_d domains disappear as the phase boundary is crossed in a first order phase transition. Again, despite the reversal in proportion, the domain boundaries are convoluted with low line tension in comparison with the more continuous L_o phase image in Figure 5.2.

Sample C (1-1-1, DOPC-SM-Chol) in the middle of the transect is close to the critical point. At 24.0 ^oC the domains are approximately 50 : 50 L_d–L_o, and quite convoluted in nature. Around 26 ^oC, the domain edges suddenly roughen and break up, but do not disappear suggesting either a critical point has been reached or the conditions are very close to a critical point. The pre-existing domain structure breaks down and is replaced by a more uniform spread of small domains. As the temperature increases (at considerably higher temperatures than the surrounding first order phase boundary), these small domains persist, although getting smaller and smaller, until they disappear below detectable limits around 34^oC.

As the critical composition furthest from the room temperature phase boundary Sample E (30-48-22 DOPC-SM-Chol) shows the longest run of pre-critical images (Figure 5.3E). The images produced are very similar to those of sample C, just at higher temperatures. A number of the compositions close to samples D and E showed behaviour indicative of a critical point at some point in the temperature ramp. It is unlikely that each of these compositions lie exactly on the critical point line (the non 50 : 50 molar ratio of phases just below T_c being one indicator), suggesting that the critical behaviour extends a short compositional distance from the exact line of critical points

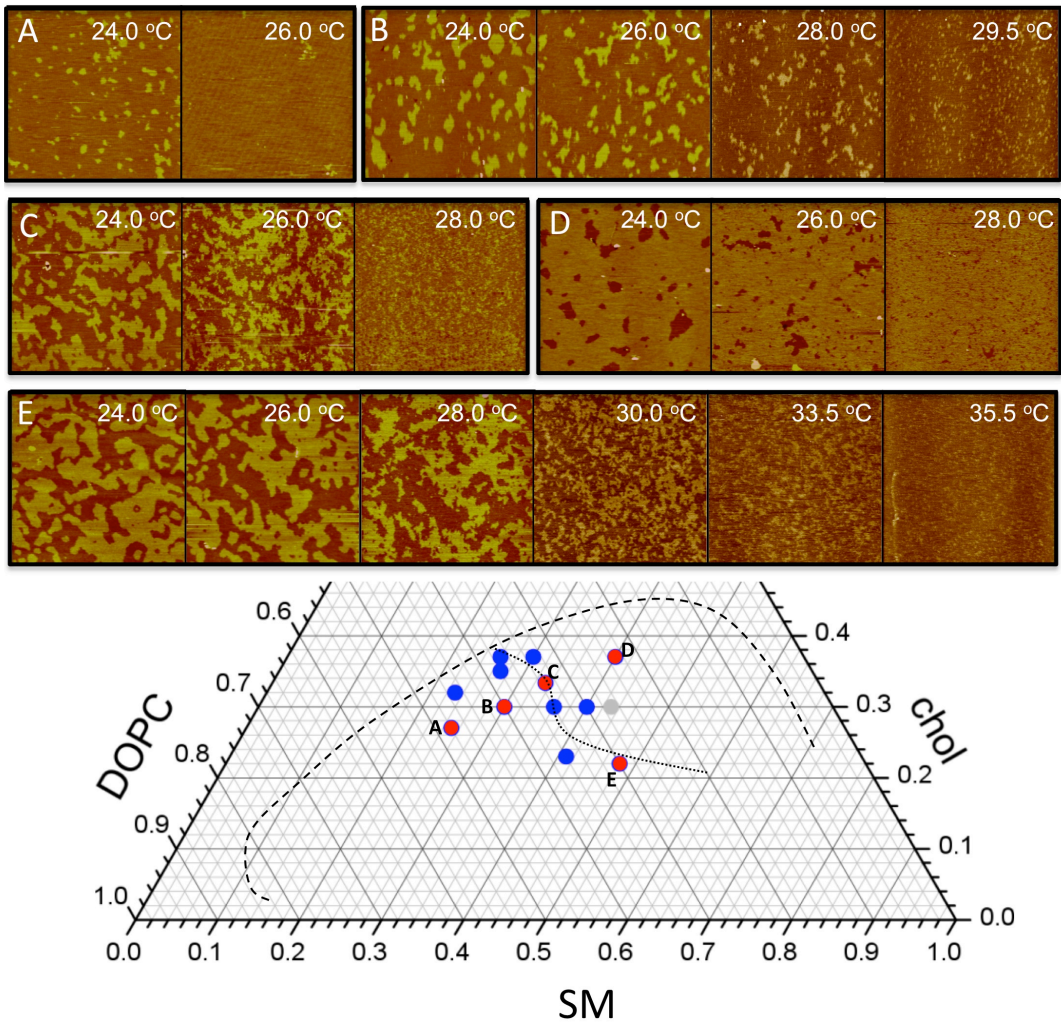

Figure 5.3 AFM imaging of DOPC-SM-Chol samples A: 48-25-27, B: 40-30-30, C: 33.3-33.3-33.3, D: 23-40-37 and E: 30-48-22 at temperatures ranging from room temperature up to the miscibility temperature. Compositions focusing on the critical region. Samples A–D indicate a transect perpendicular to the estimated line of the critical points vs temperature. To the left of this critical line compositions A and B show that L_o domains extinguish into the surrounding L_d phase with increasing T. To the right (composition D), the minority L_d phase is gradually extinguished until a single L_o phase remains. On, or close to, the critical line (C and E), rather than undergoing a simple first order phase transition, the domains gradually roughen below T_c, then suddenly break up into many very small compositional fluctuations, which persist for 5-6 degrees above T_c. The correlation length for these fluctuations diminishes as the temperature rises.

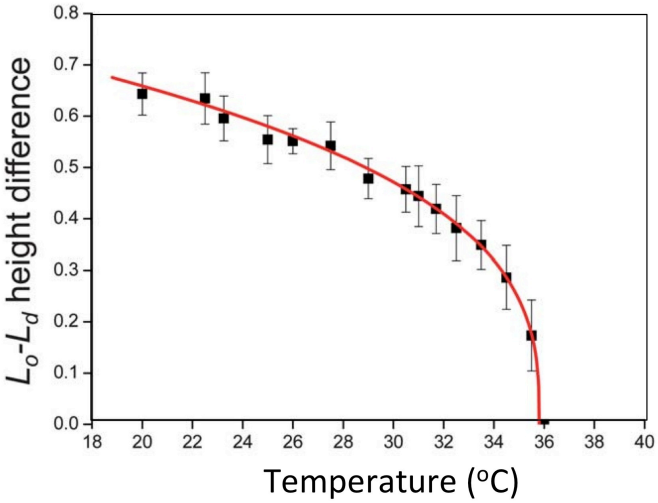

Figure 5.4: The height difference between the Lo and Ld phases approaching a mixing temperature for sample E (30-48-22, DOPC-SM-Chol).

The L_d–L_o height difference of sample E is plotted in Figure 5.4, showing a decrease in domain height difference as temperature is increased reducing down to zero upon mixing. The curve closely resembles other critical behaviour in ferromagnets, where the saturation magnetization goes to zero at the curie temperature.

5.1.4 Phase Diagram Construction

Using the method described in section 5.1.2, the Lo-Ld phase region was mapped out and plotted (Figure 5.5) for varying temperature using: the ratios of the two observed phases from all of the temperature ramp data, the exact known boundary positions as each composition crosses into the single phase region and the difference in heights between the L_o and L_d phases. The individual plots were then combined to produce a map revealing the retreat of the two-phase region towards the lower right hand SM vertex as the temperature increases. Critical points are special compositions and temperatures in the phase diagram where tie-lines merge into single points and where the compositions of coexisting phases become identical. The dashed line in Figure 5.5 and Figure 5.3 indicates the line of temperature dependent critical points.

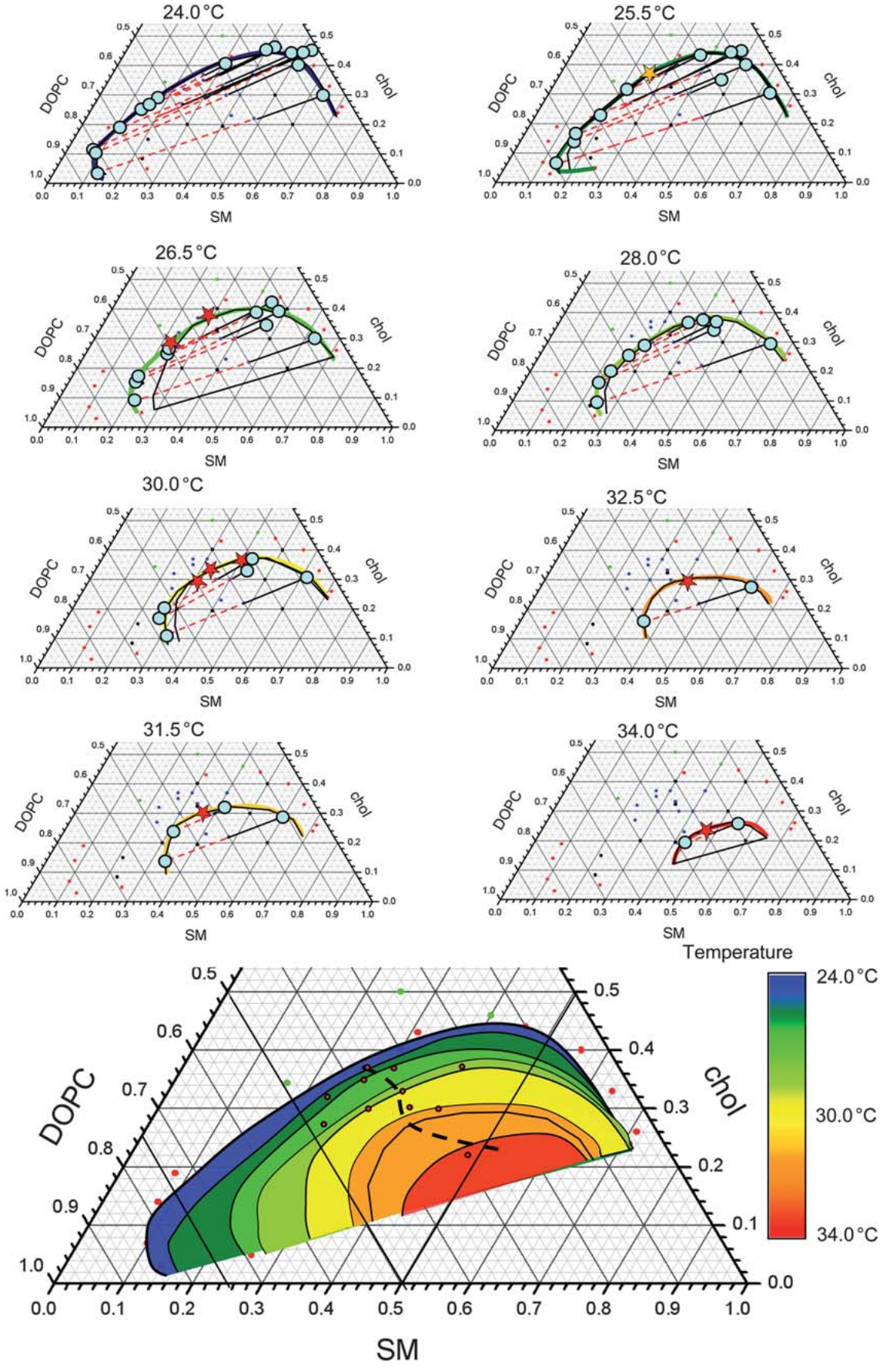
24.0 °C
25.5 °C
26.5 °C
28.0 °C
30.0 °C
32.5 °C
31.5 °C
34.0 °C
DOPC
chol
SM
Temperature
24.0 °C
30.0 °C
34.0 °C

Figure 5.5: Plots illustrating the boundary calculation of the L_o–L_d two-phase co-existence region as a function of temperature, using the area information derived from the AFM images (using the lever rule together with a correction to account for the change in area per lipid molecule across the phase diagram), the tie-line slope is indicated by the height difference in the L_o and L_d phases and definite boundary markers, where the boundary crosses each composition and the final domain structures are extinguished (for a first order transition). These positions are marked with a red star and a gold star is used to indicate the precise critical point found. A filled circle marks the composition at the end of each tie-line. (Bottom) An amalgamation of the above individual plots, together with an estimation of the line of critical points.

One interesting feature is the tilt of the tie-lines up towards the right hand side. All lipid species, including cholesterol, have the same diffusion coefficient within a single phase or domain. In other words, the diffusion is phase and not lipid molecule dependent. The driving force for lipid separation into L_d and L_o phases is the increasing difficulty for low T_m lipids to be incorporated into the highly ordered phase. Although some studies indicate that cholesterol partitions roughly equally into both phases, which would indicate that there is no specific interaction between the high T_m lipid and cholesterol, in this case the tilt of the tie-line up to the right hand side of the ternary diagram would indicate that there is indeed a specific SM–chol interaction. This result has also been found previously by Veatch [7]. This could be attributed to a specific hydrogen bonding network [136] or the complexation of SM with cholesterol [142]. The images show a large variation in structure, and are very similar to those imaged via the fluorescence microscopy of GUVs, although with the capability of distinguishing domains with diameters down to 10 nm. Domain sizes tend to be smaller than those observed in GUVs due to the supported nature of the membrane, the proximity of the surface acting as a drag force on the diffusion of domains and hence slowing coalescence into the larger domains. Ostwald ripening and coalescence events do occur in the supported membranes investigated here, just at a much slower rate as shown in Figure 5.6. Smaller domains can be seen dissolving whilst the surrounding larger domains grow. Also observed are two domains coalescing to form one. These processes minimize the free energy of the

system by reducing boundaries between the two phases demonstrating the dynamic behaviour.

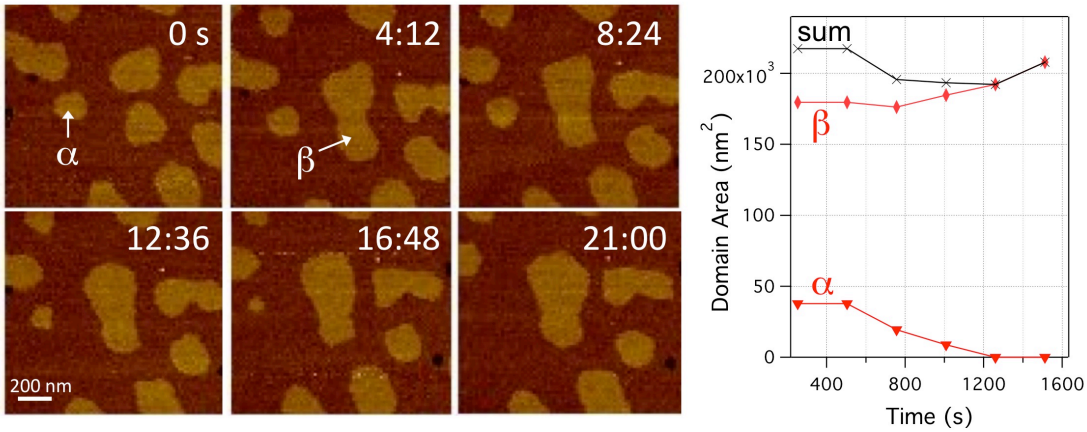

Figure 5.6: Successive AFM images of Lo domains undergoing coalescence and Ostwald ripening. Between image at 0 s and 4 min 12 s two domains are observed coalescing into a larger one (β). Over the 6 frames a smaller less stable domain, labeled α, shrinks over time whilst the larger newly formed domain β increases by a similar area as lost by α. Plot showing the measured changes in individual and total domain area with time.

5.2 High Speed AFM of Critical Behaviour

The critical behaviour of lipid membranes has been previously shown to be highly dynamic [8] and as such, much of the behaviour is lost when studied using conventional AFM scan speeds. In the following section a single composition, sample G (28-35-37 DOPC-SM-Chol), is extensively studied using High Speed AFM (HS-AFM). The higher time resolution enabled the investigation of domain line tensions at temperatures below T_c, precise observations of the transition at T_c and study of the growth and dissolution of nanoscopic domains (>20 nm) with <2 second lifetimes. Analysis of line tensions and correlation lengths showed that the behaviour can be described as a 2D Ising Model. Domain lifetimes show the first direct evidence of short lived nanoscopic domains in systems designed to emulate the lipids in the cellular membrane. These data provide more evidence that the small “raft” domains detected in real cells are not stable equilibrium phase separated domains, but non-equilibrium compositional fluctuations.

5.2.1 Sample G – Large Scale Temperature Dependant Phase Behaviour

The composition, sample G (28-35-37 DOPC-SM-Chol), which is just to the right of the critical line (Figure 5.5) was chosen as a system that would show pre-critical and post-critical behaviour in a temperature range which would be both biologically relevant and suitable for the AFM heat stage. Figure 5.7 shows an overview at large scales of the phase behaviour for increasing temperature from 26.8 ^{o}C up 38.4^{o}C. For temperatures up 33 ^{o}C the bilayer was mostly in the Lo phase (50-60% area), as expected for a composition to the right hand side of the critical line. The domain boundaries were initially very rounded and smooth at 26.8 ^{o}C and gradually became more convoluted until 32.6 ^{o}C where they begin to break down. At 33.7 ^{o}C all larger domains had completely disintegrated into much smaller domains, continuing up to 39 ^{o}C at which point Lo compositional fluctuations were no longer visible. The shift from mostly Lo phase at lower temperatures to Ld upon complete mixing is due to the non-symmetric regression of the phase boundary with temperature towards the SM richer regions (Figure 5.5).

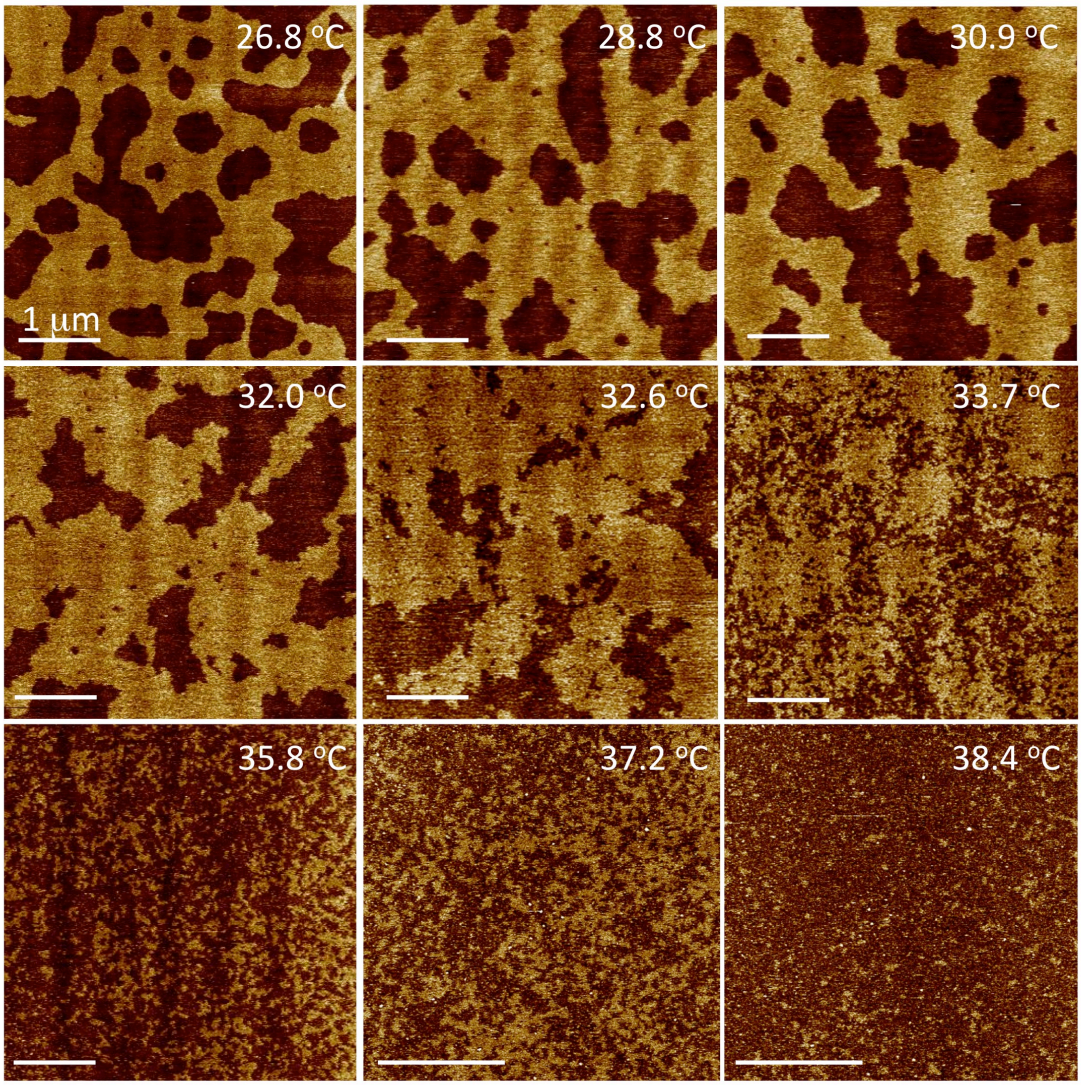

Figure 5.7: AFM images of sample G (28-35-37 DOPC-SM-Chol) for increasing temperature. The critical temperature was crossed at 33.4 ± 0.2 °C (Scale bars = 1 μm).

5.2.2 Nanoscopic Line Tension of Lipid Domains

Line tension, λ, is the 2-D analog of surface tension. Domains at equilibrium are set by a balance between the line tension at the interface between phases and the entropy of distributing the molecules between phases. As discussed in section 1.3.4.2, one of the key attributes of critical behaviour is that it is universal, meaning that many properties in the same 'universal class' behave alike. One consequence of universality is that line tensions for every system in the same universality class scale in the same way with

temperature, T. As the critical temperature T_C is approached, line tension approaches zero, according to a power law where μ is the critical exponent.

$$\lambda = \lambda_o \left|\frac{(T-T_C)}{T_C}\right|^{\mu} \tag{5.5}$$

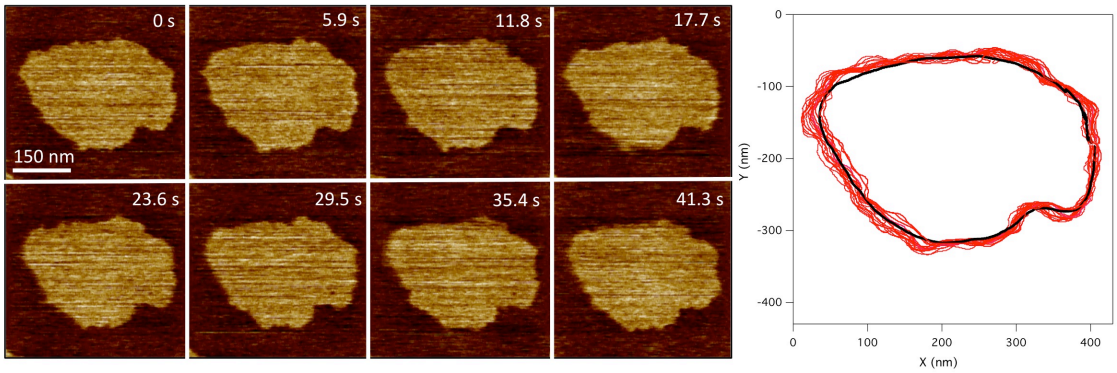

Figure 5.8: Continuous AFM images of a single Lo domain at 25.5 °C imaged at 5.9 seconds per image. X-Y plot shows several traces of the domain boundary taken from single images (red) and the 20 frame averaged domain (black).

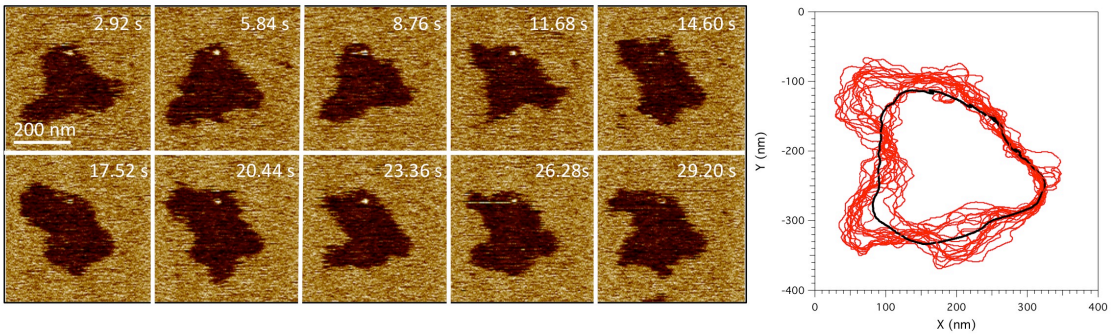

Figure 5.9: Continuous AFM images of a single Ld domain at 31.3 °C imaged at 2.92 seconds per image. X-Y plot shows several traces of the domain boundary taken from single images (red) and the 20 frame averaged domain (black).

High speed AFM allows the determination of domain line tension via the visualisation of the domain boundary dynamics which arise as capillary waves for non-fractal domains (i.e. below T_c) due to thermal fluctuations. The analysis of the fluctuation wavelengths allows the line tension to be deduced. To obtain the line tension of a particular domain, the domain perimeters were traced through a series of movie frames. For each domain, the boundary between phases was mapped as it fluctuates for at least 20

frames (typically ~ 60 s) and averaged to give the mean domain edge. Figure 5.8 shows how at lower temperatures the interface doesn't deviate much from the average whilst at higher temperatures (Figure 5.9) the fluctuations are much greater, with changes in radius of up to 50%. To acquire the line tension the capillary wave approximation for the energy of interface fluctuations was used (Eqn. 5.6).

$$E = \frac{1}{2}\lambda \int_0^L dx \left(\frac{\partial r}{\partial x}\right)^2 = \frac{\lambda L}{2}\sum_k k^2 \; r(k)r(-k) \tag{5.6}$$

Where L is the smooth, mean perimeter of a domain, k = 2πn/L with integer mode index n, r(x) is the radius as a function of position and r(k) is the Fourier transform of r(x):

$$h\,(k) = \frac{1}{L}\int_0^L dx\, r(x)e^{-ikx} \tag{5.7}$$

Since Eqn. 5.6 is quadratic, the equipartition of energy theorem applies such that each capillary mode carries on average $k_BT/2$:

$$\langle h(k)h(-k)\rangle = \langle |h(k)|^2\rangle = \frac{k_bT}{\lambda L k^2} \tag{5.8}$$

The values of $|h(k)|^2$ are evaluated by firstly converting the domain boundaries to a set frames in x, y coordinates using an imageJ macro (appendix) to extract the perimeter from binary formatted AFM images (Figure 5.10A). The perimeters were then converted to radii using the center of mass position of the binary image (x_{com}, y_{com}) and calculating the distance with Eqn. 5.9:

$$\sqrt{(x_{com}-x)^2 + (y_{com}-y)^2} \tag{5.9}$$

The radii as a function of position were then averaged over 20 frames allowing the radial deviations to be calculated from the difference between the average and individual traces (fig 5.10 C,D).

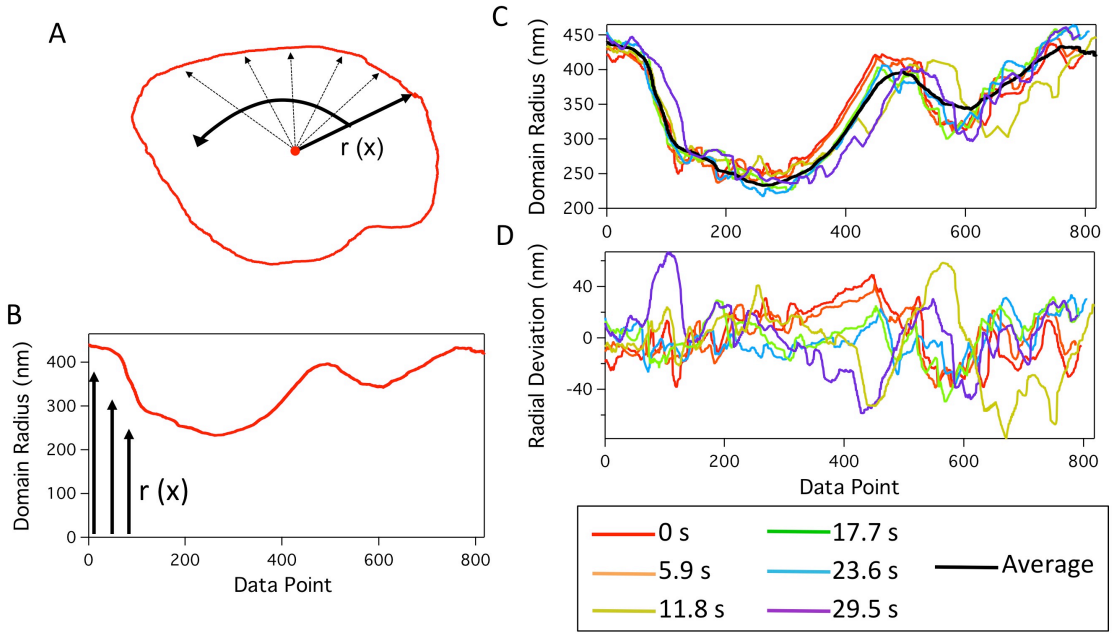

Figure 5.10: Extraction of radial deviations from AFM image sequences. (A) AFM images are thresholded and converted to binary images using imageJ from which the shape x-y coordinates are extracted and plotted. (B) Each point on the perimeter is converted to a radius using it's distance from the domain center of mass i.e. $((x_{com} - x)^2 + (y_{com} - y)^2)^{1/2}$. The radii for 20 domains are then averaged as a function of position (C), additional lines show traces from individual frames at 6 time points. The traces from each frame are then subtracted from the average trace to give the radial deviations (D).

Fourier transforms of the radial deviations were performed on each trace, outputting the magnitude squared $|h(k)|^2$ values for varying wavenumber k. $|h(k)|^2$ was then averaged over all movie frames at one temperature and plotted in a log-log plot against k for modes two through fifteen (Figure 5.11). Modes 2 through to fifteen typically include deviation wavelengths ranging from approximately 1 μm to 100 nm and thus were well within the resolution range of the AFM. By fitting $|h(k)|^2$ vs. k to a 'y = A.x^{-2}' function the line tension was determined from the constant A for known average perimeter length and temperature (using Eqn. 5.8). At room temperatures, values for the line tension were found to be of the order

0.6 pN, in close agreement with the values previous studies found using fluorescence microscopy of GUVs [9]. Line tension has also been previously determined by Lee et. al. using fluorescence microscopy to relate Lo-Ld domain size distribution to line tension in model cytoplasmic myelin lipid monolayers [143], this work found line tensions on the order 3-10 fN.

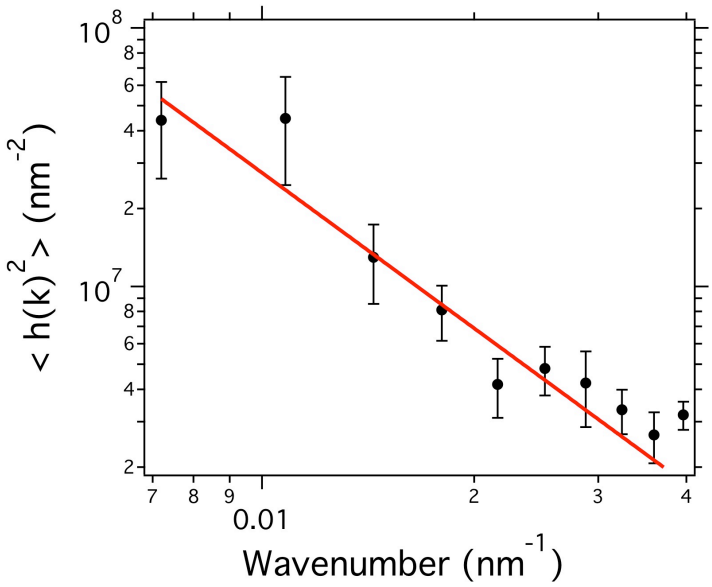

Figure 5.11: Log-log plot of the spectrum of radial deviations vs. wavenumber k for a domain at 25.5 ^{o}C with a mean perimeter of 2140 nm and mean radius of 340 nm. Line is a fit to the equation $h(k)^2 = k_BT/(L\lambda k^2)$. Only the data points from the second through the fifteenth wavenumbers are used for the fit. Error bars represent standard deviations from measurements over the series of movie frames.

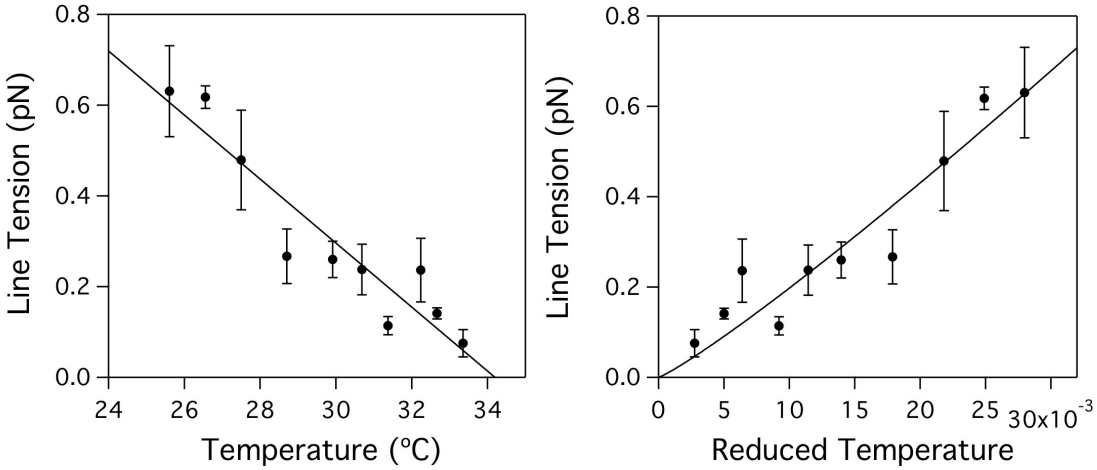

Figure 5.12: (Left) Line tension of single domains as function of temperature for both isolated Lo and Ld domains, straight line fit intercepts the x axis at the critical temperature. (Right) Line tension plotted against the reduced temperature T_R. Fitting to the power law in Eqn. 5.5 gives a value for the critical exponent μ of 1.02 ± 0.19.

Analysis of domain boundary fluctuations for varying temperature (Figure 5.12) shows that as temperature is increased, line tension decreases linearly to a minimum of 0.08 ± 0.03 pN at 33.4 °C. The intercept of this linear relation with the x-axis indicates zero line tension and thus the critical temperature. For this composition the critical temperature as determined by the zero line tension is 34.2 °C. The model by which this critical behaviour may be understood depends upon its universality class. Any system that belongs to the same class should exhibit the same critical behaviour and scale the same way with temperature whether it is the spin in ferromagnets or liquid crystal orientations. The temperature scale associated with critical point behaviour can be normalized by the introduction of the reduced temperature:

$$T_R = \frac{T - T_C}{T_C} \tag{5.10}$$

By plotting the reduced temperature T_R against the line tension (Figure 5.12) the critical exponent, μ, was found by fitting to the power law given in Eqn. 5.5 with free variables λ_0 and μ. A best fit value of 1.02 ± 0.19 was found for critical exponent, the value of μ should depend only upon the model. For the 2D Ising model, the exponent μ should equal 1, for the 3D Ising model μ = 0.630 and for mean field theory μ = 0.5, thus these data suggested the critical fluctuations are best described by the 2D Ising model in agreement with previous fluorescence microscopy work on GUVs.[9]

5.2.3 Crossing The Critical Temperature

By imaging with high speed AFM during a gradual temperature ramp, the temperature at which the behaviour becomes critical can be accurately determined. The change in phase behaviour when increasing the temperature of Sample G (30-48-22 DOPC-SM-Chol) close to the critical temperature shows when Tc is crossed the domain structure suddenly breaks down into critical fluctuations with a length scale smaller than the pre-existing domains (Figure 5.13).

The images suggest the critical temperature was crossed between 33.23 and 33.57 ^{o}C thus giving a critical temperature of 33.4 ± 0.2 ^{o}C, in reasonable agreement with the 33.7 ^{o}C measured by line tension. Not only do the edges of the domain become ever more convoluted as T_C is crossed but new small (<150 nm) Lo domains were observed nucleating in the Ld phase and visa versa. Domains in the 40-130 nm diameter range were observed to completely restructure or move with each scan displaying the dynamics of the critical phase behaviour. The dissolution and nucleation of domains at and above T_C are investigated in section 5.2.5.

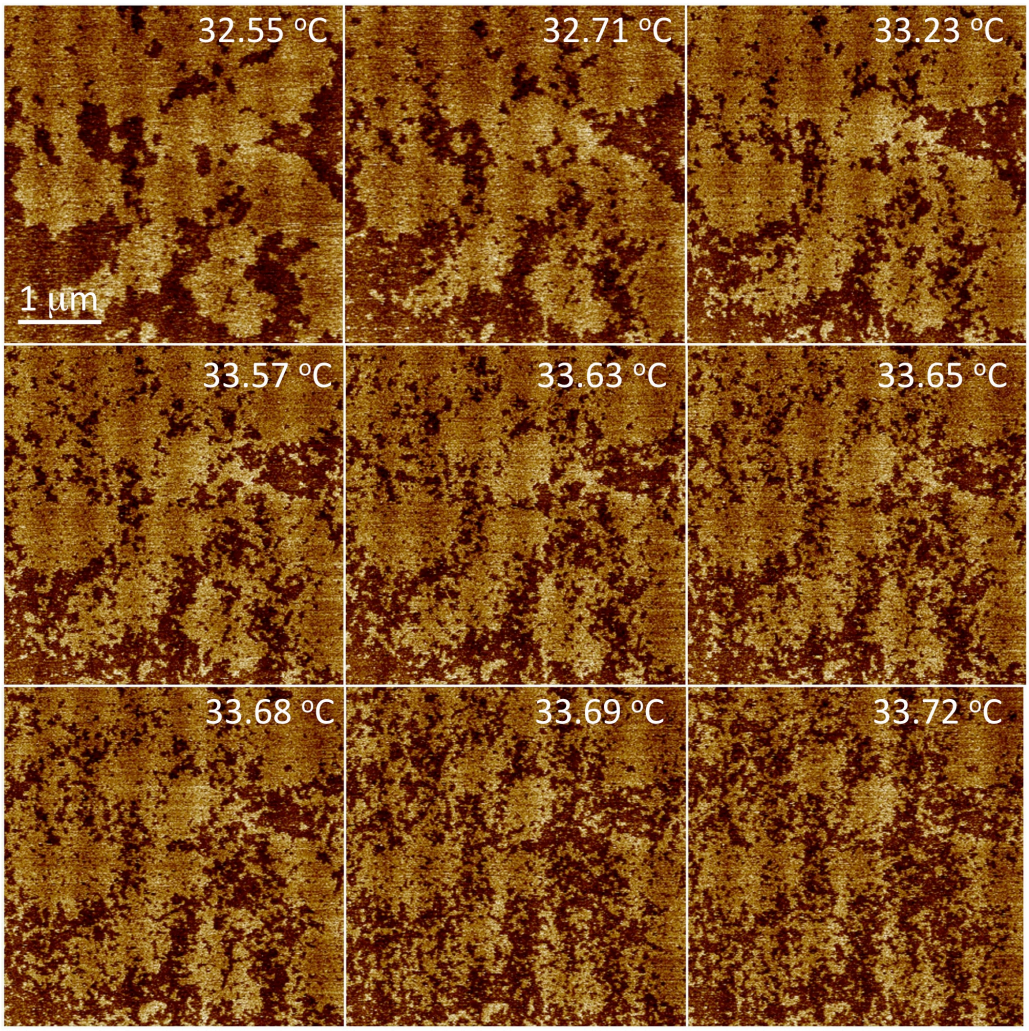

Figure 5.13: AFM images of composition 28-35-37 DOPC-SM-Chol for increasing temperature about the critical temperature 33.4 °C (Scale bars = 1 μm, imaging at 49 s per frame).

5.2.4 Correlation Length Analysis

As for line tension, correlation lengths, ξ, for critical systems in the same universality class scale with temperature. As the critical temperature is approached from above T_C, correlation lengths become large, diverging according to the power law:

$$\xi = A\left|\frac{(T - T_C)}{T_C}\right|^{\nu} = AT_R{}^{\nu} \tag{5.11}$$

where ν is the critical exponent and A is a constant. The correlation function, or autocorrelation, is a measure of the probability of finding a similar structure (or fluctuation) as a function of distance. A correlation of 1 will indicate full correlation, 0 means random or no correlation, and -1 would be an anti-correlation. The correlation length, ξ, calculated from the correlation function, characterises the typical size of fluctuations as the temperature approaches T_C from a higher T. The order parameter being measured is the density of the bilayer. As these fluctuations are random within the plane of the bilayer, a radially averaged correlation function can be used. This function was run as a Macro in Image J (NIH) and used to analyse each image once they had been carefully leveled and converted into a binary format (Figure 5.14).

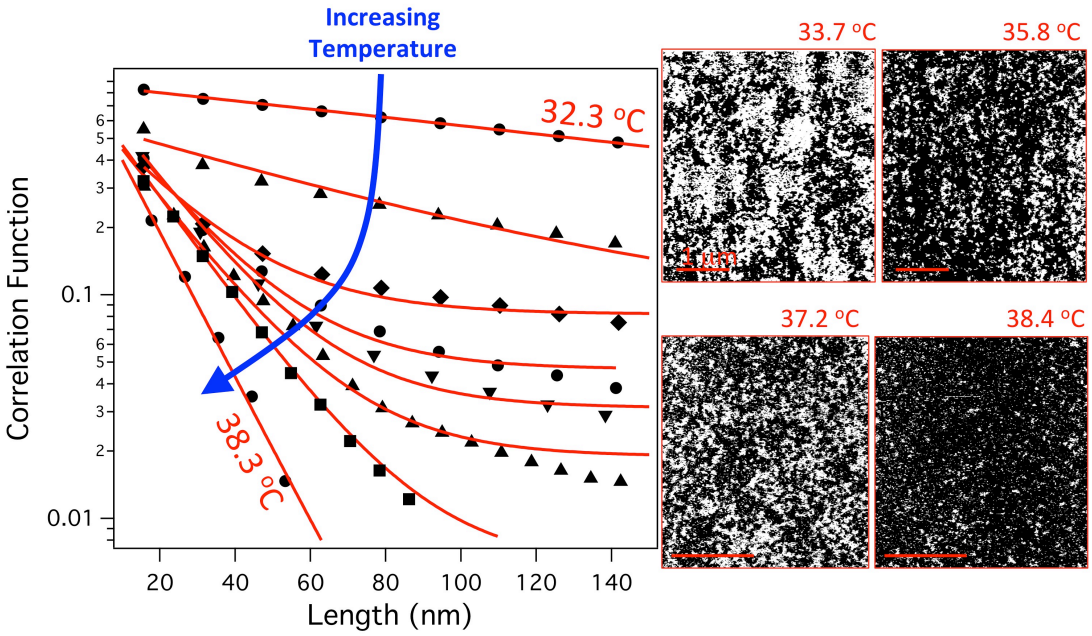

Figure 5.14: Semi-log plot of the radially averaged correlation function of sample G for different temperatures. Each line show fits to the exponential functions used to determine the correlation length. The binary AFM images illustrate the structures observed (scale bar = 1 μm).

Figure 5.14 shows a plot of the correlation functions for the image sequence of sample G. The correlation functions fit exponential decays, whose decay length is characteristic of the correlation length. It can be clearly seen that the correlation length drops monotonically with an increase

in T above T_C. At a temperature of 33.8 °C the correlation length was 90 nm, dropping to 12 nm at 37.5 °C, reflecting the existence of a smaller correlation between the fluctuating domains. According to universality these critical fluctuations should scale the same way with temperature for systems in the same class with the correlation length always becoming very large as T_C is approached. The expected behaviour is given by Eqn. 5.11 where the term in the outer brackets is the reduced temperature (T_R) in Kelvin and ν is the critical exponent, which has a value particular to the model. This power law exponent is universal, but the value of the constant A depends upon the system and should be related to the size of the smallest natural length (e.g., a molecular size). The value of T_C was obtained by plotting the inverse of the correlation length against temperature (Figure 5.15, left) giving a straight line which, when extrapolated to the x-axis (and hence $\xi = \infty$), gives T_C. By this method Tc was found to be 32.5 °C, 0.9 degrees lower than the temperature estimated by looking at the images (Figure 5.13) and 1.2 degrees lower than via the line tension.

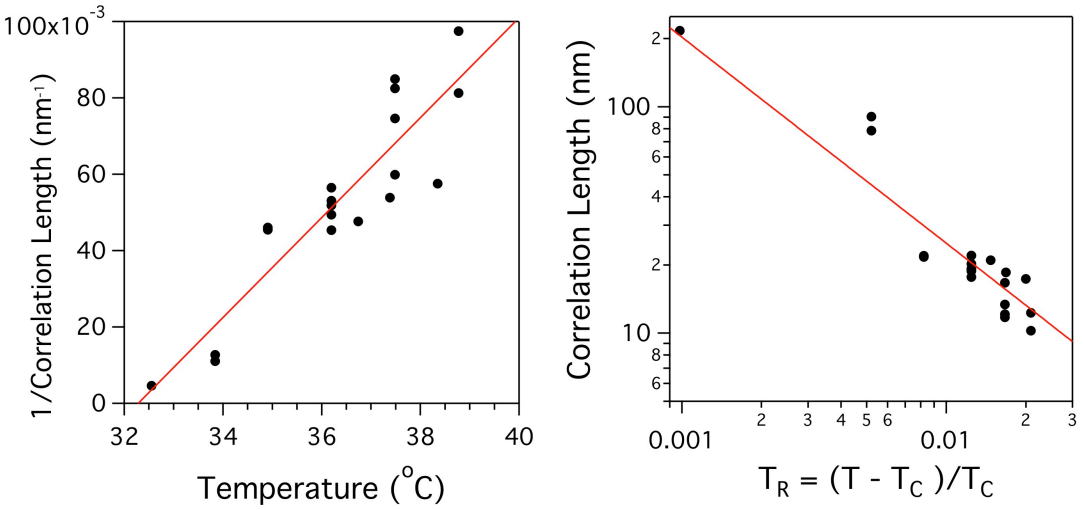

Figure 5.15 (Left) The inverse of the correlation length ($1/\xi$) plotted against T for sample G. The x-axis intercept gives the value of T_C to be 32.5 °C. (Right) Correlation length ξ plotted against the reduced temperature. The slope of the line gives the critical exponent value for ν of 0.91.

The plot of log ξ against log T_R is given in Figure 5.15 (right) for two temperature ramps of two preparations of sample G. The data follows a roughly straight line with scatter, with a slope 0.91. This best fit value is

closest to the value for the 2D Ising model of 1. This indicates that sample G is best described by the 2D Ising model agreeing with the critical exponent obtained via analysis of the line tension. The non-exact correspondence to the 2D Ising model may be due to fluid hydrodynamic effect on the domain formation kinetics and also that of the substrate. Recent work by Haataja [144,145] shows theoretically that large fluctuations in compositional domains will induce the flow of lipid components and domain structures, thereby inducing flow fields in the surrounding fluid. The water is not a passive structure, its motion interacts and couples with the membrane, changing its behaviour. However, from a theoretical viewpoint, these dynamics should not affect energetic properties, such as ν.

5.2.5 Lipid Domain Lifetime Analysis

Near and above the critical temperature domain dissolution and nucleation was observed while imaging at large scales. To further investigate the nature of these fluctuations high speed AFM imaging was used at smaller length scales, at imaging speeds as low as 1 frame per second. Both Lo domains in a mostly Ld phase and Ld domains in a mostly Lo phase were observed transiently appearing and disappearing.

Figure 5.16 shows a selection of images taken from a 50 frame series of the same area. The continual imaging of the same point showed no notable change to the total Lo fraction which was initially 8.2% at frame 1 and finished at 7.6% by frame 50 (standard deviation in area fraction over 50 frames was 0.82%). This suggests that the repeated imaging of the same area at low force for many scans does not change the inherent phase behaviour.

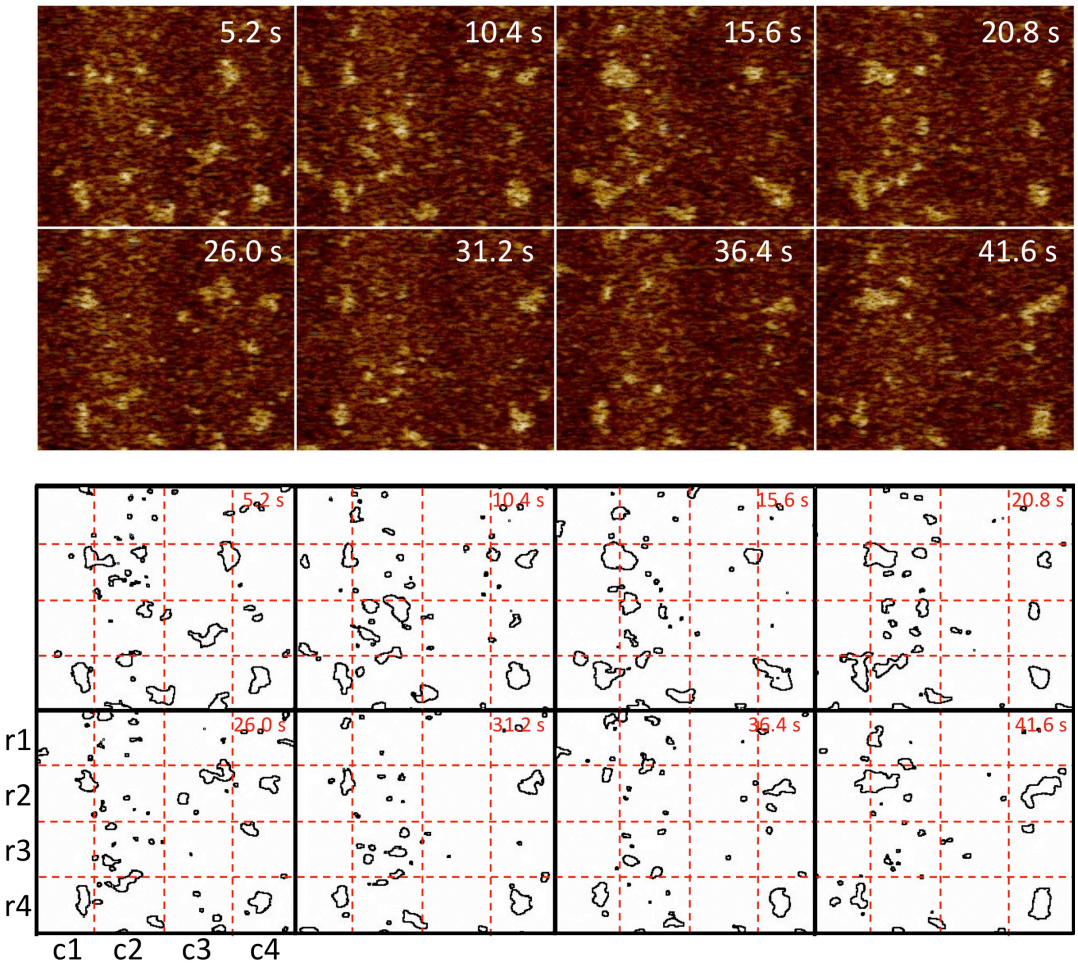

Figure 5.16: (Top) High speed AFM imaging of dynamic domain fluctuations at 33.7 ^{o}C at a imaging speed of 5.2 s per frame (scan size is 1.2 x 1.2 μm). (Bottom) Lo domain outlines of AFM images in top panels obtained via analysing particles of binary converted images used to track domain dynamics. Each panel is split into 16 with row reference r(n) and colunm reference c(n) (n =1,2,3 and 4).

To track the changes in individual domains images were rounded using a median filter to reduce noise and converted to binary format. From binary images the domains were analysed using the 'Analyze particles' function in imageJ (NIH) outputting domain area and outline whilst assigning each domain in each frame a number. Overlaying a labeled grid onto the images highlights frame to frame changes of each domain (Figure 5.16, bottom). Some domains, such as the one in (r4, c4), show no net change in the domain area over time, with only small fluctuation in shape and radius. Other domains can be seen spontaneously appearing and disappearing only being visible in one image as observed for the domain at (r2, c4) at the 10.4 s frame.

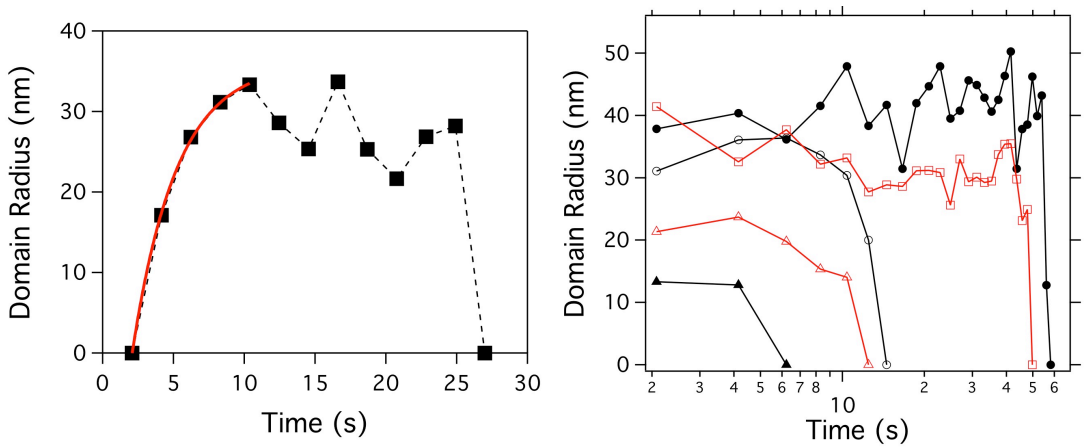

Figure 5.17: Single domain nucleation and dissolution for sample G at 35.8 °C. (Left) Tracking domain radius with time for an Lo domain which nucleates in the Ld phase, maintains its size for 20 s before abrupt dissolution. (Right) Radius vs. log time plot of different domains with various initial radii. Data was analysed from a AFM 46 image sequence with a 2.2 seconds per image frame rate.

Figure 5.17 shows an example of a domain at 35.8 °C being imaged every 2.2s, and this high time resolution allows 4 data points to be collected during the domain nucleation. Fitting the nucleation to an exponential function, $r = A.exp(t/\tau)$ where r is the domain radius, A is a constant, t is time and τ gives a characteristic time constant. Fitting of this equation gave a value for τ of 2.8 s. The domain then stays stable with small fluctuations in the mean radius of ~30 nm for 20 s before disappearing immediately within 2.2s preventing any intermediate dissolution stages to be captured. Figure 5.17 (right) shows the behaviour of multiple domains, with the starting radius taken from the spontaneous nucleated radius, as can be seen the lifetime of the domain increases with domain radius. The rate of dissolution appeared to have no dependence on initial radius, domains ranging from 20 to 80 nm domains were observed dissolving within 1-2 frames (2-4 seconds) while some domains showed slowed dissolution at rates similar to the nucleation rate in Figure 5.17 (left).

Analysis of the lifetimes of different sized domains (Figure 5.18) showed the smaller the domain the shorter the lifetime. This result is as expected since smaller domains are less energetically favorable having a large perimeter, and hence line tension, relative to area. As temperature is increased further the fluctuations become even more dynamic and domain

lifetimes become shorter. Figure 5.18 shows a comparison between the domain size-lifetime relations at different temperatures. As the temperature is increased, domains of comparable size have shorter lifetimes. The plots follow a square power law, $\tau = A.r^2$, where τ is the domain lifetime, r is the peak radius and the lifetime coefficient A(T) is a constant which varies with temperature. The fitting to squared radius relationship implies the lifetime is linearly related to its maximum area.

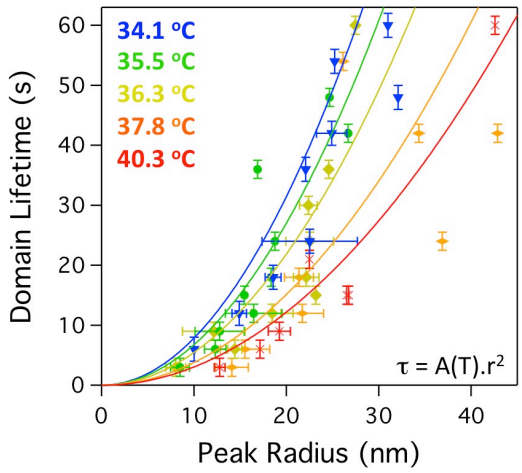

Figure 5.18: Analysis of domain lifetime with the maximum radius each domain achieved within its lifetime with varying temperature. Each data point with radius error bars represents the average of multiple domains. The data was fit to power laws with an exponent of 2 and zero offset.

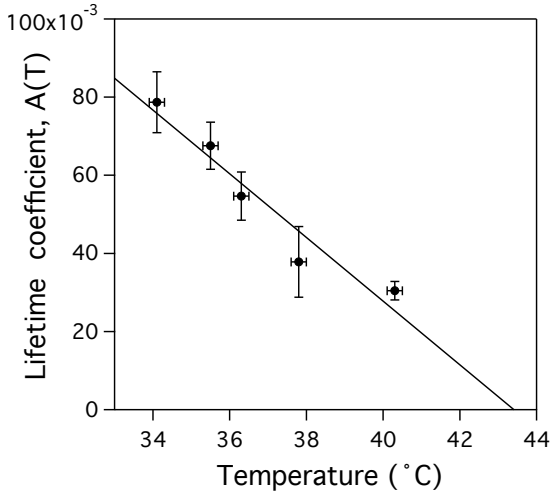

Figure 5.19: Domain lifetime coefficient, A(T), dependance on temperature for experimental. The lifetime coefficient was found by fitting radius lifetime curves to $\tau = A \cdot R^2$.

Figure 5.19 shows how as temperature is increased above T_c the lifetime coefficient from Figure 5.18 also decreases. Linear fits to the temperature dependence of A(T) suggest it tends towards to zero crossing at 43.4 ^oC which closely coincides with the temperature at which no domain are visible.

Nucleation in metastable states has been an area of much theoretical and experimental activity since the time of Maxwell and Van der Waal. Classical nucleation theory was worked out mainly by Volmer, Becker and D¨oring, Zeldovich, and Frenkel. Under the treatment of relaxation of an initially homogeneous metastable state as a kinetic process, triggered by the creation of spherical clusters of the new, stable, phase as thermal fluctuations in the metastable phase, the classical theory provides the fundamental nucleation rate:

$$J = \alpha \exp\left(-\frac{\Delta G^*}{k_B T}\right), \tag{5.12}$$

Where α is a pre-exponential factor, ΔG^* is the minimum work needed to create critically large cluster of radius R_c, k_B is the Boltzmann constant, and T is the temperature of the system. The nucleation rate J gives the number of possible clusters of the new phase per unit area per unit time. The activation barrier to nucleating a 2D disk from the melt is given by:

$$\Delta G^* = \frac{\pi \lambda^2 a_g T_m}{\Delta H . \Delta T} \tag{5.13}$$

Where a_g is the molar area of the Lo phase (3.6×10^{17} μm^2/mol for Lo phase sample G), ΔT temperature difference from the melt temperature, ΔH is the enthalpy of the phase transition (1 Kcal/mol for 1:1:1 DOPC-SM-Chol [146]) and λ is the interfacial line tension between the domains and surrounding medium. It follows that the size of the critical nucleus is:

$$R_c = \frac{\lambda a_y T_m}{\Delta H . \Delta T} \tag{5.14}$$

Applying this to sub-critical temperatures, for example $\Delta T = 3\ ^{o}C$, using a typical line tension of 1 pN [9] yields a critical radius of the order 10 nm, similar to the sizes of the transient domains observed in the critical fluctuations (Figure 5.16), however, this is only applicable for the metastable state of a system which has been quenched below T_m. The assumptions which underlie classical nucleation theory only apply to 1st order phase transitions, i.e. going from a metastable state into a thermodynamically stable one. In a critical transition, the line tension tends to zero at the critical temperature, correlation lengths tend to infinity and thus domains are a result of transient compositional fluctuations.

In two dimensions the Ising model uses a square lattice to describe phase separated systems. On each lattice site there is a variable, typically called spin (due to its application to describe the behaviour of spin moments in magnetic domains), which can be one of two values, $s_i = 1$ or $s_i = -1$. Each spin interacts with its nearest neighbor on the lattice through an exchange interaction, J, which favours parallel alignment. This can be described by the Hamiltonian:

$$\mathcal{H} = -J \sum_{\langle ij \rangle} s_i s_j \qquad (5.15)$$

for which the summation runs over all pairs of nearest neighbour sites. While the one-dimensional Ising model is relatively simple to solve, the two-dimensional Ising model is highly non-trivial. The first analytical solution to the two-dimensional Ising model was found by Lars Onsager, giving an exact set of critical exponents for the 2D universality class [147]. The 2D Ising model produces a uniform, disordered phase at high temperature, two coexisting phases at low temperature, and fluctuations near the critical point.

5.2.5 Biological Relevance

In recent years, there has been a large range of opinions, speculation and varying results on the lifetimes of cellular rafts from long lived to short-lived rafts, with lifetimes ranging down to sub-milliseconds [148,149].

Fluorescent lipid analog BODIPY-GM1, which preferentially partitions into liquid-ordered phases was used to conclude that the lifetime of the observed platforms substantially exceed 2.2 s [150]. In addition to the uncertainty of the lifetime of rafts, their size also has a wide range of reported values from sub 10 nm up to 200 nm. The experimental results in this thesis show critical fluctuations are capable of replicating proposed cellular phase behaviour with 5 - 20 nm radius Lo domains being directly observed with sub 2 second lifetimes. The data also suggests that at temperatures even further from the critical temperature domain lifetimes decrease further, however direct imaging of these features become difficult since the height difference between the domains at these temperatures becomes comparable to the AFM imaging noise and fluctuations exceed the imaging rate.

5.3 Conclusions

The fluctuating nanodomains observed at temperatures above T_C range in size from 100 nm (fractionally above T_C) down to around 10 nm (5^oC above T_C). This is a considerable temperature differential, and is equivalent to nanodomains existing in the apparently single phase region above the critical point in the 40–50 mol% range at room temperature. AFM imaging has also determined that critical behaviour extends a reasonable distance either side of the line of the critical point. This would indicate that the nanodomain region is quite substantial in size, and would be a prime candidate for the transient and small, but definitely present, raft like structures in cell membranes, as determined by NMR and FRET measurements.

The presence of a spinodal domain structure at particular compositions in the two-phase region can now also be explained. If the thermal history of the sample takes the composition through a critical region during cooling, then a spinodal structure will result. On supported membranes, this continuous percolating structure may be rather fine as the surface drag prevents domain coalescence into larger spinodal swirls. Away from this critical region, first order phase transitions occur and the mechanism will revert to a nucleation and growth mode, leading to isolated domains.

This work demonstrates that AFM can be an illuminating technique in the study of critical phenomena, obtaining results which are agreement with other recent work, but most importantly bridging the length scales from fluorescence microscopy of GUVs (low resolution) to the molecular scale measurements (NMR, FRET). In doing so the data provides direct existence of transient nanodomains within the high cholesterol single phase in the vicinity of a critical point. The phase separation is consistent with a critical phase transition that follows the 2D Ising model both in terms of the line tension and correlation length, in agreement with recent papers by Honerkamp-Smith and Veatch. In summary, compositional fluctuations were measured and characterised, with nanodomains 10–100 nm in diameter existing at temperatures up to 5^oC higher than T_C. The temperatures where

these structures were found ranged from 24 ^{o}C to nearly 40 ^{o}C (dependent upon composition), well within in the biological range. As this simple model system has been found to have a phase diagram nearly identical to that of biologically derived plasma membranes, this finding must have important implications to the study of lipid rafts in real cell membranes.

Chapter 6
Actin Binding Transmembrane Proteins in Phase Separated Lipid Bilayers

As discussed in the previous chapter it has been proposed that critical fluctuations of small domains are what define lipid rafts. By their nature critical systems are sensitive to perturbations and therefore interactions with membrane proteins and the actin cytoskeleton are believed to potentially provide routes to the stabilisation of domains [5]. This chapter builds on current model systems, increasing the complexity and relevance by incorporating a GPI anchored transmembrane actin binding protein into phase separated supported membranes. Although most interactions between the actin cortex apparently involve intermediary proteins, there are a small number of direct linkages between actin and membranes. One such is the 17-kD transmembrane protein ponticulin from *Dictyostelium* amoeba. Ponticulin has been shown to be responsible for 96% of the actin binding to the *Dictyostelium* membrane and almost all membrane associated actin nucleation. Although the structure has not been solved, the protein is proposed to have one side with an actin-binding site, at which binding is thought to be largely electrostatic with the other cytoplasmic domain containing a glycosylphosphatidylinositol (GPI) anchor [45]. GPI anchored proteins when in solution have the ability to insert into the lipid bilayer of cells [151] and have been well documented to be raft active proteins found in detergent resistant membranes, extracted from cell membranes at low temperatures. Extraction of *Dictyostelium* membranes found 75% of total cellular ponticulin partitioned into the detergent-insoluble pellets. With latrunculin B pretreatment to depolymerise the actin, ponticulin displayed even partitioning between the pellet and supernatant fractions, suggesting actin-ponticulin interactions may influence lipid organisation or that the protein exists preferentially in raft like domains. This may provide an ideal route to raft stabilisation through protein and actin interactions, however since detergent solubilisation experiments are done at 4^{o}C they often do not represent a true picture of lipid organisation at physiological temperatures.

6.1 Ponticulin Localisation

Initially control experiments using a 3:2:2 DOPC-sphingomyelin-cholesterol lipid mix without ponticulin were performed with vesicles prepared via the detergent solubilisation/rapid dilution method (section 3.4.3). Initial results showed incomplete bilayer formation even after hours of incubation with a mica substrate. Subsequently, it was found that a second rapid dilution and centrifugation step was required to remove additional detergent allowing the vesicles to form a complete bilayer within 2-3 hr. AFM imaging of bilayers formed on mica by this method showed phase separation into liquid ordered and liquid disordered domains with minor defects and only a few bound vesicles per 100 μm^2 scan area (Figure 6.1 A). The area fraction of the Lo phase was found to be 42% $\pm$ 5% with a height difference between the two phases of 0.8 $\pm$ 0.2 nm. These characteristics are in agreement with the ternary phase diagram in Figure 5.5.

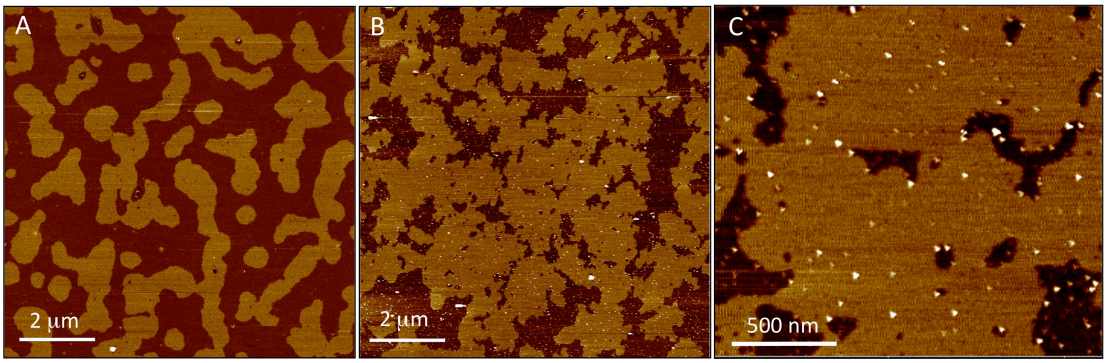

Figure 6.1. AFM images of 3:2:2 DOPC-sphingomyelin-cholesterol lipid bilayers (A) without and (B) with ponticulin reconstituted vesicles. (C) Higher resolution image showing ponticulin protruding from the membrane.

When ponticulin was incorporated into vesicles, bilayer formation proceeded as with vesicles without ponticulin. Imaging of the ponticulin bilayers showed a change in phase area and structure (Figure 6.1B). The area fraction in the Lo phase increased to 65 $\pm$ 4 % and the domain boundaries became much less smooth and rounded. Ruffling of the domain edges implies that the energy penalty required to sustain the interface between the two phases is reduced and therefore the line tension has been

lowered by the incorporation of ponticulin. The significant increase in the area of ordered domains can be explained by the probability of nucleation sites arising from the GPI anchors upon cooling. Also the additional number of fatty acyl tails of the GPI anchor contribute to a different composition of the overall membrane.

AFM imaging at smaller scales (Figure 6.1 C) shows the bilayer has a high density of small objects 0.5 - 3 nm in height, indicating that ponticulin has extracellular domains protruding out of the bilayer. The locations of these points were analysed (Figure 6.2) classing each point to Lo, Ld or interface (defining the interface as a 50 $\pm$ 30 nm wide area in the Ld circumventing the Lo phase).

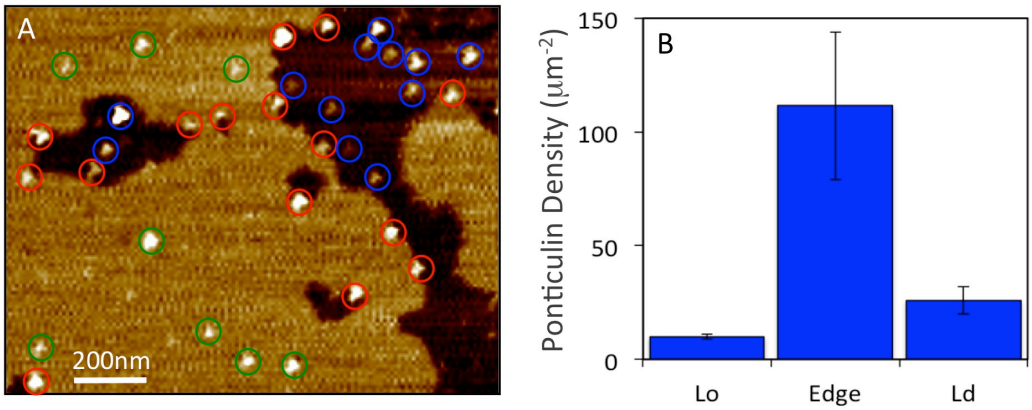

Figure 6.2. (A) AFM image of 3:2:2 DOPC-SM-Chol bilayer with ponticulin highlighting the assigned region in which each ponticulin is found (green = Lo, red = edge, blue = Ld). (B) Bar chart of ponticulin density for each region (n = 270).

The number density of ponticulin in each region is 110 $\pm$ 30 μm^{-2}, 26 $\pm$ 6 μm^{-2} and 10 $\pm$ 1 μm^{-2} for the edge, Ld and Lo respectively (Figure 6.2 B). The error associated with the density values in each region comes from errors in determining the area classed as boundary area. In comparison to a random uniform distribution in which the ponticulin density is the same in each region, there is over 5 fold greater number points found at the boundary than expected, a 2 fold decrease in points found in the Lo phase and the expected number of points found in the Ld phase. The ponticulin density values are lower than estimates for the native membrane of ~300 ponticulin/μm^2 and lower than previous results for ponticulin reconstituted

EggPC lipid bilayers in which a density of 250 ponticulin/μm^2 was obtained [103]. These results are in agreement with the hypothesis that ponticulin localises to domain edges. The fact that half the expected ponticulin density is observed in the Lo could signify that half of the protein in the Lo phase is mobile and able to distribute to the phase interface. Although one might expect to observe ponticulin preferably in the Lo phase due to the GPI anchor it may be that the transmembrane portion of ponticulin is better hydrophobically matched to the Ld phase. Hydrophobic matching of proteins to their surrounding membrane lipids arises due to favourable interactions between the hydrophobic regions of the protein and the acyl chains of the lipids. It has been previously demonstrated that the bilayer thickness can influence integral protein sorting, activity and microdomain formation [152].

6.2 Ponticulin Structure

Studying the heights of the extra cellular domains protruding out of the membrane gives a distribution with two peaks, a sharp first peak at 0.8 ± 0.2 nm with a secondary peak at 1.7 ± 1.0 nm (error = σ) (Figure 6.3). Integration of these peaks (excluding overlap) gives counts of 110 and 128 for the 0.8 nm and 1.7 nm height peaks respectively. This double height distribution suggests the protein resides almost evenly in the two different possible orientations. Ponticulin is thought to have a sugar chain on one side with the GPI anchor which could correspond to the 1.7 nm peak which has a wider distribution. The other side has an actin binding site which one would expect to be smaller and have the tighter height distribution as seen with the 0.8 nm peak (Figure 6.3).

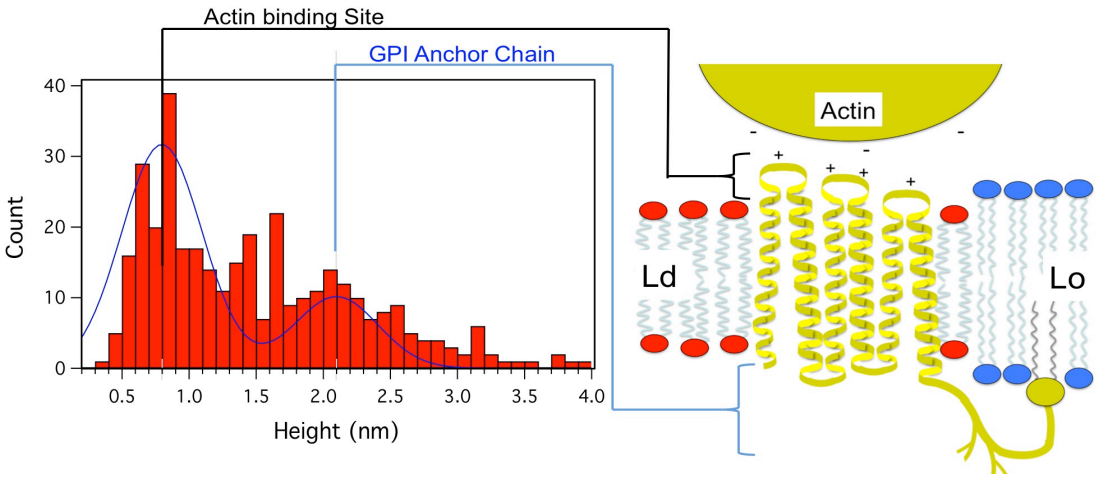

Figure 6.3. (Left) Histogram showing the height distribution of the extracellular domains of ponticulin relative to the Ld phase with a double peak Gaussian fit. (Right) Hypothetical model of ponticulin structure [45] and its location within phase separated membranes.

6.3 G-actin Binding to Ponticulin

Incubation of G-actin with ponticulin containing bilayers allowed tracking of the G-actin-ponticulin binding process. Figure 6.4 shows images at 10 min and 30 min after G-actin incubation taken from a sequence of images. Monomers bind to both existing ponticulin points, increasing their size, and also to some areas which appear to have no ponticulin. Line profiles of a ponticulin protein at the edge of a domain before and after G-actin binding (Figure 6.4C) show a height change from 1.9 nm to 4.8 nm corresponding to a ~3 nm increase, consistent with the dimensions of G-actin (3.5 nm x 5.5 nm x 5.5 nm) [47].

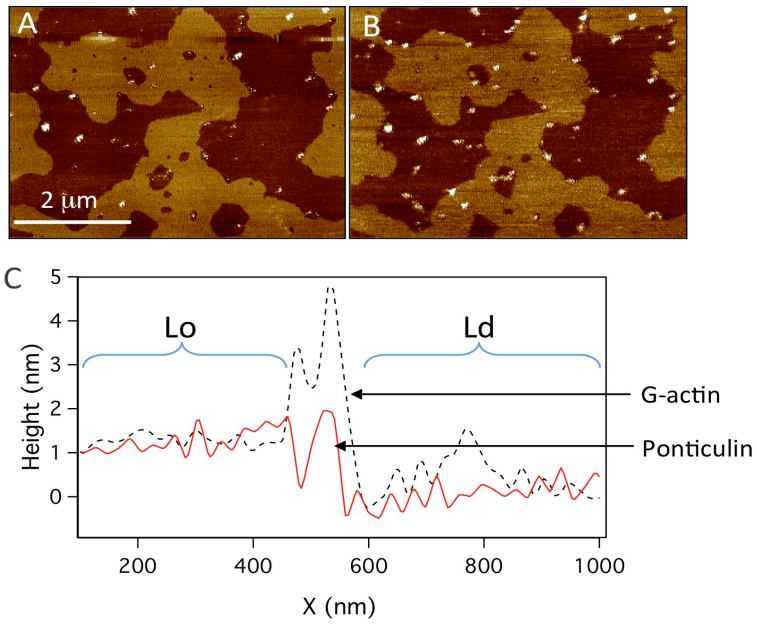

Figure 6.4. AFM images of bilayers containing ponticulin (A) 10 min and (B) 30 min after G-actin incubation. (C) Line profiles of a ponticulin molecule at the edge of a domain before (red filled line) and after (black dashed line) G-actin binding.

Imaging over time allowed the number of G-actin monomers bound to the bilayer within a 100 μm^2 area to be tracked. Results show a linear relation between monomer number and time (Figure 6.5). Analysis of the location of G-actin binding at 10 min and 30 min after G-actin incubation shows that the majority of binding is as expected: to the domain edge regions (Figure 6.5). The binding of G-actin to edge regions with no visible ponticulin may occur due to the height of the extra cellular domain matching

that of the Lo phase thus ponticulin may be in higher concentrations at the edge than is visible by AFM. 57% of surface bound G-actin is at the edges of domains, whilst a random distribution would give 10.4 ± 2% suggesting 46.3% of the ponticulin within the membrane has actively located. Given that height data of ponticulin showed two populations of heights that may correspond to the two possible orientations, G-actin appears to bind to both terminals of ponticulin. The observation that G-actin appears to bind linearly with time may be due to AFM tip interactions reducing binding, by removing monomers while scanning across the surface.

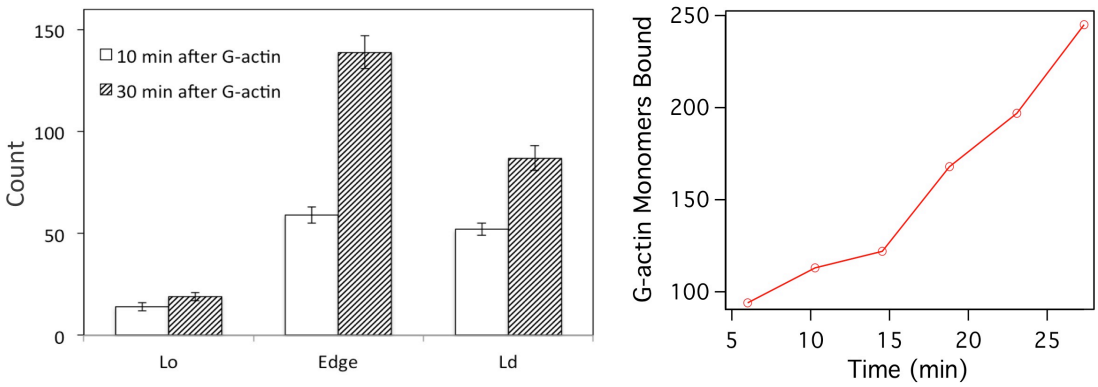

Figure 6.5: (Left) Bar plot showing location of G-actin binding at 10 min and 30 min after G-actin incubation. (Right) Number of G-actin monomers bound to bilayer with time in a 100 μm^2 area.

6.4 Effect of Ponticulin on Domain Behaviour

As discussed in chapter 5, the interfacial line tension of a lipid domain gives an indication of the energy penalty required to maintain coexisting phases. The ratio of domain area to domain perimeter has been shown to be proportional to the interfacial line tension energy [143]. Figure 6.6A shows how this ratio varies with increasing temperature for both the systems with and without ponticulin. At room temperature the area divided by the perimeter of the membrane containing ponticulin is at almost half of that of the lipid only system. As temperature is increased, the area/perimeter of both systems remains relatively constant up to 35 ^{o}C, at which point it begins to decrease, reaching zero at 40 ^{o}C. The highest temperature at which two phases could be seen was 44 ^{o}C and 40 ^{o}C for the lipid only and the ponticulin membrane systems respectively. AFM images from which the area/perimeter ratio was measured showed Lo domains breaking up into smaller and smaller domains as the temperature approached single Ld phase for the lipid only system (Figure 6.6 B). For the ponticulin membrane (Figure 6.6 C) the domains also broke up but maintained fractional Lo coverage. Additionally, the domains gained holes i.e. patches within large Lo domains became Ld. At 38.5^{o}C, the difference between the two systems' domain stability can be clearly observed in the AFM images at the same temperature (Figure 6.6 B,C).

Protein incorporation has been previously shown to stabilise domains above their miscibility temperature. Here, the opposite is observed with ponticulin acting to decrease the line tension between the two phases. Although this may be unexpected it further confirms its binding affinity for the domain boundary. Previous studies of histidine-tagged green fluorescent protein binding to nickel lipids in phase separated GUVs showed similar results, with the binding causing a reduction in line tension which was attributed to binding at the boundary between the two phases [153]. A number of other proteins have been reported to localise at domain boundaries [154] including anti microbial peptides and ion channels [155]. For cases in which the hydrophobic thickness of the membrane protein is in between the hydrophobic thicknesses of two different lipid domains, both

experimentally and theoretically it was shown that proteins accumulate at the domain boundaries, where the hydrophobic thicknesses most favour the matching requirements [156].

Although ponticulin alone appears to reduce the transition temperature, when compared to a lipid only system the purpose of its GPI anchor could be through stabilisation of raft like domains upon triggering via actin polymerisation. The picket fence model describes actin binding proteins as pinning points (picket) to which actin can bind and subsequently trap raft associated lipids (fence) [157]. Observation of compartmentalisation of lipids which undergo hopping within a number of different cell types has provided strong evidence for this model [158]. Applying the observations in this thesis to this model suggests the GPI anchor is used to surround domains and increase the probability of polymerisation of actin, thus acting as a fence in these transient domains. Further the actin nucleation power of ponticulin could allow direction of these proteins to the domain edges in order to trigger polymerisation.

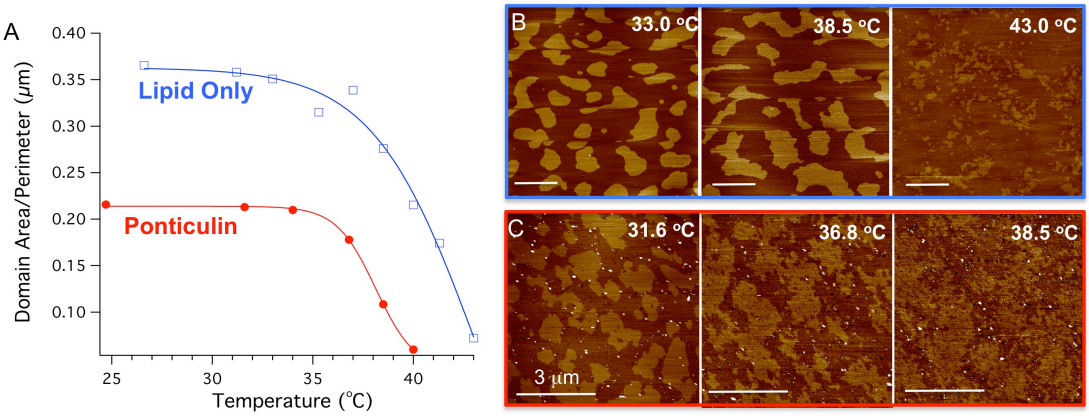

Figure 6.6 (A) Lo domain area divided by domain perimeter as measured from images at various temperatures, providing a proportional measure of the domain line tension as a function of temperatures as the phase boundary is crossed. The typical AFM images at various temperatures used to obtain area/perimeter values without and with ponticulin in the membrane are shown in image series (B) and (C) respectively (scale bar = 3 μm).

6.5 Conclusions

The observation that the transmembrane GPI-anchored ponticulin in supported bilayers spontaneously localises to domain boundaries shows that lipid order plays an important role in the interaction between cytoskeletal proteins and the membrane. The present experiments indicate that, at room temperature, ponticulin not only favourably exists in the Ld domains, at the boundary between the Lo-Ld of the DOPC/SM/Cholesterol supported bilayers model systems, but also that this decreases the line tension between the two phases.

Chapter 7

Actin Polymerisation at Cationic Lipid Bilayers

The focus of this chapter is on investigating the phenomena of actin polymerisation from non-polymerising bulk conditions to the surface of positively charged membranes. Using AFM, QCM-D and Fluorescence microscopy of supported lipid bilayers under varying conditions, the factors governing the actin polymerisation dynamics and filament organisation are studied. This was carried out with a view to creating biomimetic actin-membrane structures, actin based coatings for drug delivery systems and understanding the underlying mechanisms for biological relevance.

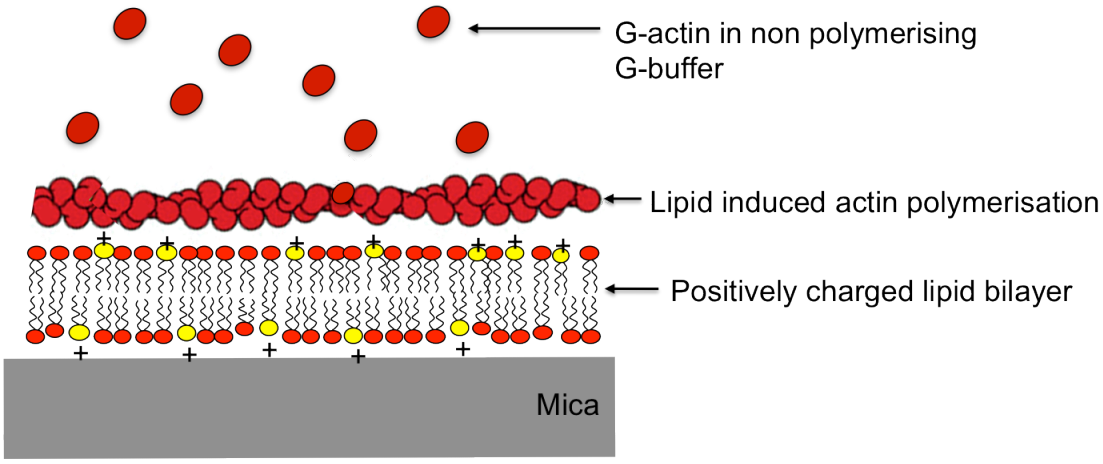

Figure 7.1: Schematic showing actin polymerisation at cationic supported lipid bilayers in non-polymerising bulk conditions.

This chapter looks at actin interactions with bilayers in fluid and gel states. Therefore, initially the lipid diffusion properties of both the lipids and actin monomers were investigated. The bilayer formation and integrity were also studied before observing the interaction of G-actin with a range of charged lipid fractions in both the gel and fluid membranes. Subsequently the effect of varying the buffer pH on actin coverage and polymerisation rate was investigated. Finally a model of the adsorption/diffusion process was developed to provide a description of the experimental data.

Previous studies of actin and bilayer interactions have focused on the addition of pre-polymerised filaments to supported bilayers. G-actin and F-actin binding to Egg PC bilayers through the transmembrane protein ponticulin was achieved by Barfoot et al. [103]. Shi et al. used electrostatic binding of F-actin on charged lipid bilayers to form actin paracrystals, with the tight packing allowing single actin monomers to be directly resolved by AFM in the contact mode [159]. Alternative techniques for forming binding actin have utilised intermediary linkers; for example, biotinylated G-actin has been used as a nucleator for filament formation when attached via streptavidin, and actin binding proteins with an additional histidine tag to link actin to Ni-NTA tagged lipids [160-163].

In addition to ATP and salts, it has been shown that actin polymerisation can also be induced at lipid membrane surfaces, under non-polymerising conditions, provided that the lipid membrane contains charged lipids, or surfactants, to nucleate filament formation [164,165]. Renault showed that actin could be polymerised, under non-polymerising conditions beneath Langmuir monolayers of Egg PC containing 25% charged surfactant (stearylamine). TEM data of films transferred to grids showed mostly the formation of dense structures consisting of highly aligned filaments i.e. paracrystals, with single filaments only being obtained under turbulent flow conditions [164]. The formation of actin paracrystals from non-polymerising bulk was first observed by Laliberte and Gicquaud on liposomes containing varying fractions of stearylamine, showing that the actin layer depolymerised if the liposomes were solubilised with Triton-X [165]. Although these studies demonstrated the formation of paracrystals on fluid bilayer surfaces, the mechanism for charged-lipid induced nucleation is still not well understood. More recently, attempts to create more complex structures based on actin architectures have utilised electrostatic self-assembly of F-actin and charged lipid membranes to form complex multilayered tubular structures [166] or 3D crystallisation of fluorescent quantum dots within a stacked actin-lipid membrane template [167].

The dynamics of actin polymerisation have been extensively studied with a variety of fluorescence techniques in bulk and at liposome surfaces

[163,168,169], but there have only been two high resolution AFM studies. Using HeLa cell extracts on mica, Lehto et al. imaged actin polymerisation after adsorbing endosomes, followed by the addition of cytosol from the HeLa cells [170]. More recently, high-speed AFM techniques were used to study the process of polymerisation of actin onto biotinylated-actin nucleation sites attached to a 2D streptavidin crystal. In this study, high imaging forces could be used to break the filament to simultaneously observe growth at both the "barbed" and "pointed" ends of the F-actin filament, with data showing the addition of either monomers or dimers at rates comparable to bulk studies [160].

7.1 Bilayer Characterisation

DOPC-DOTAP (fluid phase) and DPPC-EDPPC (gel phase) lipid bilayers were formed on the surfaces required for the multiple characterisation techniques used (mica, glass and SiO_2). Vesicles were prepared by the tip sonication method. Then the bilayers were formed by the vesicle rupture and fusion process.

7.1.1 QCM-D

The formation of the planar DPPC-EDPPC and DOPC-DOTAP bilayers was followed by QCM-D at 40^{o}C and 22^{o}C respectively. Figure 7.2 shows QCM-D data after injection of vesicles onto SiO_2 modified crystals. The characteristics of cationic bilayer formation have been previously described by Richter et. al. [101]. Neutral lipid vesicles typically show a two phase process whereby a build up of vesicles on the surface creates a large frequency change (Df ~ -30-60 Hz), followed by rupture at a critical surface concentration upon which the frequency change reduces to an equilibrium (Df ~ -25 Hz). However the positively charged 4:1 DOPC-DOTAP and 4:1 DPPC-EDPPC vesicles show direct rupture when they contact the substrate, due to the net negative charge on the substrate. The QCM-D response to the different formation pathways of bilayers has been previously well reported [101]. The frequency shift after bilayer formation was found to be -20 Hz and -25 Hz for DOTAP-DOPC and EDPPC-DPPC bilayers

respectively, with a dissipation value always less than $0.7x10^{-6}$ (Figure 7.2). This low dissipation value means that the Sauerbrey relationship (Eqn. 2.14) can be used to measure the thickness change after bilayer formation, based on frequency change. Taking into account the average molecular lipid weight and the lipid molecular area, gave values of 4.3 ± 0.2 nm for DPPC-EDPPC and 3.6 ± 0.1 nm for DOPC-DOTAP. The thickness of the DOPC-DOTAP appears to be lower than the expected value for a typical bilayer and thus suggests that there may be defects present. It is noted that the thickness of the DPPC-EDPPC bilayer should change upon cooling to 22°C as it changes state from a fluid phase bilayer to a gel phase bilayer, in which the lipids will have smaller lateral molecular area. This is process expected incur some defects.

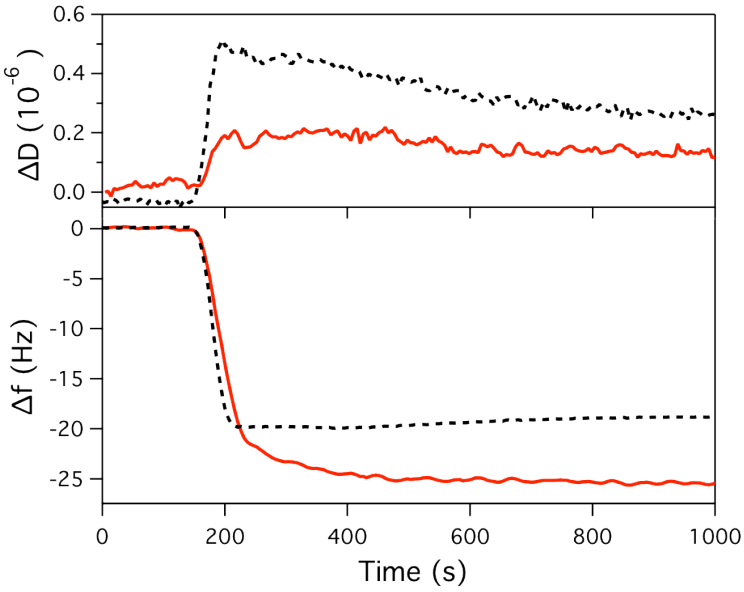

Figure 7.2: QCM-D response after the addition of 0.5 mg/ml DPPC-EDPPC 4:1 vesicles at 40°C (red) and DOPC-DOTAP 4:1 vesicles at 22°C (dashed black) to SiO_2 modified crystals. The upper panel is dissipation change and the lower panel is change in frequency. The average thickness obtained for the formation of this bilayer is 3.6 ± 0.1 nm and 4.3 ± 0.2 nm for the DOPC-DOTAP and DPPC-EDPPC bilayers respectively.

7.1.2 AFM

AFM imaging of lipid bilayers on mica was used to study the surface topography before the addition of actin. Typically, the observed topographical image of a 4:1 DOPC-DOTAP lipid bilayer by AFM was feature free, showing no bilayer defects (Figure 7.3 A). Force spectroscopy was used to establish the bilayer thickness/integrity by pushing the tip through the lipid bilayer. This 'push-through' displayed a characteristic 5 nm jump in the approach curves as the AFM tip penetrated the bilayer and came into contact with the underlying mica surface (Figure 7.3 C). AFM imaging of 4:1 DPPC-EDPPC bilayers often showed bound vesicles still attached to the surface and required a greater force to penetrate the bilayer when performing force spectroscopy measurements.

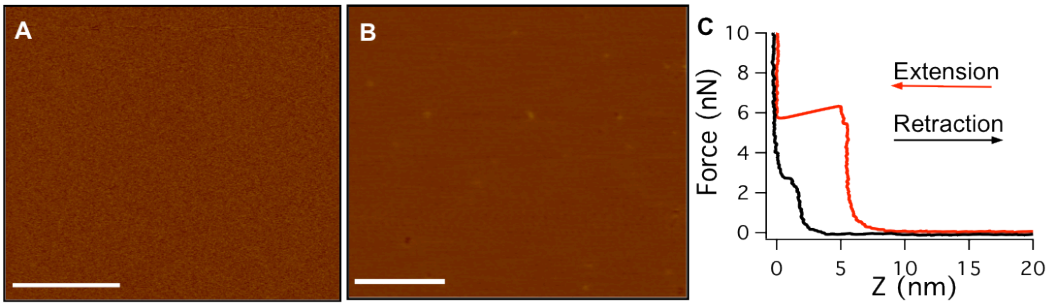

Figure 7.3: AFM images of 4:1 DOPC-DOTAP (A) and 4:1 DPPC-EDPPC (B) supported lipid bilayers on mica (scale bars = 1μm). (C) Typical force spectroscopy measurement of a 4:1 DOPC-DOTAP lipid bilayer.

In some 4:1 DPPC-EDPPC bilayers, phase separation was observed thus a range of DPPC-EDPPC compositions were studied to determine the lipid content in each phase. Figure 7.4 shows images of several different compositions covering the full range from single gel phase at high DPPC concentrations to single fluid phase at high EDPPC concentrations. These results were unexpected since EDPPC has previously been shown to be in a gel phase at room temperature by DSC [171]. The height difference between the two phases was found to be on average 1.5nm with no trend when changing composition.

To determine the composition of these domains, domain area fractions were converted into lipid fractions using the lever rule for each sample. Lipid areas per molecule of 0.47 nm^2 and 0.72 nm^2 were used for the gel and fluid phase respectively [172]. Plotting the mole % of lipids in the gel phase against mole % of DPPC in the whole system (Figure 7.5) gave a roughly linear relation, which was expected. The intercepts at 100% gel phase and 0% gel phase give compositions of gel phase: 92% DPPC, 8% EPC and fluid phase: 28% DPPC, 72% EPC. The composition of lipids within each phase remains constant throughout DPPC-EDPPC samples, displaying phase separation.

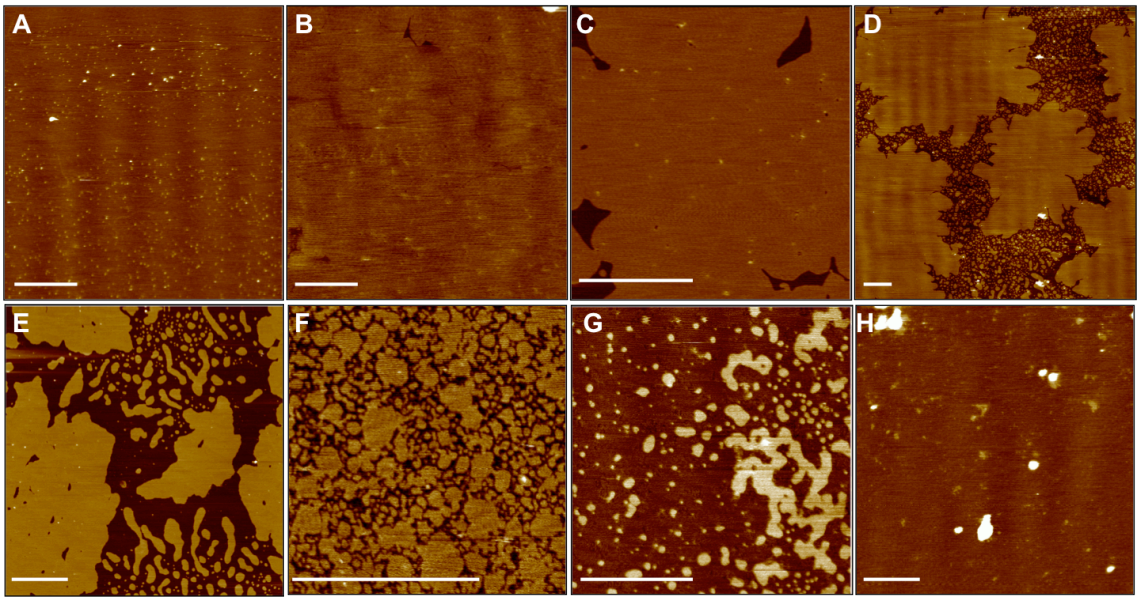

Figure 7.4: AFM images showing phase separation of DPPC bilayers containing (A) 5%, (B) 10%, (C) 20%, (D) 25%, (E) 40%, (F) 50%, (G) 60% and (H) 70% EDPPC at room temperature (scale bar = 2 μm, z-scale = 7nm).

.

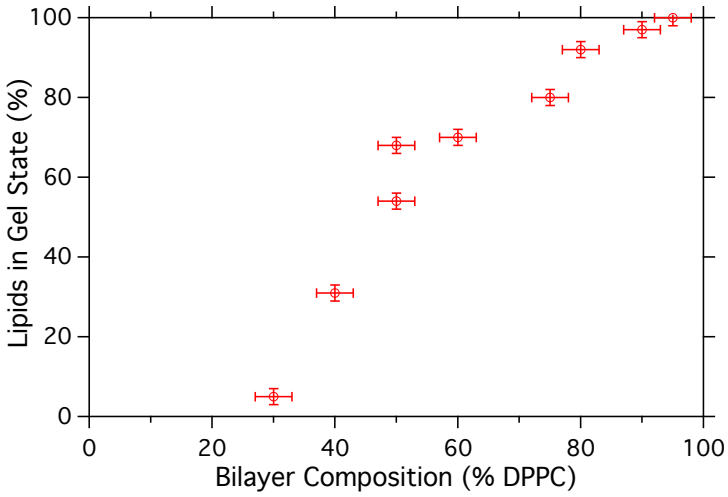

Figure 7.5: Molar fractions of lipids in the gel phase (determined using the lever rule and data in Figure 7.4) versus molar percentage of DPPC in the whole bilayer. This plot allows calculation of domain composition.

7.1.3 FRAP

4:1 DOPC-DOTAP and 4:1 DPPC-EDPPPC lipid bilayers containing 0.5 % (w/w) Texas-Red-DHPE head labelled lipid fluorophore, were studied using fluorescence recovery after photobleaching (FRAP), on glass coverslips. Representative images for each system are shown in Figure 7.6 and Figure 7.7. The almost complete recovery of the bleached area after 2 min confirmed that the DOPC-DOTAP fluid lipid bilayer was mobile. The method of data analysis used in this work is described in Section 2.2.2. The DPPC-EDPPC bilayer showed almost no recovery with only a 4% recovery over 14hr which was expected for a gel phase bilayer. Fitting the recovery data of each system gave diffusion coefficients of 3.2 $\pm$ 0.4 mm^2/s for DOPC-DOTAP bilayer and 0.004 $\pm$ 0.005 mm^2/s for the DPPC-EDPPC.

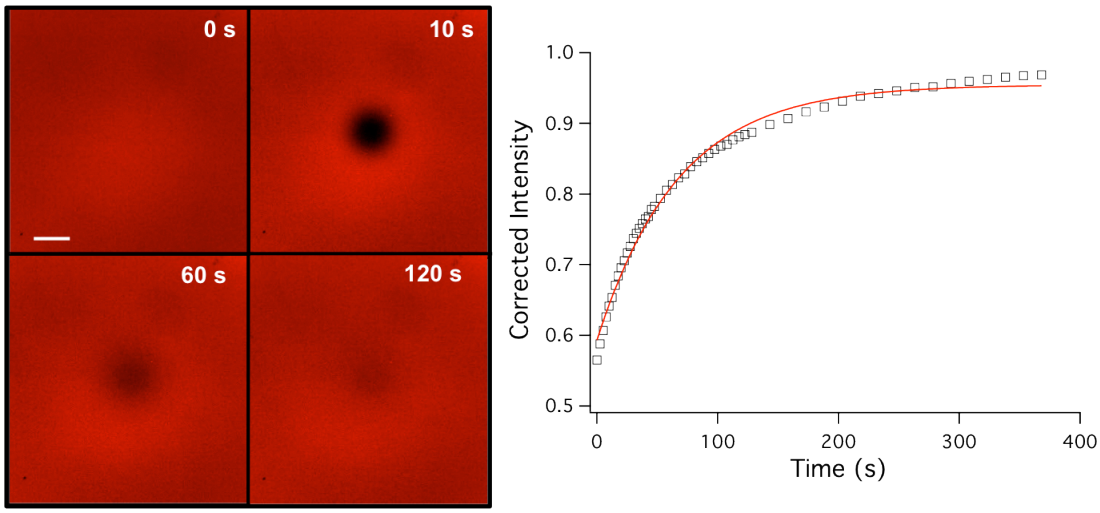

Figure 7.6: (Left) Selected images of a 20% DOTAP, 79.5 % DOPC (0.5% Texas red DHPE) bilayer showing the recovery of a photobleached spot over time. The time for each image is noted on the images (scale bars = 30μm). (Right) Typical plot of normalised fluorescence intensity change of the bleached area, with line fit used to determine an average diffusion constant of 3.2 ± 0.4 $\mu m^2/s$.

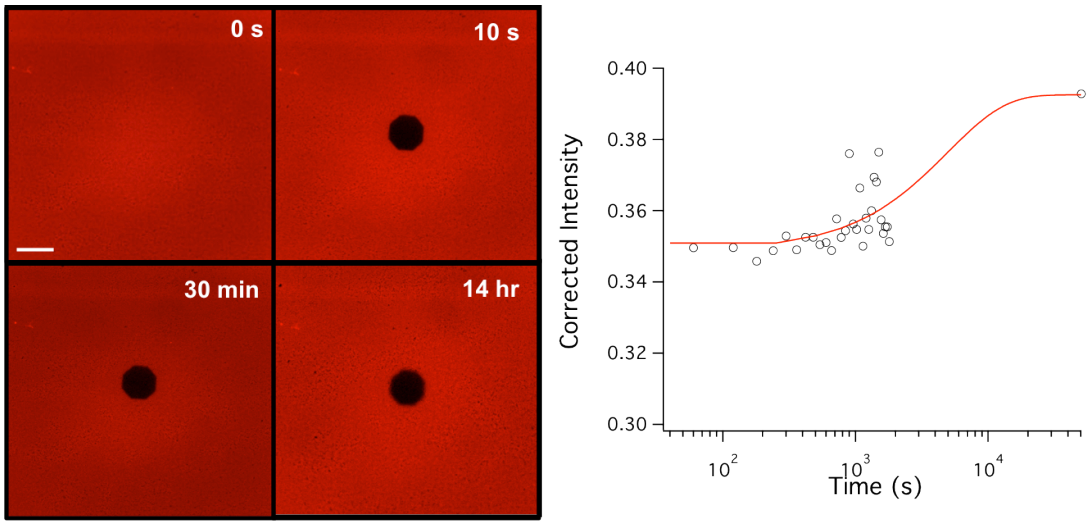

Figure 7.7: Selected images of a 20% EDPPC, 79.5 % DPPC (0.5% Texas red DHPE) bilayer showing the recovery of the photobleached spot over time. The time for each image is noted on the images (scale bars = 30μm). (Right) Typical plot of normalised fluorescence intensity change of the bleached area, with line fit used to determine an average diffusion constant of 0.004 + 0.005 $\mu m^2/s$.

7.2 Actin Adsorption and Polymerisation on Fluid-Phase Lipid Bilayers

Following the formation of DOTAP-DOPC fluid lipid bilayers with various DOTAP concentrations, the bilayers were incubated with G-actin in G-buffer conditions. For the TIRF microscopy work described in this section, all actin used was rhodamine labelled. AFM was used to characterise the actin structures bound to the lipid bilayers both qualitatively and quantitatively, allowing an understanding of the actin filament properties and their organisation. QCM-D was used to follow the kinetics of the binding process at various actin and DOTAP concentrations.

7.2.1 TIRF Microscopy

To investigate the mobility of G-actin bound to a fluid lipid bilayer, TIRF microscopy was used to sample only G-actin very close (~300 nm) to the membrane surface. The experiments were performed using 1 nM Rhodamine G-actin. Figure 7.8A shows TIRF images taken from a typical 50 image series of a diffusing G-actin, at the surface of a 20% DOTAP-DOPC bilayer on glass. Particle tracking, shown by the line trajectory (Fig. 7.8A), suggests the G-actin molecule is performing a 2D random walk whilst bound to lipids in the bilayer. Higher G-actin concentrations made tracking of single molecules problematic due to overcrowding. The diffusion constant of a single particle can be calculated by its mean squared displacement (MSD) over time using Eqn. 4.6 with a qi value of 4 (for 2D diffusion). For each single particle, the displacement from one image to the next was squared. All these values for a 50 image set were then averaged to give the MSD for that particle. The MSD of 39 particles was then converted into diffusion constants, plotted in Fig. 7.8B, giving a diffusion coefficient of G-actin as 2.2 $\pm$ 1.1 $\mu m^2/s$. Previous work determining the diffusion constant of membrane bound proteins such as streptavidin and MexA using Fluorescence recovery after fringe Pattern Photobleaching (FRAPP) have shown diffusion constants of 1.6 $\mu m^2/s$ and 4 $\mu m^2/s$ for each protein respectively. The data showed that the single anchoring point of MexA led to the same diffusion constants as the lipids, while the streptavidin, which has two anchoring points to the

membrane, had a reduced diffusion constant (~half of the membrane component) [173]. Since G-actin binds electrostatically via its -8e net negative charge (depending on pH), it is possible that a single G-actin monomer binds to a number of DOTAP lipid head groups. A typical 20% DOTAP-DOPC bilayer, assuming a symmetrical bilayer, on average would have ~9 DOATP molecules below a G-actin monomer. Mica induced asymmetry on average would leave only 3 DOTAP heads, however others could then potentially be flipped as reported previously [174]. For the other G-actin orientation, these values would need to be 5.5 lipids for symmetric and 2 for asymmetric bilayers.

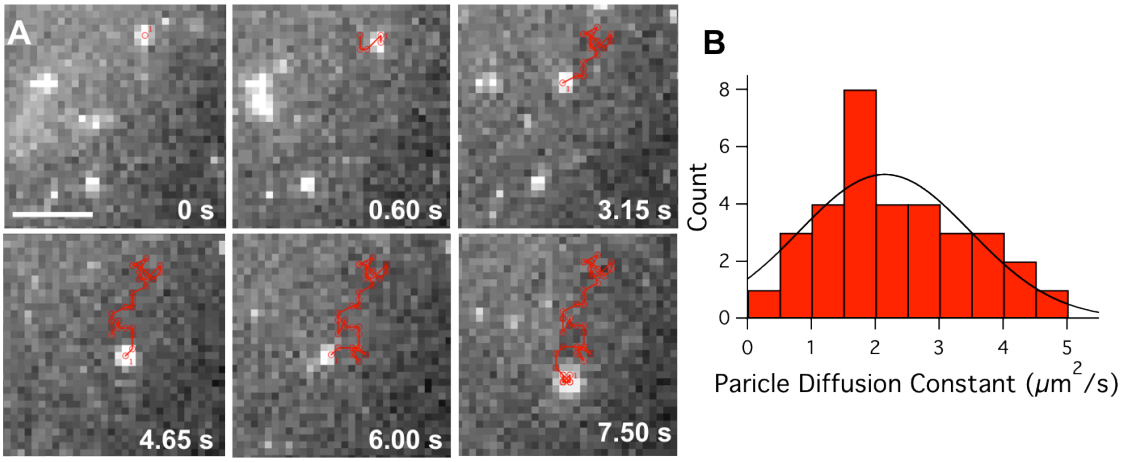

Figure 7.8 (A) Total internal reflection fluorescence (TIRF) images of rhodamine labelled G-actin (1 nM) at the surface of a DOPC bilayer with 20% DOTAP. The images have been taken from a series of 50, the red line shows the trajectory traced over time (scale bar = 4 μm). (B) Histogram and Gaussian fit of G-actin diffusion constants.

In addition to mobile actin, immobile fractions of G-actin were observed. The mechanism for why some actin is mobile whereas other actin is not may reflect the number of lipids binding per G-actin monomer. A dramatic reduction in the monomer diffusion coefficient would be expected when a monomer is bound to multiple lipids than say when it is bound to a single lipid.

7.2.2 AFM

The interaction of G-actin under non-polymerising conditions, with DOPC-DOTAP lipid bilayers was investigated using AFM. The concentration of the cationic lipid DOTAP was varied between 0 and 30% mole fraction. G-actin was introduced at 0.1 uM and incubated for 20 min.

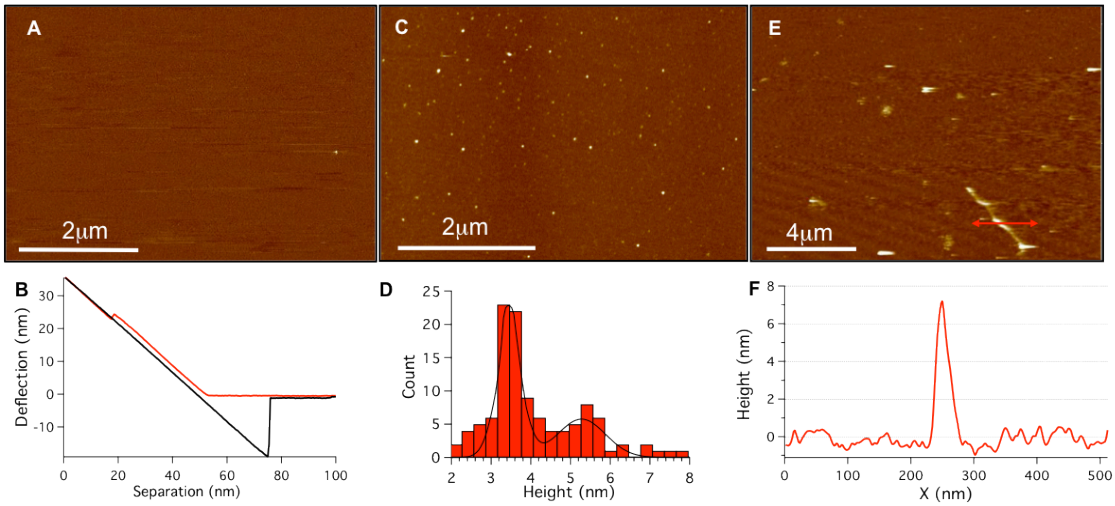

Figure 7.9: AFM data of G-actin binding to fluid bilayers at low DOTAP concentrations. (A) DOPC bilayer after G-actin incubation with (B) force spectroscopy measurement showing that the bilayer remains intact. (C) G-actin monomer binding to a 5% DOTAP – DOPC bilayer with (D) height distribution of monomers. (E) G-actin binding and single filament polymerisation at the surface of a 15% DOTAP – DOPC bilayer with (F) line profile across filament.

For pure DOPC bilayers no adsorption of G-actin was observed (Figure 7.9A). As the fraction of DOTAP was increased to between 1%-12.5% the adsorption of a small number of G-actin monomers was observed. Fig. 7.9 C shows a G-actin density of ~4 μm^{-2} on a 5% DOTAP surface; this value is much lower than the surface charge would allow (~10^4 μm^{-2} based on 7 charged lipids per G-actin). Since the TIRF data (Figure 7.8) showed both highly mobile monomers and an immobile fraction of actin, it therefore seems probable that when using AFM, only the immobile fraction is observed. Height analysis of the immobile bound G-actin gives peaks at 3.5 ± 0.3 nm and 5.3 ± 0.6 nm (Figure 7.9 C). These values are consistent with the dimensions of G-actin (3.5×5.5×5.5 nm) obtained from structural models [47]. The peak at the smallest dimension of 3.5 nm is dominant whilst

probability would give the 5.5 nm dimension twice as often. This suggests that the monomers preferentially lie flat to optimise interaction with the bilayer. However it should be noted that this might only be a property of immobile G-actin that have maximised binding to a number of charged lipids.

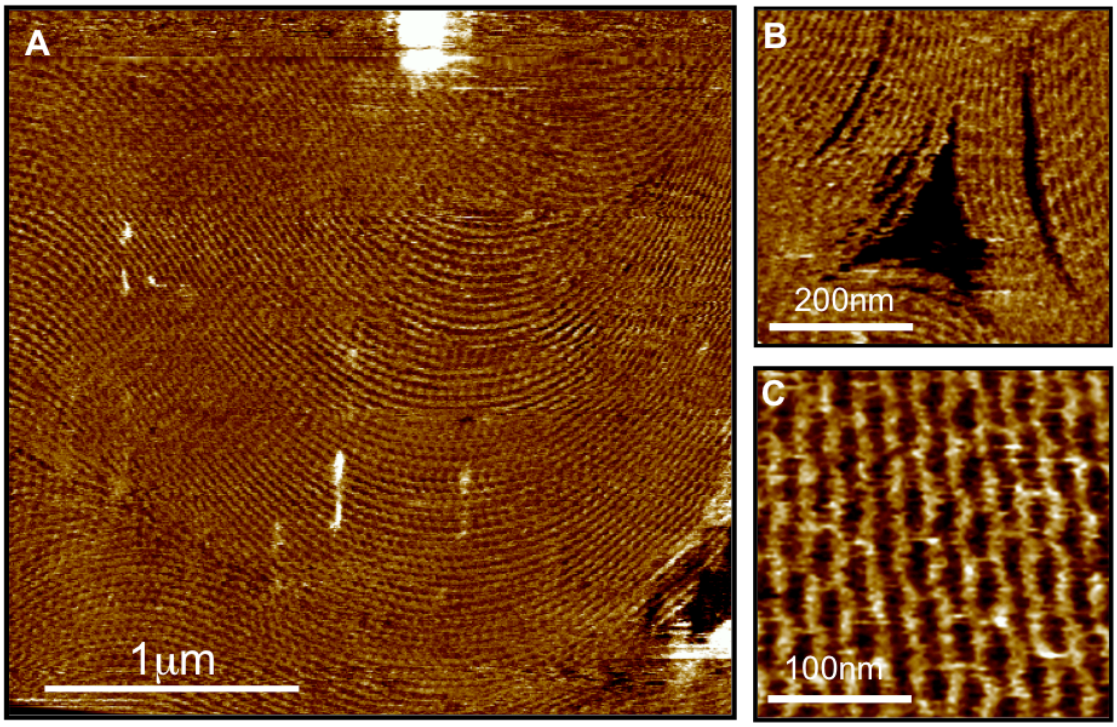

Figure 7.10: (A) Actin polymerization at a 20% DOTAP – DOPC bilayer under G-buffer conditions. (B) Image of liquid crystal defect and (C) high-resolution image of parallel filaments (z-scales = 6 nm).

At 15% DOTAP a low density of highly mobile or possibly loosely bound single filament features were observed (Figure 7.9 E), indicating a critical threshold had been passed for nucleation of filament growth. For DOTAP concentrations >18%, a near complete monolayer of ordered F-actin filaments was formed (Figure 7.10 A-C), whilst there was still no evidence of polymerisation in the bulk. This sharp transition from almost no coverage to a full monolayer suggests that there is a critical threshold for polymerisation or that the charge presented in the outer bilayer leaflet may change abruptly above a certain critical concentration. Previous work binding pre-polymerised filaments to charged membranes does not appear to have shown this same critical threshold effect [159,166,167,175]. The surface

coverage on the 20% DOTAP samples was estimated, using bearing analysis, to be between 97%-100%. However, the 'packing fraction', defined as the ratio of the filament diameter to average distance between neighbouring filaments ranges from 0.5 for parallel filaments to 0.22 for areas with high curvature such as in Figure 7.10 A. Packing fraction analysis was performed by manually tracing lengths of each individual filament and multiplying by the known width of F-actin to give an area covered by the filaments. This was then divided by the total area to give the packing fraction.

TIRF microscopy showed that actin monomers, when bound to a single charged lipid or multiple charged lipids, will have a larger residency time on the surface. This larger residency time, coupled with the reduced dimensions for diffusion (2D) in the plane of the membrane leads more readily to dimer formation as the precursor to filament formation [176]. The mobility of the DOTAP/actin complexes allows the filaments to align during growth to form 'finger print' textures similar to those observed in calamitic liquid crystals [177]. The almost complete surface coverage has some topological defects, characteristic of liquid crystals, with evidence of disclination lines and ±1/2 type defects (Figure 7.10 B).

In some regions, highly ordered bright lines were observed to run perpendicular to the filament direction, demonstrated in Figure 7.11, representing paracrystal formation. The bright bands appear due to the alignment of the actin repeat units in neighbouring filaments. Fig. 7.11B shows a high-resolution image of such a paracrystalline region. The filaments lie in the direction shown by the red line, which gives a characteristic profile (Figure 7.11D) with a 38 nm half-helical repeat, as expected for actin [178]. The blue line traces, perpendicular to the filaments provide a measure of the inter-filament spacing, estimated to be 19 ± 1.1 nm (Figure 7.11C). The formation of paracrystals is expected to occur after the polymerisation process, as filaments re-orient on the fluid membrane into configurations which are most favourable in terms of lateral electrostatic interactions of filaments. Previous studies of pre-polymerised filaments support this dependence on membrane fluidity, showing the formation of

actin paracrystals on fluid phase membranes, but not on gel phase ones [175].

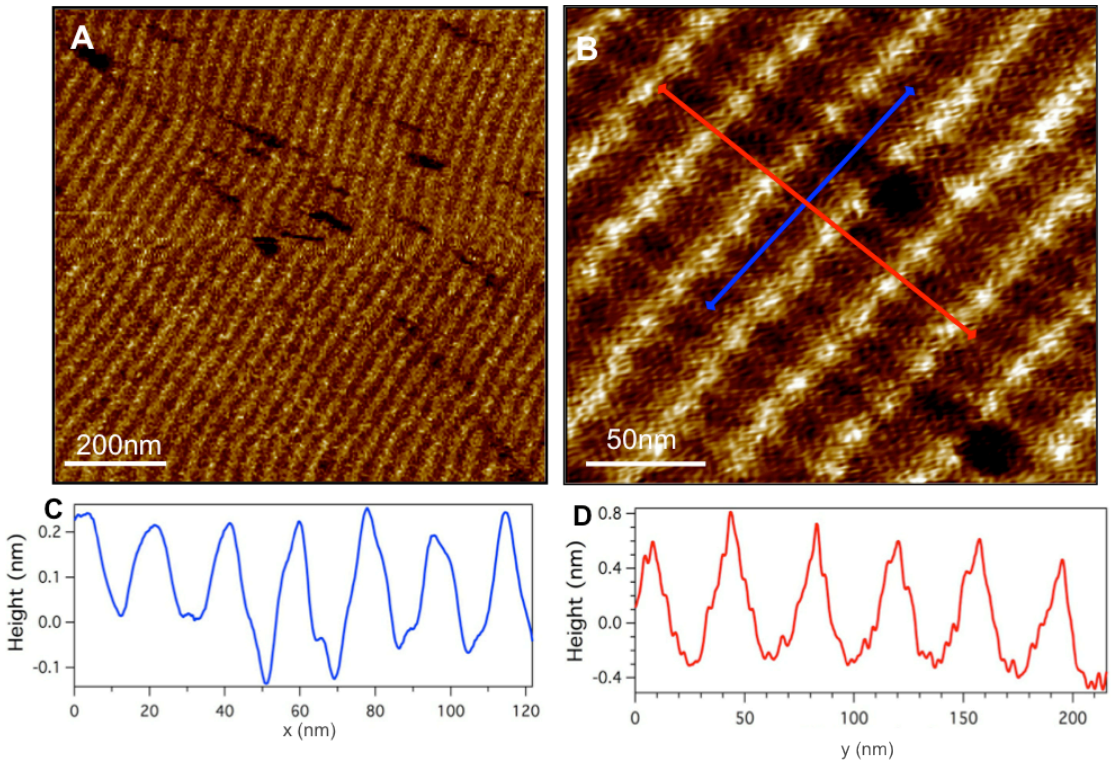

Figure 7.11: (A) AFM data showing surface topography of actin paracrystals polymerised on a cationic fluid lipid bilayer (DOPC with 20% DOTAP) in G-buffer conditions. (B) High resolution scan showing the individual filaments within the paracrystal. The visible periodicity is caused by the alignment of the helical repeats of parallel filaments. Line profiles (C) and (D) show inter-filament spacing and helical repeat in the actin paracrystal.

The packing fraction obtained in paracrystalline regions was found to be 0.5, significantly smaller than observed for 2D paracrystals prepared in polymerisation buffer, which typically gave an inter-filament spacing of 7-8 nm [159] and therefore a packing fraction closer to 1. The packing is however comparable to results found in TEM studies of actin polymerised by amine containing lipid surfaces [164]. The difference in packing between polymerisation buffer and lipid-induced polymerisation appears to arise due to the lower divalent cation concentration in the non-polymerising buffer (0.02mM $CaCl_2$) compared to the polymerising buffer (2mM $MgCl_2$). The higher concentration of divalent cations is great enough to allow binding of Mg to several low affinity sites on F-actin [48] thus reducing the overall

charge of filaments. This may then permit closer packing and allow adjacent filaments to bind to each other as previously shown in bulk solution [179].

7.2.3 QCM-D

Observation of polymerisation dynamics with AFM were problematic because the filaments appeared to be highly mobile and grew too fast. Therefore, QCM-D was used to follow the adsorption kinetics of G-actin on pure DOPC and DOPC lipid bilayers containing 20% DOTAP (Figure 7.12 A, B). As observed in the AFM experiments, pure DOPC bilayers showed no adsorption of G-actin, hence confirming that the interaction is purely electrostatic. The 20% DOTAP bilayer showed large changes in both frequency and dissipation until saturation was observed after ~ 30min. The change in frequency with time could be fit to an exponential with a time constant of 570 ± 10 s. Previous studies on the kinetics of G-actin adsorption to lipid monolayers containing charged surfactant found similar exponential behaviour using ellipsometry, but at slower rates with time constants of the order of 1800 s [164]. This difference can be partially explained by this previous study having used a lower actin concentration (0.06 mM, compared to 0.1mM used here) and having used different lipids. Since the dissipation was relatively high, the Sauerbrey relation did not apply here, so the dissipation and frequency curves were modelled as a two layered Kelvin-Voigt model (Section 2.4.2), with the bilayer as the first layer, assumed to be constant over time, and the actin as the second layer. Modelling gave an actin layer thickness of 3.3 ± 0.2 nm. Converting the volume of this single uniform layer to rods formed from uniform spheres with a 3.75nm radius gives a packing fraction of 0.56 ± 0.03 which is in reasonable agreement with the AFM observations of actin polymerisation on fluid-phase bilayers (Figures 7.10 and 7.11).

Varying the DOTAP concentration between 0 and 30% showed no adsorption on bilayers with 0, 5 and 10% DOTAP (Fig 7.12 C). At 20% and 30%, actin bound at different rates (increasing with charge) however the same total equilibrium coverage was achieved for each. By varying the actin concentration a critical concentration at which polymerisation is triggered was observed. Figure 7.12D shows the adsorption rate of actin on a 20% DOTAP-DOPC bilayer ranging from 4 nM up to 100 nM. The results show a linear relation, suggesting that the process is diffusion limited and polymerisation might not be deducible by this technique.

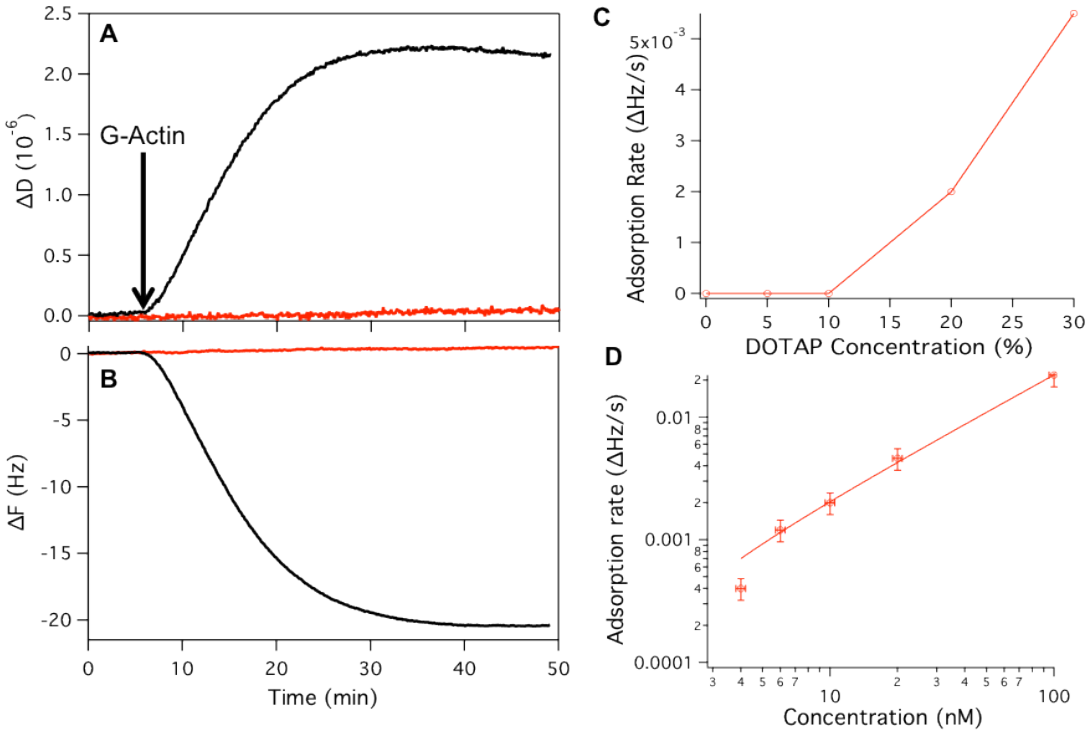

Figure 7.12: QCM-D showing (A) the dissipation change and (B) the frequency change of G-actin (100 nM) adsorption to a 20% DOTAP – DOPC lipid bilayer (black line) and a pure DOPC bilayer (red line). (C) Plot of initial gradient of frequency change due to G-actin adsorption for different bilayers containing various DOTAP concentrations. (D) Plot of initial gradient of frequency change for various G-actin concentrations on 20% DOTAP – DOPC bilayers.

7.3 Actin Adsorption and Polymerisation on Gel-Phase Lipid Bilayers

7.3.1 AFM

To investigate the importance of lipid mobility on the type of actin structures formed, actin polymerisation at DPPC - EDPPC lipid bilayers were studied. Figure 7.13A shows the filament structure found after the incubation, at room temperature, of a gel phase lipid bilayer (80% DPPC, 20% EDPPC) with G-actin. Notwithstanding the presumably reduced mobility within the gel phase, polymerisation was still nucleated by the charged lipids. However, the filament coverage (32 ± 2%) was significantly lower than for the fluid phase system (>97%), and individual F-actin filaments displayed a reduced ability to re-orient to achieve high-density packing. Repeating the experiment with the actin incubation at 45^{o}C i.e. just above the gel to fluid phase transition, for 15 min, before cooling for 30 min for imaging, gave a significant increase in surface coverage to 78 ± 8% (Figure 7.13B) and showed a return of the actin textures more closely resembling the densely packed actin shown in Figure 7.9. The different structures observed for actin incubation above and below the phase transition demonstrates that the diffusivity of the nucleation site (in this case EDPPC/actin complex) plays a significant role in controlling the morphology of the actin structures formed. It should be noted that for these systems, actin ‘agglomeration’ (shown by the large white objects) was observed (Figure 7.13A), which presumably arose as a result of 3D nucleation. Images of the gel phase membrane before (Figure 7.4) and after the addition of actin show that these large agglomerates only appear after actin addition. The comparison of the helical repeat between the fluid phase polymerised actin (38nm) and gel phase (39 $\pm$ 1 nm) shows no detectable difference (within error) (Figure 7.13 C, D).

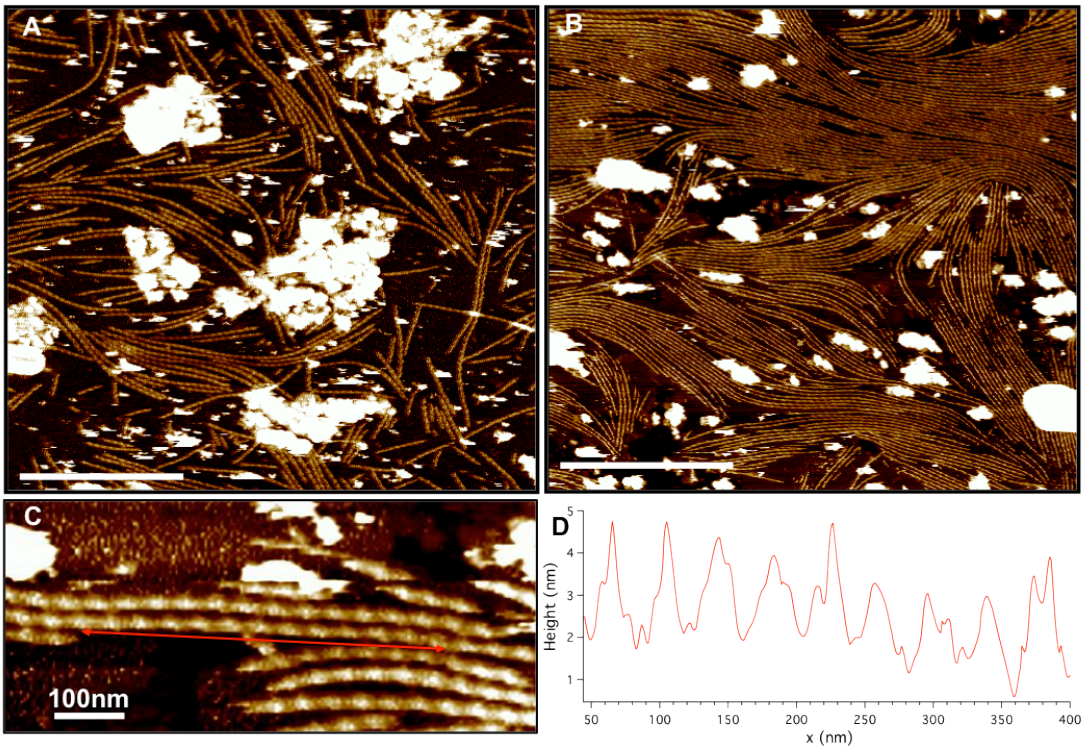

Figure 7.13: Actin polymerisation on gel phase 20% EDPPC - DPPC bilayers. (A) AFM image after actin incubation at room temperature and (B) after 15min incubation at 45°C, followed by a 30 min cooling period (scale bars = 1 µm). (C) High resolution image with (D) line profile used to obtain a half helical repeat distance of 39 ± 1 nm.

To investigate the charge required to nucleate polymerisation on gel phase bilayers, the EDPPC concentration was varied in DPPC bilayers from 0-20%. Bilayers with 0% and 1% EDPPC showed no interaction with G-actin, while for 5%, 15% and 20% EDPPC actin polymerised to the same degree (Figure 7.14 A-E). Hence the critical concentration of charged lipid is significantly lower than found for the fluid bilayer system (18%). This difference is critical to the upper leaflet (UL) compared to the lower leaflet (LL) (adjacent to the mica surface) for the fluid and gel phase systems. Previous studies have shown that supported fluid lipid bilayers containing charged lipids display significant leaflet asymmetry on mica. It was found that for bilayers containing between 10 and 20 % charged lipids, the fraction of charged lipids in the upper leaflet compared to the lower leaflet (UL:LL) varies from the symmetric 1:1 to the asymmetric 1:3 [180]. Since rates of flip-flop in the gel phase are in orders of magnitude slower than that for fluid

systems, it is reasonable to assume that the fluid system is more likely to be susceptible to lipid asymmetry than the gel system. Also, given that the lateral lipid density in the gel phase is higher than that in the fluid phase by a factor of 1.4 to 1.5, the gel has a higher charge density of roughly 1.4-1.5 fold (based on values for DOPC and DPPC area per headgroup [172,181]). If both of these factors are taken into account (i.e. ~ 50 % increase in charge density plus 1:3 asymmetry in the fluid but not gel), then the critical composition for filament formation would change from 18% in the fluid system down to a predicted 4% for the gel phase system. This is in good agreement with observations of the gel system found within this thesis.

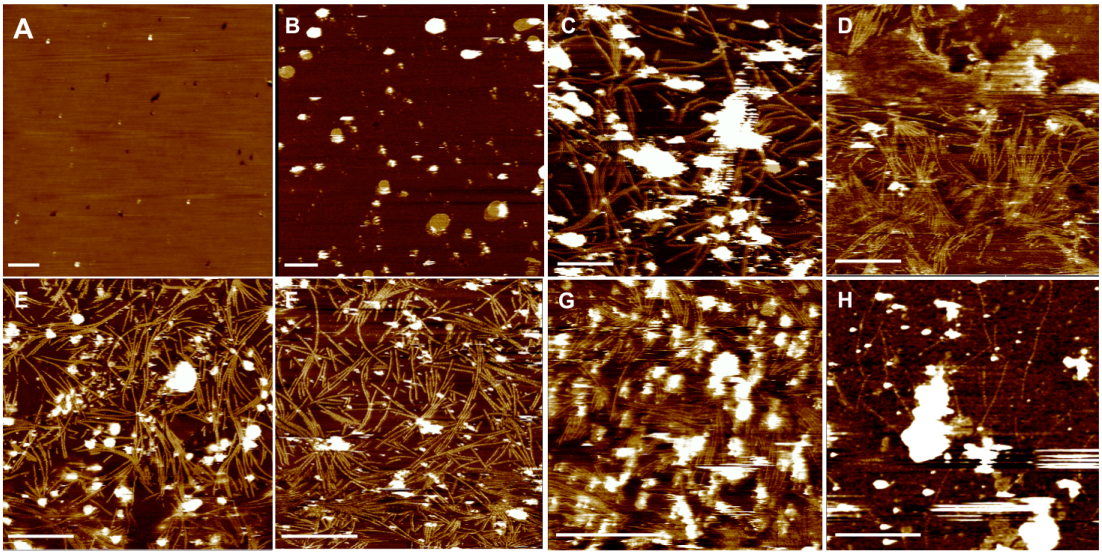

Figure 7.14: AFM images of actin polymerisation on DPPC lipid bilayers with varying concentrations of EDPPC: (A) 0%, (B) 1%, (C) 5%, (D) 15%, (E) 20%, (F) 25%, (G) 50% and (H) 70% EDPPC (scale bar = 1 μm).

Increasing the EDPPC concentration above 20% shows actin still polymerises despite the phase separation with actin having a slight preference for the gel phase. At the highest charge of 70% EDPPC where the underlying bilayer is almost all fluid phase, the actin density is greatly reduced.

7.3.2 QCM-D

The QCM-D response to G-actin incubation after forming a 20% EDPPC bilayer (Figure 7.15) shows similar kinetic behaviour to that observed with the fluid bilayer system. Exponential fitting to frequency change gives a time constant of 350 s with an end frequency change of -10.2 Hz, corresponding to a layer of filaments with a packing density of 0.29. This is slightly greater than expected from AFM imaging (0.1 packing fraction). However, the AFM analysis here excludes the regions of 3D growth and actin agglomerations observed, whereas QCM-D measures all adsorption. Once the actin filaments have formed on the surface, they are not easily dislodged by washing with buffers including those of high ionic strength (eg 1M $CaCl_2$). This suggests a tight binding of the actin filaments to the surface, thus making this system not only biologically interesting but also robust for possible applications.

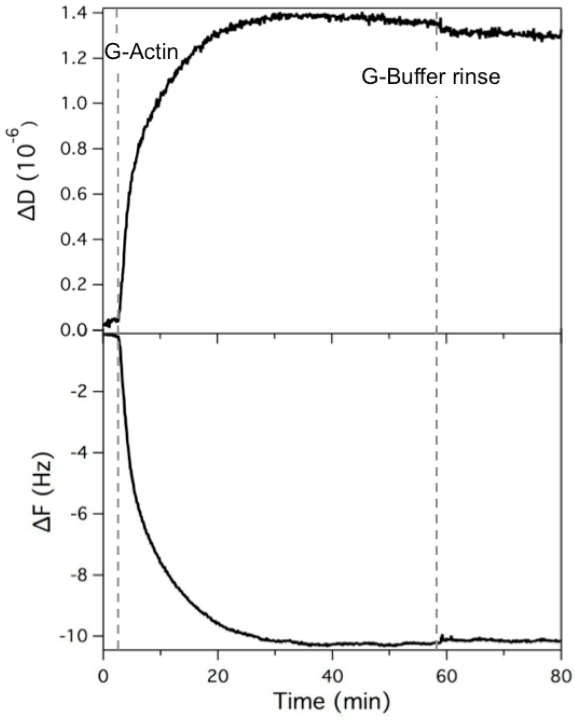

Fig 7.15 QCM-D showing changes in frequency and dissipation observed upon adding 100 nM G-actin to a 4:1 DPPC-EDPPC lipid bilayer at room temperature with a continual G-buffer rinsing step from 58 min onwards.

7.3.3 Time Lapse AFM

Since the filament mobility on gel phase bilayers was relatively slow, the growth of individual filaments could be visualised at standard AFM scan rates (2Hz). This allowed various phenomena to be observed such as filament annealing, whereby two filaments associate to form one (Figure 7.16A). Filament annealing has previously been well studied *in vitro* and is believed under certain conditions to play a role in filament elongation *in vivo* [182,183]. Since annealing is a probabilistic event of a barbed end meeting a pointed end, 2D confinement will increase the probability of annealing. However the contribution to total filament growth by annealing observed here remains relatively small: 3 occurrences from ~300 filaments, most likely due to filament rotation and diffusion limited by the underlying gel phase membrane. Annealing may play a more significant role on fluid membrane systems where filament diffusion and rotation is expected to be greater.

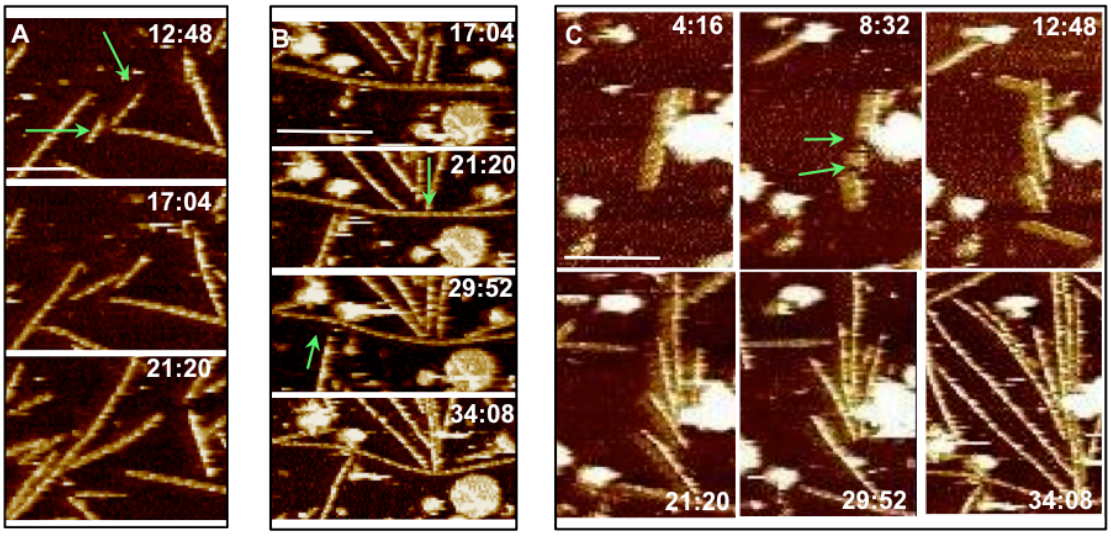

Figure 7.16: Time lapse AFM image sequences showing: (A) the process of filament annealing whereby two filaments associate to form a single filament, (B) a filament being forced to bow by the growth of other surrounding filaments and (C) a single filament being broken into smaller fragments by the AFM tip, followed by growth from the new free ends (time stamp - min:s, scale bars = 200nm).

Force generation, where polymerising filaments can be seen to bend other obstructing filaments as they grow, was also observed (Figure7.16 B). When actin filaments elongate in close proximity to a biological load, they are believed to generate forces through a ratcheting mechanism. This is where thermal fluctuations allow for periodic insertion of new protein subunits in the polymer, despite the presence of a counteracting load force [184]. Although it does not play a huge role in the actin morphologies observed on the gel phase bilayers, the increased filament diffusion on fluid membranes would allow greater bending fluctuations and hence more filament bending due to the polymerisation of colliding filaments.

Figure 7.16 C shows the action of filament breakage by the AFM tip, followed by growth from each of the new ends, all in the same direction. This preferential growth from the plus end demonstrates the polarisation of the actin filament whereby all subunits point toward the same filament end, and is consistent with the myosin head based decoration of actin filaments studied by EM [185].

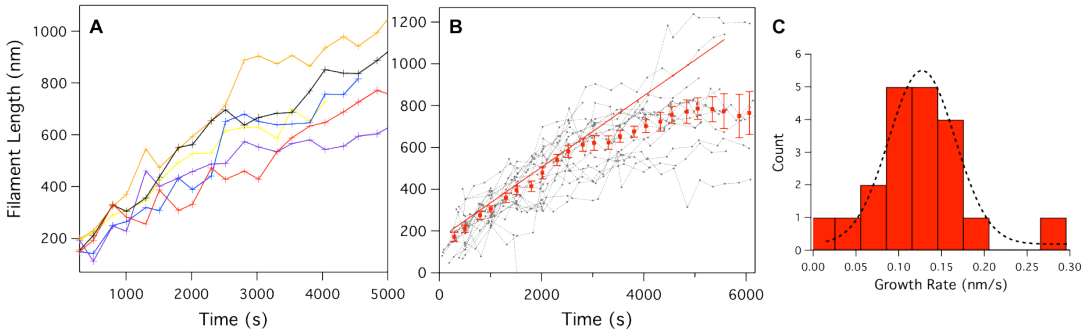

Figure 7.17: Tracking filament length with time taken from a sequence of AFM images. (A) Traces from 6 typical individual filaments, (B) traces from 19 filaments (grey lines) and an average of all filaments with linear fit (red points and line). (C) Histogram of filament growth rates based on linear fits to changes in length over initial linear growth regime.

Tracking the filament length between AFM scans allowed determination of the filament growth rate. Individual filaments were seen to grow at a relatively consistent linear rate of 30-50 nm per 4 min scan (Fig 7.17A). Instances where scanning forces drifted too high can also be seen by

shrinking of filaments which then continue to grow as the tip force is reduced. Figure 7.17B shows filament length vs. time for many different single filaments (grey) with the averaged length plotted in red. In most cases the growth remains linear until reaching another obstructing filament at which point, depending on the available space, the obstructing filament is moved or bent as can be seen in Figure 7.16B. This linear growth is characteristic of filaments in bulk solution [169].

Fitting the filament length vs. time plots for a number of filaments gave a distribution of filament growth rates centred around 7.8 ± 0.7 nm/min (Figure 7.17C). This rate is significantly slower than that observed under polymerising conditions using AFM, in cell extracts on mica (91nm/min) [170], on streptavidin substrates (110 nm/min) [160], or in bulk solution with TIRF microscopy (600 nm/min) [169].

7.4 Effect of pH on Lipid membrane Induced Actin Polymerisation

The effect of pH on the polymerisation of actin in bulk solution has been well characterised, with faster polymerisation rates and a decrease in the critical concentration of G-actin required as the pH is reduced [186]. The driving force for this is a reduction in the net charge per actin monomer as the pH approaches the isoelectric point: pI = 5.5. Excluding the acidic vesicles, the range of pH in cytoplasm is generally bounded by a range between ~ 6.5 - 8.0 [186]. Thus the pH of the buffer was varied between 6.5 and 7.8 and the actin structures produced at room temperature on 20% EDPPC – DPPC bilayers were imaged with AFM. QCM-D and Time lapse AFM were also used to determine the effects of pH on adsorption and polymerisation rates.

7.4.1 AFM

20% EDPPC – DPPC bilayers were formed on mica, then rinsed with a 5 mM Tris buffer adjusted to the appropriate pH. G-actin was then added in the pH adjusted G-buffer and allowed to polymerise for 30 min. The results (Fig 7.18) show a clear difference in surface coverage, agreeing with what one might expect: that a lower pH increases polymerisation. The packing fraction achieved at pH 6.5 with a gel lipid bilayer of 0.28 is similar to that obtained with fluid lipid bilayers of 0.35. At higher buffer pH values, a decrease in actin coverage is observed with shorter filament lengths. These data show pH is a useful control of surface coverage, a characteristic which could be useful in future applications. The actin coverage increased in a sigmoidal manner from ~ 20% to 90% as the pH was reduced from 7.8 to 6.5. It should be noted however that after the 30 min period, some of these systems may still be undergoing polymerisation.

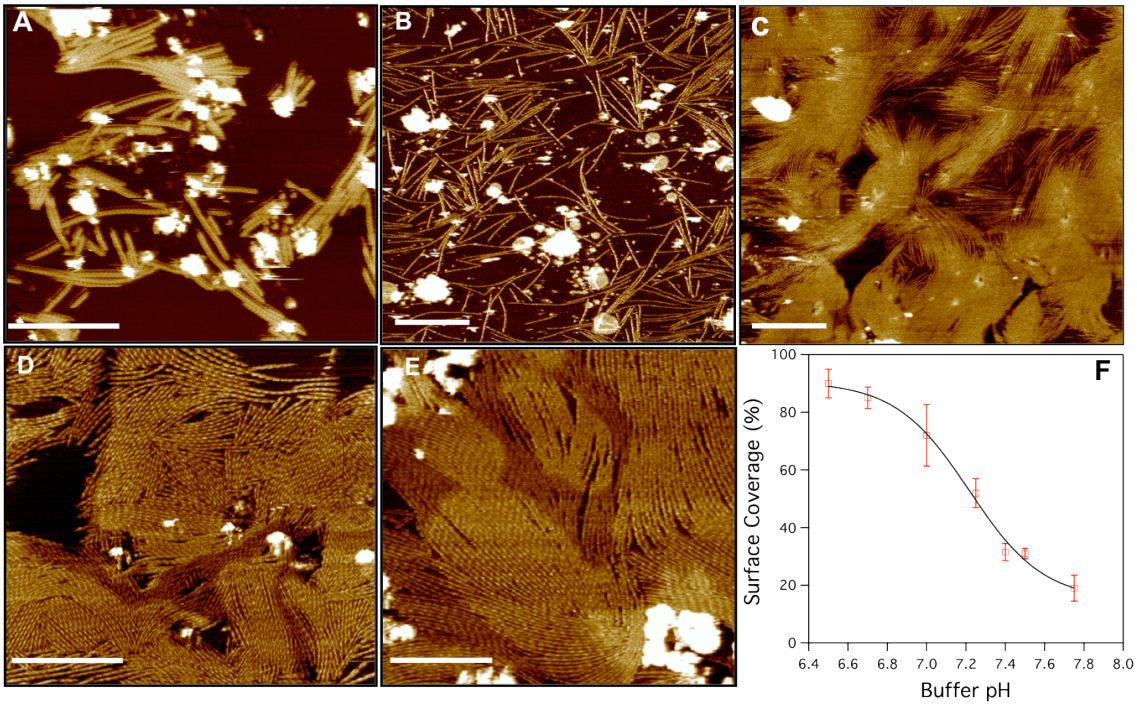

Figure 7.18: Effects of varying buffer pH on surface induced actin polymerisation on gel phase cationic lipid bilayers (4:1 DPPC/EDPPC). Panels A, B, C, D and E represent pH 7.75, 7.5, 7.0, 6.7 and 6.5 respectively. (F) Surface coverage, as calculated considering the area of each individual filament as a function of buffer pH.

7.4.2 Time Lapse AFM

Time lapse AFM imaging at various buffer pH values (Figure 7.19 A-C) shows the polymerisation dynamics of many filaments over hours. The polymerisation characteristics alter with pH; at lower pH values polymerisation often nucleates along the sides of existing filaments (Figure 7.19 A, B) whilst at a higher pH value of 7.5, nucleation is random (Figure 7.19C). Although the data at lower pH was limited due to fast growth rates and interactions between filaments altering filament positions, it was still possible to track length changes of several filaments with time. As with polymerisation at pH 7.5, the filaments at pH 6.5 appeared to grow linearly and with no visible loss/depolymerisation from the negative end. The average growth rate of 28 ± 4 nm/min however is much greater than that found at pH 7.5 (7.8 ± 0.7 nm/min). The growth of multiple membrane-actin layers is observed under pH 6.5 buffer conditions, which suggests that the polymerisation of actin is drawing out lipid from the underlying bilayer.

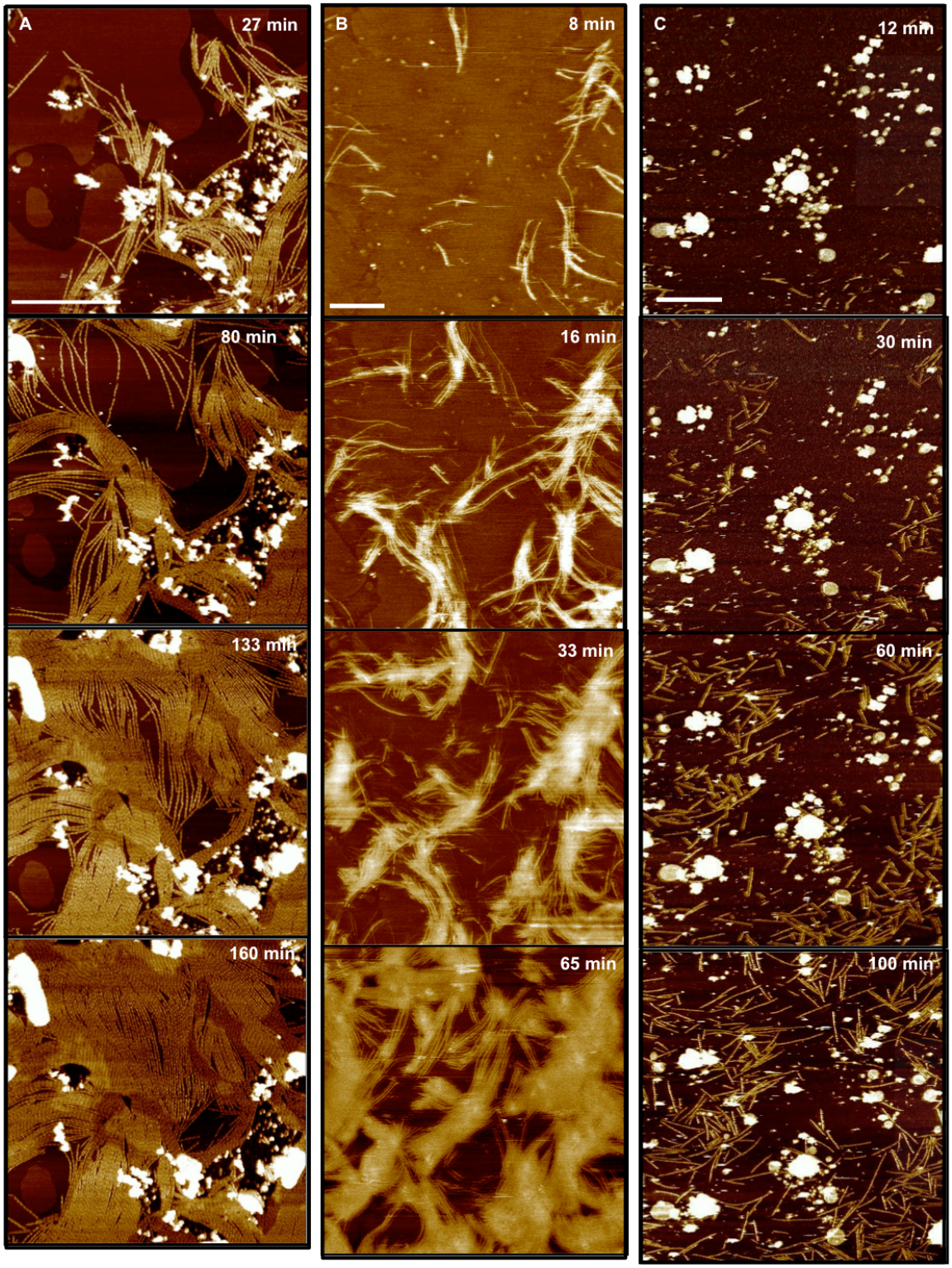

Figure 7.19: AFM images taken from image sequences of actin polymerisation on 1:4 EDPPC-DPPC bilayers in G-buffer at pH 6.5 (A), 7.0 (B) and 7.5 (C). (scale bars = 1µm).

The time dependent actin coverage (Figure 7.20A) obtained from time lapse AFM shows that decreasing the pH from 7.5 to 6.5 leads to an increase in both the rate and amount of coverage achieved. Counts of filament number to give filament density (Figure 7.20B) with time show that the increase in coverage observed at lower pH is not only due to an increased polymerisation rate but also due to the total number of filament nucleation events. This has been previously observed in bulk with decreasing pH [187].

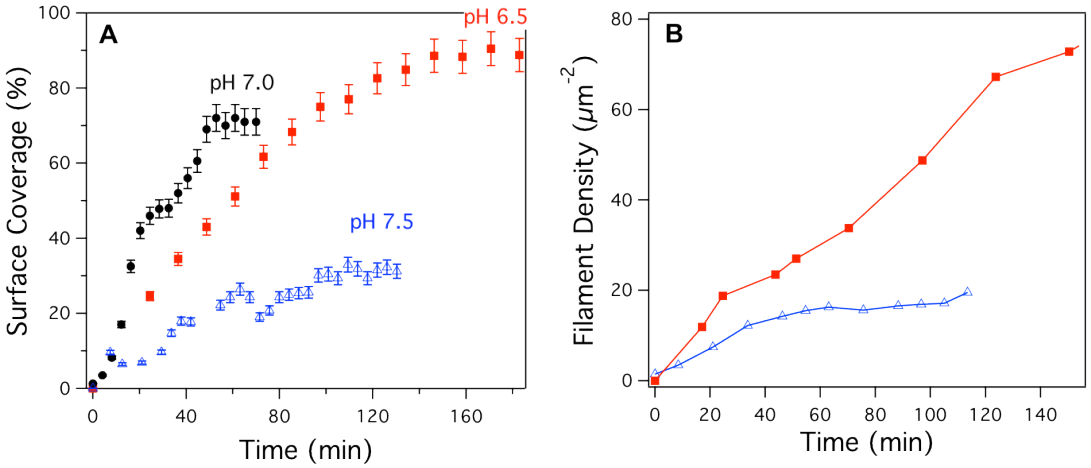

Figure 7.20: Total actin surface coverage from time lapse AFM data as a function of time at pH 6.5 (filled squares), pH 7.0 (filled circles) and pH 7.5 (triangles) with exponential curves fitted.

7.4.3 QCM-D

Figure 7.21A shows the frequency shift obtained in QCM-D experiments for DPPC/EDPPC bilayers with pH varying between 6.5 and 7.8. The results suggest an approximately linear adsorption followed by saturation, with rates and saturation points depending on pH. As observed with the AFM, decreasing the pH led to an increase in the actin coverage as well as the rate of adsorption (Figure 7.21B). This is most likely due to a reduction in the electrostatic interactions both between actin monomers and between G-actin and charged lipids. As a result fewer charged lipids are required per G-actin monomer and the filaments polymerise more readily. The saturation time was at least 2-fold quicker when determined by QCM-D, compared to the AFM imaging. Investigations of varying AFM scan intervals between 4 and

13 minutes have shown that this is not due to tip interactions and that the difference therefore most likely arises as a result of the different flow conditions used between the AFM (static) and QCMD (40 ml/min) suggesting that reaction is strongly affected by diffusion.

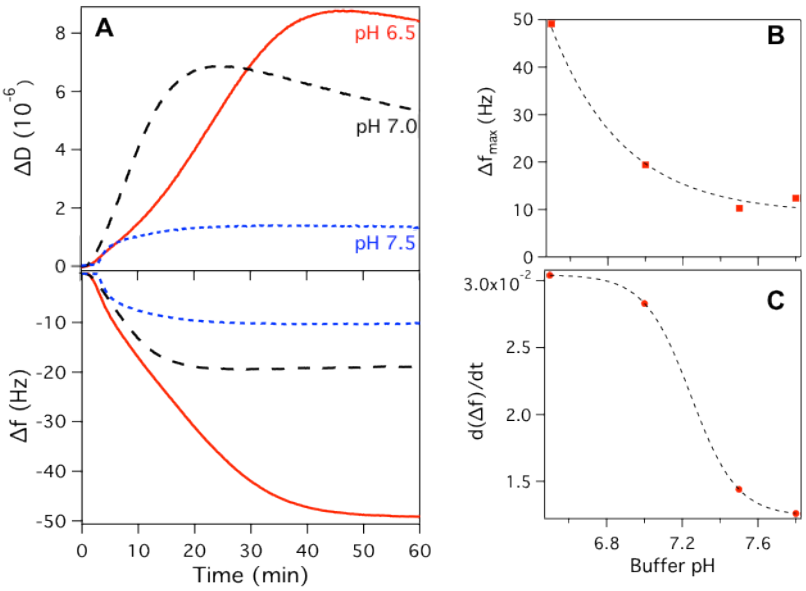

Figure 7.21: (A) QCM-D data showing actin adsorption on gel phase 4:1 DPPC-EDPPC bilayers for buffers at pH 7.8, 7.0 and 6.5 (blue, black and red). Maximum change in frequency (B) and adsorption rate gradient (C) as a function of buffer pH.

The higher final coverage values obtained for the lower pH values is most likely due to the combination of an increased filament mobility and an increased rate of nucleation (as observed with AFM), as fewer lipids are required to bind a single filament/monomer. The dissipation provides an indication of how tightly bound the adsorbed material is, or it's coupling to the aqueous phase. In all cases the dissipation reached a maximum in sync with the changes in frequency, before then decreasing while frequency remained constant, suggesting filaments may be ordering to form more tightly packed structures (or that bound G-actin may be polymerising via 2D diffusion). The high dissipation values reached for pH 6.5 and 7.0 may also be due to the formation of actin membrane multilayers as observed by AFM. It should be noted that when the changes in dissipation are relatively high the changes in frequency do not simply reflect mass adsorption in a linear

manner. The pH dependence thus provides useful insight for understanding the mechanism of actin polymerisation at surfaces.

7.5 Model of Lipid Charge Induced Actin Polymerisation

Actin monomers carry a high negative charge; typically ~ -7e (depending on buffer conditions) and thus electrostatics play a significant role in polymerisation. In bulk polymerisation this charge is reduced and screened by the binding of Mg^{2+} or Ca^{2+} to a single high affinity site and binding of Ca^{2+}, Mg^{2+} and K^{+} to several lower affinity sites (K_d values of 0.15 mM for Ca^{2+} and Mg^{2+} and 10 mM for K^{+}) [48]. Therefore 2 μM $CaCl_2$ provides a high enough concentration for Ca^{2+} binding to the single high affinity site of G-actin without binding to the low affinity sites. Since there is no Mg^{2+} or K^{+} in G-buffer the G-actin monomers still carry a high enough negative charge to prevent polymerisation in bulk. For polymerisation to proceed under these conditions the charged lipid within the bilayer must neutralise the excess charge on the actin. Previous studies of actin filaments grown at charged membranes have shown only roughly half of the ATP bound to the F-actin subunits is hydrolysed to ADP as opposed to the usual ~ 80% hydrolysis when polymerised in bulk with salts [165]. This incomplete ATP hydrolysis on charged membranes suggests some direct interaction between the lipids and actin monomers that may prevent hydrolysis. On a lipid bilayer roughly half of the monomers of the filament are in contact with the membrane potentially providing a route prevent hydrolysis through direct binding of the lipid headgroup to specific sites on the actin (leaving only the half subunits exposed to hydrolysis). Observations of no depolymerisation or detachment after rinsing (Figure 7.15) agree with this argument of direct G-actin binding to lipids and may explain the preferential flat orientation of G-actin monomer binding observed (Figure 7.9).

The charge of a G-actin monomer can be estimated using the Tanford-Kirkwood method [188-191], with the MacroDox charge set which takes protein data bank information to calculate electrostatics under defined conditions (Northrup et al., 1997).

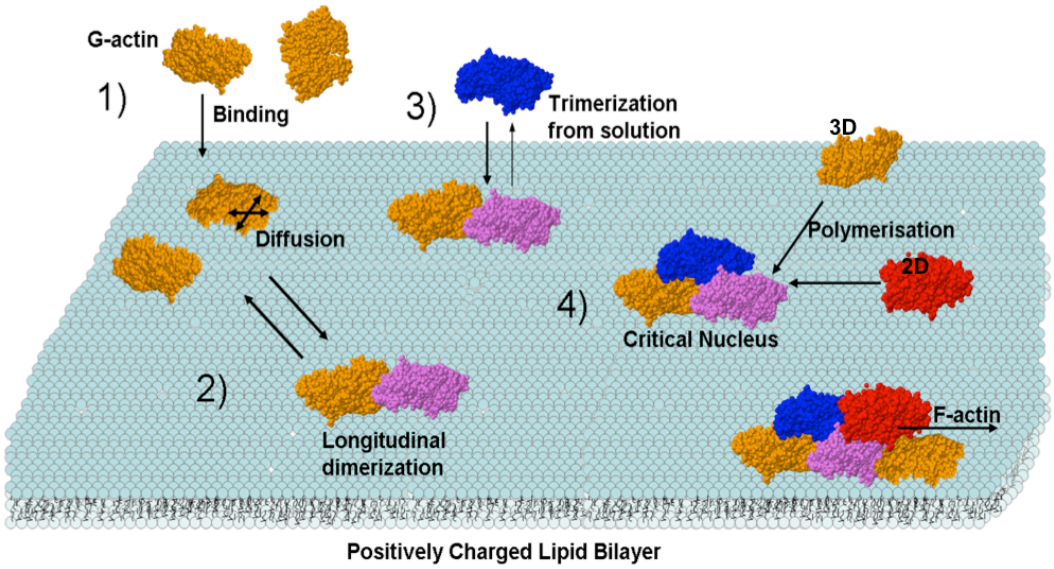

Figure 7.22: Schematic description of the surface induced self-assembly of G-actin into filaments on a positively charged lipid membrane. 1) Monomeric actin binds to the membrane in a flat orientation where it diffuses at a rate dependant on the lipid mobility. 2) In-plane dimers form via diffusional collision, 3) G-actin from solution binds to form a trimer. 4) Trimer forms a critical nucleus from which polymerisation can occur via addition from solution and/or adsorbed diffusion.

For the pH range of 6.5 to 7.8, the method predicts total net charges ranging from -4.1 to -7.7 respectively. An actin monomer lying flat as AFM suggests (55 × 55Å) would cover ~ 40 or 65 lipids on a fluid or gel state lipid bilayer respectively. Therefore an area of fluid bilayer with 20% charge at pH 7.5, beneath a single G actin monomer, would on average have 8 positive charges and be able to neutralise the -7e charge of the G-actin monomer. A combination of an overall reduction in charge of the monomers via surrounding lipids and increased actin concentration though 2D confinement with access to monomers from solution may then allow polymerisation to occur. Simulations of bulk polymerisation have previously shown the most critical step in the nucleation process is the formation of a trimer which has a

large dissociation rate constant [176]. The simulations predict that a nucleation pathway of a longitudinal dimer followed by trimer formation is > 30 fold more favourable than from cross-filament dimer to trimer. Applying this scheme of polymerisation to charged lipid bilayers in which monomers are in, or close to, the orientation required for longitudinal dimer formation enhances the potential to polymerise in non-polymerising bulk conditions. This potential is further enhanced by the effect that adsorption at the membrane surface will lead to locally higher concentrations than in the bulk. The 3rd monomer required to form the trimer could come directly from the solution (Figure 7.22). In the trimer state the association and dissociation rate constants are approximately equal to that of a full filament and thus form the critical nucleus. Polymerisation from then on could continue via monomer 2D diffusion on the membrane or 3D diffusion from the bulk.

7.4.1 Polymerisation Model

To gain insight into the significance of the contributions to polymerisation from bulk 3D diffusion and 2D diffusion of lipid bound monomers each process can be modelled based on the probability that a monomer arrives at the right angular orientation (P_{rot}) in a given characteristic time ($\tau = R^2/2dD_d$). This characteristic time between arrival of monomers separated by a mean distance R (estimated via concentration c where $R \approx c^{-1/3}$ in 3D and $c^{-1/2}$ in 2D) is set by the diffusion constant D_d (in d dimensions). The rate of polymerisation can then be estimated as:

$$k_{on} = \frac{P_{rot}}{\tau} e^{-\frac{\Delta G}{k_b T}} \qquad (7.1)$$

Where ΔG describes the energy barrier once monomers have adsorbed. The charged membrane can be expected to remove the Coulomb barrier that would be present for free monomers in solution. Table 7.1 shows the estimated arrival times, rotational probabilities and energy barriers for polymerisation in 2 and 3 dimensions.

	3D	*2D*
τ	$\frac{1}{6D_{3d}c_{3d}^{2/3}}$	$\frac{1}{4D_{2d}c_{2d}}$
P_{rot}	$\frac{1}{4\pi}$	$\frac{1}{2\pi}e^{-\frac{\Delta G_{rot}}{k_bT}}$
ΔG	ΔG_{3d}	$\Delta G_{3d} - \frac{q^2 e^{\left(-\frac{r^*}{\lambda_D}\right)}}{4\pi\epsilon r^*}$

Table 7.1. Arrival times (t), rotational probabilities (P_{rot}) and energy barriers (ΔG) of monomer association for polymerisation in 2 and 3 dimensions where D is the diffusion constant, q is the monomer change, $\lambda D \simeq 3.9$ nm is the membrane screening length and r^* is the monomer-monomer capture distance at the top of the Coulomb barrier (expected to be of order Angstroms).

Assuming that the adsorbed monomers are at, or close to the correct polar angle for interaction, only a small rotational barrier ΔG_{rot} needs to be overcome to tilt the monomer, into or out of the membrane. This leads to the following capture rates:

$$k_{2d} = \frac{4D_{2d}C_{2d}}{2\pi}\exp\left(-\frac{\Delta G_{3d}+\Delta G_{rot}}{k_bT} + \frac{q^2 e^{-\frac{r^*}{\lambda_D}}}{4\pi\epsilon r^* k_bT}\right) \quad (7.2)$$

$$k_{3d} = \frac{6D_{3d}c^{2/3}}{4\pi}\, e^{-\frac{\Delta G_{3d}}{k_bT}} \quad (7.3)$$

Where the diffusion rate in 3D is 50 $\mu m^2/s$ [164] and ΔG_{rot} is approximated as 0.5 kcal/mol based previous theoretical estimations [192]. ΔG_{3d} is estimated as 3.5 kcal/mol in reasonable agreement with previous models [176]. For the 2D monomer diffusion rates a value of 2.2 $\mu m^2/s$ for

fluid phase bilayers was used, as determined by TIRF microscopy (Figure 7.8), and for the gel phase the diffusion rate of the lipids (0.004 $\mu m^2/s$) was used, as determined via FRAP experiments (Figure 7.6).

7.4.2 Aggregation Kinetics

In the absence of aggregation monomers will adsorb to the surface. A model, for equilibrium adsorption kinetics can be given as:

$$\frac{dc_a}{dt} = \frac{1}{\tau_0}(c_a - \overline{c_1}) \tag{7.4}$$

Where c_a is the number of monomers per area that have absorbed from the bulk; $\overline{c_1}$ is the equilibrium coverage in the absence of aggregation, and τ_0 is the time equilibration. This can be obtained from a model of adsorption and desorption, whose rate constants determine τ_0. This gives the following kinetics of adsorption:

$$c_a(t) = \overline{c_1}\left(1 - e^{-\left(\frac{t}{\tau_0}\right)}\right) \tag{7.5}$$

However another choice is to assume irreversible adsorption to the membrane through a constant diffusive flux J_{ext}. This flux can be estimated from simple diffusive augments in terms of number per unit area per unit time:

$$J_{ext} = 6D_{3d}c_{3d}^{\frac{4}{3}} \tag{7.6}$$

Since not every monomer that contacts the membrane will bind, the monomer binding rate is given by $A.J_{ext}$, where A is the probability of binding. Polymerisation of these bound monomers can then be modelled by the contributions from bulk using this same diffusive flux argument J_{ext} but moderated by the coulomb barrier for adsorption, or:

$$J_{ext,p} = k_{3d} c_{3d}^{\frac{2}{3}} \quad (7.7)$$

Aggregation can occur from monomers adsorbed onto the surface, or by lengthening filaments (including monomers) already on the surface. Assuming irreversible monomer adsorption from the bulk the time dependent concentrations of monomers and aggregations of j follows as:

$$\frac{dc_1}{dt} = J_{ext}(1-\phi)c_1 - k_{2D}(c_1)\sum_{j=1}^{N-1} c_j - J_{ext,p}(1-\phi)c_1 \quad (7.8)$$

$$\frac{dc_j}{dt} = k_{2D}(c_1)c_1 c_{j-1} - J_{ext,p}(1-\phi)c_{j-1} \quad (j = 2 \ldots N) \quad (7.9)$$

Where c_j represents the concentration of aggregates of j. In this model, monomers can only adsorb where there is no actin giving a rise to the $(1 - \phi)$ term, where the area fraction of free sites is given by:

$$\phi(t) = a\sum_{i=1}^{N} n c_n(t) \quad (7.10)$$

Where, a, is the area per monomer. Solving Eq. 7.8 and 7.9 numerically with time, for j = 2…200 for the gel and fluid systems (Figure 7.23A, B) allows modelling of the results expected from QCM-D. The model predicts that for gel phase bilayers, 75% of the actin is polymerised by additional actin arriving directly from the bulk phase with 25% contribution from surface diffusion. By changing the diffusion coefficient to represent the fluid phase, the model suggests that polymerisation is initially dominated by monomers arriving by 2D diffusion at the membrane but over time as more filaments are established the 3D component plays an increasing role, eventually leading to almost equal contributions from 2D and 3D (Figure 7.23B). These results show that controlling the membrane viscosity offers a simple but important route for controlling the morphology of the actin structures produced.

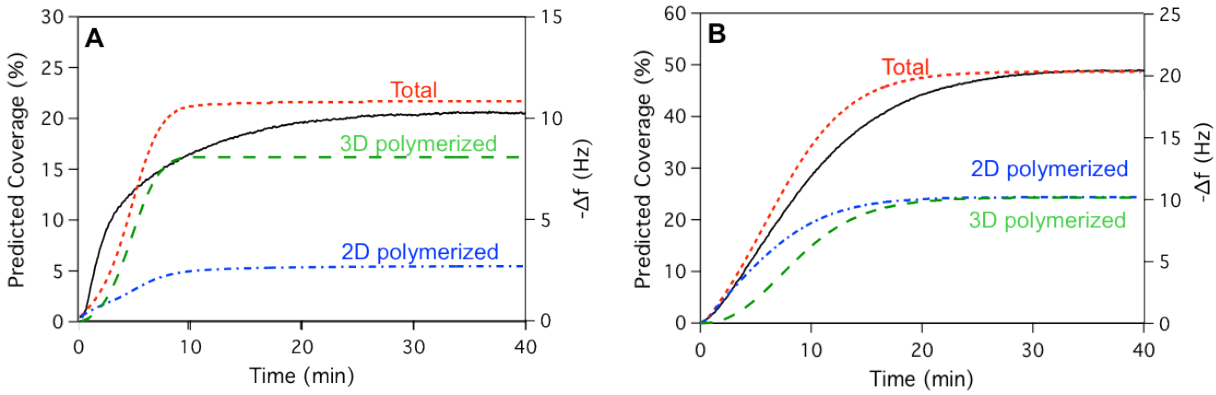

Figure 7.23: Model for growth via surface diffusion (2D (dash-dot)), or via addition from bulk phase (3D (long dash)) and total actin bound (dash) on gel phase (A) and fluid phase (B) bilayers as a function of time. The experimentally obtained data, from QCM-D, are shown as solid lines in each case and represent actin binding to 4:1 DPPC-EDPPC and 4:1 DOPC-DOTAP bilayers.

7.4.3 Model Assumptions

In the polymerisation and aggregation model a number of assumptions were made to simplify calculations, these were as follows:

1. All motion of aggregates on the surface was ignored and hence filament-filament aggregation (annealing) was ignored
2. Polymerisation occurs only from one end
3. No alignment of filaments (no nematic phases)
4. No correlations of filaments
5. Irreversible aggregation

7.5 Actin Polymerisation on Phase Separated Cationic Lipid Bilayers

By combining the fluid and gel systems to create a four-component lipid bilayer, the effects of actin on lipid organisation and lipid organisation on actin polymerisation can be investigated using phase separated systems. A total of 7 different lipid compositions were studied, at pH 7.5, all with 20% total charged lipid but with varying ratios of DPPC to DOPC-DOTAP-EDPPC and DPPC-EDPPC to DOTAP-DOPC. Depending on the lipid mixture used these bilayers showed phase separation with gel domain areas ranging from 18% to 80% (Figure 7.24).

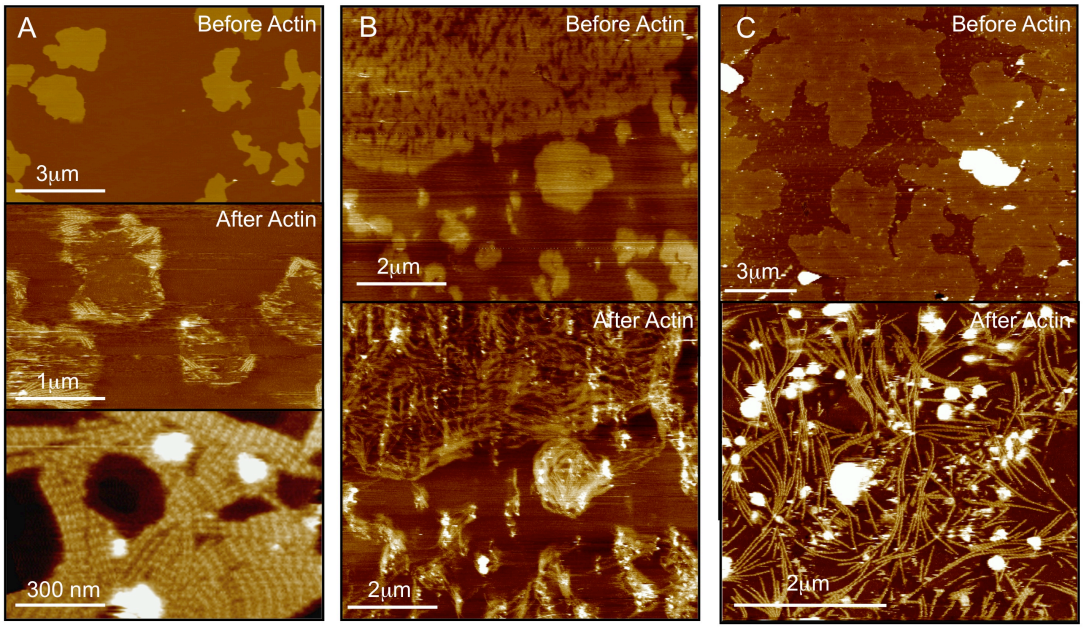

Figure 7.24: AFM images of phase separated charged bilayer systems before and after G-actin incubation for 30 min. Sample composition are: (A) 9.4% EDPPC, 37.4% DPPC, 10.6% DOTAP and 42.6% DOPC, (B) 12.1% EPC, 47.8% DPPC, 7.8% DOTAP and 32.2% DOPC, (C) 9.3% EPC, 60% DPPC, 6% DOTAP and 24.7% DOPC.

Comparison of phase area of these 4 component lipid systems with that of the binary EDPPC-DPPC lipid mixtures (Figure 7.4) shows strong evidence that only the DPPC component is responsible for the gel phase separation since the DPPC fraction to gel phase area ratios are fitting that of the EDPPC-DPPC mixtures (Figure 7.5). After the addition of actin, growth of filaments is observed predominantly on the gel phase (Figure 7.24) for the

majority of samples with more fluid phase area than gel phase. Above 50% gel phase area the system appears to revert to the gel phase polymerisation kinetics with low density single filaments growing across either domain (Figure 7.24C).

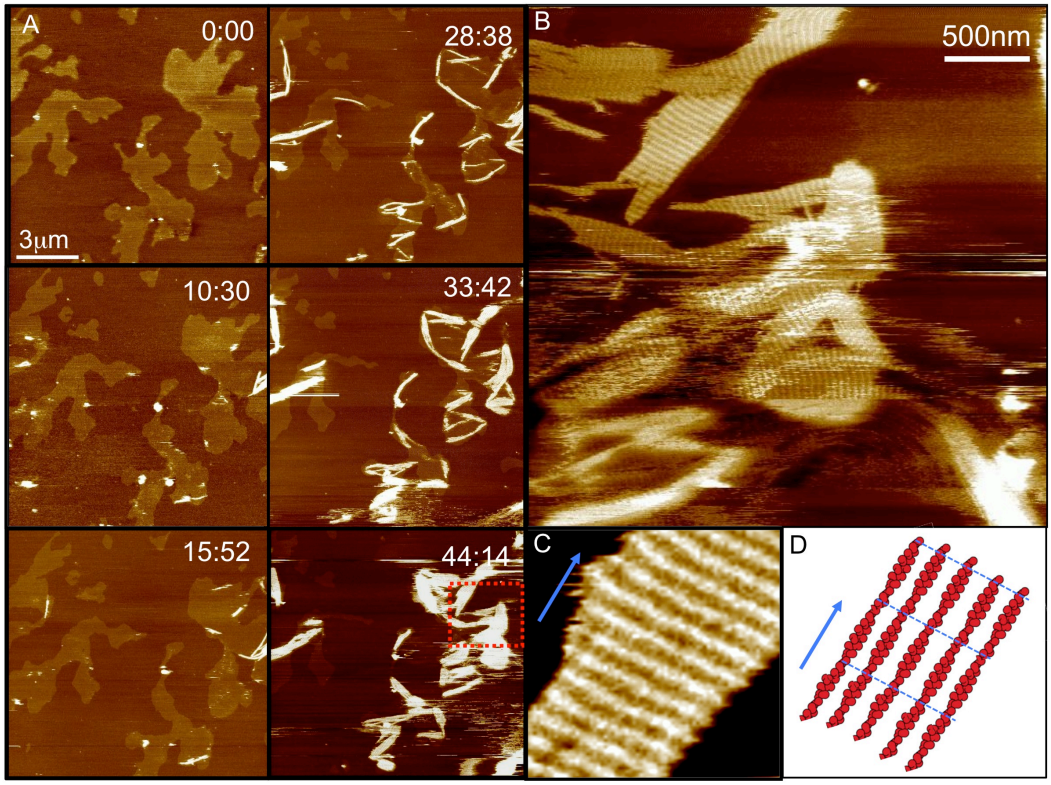

Figure 7.25: (A) Time lapse AFM (time stamp, 00:00 min:sec) sequence showing the selective growth of actin paracrystals on the gel phase of a 12.1% EPC, 47.8% DPPC, 7.8% DOTAP, 32.2% DOPC lipid bilayer (scale bar = 3 μm). (B) Higher magnification image of the area highlighted in frame 44:14. (C) Higher magnification image of B showing paracrystal morphology and filament direction (D).

Using a lipid composition of 12.1% EPC, 47.8% DPPC, 7.8% DOTAP, 32.2% DOPC bilayers consisting of gel domains ~3μm in diameter and with ~30% area coverage were formed. After the addition of G-actin time lapse AFM reveals the relatively slow growth of only actin paracrystals on the denser gel phase (Figure 7.25A). During this growth, the size of the lipid domains and the overall gel coverage decreases. The filament formation appears to initiate from the domain edges, and then avoid the fluid phase as they grow. Higher magnification images show the filaments are arranged into

actin paracrystals generally following the longest axis of the domain (Figures 7.25 B,C).

Using the lever rule and methods described in section 5.1.2 the expected compositions of each phase and therefore the charge density can be deduced. The calculated fluid phase composition of the sample shown in Figure 7.25 is: 17% EDPPC, 30% DPPC, 10% DOTAP and 44% DOPC, while the gel phase is made up of 2.3% EDPPC, 90% DPPC, 1.5% DOTAP and 6.2% DOPC. The combined charged lipid in the fluid phase is 27% and should therefore polymerise the actin however the DOTAP concentration is below the required 18% to cause polymerisation on a fluid system suggesting EDPPC is not effective at polymerising actin in the fluid phase. Experiments showing no polymerisation on DOPC-EDPPC bilayers agree with this hypothesis. The gel phase has a total charge of ~4% which is enough to polymerise low density single filaments at pH 7.5. This explains the observations seen with large gel phase fractions. However the charge density in the gel phase is not great enough to support the amount negative charge from dense actin paracrystals seen in Figure 7.25. Analysis of the domains as the actin grows shows a decrease in domain size with time demonstrating the actin is having an effect on the lateral organisation of lipids. From these observations two possible mechanisms could be suggested: a) that as the actin grows on the gel domain it recruits charged lipid from the other phase hence increasing lipid mixing. Under this hypothesis diffusion of the lipids is reduced as they enter the domain therefore creating higher charge concentration at domain edge hence nucleating polymerisation. Or b) an alternative would be that actin-lipid complexes rapidly diffusing in the fluid phase slow as they enter the domain at the boundary creating an increased actin concentration, then as filaments polymerise the lipid-actin complex becomes trapped in the domain hence increasing lipid mixing. For samples with over 50% gel phase area fraction, most of the lipid is in the gel phase and the effects of the smaller surrounding reservoir are greatly reduced.

As a four lipid component system there are a huge number of possible combinations which could be studied. The phenomenon of

electrostatic domain remodeling has been previously observed with lipid-cation and lipid-protein interactions [193-195]. These previous studies showed organisation of lipids into domains from mixed phases due to clustering of the negative charge, our system is different in that there is already phase separation and the protein binds to the domain of lower charge thus having the opposite effect, mixing charges to create a more homogeneous bilayer.

7.6 Conclusions

The results in this chapter show that lateral diffusion of the G-actin/cationic lipid complexes determine the degree and rate of actin polymerisation with higher diffusion coefficients increasing both rate and total amount of actin polymerised. QCM-D and AFM data show that G-actin has no interaction with neutral DOPC bilayers. The lipid charge required to induce polymerisation depends on the membrane phase due to differences in lipid density and ability to change leaflet asymmetries. Fluid bilayers are known to have lipid leaflet distributions influenced by the charge presented by the support surface thus leading to a reduced charge at the exposed monolayer /ambient interface. The denser gel phase bilayers, which have much slower rates of lipid flip-flop, are expected to be more symmetric and thus require less total charge lipid in the membrane to promote polymerisation. Investigating single filament growth dynamics through time lapse AFM has revealed linear filament polymerisation rates. Further, pH provides an additional handle on controlling the rates of nucleation and polymerisation as well as the total amount of actin polymerised. In addition to providing insight into polymerisation processes this work provides a simple 2 step method to creating a stable 2D actin network membrane substrate. The benefits of this system come from the ability to control coverage and not requiring bulk polymerisation, phalloidin or additional linker proteins. This could therefore be useful for various applications requiring site localised self-assembly or directed growth.

Chapter 8

Self Assembled Actin Coated Lipid Microbubbles

In the following chapter, the results from chapter 7 are utilised to self-assemble actin filaments to the outside of lipid microbubbles using cationic lipids to polymerise the actin only at the microbubble surface. This biomimetic coating creates a thin mesh that provides a route for tuning the mechanical properties of microbubbles to obtain desired ultrasound responses. In addition the actin shell maintains a simple method for payload and targeting ligand attachment. The coating of microbubbles with pre-polymerised filaments was also investigated to show this route is much less efficient. The actin polymerisation and binding at the bubble surface was investigated with fluorescents microscopy. Using force spectroscopy measurements with tipless cantilevers to compress and deform the microbubbles with and without the actin coating showed the actin layer significantly increases microbubble stiffness and elasticity. Resistance to gas permeation was studied through dissolution experiments showing the additional actin layer reduces gas diffusion across the shell and thus increases bubble lifetime.

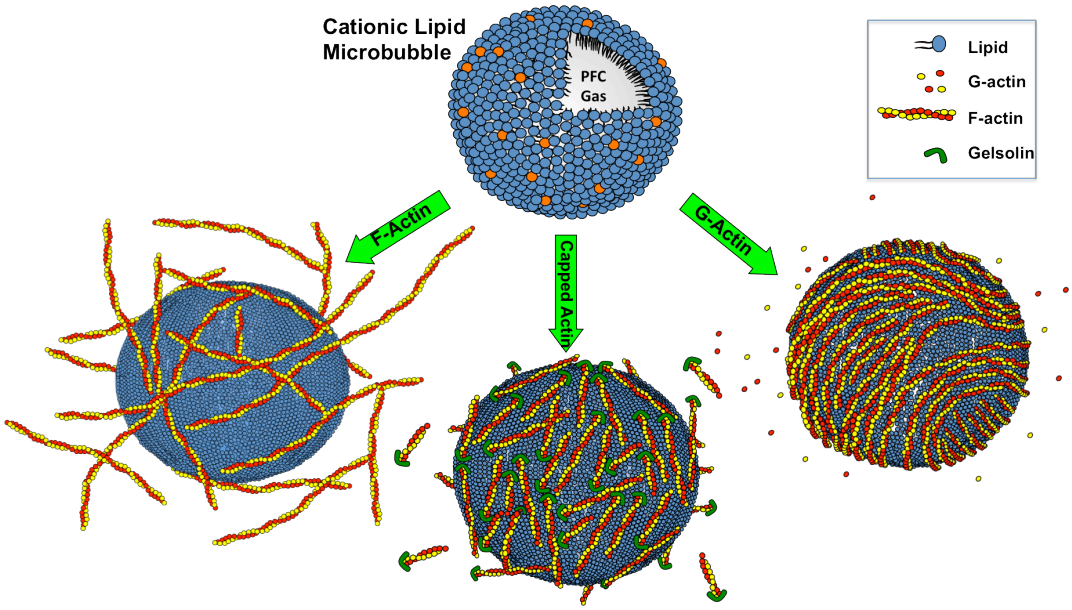

Figure 8.1: Schematic showing a cationic microbubble consisting of a fluorocarbon (C_3F_8) gas core with a lipid monolayer shell. Arrows point to types structures formed after adding pre-polymerised F-actin, controlled length F-actin filaments and G-actin in non-polymerising conditions.

8.1 Formation of Stable Cationic Lipid Microbubbles

The formation of actin coated microbubbles requires a 2 step process, the first of which is the creation of a population of stable lipid microbubbles. The driving force for the dissolution of bubbles is the Laplace pressure, the pressure difference between the inside and the outside of a curved surface. The pressure difference is caused by the surface tension of the interface between liquid and gas. For a spherical object of radius, R, such as a bubble, the pressure difference, ΔP, can be described by the Young-Laplace equation:

$$\Delta P = \frac{2\gamma}{R} \tag{8.1}$$

Where γ is the surface tension. For a simple gas bubble a radius of 1 mm has minor extra pressure. However when the radius is ~2 µm, the bubble has twice atmosphere pressure inside the bubble compared to outside and therefore the bubble quickly dissolves within seconds. The addition of a lipid shell contributes two stabilising components: a reduction in surface tension (thus reducing the pressure difference) and an increase in the resistance to gas leaving the core. Stabilisation of microbubbles can be further enhanced through the use of perfluorocarbon gas which is less soluble in solution than air.

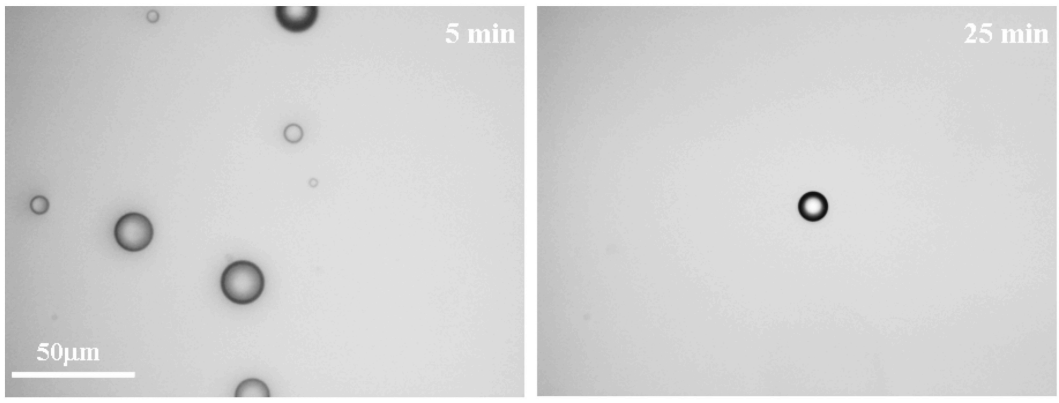

Figure 8.2: 1:4 DOTAP-DOPC microbubbles generated via the shaking method observed in 50 µm deep volumes (Left) 5 min and (Right) 25 min after production.

Figure 8.2 shows the result of the shaking method of forming lipid microbubbles, briefly this involved sonicating a lipid solution, then saturating lipid solution and its vial headspace with fluorocarbon (C_3F_8) gas, followed by fast mechanical agitation for 10 seconds. The lipid composition used in Figure 8.2 was DOPC with 20% DOTAP with the objective of recreating the actin structures found on DOPC-DOTAP lipid bilayers (section 7.2). The results however showed a very low concentration of lipid microbubbles with many of the bubbles dissolving before they could be imaged, at 5 minutes only large more stable bubbles were observed and after 25 minutes almost all bubbles had dissolved.

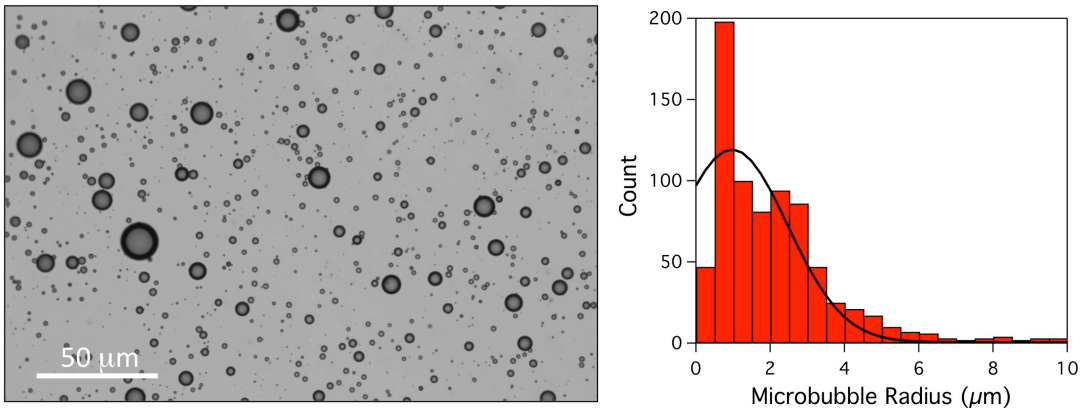

Figure 8.3: (Left) Image of 1:4 EDPPC-DPPC microbubbles generated via the shaking method observed in a 50 μm deep volume. (Right) Histogram of EDPPC-DPPC microbubble radius, gaussian fit has a peak at 1.0 μm with a standard deviation of 0.7 μm.

The lipid packing has been shown to play particular importance in bubble lifetimes [196], when the lipids are in a fluid state the resistance to gas permeation is greatly reduced and, as shown for the DOPC-DOTAP mixture, the bubbles dissolve quicker than is practical for experimentation or potential use as a contrast agent. DPPC has fluid-gel transition temperature of 41 ^{o}C and is in the more densely packed gel phase both at experimental room temperature and at body temperature. The formation of DPPC-EDPPC microbubbles via the shacking method shows the use of gel phase lipids increases bubble count (Figure 8.3). The concentration of bubbles at 5 min after formation was found to be 4 x 10^8 per ml, with an average radius of 1 μm and a standard deviation of 0.7 μm (Figure 8.3 (right)).

To test the stability of EDPPC-DPPC microbubbles, the C_3F_8 saturated solution was slowly rinsed with 5mM Tris buffer (with no gas treatment) being careful not to disrupt the bubbles which had been allowed to rise to the top glass surface. The population of bubbles with radii below 3 μm was then tracked over time until all bubbles had dissolved below 500 nm. Figure 8.4 shows the normalised bubble count with time, taking 400 min for almost all bubbles to dissolve. The data fits an exponential decay curve implying a stochastic process with a half life of 61 minutes. These bubbles provide a relatively stable system with lifetimes reasonable for further experiments and for which actin constructs may be built to further enhance stability and mechanical properties.

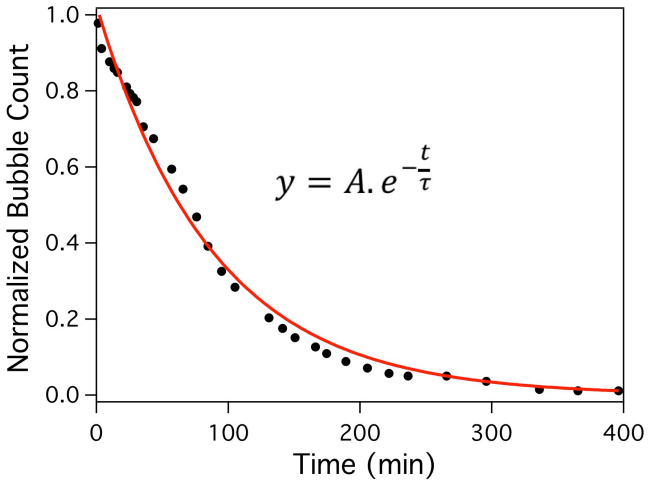

Figure 8.4: Normalised bubble count with time showing the lifetime of a population of EDPPC-DPPC (1:4) microbubbles with starting radii below 3 μm. The exponential fit to the data gives a decay constant of 88 min corresponding to a half life of 61 min.

8.2 Pre-Polymerised Actin Mircrobubbles

The first route taken to coating microbubbles with actin was by incubating positively charged microbubbles and using the electrostatic interaction to bind negatively charged pre-polymerised actin.

8.2.1 Uncapped Actin Mircrobubbles

Using mica as a substrate for AFM allows imaging of actin on a flat surface and is used in this thesis as a filament length characterisation technique. Actin was pre-polymerised in solution using polymerisation buffer and stabilised with phalloidin, a toxin which prevents depolymerisation, to keep the filaments from undergoing continual polymerisation and depolymerisation whilst imaging.

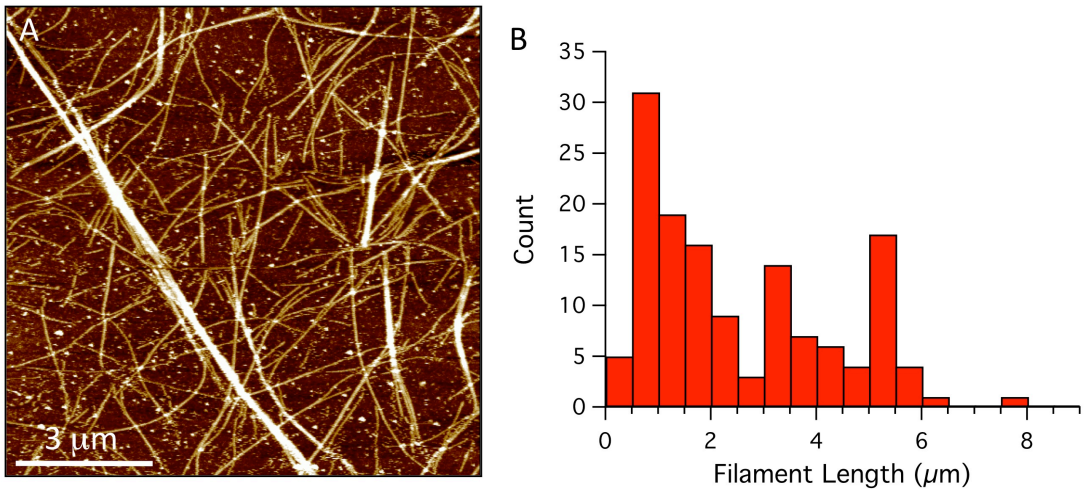

Figure 8.5: (A) AFM image of F-actin electrostatically bound to a nickel modifed mica surface (z-scale = 20 nm). (B) Histagram showing filament contour length distribution for single filemants.

Since under normal conditions both mica and actin are negatively charged, the surface was incubated with 2 mM nickel chloride to form an excess positive charge. Figure 8.5 (A) shows an AFM image of actin filaments bound to the surface with random orientations and filaments overlapping each other. Measuring contour lengths of these filaments gives a wide distribution of single filament lengths up to 9 µm with an average of 1.8 µm (σ = 1.7µm) (Figure 8.5 B). Also, by measuring end-to-end distance

in relation to contour length and fitting a worm-like chain model, an estimated persistence length can be calculated [197]. A value of L_p = 19 μm was obtained with this method, agreeing with previous data (L_p = 18 ± 1μm) of phalloidin stabilised F-actin [198]. As can be seen by the brighter, thicker regions (Figure 8.5), filaments have the capacity to bundle together in these conditions, the cause of this was found to be due to excess divalent ions in solution from the polymerisation buffer. Figure 8.6 shows the effect of increasing the $MgCl_2$ concentration in the imaging buffer. Small amounts of filament bundling can be seen at 10 mM $MgCl_2$, while at 50 mM almost all of the bound actin is associated with a bundle. This bundling is consistent with light scattering observations which have shown F-actin solutions undergo a sharp transition at 30 mM $MgCl_2$ [179]. This bundling effect would be disadvantageous to the coating of microbubbles since it increases the persistence length of filaments well beyond the typical microbubble radius however it may have application in other nanotechnology systems which require stronger/longer constructs.

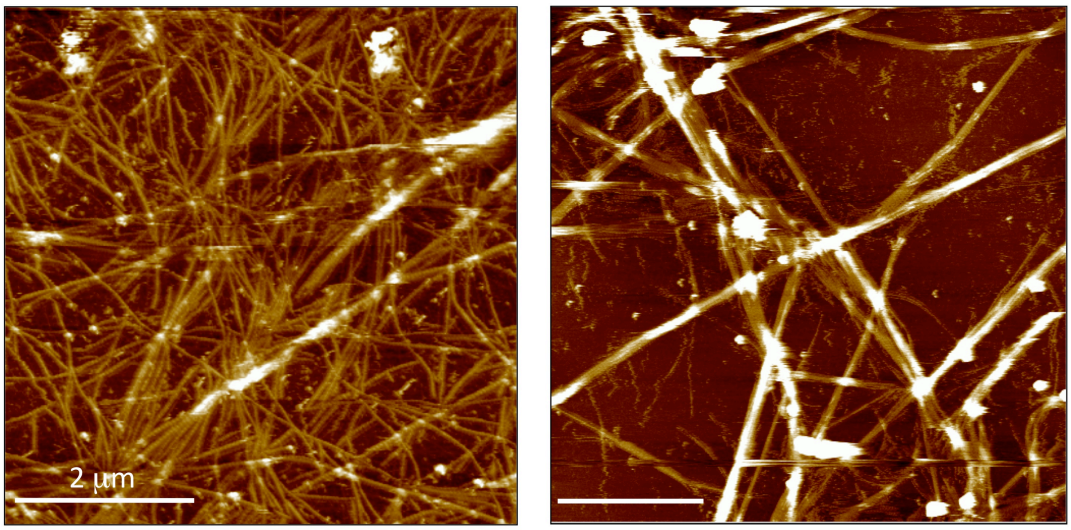

Figure 8.6: AFM images of F-actin electrostatically bound to a nickel/magnesium modified mica surface with (A) 10 mM $MgCl_2$ and (B) 50 mM $MgCl_2$ in the imaging solution.

Images obtained at smaller scan sizes allowed for more detailed analysis of the filaments (Figure 8.7 A). Cross sectional analysis was used to investigate the helical pitch (Figure 8.7 B) of the F-actin filaments giving a mean of 38 ± 1 nm (n=24) for the half pitch in agreement with results found previously via x-ray scattering [199].

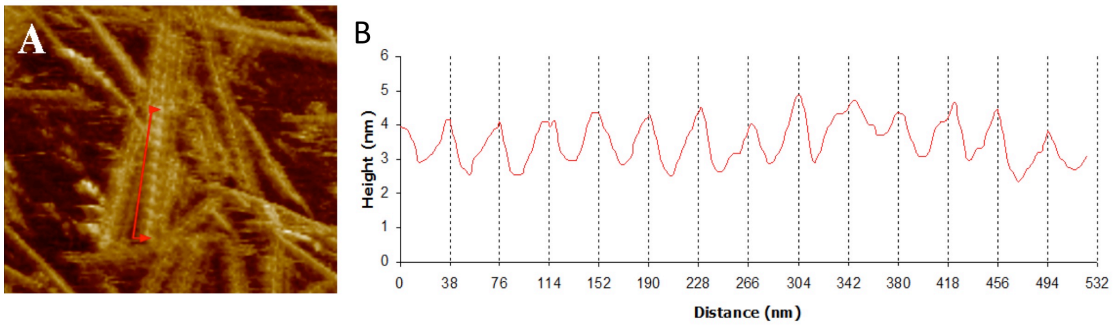

Figure 8.7: (A) AFM images of F-actin on smaller scan sizes revealing the individual filament helical pitch as measured by taking a section profiles along the axis of the filament (B). The pitch was found to be 38 ± 1 nm.

By incubating DPPC:EDPPC:FITC-DHPE (80:19.5:0.5) lipid microbubbles with pre-polymerised filaments containing 5% actin fluorescently labelled with rhodamine. Fluorescence imaging at low concentrations of F-actin showed single or filament bundles binding to the sides of the microbubbles (Figure 8.8 A). At higher F-actin concentrations, aggregations of microbubbles trapped in large-scale filament networks were observed (Figure 8.8 B). As persistence length of F-actin was found to be 19 μm, much greater than typical microbubble radii (2-5 μm), difficulties attempting to coat microbubbles effectively this way are expected and consistent with the observations.

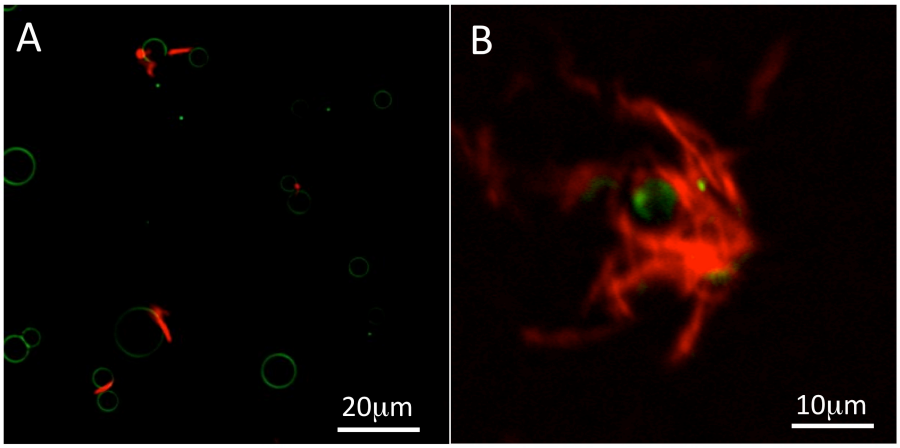

Figure 8.8: F-actin with 5% rhodamine labeled actin incubated with DPPC-EDPPC (4:1) with 0.5% FITC-labelled lipid microbubbles at actin concentrations of (A) 0.04 mg/ml and (B) 0.2 mg/ml.

8.2.2 Gelsolin Capped Actin Mircrobubbles

Since filaments easily grow to lengths much greater than general microbubble diameters (2- 5μm), length control is vital to reduce multiple bubbles binding to single filaments and to increase filament surface density. The second approach to coating microbubbles with actin involved reducing the filament length using the severing and barbed end capping protein gelsolin. The average filament lengths obtained *in vitro* have been shown to be dependent on the gelsolin to F-actin ratio [52]. As shown in Figure 8.9 (A) using gelsolin-actin ratio of 1:113 created much shorter filaments which preferentially packed parallel in an almost 2D nematic phase. The filament length distribution of the capped filaments (Figure 8.9B) gave a mean length of 330 (σ = 206 nm). This result is in line with previous experimental fits and theory which predict an average length of 305 nm ± 30 nm (error based on actin:gelsolin ratio measurement accuracies) [52].

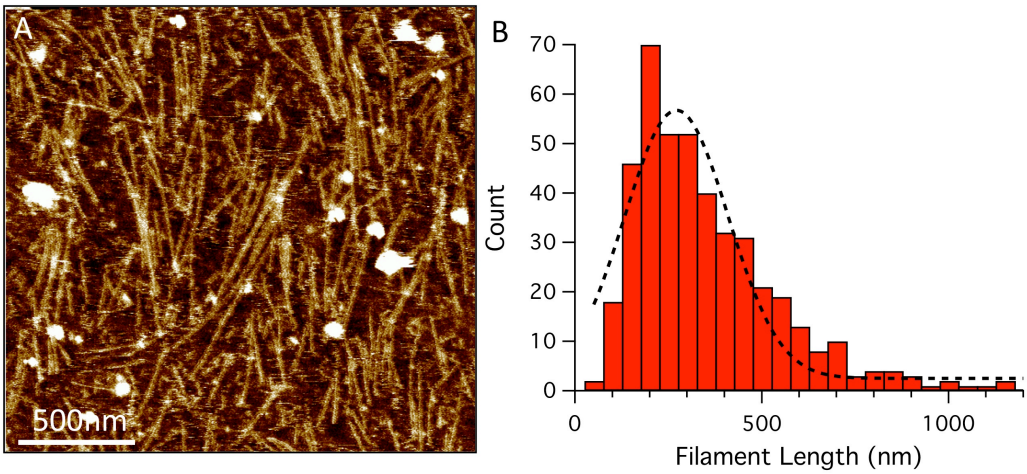

Figure 8.9: (A) AFM image of gelsolin severed and capped F-actin electrostatically bound to a nickel modifed mica surface. (B) Histogram showing filament length distribution.

Figure 8.10 shows how gelsolin capped actin filaments can regrow over time, this is due to filament annealing whereby short filaments join together via end-end association (as observed in section 7.3.3 on membranes). In uncapped solutions this process has been previously shown to occur within a few minutes after mechanically breaking filaments. This study also revealed annealing in the presence of capping proteins still occurs but over

several hours intermittently during the short periods of time whilst the gelsolin uncaps and recaps [182]. These results are consistent with our observations. This process of annealing is why more simple physical methods to control length such as sonication and syringe shearing may be unpractical and produce unpredictable length distributions to coat microbubbles with actin. The ability of Gelsolin to displace and sever phalloidin stable filaments is displayed in Figure 8.10 C.

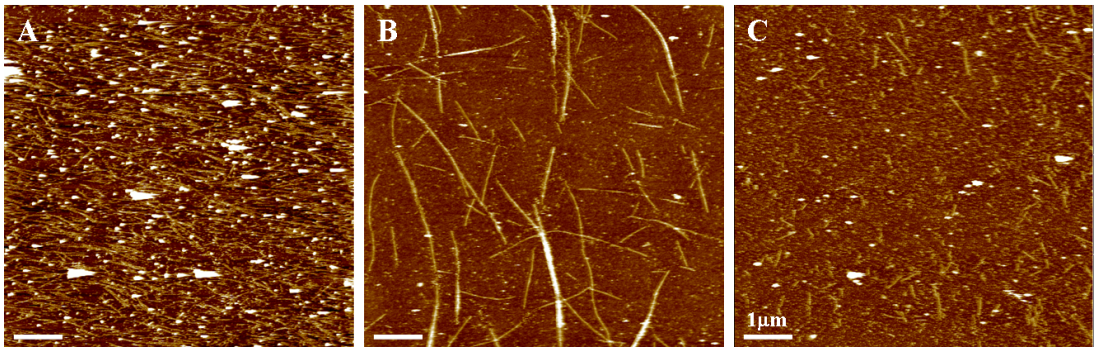

Figure 8.10: AFM images showing how the length of actin filaments can be varied:(A) Gelsolin added to G-actin before subsequent polymerisation and stabilisation with phalloidin (1:113 gelsolin-actin ratio), mean length = 330 nm. (B) Same filament sample 24 hr after removal of Calcium via the centrifugation step showing an increase in mean length to 760 nm. (C) image of the same filament sample after incubation with additional gelsolin producing a mean length of 207 nm displaying ability of gelsolin to sever phalloidin-F-actin.

Figure 8.11 shows fluorescence images of EDPPC:DPPC microbubbles incubated with gelsolin-actin (1:113) filaments. A fraction of bubbles were observed being coated by a shell of multiple filaments with some longer filaments extending away from the microbubble surface. Higher concentrations of actin may increase bubble coating efficiency however this will be at the cost of increased filament annealing and therefore may increase filaments lengths.

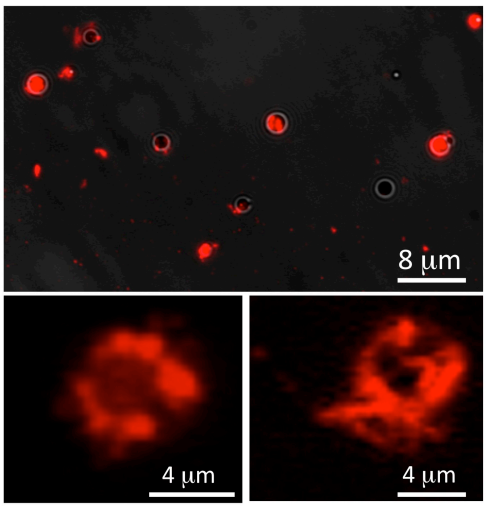

Figure 8.11: (4:1) DPPC:EDPPC lipid microbubbles coated with gelsolin capped F-actin containing 5% rhodamine labelled actin. (Top) composite bright field image with fluorescence image of population of bubbles. (Bottom) higher resolution images of selected bubbles with high density actin coatings.

8.3 Actin Coated Microbubbles via Lipid Induced Polymerisation

The third approach to coat microbubbles with actin was based on translating the surface induced polymerisation of G-actin observed on cationic lipid bilayers (Chapter 7) to the surface of lipid microbubbles. Data on supported lipid bilayers showed in the case of fluid bilayers, where filaments are mobile and could undergo lateral diffusion, a densely packed almost complete single monolayer of aligned filaments was formed (Figure 7.10). Conversely, on the less mobile gel-state lipid bilayers filaments were less able to accommodate changes in alignment during filament growth, resulting in reduced coverage (Figure 7.13).

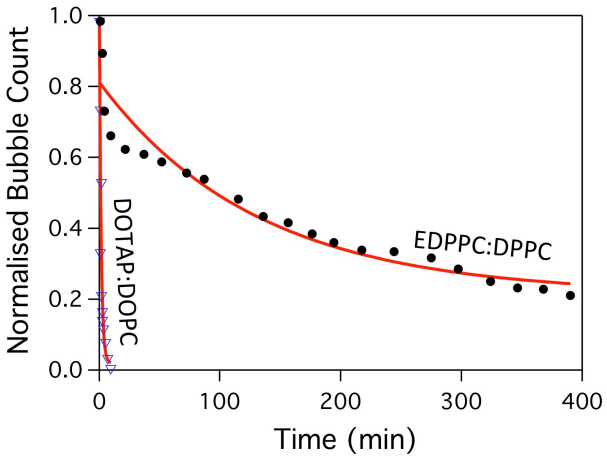

Figure 8.12: Normalised bubble count against time in non-saturated buffer conditions for populations of EDPPC:DPPC and DOTAP:DOPC (1:4) actin coated micribubbles with starting radii below 3 μm. The exponential fits to the data give half lifes of 126 min and 1 min for EDPPC:DPPC and DOTAP:DOPC respectivly.

The addition of G-actin to fluid state lipid microbubbles (DOPC:DOTAP 4:1) increased bubble lifetimes to a measurable half life of 1 min 3 seconds (Figure 8.12). Whilst this shows the actin layer increased the resistance of the shell to gas permeation, the lifetime remains too low for any potential application. Fluorescence microscopy of the actin layer around the larger, more stable DOPC:DOTAP microbubbles (Figure 8.13B) showed the formation of a homogeneous shell of actin, in agreement with the AFM data showing dense actin layers on lipid bilayers.

Adding an actin coating to gel state lipid microbubbles (EDPPC:DPPC) increased bubble lifetime from 68 min without actin, to 126 min with actin. Imaging the actin coating via fluorescent actin showed similar though less uniform actin coatings (Figure 8.13 A,C) than with the DOPC:DOTAP microbubbles. Figure 8.13 D shows 5 images of the same actin coated bubble at different focal depths to produce a semi-3D image from the top surface to the mid-section. The inhomogeneity of the actin shell is particularly evident at the top surface image of the bubble. In spite of the presence of defects within the adsorbed actin layer, the increase in bubble lifetime represents a significant increase in the shell resistance to gas permeation.

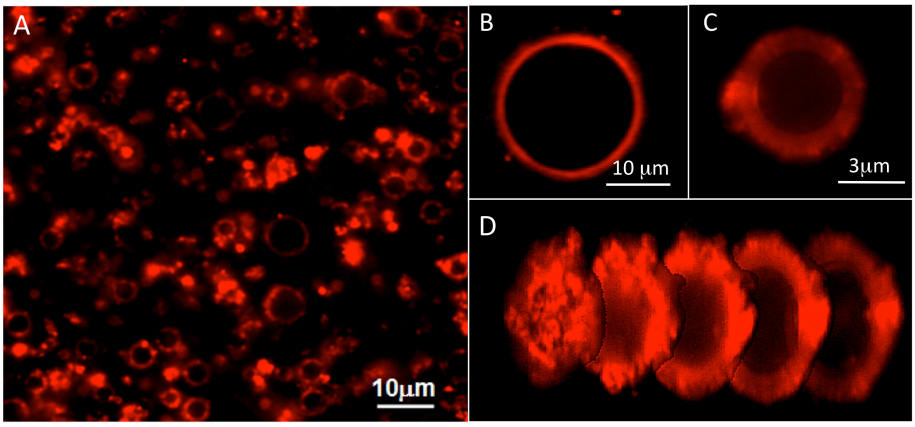

Figure 8.13 G-actin interactions with cationic microbubbles. (A) Typical distribution of EDPPC/DPPC (1:4) microbubbles coated with 5% fluorescent (Rhodamine) actin. Fluorescence images of single actin coated bubbles composed of lipids (B) (4:1) DOPC/DOTAP and (C) DPPC/EDPPC (4:1). (D) Z-slices of microbubble in (C) created by varying optical focus from top bubble surface to mid-cross-section.

Of all the coatings investigated by fluorescence microscopy and AFM, using surface induced polymerisation to coat gel-state lipid microbubbles had the most desirable properties in terms of lifetime, ease of creation and coating efficiency. Thus AFM force spectroscopy, dissolution and liposome loading experiments were carried out on this bubble type and compared to lipid only microbubbles.

8.3.1 Microbubble Dissolution

Whilst the lifetime of microbubbles in buffer solutions which have had no gas treatment is useful for understanding behaviour in typical experimental conditions or for storage, extracting physical parameters about the shell properties becomes complicated in solution with multiple gas components. The following section investigates the single bubble dissolution behaviour of lipid only and lipid-actin microbubbles in degassed solutions allowing the determination of the shell resistance to gas permeation [200].

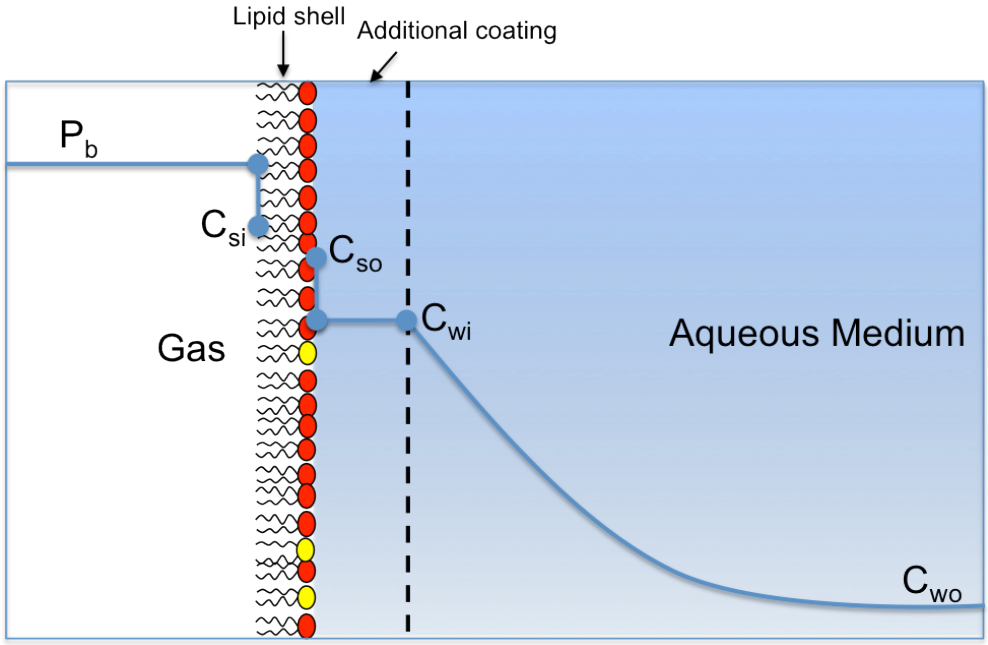

Figure 8.14: Illustation showing the concentration profile of gas molecules (C) exiting the gas core of a lipid-coated microbubble and permeating into the surrounding degassed aqueous medium. Where C_{si} and C_{so} are the molar concentrations of gas at the shell boundaries, and C_{wi} and C_{wo} are the molar concentrations of gas at the water layer boundaries.

Epstein and Plesset developed a mathematical model for the diffusion-limited dissolution of a bubble with no shell in a stagnant, degassed medium that included the effects of surface tension [201]. Starting with the diffusion equation and appropriate boundary conditions, they obtained an expression for the concentration profile of gas in the surrounding aqueous medium. This expression was then solved to determine the molar flux at the bubble wall

and coupled to a mole balance over the bubble volume in order to obtain an expression for the change in bubble radius (R) with respect to time (t):

$$-\frac{\mathrm{dR}}{\mathrm{dt}} = \mathrm{H}\frac{1 - \mathrm{f} + \frac{2\sigma}{\mathrm{P_a R}}}{1 + \frac{4\sigma}{3\mathrm{P_a R}}}\left(\frac{D_W}{R} + \sqrt{\frac{D_W}{\pi t}}\right) \tag{8.2}$$

Which shows that the primary driving forces for dissolution are the magnitude of Ostwald partition coefficient of the gas, H, the surface tension of the interface, σ, the degree of gas saturation in the aqueous phase, f, the pressure, P, and the diffusivity of gas in solution, D_w. This equation was then further modified to include additional shell properties by introducing a mass transfer resistances term, R_{shell}, which accounts for the gas permeation resistance of the lipid shell [196,200].

$$\frac{\mathrm{dR}}{\mathrm{dt}} = -\frac{\mathrm{H}}{\frac{\mathrm{R}}{\mathrm{D_w}} + \mathrm{R_{shell}}}\left(\frac{\left(1 + \frac{2\sigma}{\mathrm{P_a R}}\right) - \mathrm{f}}{1 + \frac{4\sigma}{3\mathrm{P_a R}}}\right) \tag{8.3}$$

To apply this model to the microbubbles used in this work values of 5.2×10^{-4} and 7.45×10^{-4} m^2s^{-1} were used for the Ostwald coefficient and diffusivity of C_3F_8 in water (D_w) as previously determined [61]. A degassed buffer was used and hence a value of 5/6 was used for f [196]. The surface tension of the bubbles was assumed constant throughout at a value appropriate for DPPC of 62 mN/m, as determined by Borden et al from measurements of the collapse pressure of a Langmuir monolayer [196].

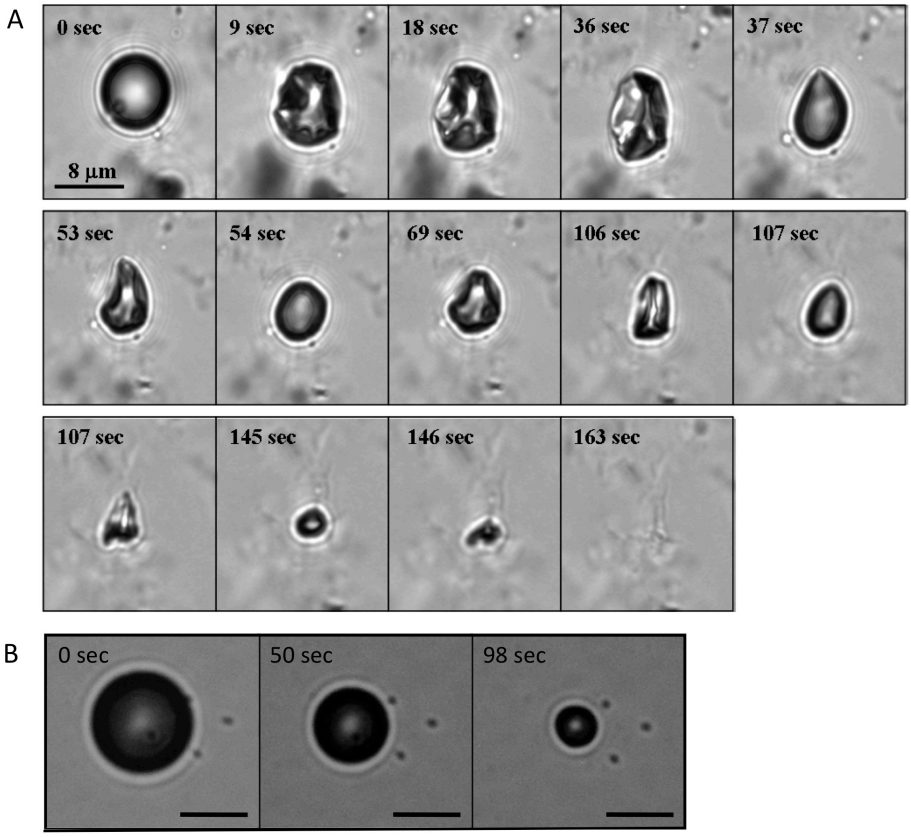

Figure 8.15: Light microscopy images over time of (A) actin coated and (B) DPPC:EDPPC lipid only microbubbles in degassed buffer conditions.

To follow the dissolution of microbubbles, lipid microbubbles were created by the shaking method, coated with actin via incubation with G-actin and held in a fluid cell. Several cell volumes full of buffer which had been stirred and sonicated under vacuum were then flowed through the cell before imaging and tracking the dissolution behaviour of individual bubbles. Figure 8.15 shows a clear difference in character of the dissolution between lipid only and actin lipid shells, the lipid only bubbles dissolve quickly and continuously, whereas actin coated bubbles undergo buckling and folding followed by discrete events where the microbubble returns to spherical geometry shedding the shell (actin and lipid) in the process. The discrete shedding was observed with the majority of actin coated bubbles and was rarely seen with lipid only bubbles. Analysis of the bubble radius with time (Figure 8.16) further highlights this difference between a quick smooth dissolution for lipid only and slow discrete steps in shedding of microbubble material for actin coated bubbles. To determine the shell resistance to gas permeation, R_{shell}, the reduction in microbubble radius with time was

numerically fit to Eqn. 8.3 with R_{shell} as the free parameter. As shown by the dashed line fits in Figure 8.16, the model was able to fit the dissolution curves very closely.

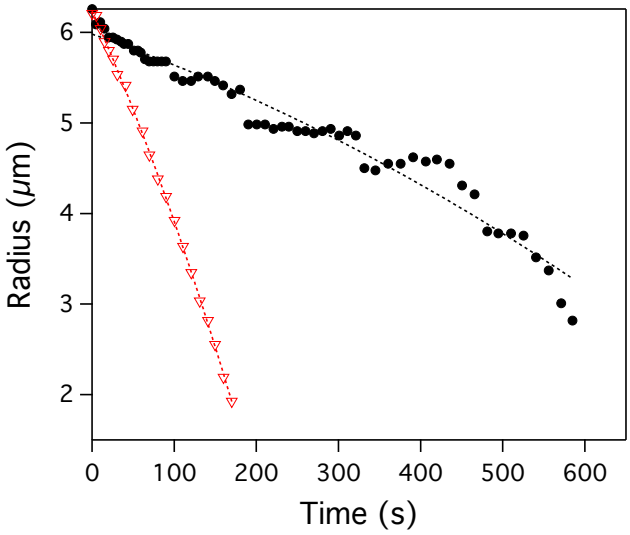

Figure 8.16: Typical radius time plots showing the dissolution of actin-coated microbubbles (triangles) and lipid only bubbles (circles) in a degassed environment.

The average value obtained for the shell resistance of DPPC:EDPPC (4:1) was 64 ± 41 s/cm (Figure 8.17) and is in agreement with previous experimental results obtained for a similar microbubbles composed of DPPC:PEG-40 (9:1) (51 ± 27 s/cm) [196]. The additional actin increased the average shell resistance to 293 ± 122 s/cm (Figure 8.17). Previous studies on varying lipid chain length have shown equivalent changes when increasing the lipid carbon chain length from 16 (as used here) up the 22, increasing from 51 ± 27 s cm^{-1} up to 315 ± 72 s cm^{-1} [196]. This increase in resistance is as expected for an additional layer which provides both additional mechanical stability and a 2nd barrier to gas flow. The distribution of R_{shell} values showed a larger variance for actin coated bubbles because the actin shell is not as uniformly distributed as the lipids and collapse may be strongly affected by particular filament arrangements. This may also explain the small peak at lower values suggesting there's a fraction of bubble which may be partially or uncoated. This data shows the actin coating increases microbubble stability through a higher impedance of the

shell to gas permeation, a property particularly important in the presence of turbulent flow in the surrounding medium, as is likely while traveling through the blood stream.

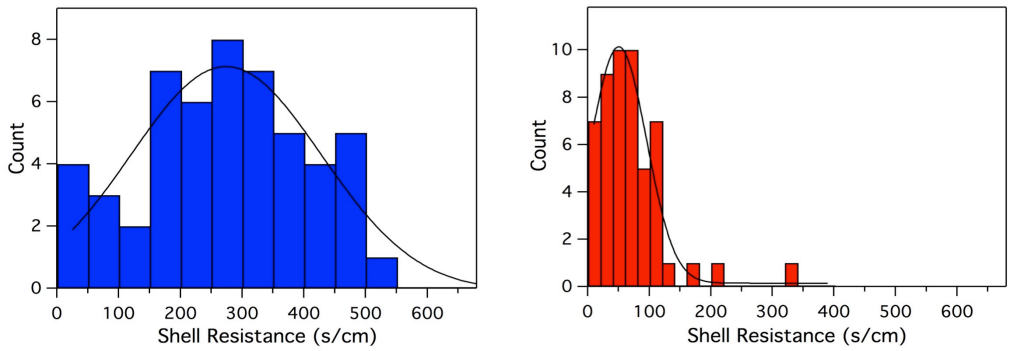

Figure 8.17: Histograms of the fitted shell resistance values for populations of DPPC:EDPPC (4:1) bubbles with actin (left) and without.

8.3.2 Force Spectroscopy of Microbubbles

The mechanical properties, in particular the stiffness, of microbubbles dictate their behaviour within an ultrasound field (section 1.6.2). Using tipless cantilevers to compress and relax single bubbles (Figure 8.18), force spectroscopy measurements were performed to obtain bubble stiffness and elastic moduli values.

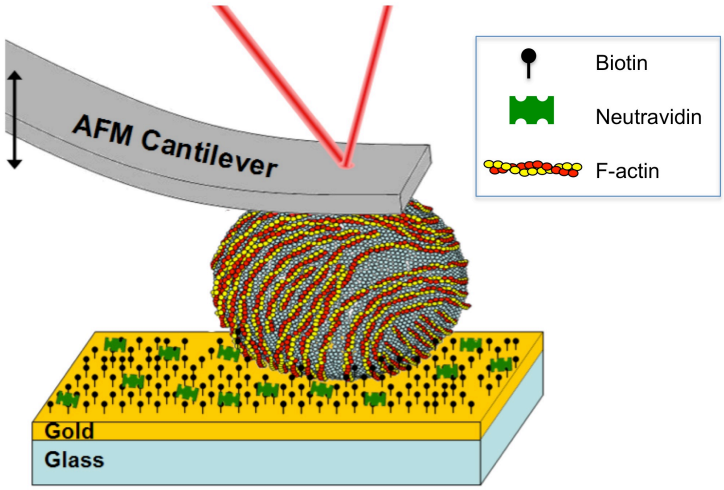

Figure 8.18: Illustration of the force spectroscopy set up, the microbubble is attached to a gold substrate via biotin thiol–neutravidin linked to the microbubble through biotin actin or biotin lipid depending on microbubble type.

As illustrated in Figure 8.18, to hold the microbubbles to the surface and prevent slippage upon compression, the bubbles were attached to a gold substrate coated with a biotin thiol SAM via neutravadin. In the case of lipid only DPPC:EDPPC microbubbles, 2% DOPE-biotin was included in the microbubble lipid shell to allow binding to the neutravidin bound to the substrate. In the case of the actin coated bubbles 10% biotinylated actin was included in the actin mix allowing binding via the actin shell.

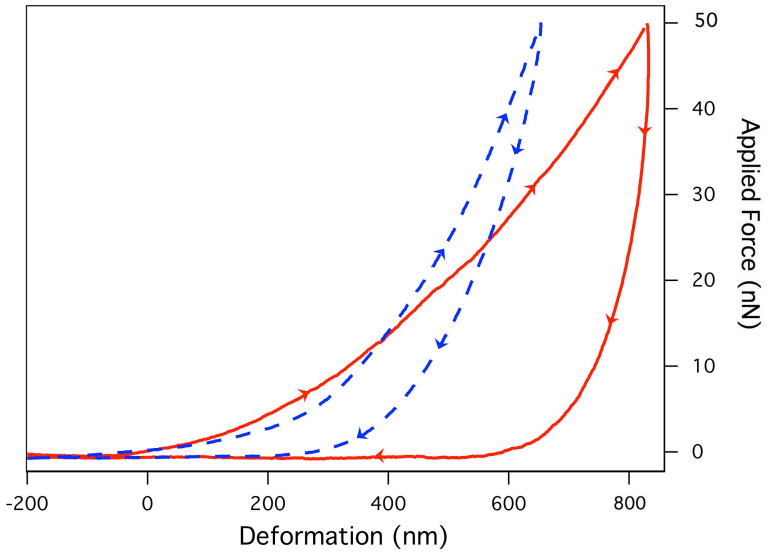

Figure 8.19: Typical force–deformation plots for actin coated (dashed lines) and lipid only (full lines) microbubbles with arrows indicating force loading and unloading.

Before performing force spectroscopy measurements on bubbles the tipless cantilevers were calibrated to find the deflection sensitivity and tip spring constant by undertaking a force curve on a hard surface (i.e. clean glass) and performing a thermal tune respectively (for full details see section 3.6.4.2). This calibration step also allowed the cantilever maximum force range to be tested on the hard surface. It was observed for cantilevers with typical spring constants of 0.1 mN/m, the force-distance curves became non-linear for forces greater than 100 nN, showing increased deformation per applied force. To avoid this, stiffer tips could have been used however this would reduce sensitivity at the lower force spectrum. Figure 8.19 shows typical extension and retraction force-indentation curves obtained when compressing microbubbles with and without an actin shell. The stiffness of a

given microbubble was obtained by taking the gradient of the extension curve for a series of increased applied forces. At smaller indentations the actin coated and lipid only bubbles show similar behaviour, as the indentation increased beyond 300 nm the actin coated bubble requires more force to compress and thus becomes stiffer than the lipid only bubble. The retraction/unloading curves show similar rates for each bubble with the tip detaching from the bubble surface (zero applied force) after 200 nm and 300 nm deformation for the lipid only and actin bubbles respectively. Force curves were typically repeated 50 times on the same bubble, the first 5-10 curves often showed variations between each and thus were disregarded in the analysis, however force curves 10-50 showed very consistent reproducible behaviour. For the actin coated microbubbles slipping of the bubble under the tip was more frequently observed implying the attachment to the substrate wasn't as great as for the lipid only bubbles.

Figure 8.20 shows averaged stiffness data for populations (21 bubbles with 50 force curves taken on each) of bubbles of comparable radius (3-5μm), over which there was no apparent radial dependence on stiffness. At 10 nN the stiffness of both microbubble types is roughly the same with, and without actin at 52 $\pm$ 5 mN/m in agreement with previous published data on lipid microbubbles for similar forces [81,202,203]. As the applied force is increased, the stiffness of both bubble types increases with the actin coated bubbles becoming stiffer than the lipid only bubbles. At 50 nN applied force the stiffness of actin coated bubbles is ~40% greater than that of uncoated bubbles. This increase in stiffness is as expected and has been previously observed on lipid membranes through an increase the membrane bending modulus in the presence of actin filaments [204].

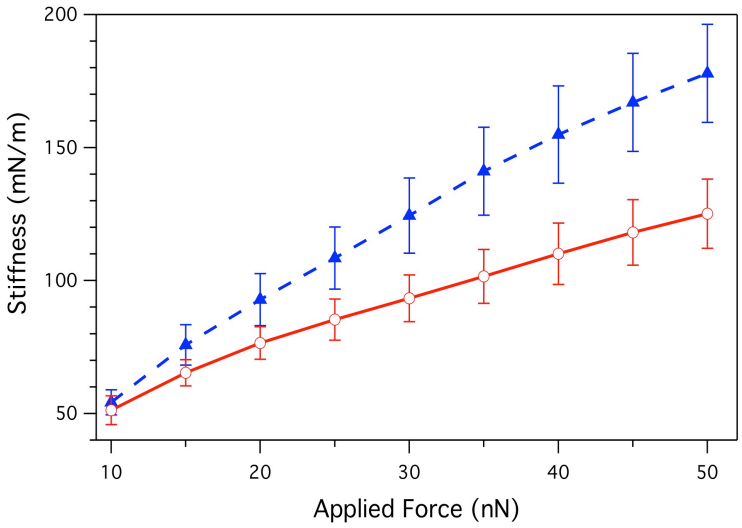

Figure 8.20: Average force dependent stiffness for bubbles (n = 21) with (filled triangles) and without actin (open circles).

A more notable difference caused by the actin coating is seen in the hysteresis between loading and unloading. The hysteresis is an inherent indication of the microbubble elasticity and can be quantified by a plasticity index (η) determined by the ratio between areas under loading and unloading curve [205,206]. The index of plasticity covers a range from 0 (fully elastic) to 1 (fully plastic). Analysis of the curves of many bubbles of comparable sizes give an average plastic index value of 0.78 $\pm$ 0.02 for lipid only microbubbles. Bubbles coated with actin have a plastic index of 0.47 $\pm$ 0.03, suggesting the actin coating produces a more elastic shell than lipid alone. Previous AFM measurements of microbubbles have shown the addition of coatings such as polyethylene glycol (PEG), streptavidin and Quantum dots increase the plasticity in contrast to the actin coating [206]. AFM studies on cells have found plastic index values ranging between 0.3-0.5 for melanoma cells which then increases to 0.7-0.9 after incubation with a toxin, cytochalasin D, which the depolymerises actin filament [205]. Direct comparison between cells and microbubbles is not ideal however these results appear to agree well with the principle that actin increases elasticity of lipid structures.

8.3.3 Liposome Loading Actin coated microbubbles

In addition to the binding to surfaces for force spectroscopy studies, the incorporation a fraction of biotinylated actin into the actin coating permits the attachment of payloads, such as liposomes or targeting agents such as antibodies. The link is made via biotin-lipid in the liposome shell to which streptavidin is then bound, these liposomes were incubated with the actin coated bubbles with 5% biotin-actin (Figure 8.21A). Figure 8.21 shows the co-localisation of rhodamine labelled actin (red, Figure 8.21B) around lipid microbubbles and soluble dye loaded liposomes (green, Figure 5c) at the surface of lipid microbubbles. In principle this actin-biotin-streptavidin system could be extended to antibodies and targeting agents hence actin coatings maintain the diverse functionality permitted by lipid only microbubbles. The network nature of actin filaments may allow improvements in cargo load to be made over lipid only systems through entrapment.

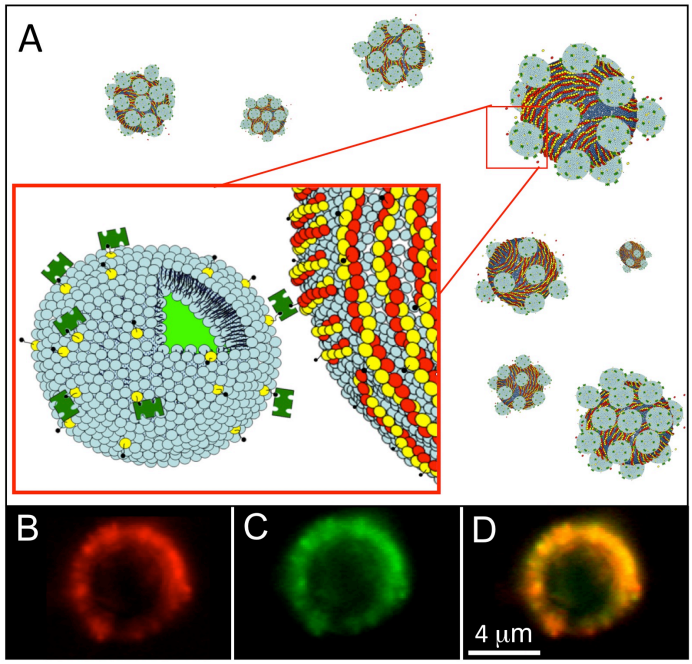

Figure 8.21: (A) Illustration showing the attachment of dye loaded liposomes to the exterior of actin coated microbubbles. The liposomes contain a fraction of biotin–lipid which are then bound to neutravidin, these are then bound to actin-microbubbles through using 5% biotin–actin in the actin microbubble shell. Fluorescence images with (B) red highlighting rhodamine actin and (C) green showing fluoresent luciferin within the 100 nm liposomes with (D) the composite image.

8.4 Conclusions

In summary, this chapter has shown the methodology to produce a new type of microbubble shell with a simple self-assembly protocol, capable of cargo carry and which may in the future be easily adapted to include various actin binding proteins to obtain desired characteristics. The additional coating provides many advantages including the ability to tune microbubble stiffness and elasticity. The three fold increase in resistance to gas permeation offered by the actin coating gives these bubbles longer lifetimes *in vitro* and would allow them to survive longer *in vivo*. Finally, with the wealth of knowledge of actin in cells and abundance of actin binding proteins that can be applied to further modify and tune desired properties this coating may pave the way to controlling the ultrasound response.

Chapter 9
Conclusions and Future Work

The overall aim of this thesis was to construct minimal model cell membrane systems to develop a better understanding of how they function, how the information can related to real cellular membranes and how it may be utilised for bio-nanotechnology applications. The work in this thesis has shown how this can be achieved primarily using AFM and high-speed AFM not only to study lipid membranes and protein interactions at the relevant spatial/time scales, but also to create and pattern membranes.

In chapter 4 the deposition of lipid bilayers from the apex of AFM tips in solution was investigated with the aim of understanding the effects of confining biological components to low dimensions. By varying tip velocity, the deposition was controlled, allowing 6 - 200 nm wide bilayer channels to be created. The systematic studies of lipid and protein diffusion behaviour gave new insight into the mobility and packing of lipids in close proximity of bilayer boundaries. The outcomes of this study are not only important for understanding lipid/protein behaviour near pores and ruptures in cellular membranes but also for numerous potential future studies which may utilise the advantages of reduced dimensionality. While this technique showed it was possible to deposit lipid bilayers with 6 nm resolution via simple raster scanning, the work towards using this technique to form specific patterns is still in its infancy. Understanding and controlling the exact velocity and contact behaviour would allow the creation of patterned lipid bilayers at scales far lower than previously achieved. At these reduced dimensions the systems approached handfuls of lipid molecules and additional studies would provide further understanding to the roles of confinement in biological membranes. The introduction of functional membrane proteins would allow the study of protein-protein and protein-lipid interactions. In addition it would allow studies of protein processes that rely diffusion in order to perform biological tasks such as photosynthesis, catalytic processes at membranes, and exchange of species between cells and their surroundings.

In chapter 5, the phase diagram of a model cell membrane lipid composition of DOPC-SM-Chol was mapped out with temperature, focusing particularly on regions of critical behaviour. Analysis of the nature of the critical fluctuations with high speed AFM allowed the critical exponents for line tension and correlation length to be determined, both suggesting the system can be described by a 2D Ising model. The critical phase dynamics above the critical temperature were shown to have nanodomains in the size range of 10-100's of nanometres with lifetimes of less than 2 seconds. This provides some of the first direct evidence that the small "raft" domains detected in real cells can be replicated by non-equilibrium compositional fluctuations. While the biophysics of these model systems is important for understanding lipid-lipid interactions, increases in complexity by the addition of membrane proteins would take the model system a step closer to cellular membranes. Investigating how proteins interact with non-critical domains was observed in chapter 6 using the actin binding protein ponticulin. The next natural step would be to polymerise an actin network bound to the ponticulin and study the effects on critical lipid behaviour observed in chapter 5.

Studies of actin polymerisation induced at positively charged bilayers in chapter 7 not only provided new insight into the phenomenon but also described a simple novel method to create 'synthetic', robust actin-membrane scaffolds with controllable coverage. The theoretical modelling of the actin polymerisation process showed the screening of the electrostatic charges between actin monomers permits their 2D association which in turn allows polymerisation to proceed either from solution or diffusion in the membrane. Both the effects of charge and lipid diffusion may be important factors in cellular membranes for which the binding of actin to membrane proteins is electrostatic such as ponticulin. The behaviour on phase separated systems showed it was possible to restrict the actin growth to one phase. Future work on these phase-separated systems could include controlling the phase separation with substrate geometry to consequently spatially control actin polymerisation.

In chapter 8 it was shown this lipid induced polymerisation process could be translated from the surface of supported lipid bilayers to the shell of lipid microbubbles to change their stability and mechanical properties. These results are not only useful to the development of more complex bubble coatings but also demonstrate the application of minimal biomimetic constructs for nano-technological applications with potential uses in synthetic biology. Future work may include more sophisticated actin shell that could be further developed from this platform by incorporating actin binding proteins. One such may be cross-linking proteins which have been shown to alter network stiffness by orders of magnitude [55]. This is in contrast to conventional flexible polymer materials, where the elasticity is relatively insensitive to cross-links [67]. Applying these proteins to the actin shell around microbubbles would allow the physical properties to be easily adapted to provide the desired mechanical response - whether it be towards subharmonic imaging or a particular drug release mechanism. Future work would also include additional characterisation using ultrasound to determine if the subharmonic signal from the microbubble is improved by the addition of these biomimetic actin shells.

Bibliography

1. Borden MA, Caskey CF, Little E, Gillies RJ, Ferrara KW. DNA and Polylysine Adsorption and Multilayer Construction onto Cationic Lipid-Coated Microbubbles. Langmuir. 2007 Aug;23(18):9401–8.

2. Liu J, Conboy JC. 1,2-Diacyl-Phosphatidylcholine Flip-Flop Measured Directly by Sum-Frequency Vibrational Spectroscopy. Biophysical Journal. 2005 Oct;89(4):2522–32.

3. Bhattacharya S, Haldar S. Interactions between cholesterol and lipids in bilayer membranes. Role of lipid headgroup and hydrocarbon chain–backbone linkage. Biochimica et Biophysica Acta (BBA) - Biomembranes. 2000 Jul;1467(1):39–53.

4. Rubenstein JL, Smith BA. Lateral diffusion in binary mixtures of cholesterol and phosphatidylcholines. Proceedings of the National Academy of Sciences. 1979; 76(1):15-18.

5. Machta BB, Papanikolaou S, Sethna JP, Veatch SL. Minimal Model of Plasma Membrane Heterogeneity Requires Coupling Cortical Actin to Criticality. Biophysical Journal. 2011 Apr;100(7):1668–77.

6. Honerkamp-Smith AR, Veatch SL, Keller SL. An introduction to critical points for biophysicists; observations of compositional heterogeneity in lipid membranes. Biochimica et Biophysica Acta (BBA) - Biomembranes. 2009 Jan;1788(1):53–63.

7. Veatch SL, Soubias O, Keller SL. Critical fluctuations in domain-forming lipid mixtures. Proceedings of the National Academy of Sciences. 2007. 104(45): 17650-17655

8. Veatch SL, Cicuta P, Sengupta P, Honerkamp-Smith A, Holowka D, Baird B. Critical Fluctuations in Plasma Membrane Vesicles. ACS Chemical Biology. 2008 May;3(5):287–93.

9. Honerkamp-Smith AR, Cicuta P, Collins MD, Veatch SL, Nijs den M, Schick M, et al. Line Tensions, Correlation Lengths, and Critical Exponents in Lipid Membranes Near Critical Points. Biophysical Journal. 2008 Jul;95(1):236–46.

10. Lenne P-F, Nicolas A. Physics puzzles on membrane domains posed by cell biology. Soft Matter. 2009;5(15):2841.

11. Tanaka M, Sackmann E. Polymer-supported membranes as models of the cell surface. Nature. 2005 Sep 29;437(7059):656–63.

12. Reimhult E, Höök F, Kasemo B. Intact Vesicle Adsorption and Supported Biomembrane Formation from Vesicles in Solution: Influence of Surface Chemistry, Vesicle Size, Temperature, and Osmotic Pressure. Langmuir. 2003 Mar;19(5):1681–91.

13. Lenhert S, Sun P, Wang Y, Fuchs H, Mirkin CA. Massively Parallel Dip-Pen Nanolithography of Heterogeneous Supported Phospholipid Multilayer Patterns. Small. 2007 Jan 2;3(1):71–5.

14. Pott T, Bouvrais H, Méléard P. Giant unilamellar vesicle formation under physiologically relevant conditions. Chemistry and Physics of Lipids. 2008 Aug;154(2):115–9.

15. Sackmann E. Supported Membranes: Scientific and Practical Applications. Science. 1996 Jan 5;271(5245):43–8.

16. Merzlyakov M, Li E, Gitsov I, Hristova K. Surface-Supported Bilayers with Transmembrane Proteins: Role of the Polymer Cushion Revisited. Langmuir. 2006 Nov;22(24):10145–51.

17. Renner L, Osaki T, Chiantia S, Schwille P, Pompe T, Werner C. Supported Lipid Bilayers on Spacious and pH-Responsive Polymer Cushions with Varied Hydrophilicity. Journal of Physical Chemistry B. 2008 May;112(20):6373–8.

18. Ye Q, Konradi R, Textor M, Reimhult E. Liposomes Tethered to Omega-Functional PEG Brushes and Induced Formation of PEG Brush Supported Planar Lipid Bilayers. Langmuir. 2009 Dec;25(23):13534–9.

19. Meuse CW, Niaura G, Lewis ML, Plant AL. Assessing the Molecular Structure of Alkanethiol Monolayers in Hybrid Bilayer Membranes with Vibrational Spectroscopies. Langmuir. 1998 Mar;14(7):1604–11.

20. Naumann R, Schiller SM, Giess F, Grohe B, Hartman KB, Kärcher I, et al. Tethered Lipid Bilayers on Ultraflat Gold Surfaces. Langmuir. 2003 Jun;19(13):5435–43.

21. Glazier SA, Vanderah DJ, Plant AL, Bayley H, Valincius G, Kasianowicz JJ. Reconstitution of the Pore-Forming Toxin α-Hemolysin in Phospholipid/18-Octadecyl-1-thiahexa(ethylene oxide) and Phospholipid/ n-Octadecanethiol Supported Bilayer Membranes. Langmuir. 2000 Dec;16(26):10428–35.

22. Eisenberg M, Hall JE, Mead CA. The nature of the voltage-dependent conductance induced by alamethicin in black lipid membranes. Journal of Membrain Biology 1973 Dec;14(1):143–76.

23. Singer SJ, Nicolson GL. The fluid mosaic model of the structure of cell membranes. Science. 1972;175(23) 720-731.

24. Lee AG, Birdsall NJM, Metcalfe JC, Toon PA, Warren GB. Clusters in lipid bilayers and the interpretation of thermal effects in biological membranes. Biochemistry. 1974 Aug;13(18):3699–705.

25. Karnovsky MJ, Kleinfeld AM, Hoover RL. The concept of lipid domains in membranes. The Journal of Cell Biology. 1982;94(1); 1-6.

26. Simons K, Ikonen E. Functional rafts in cell membranes. Nature 1997;387(6633): 569-572.

27. Owen DM, Magenau A, Williamson D, Gaus K. The lipid raft hypothesis revisited - New insights on raft composition and function from super-resolution fluorescence microscopy. Bioessays. 2012 Jun 14;34(9):739–47.

28. Chichili GR, Rodgers W. Clustering of Membrane Raft Proteins by the Actin Cytoskeleton. Journal of Biological Chemistry. 2007 Oct 16;282(50):36682–91.

29. Dinic J, Ashrafzadeh P, Parmryd I. Actin filaments attachment at the plasma membrane in live cells cause the formation of ordered lipid domains. Biochimica et Biophysica Acta (BBA) - Biomembranes. 2013 Mar;1828(3):1102–11.

30. Suzuki KGN, Fujiwara TK, Sanematsu F, Iino R, Edidin M, Kusumi A. GPI-anchored receptor clusters transiently recruit Lyn and Gα for temporary cluster immobilization and Lyn activation: single-molecule tracking study 1. The Journal of Cell Biology. 2007:177.4;717-730..

31. Hell SW, Wichmann J. Breaking the diffraction resolution limit by stimulated emission: stimulated-emission-depletion fluorescence microscopy. Optics letters. 1994;19(11):780-782.

32. Gustafsson MGL. Surpassing the lateral resolution limit by a factor of two using structured illumination microscopy. Journal of microscopy. 2000 May;198(2):82–7.

33. Finean JB, Coleman R, Michell RH. Membranes and Their Cellular Functions. John Wiley & Sons Incorporated; 1977.

34. Schlaepfer DD, Hunter T. Integrin signalling and tyrosine phosphorylation: just the FAKs? Trends in Cell Biology. 1998 Apr 1;8(4):151–7.

35. Woolf TB, Roux B. Structure, energetics, and dynamics of lipid–protein interactions: A molecular dynamics study of the gramicidin A channel in a DMPC bilayer. Proteins. 1996 Jan;24(1):92–114.

36. Holsinger LJ, Shaughnessy MA, Micko A. Analysis of the posttranslational modifications of the influenza virus M2 protein. Journal of Virology 1995:69(2);1219-1225.

37. Schroeder C, Heider H, M ncke-Buchner E, Lin T-I. The influenza virus ion channel and maturation cofactor M2 is a cholesterol-binding protein. Eur Biophys J. 2004 Jun 25;34(1):52–66.

38. Rossman JS, Jing X, Leser GP, Lamb RA. Influenza Virus M2 Protein Mediates ESCRT-Independent Membrane Scission. Cell. 2010 Sep;142(6):902–13.

39. Schnell JR, Chou JJ. Structure and mechanism of the M2 proton channel of influenza A virus. Nature. 2008 Jan 31;451(7178):591–5.

40. Chia CP. The integral membrane protein, ponticulin, acts as a monomer in nucleating actin assembly. The Journal of Cell Biology. 1993 Feb 1;120(4):909–22.

41. Luna EJ, Wuestehube LJ, Chia CP, Shariff A, Hitt AL, Ingalls HM. Ponticulin, a developmentally-regulated plasma membrane glycoprotein, mediates actin binding and nucleation. Dev Genet. 1990;11(5-6):354–61.

42. Shariff A. Dictyostelium discoideum plasma membranes contain an actin-nucleating activity that requires ponticulin, an integral membrane glycoprotein. The Journal of Cell Biology. 1990 Mar 1;110(3):681–92.

43. Schwartz MA. Binding and assembly of actin filaments by plasma membranes from Dictyostelium discoideum. The Journal of Cell Biology. 1986 Jun 1;102(6):2067–75.

44. Wuestehube LJ. F-actin binds to the cytoplasmic surface of ponticulin, a 17-kD integral glycoprotein from Dictyostelium discoideum plasma membranes. The Journal of Cell Biology. 1987 Oct 1;105(4):1741–51.

45. Hitt AL, Luna EJ, Hong Lu T. Ponticulin is an atypical membrane protein. The Journal of Cell Biology. 1994 Sep 2;126(6):1421.

46. Carballido-López R. The Bacterial Actin-Like Cytoskeleton. Microbiology and Molecular Biology Reviews. 2006 Dec 8;70(4):888–909.

47. Wang H, Robinson RC, Burtnick LD. The structure of native G-actin. Cytoskeleton. 2010 Jun 10;67(7):456–65.

48. Carlier MF, Pantaloni D, Korn ED. Fluorescence measurements of the binding of cations to high-affinity and low-affinity sites on ATP-G-actin. Journal of Biological Chemistry. 1986;261(23):10778–84.

49. Otterbein LR. The Crystal Structure of Uncomplexed Actin in the ADP State. Science. 2001 Jul 27;293(5530):708–11.

50. Lind SE. Reversible binding of actin to gelsolin and profilin in human platelet extracts. The Journal of Cell Biology. 1987 Aug 1;105(2):833–42.

51. Howard T. Gelsolin-actin interaction and actin polymerization in human neutrophils. The Journal of Cell Biology. 1990 Jun 1;110(6):1983–91.

52. Janmey PA, Peetermans J, Zaner KS, Stossel TP, Tanaka T. Structure and mobility of actin filaments as measured by quasielastic light scattering, viscometry, and electron microscopy. Journal of Biological Chemistry. 1986;261(18):8357–62.

53. Kasza KE, Broedersz CP, Koenderink GH, Lin YC, Messner W, Millman EA, et al. Actin Filament Length Tunes Elasticity of Flexibly Cross-

Linked Actin Networks. Biophysical Journal. Biophysical Society; 2010 Aug 9;99(4):1091–100.

54. Amos LA, Amos WB. Molecules of the Cytoskeleton. 1991. 1 p.

55. Gardel ML. Elastic Behaviour of Cross-Linked and Bundled Actin Networks. Science. 2004 May 28;304(5675):1301–5.

56. Bekeredjian R, Katus H, Kuecherer H. Therapeutic Use of Ultrasound Targeted Microbubble Destruction: A Review of Non-Cardiac Applications. Ultraschall Med. 2006 Apr;27(2):134–40.

57. Deckers R, Moonen CTW. Ultrasound triggered, image guided, local drug delivery. Journal of Controlled Release. 2010 Nov 20;148(1):25–33.

58. Price RJ, Skyba DM, Kaul S, Skalak TC. Delivery of colloidal particles and red blood cells to tissue through microvessel ruptures created by targeted microbubble destruction with ultrasound. Circulation. 1998;98(13):1264–7.

59. Leighton TG. The Acoustic Bubble. Academic Press; 1996. 1 p.

60. Marmottant P, Hilgenfeldt S. Controlled vesicle deformation and lysis by single oscillating bubbles. Nature. 2003 May 8;423(6936):153–6.

61. Sarkar K, Katiyar A, Jain P. Growth and Dissolution of an Encapsulated Contrast Microbubble: Effects of Encapsulation Permeability. Ultrasound in Medicine & Biology. 2009 Aug;35(8):1385–96.

62. De Jong N, Bouakaz A, Frinking P. Basic Acoustic Properties of Microbubbles. Echocardiography. 2002 Apr;19(3):229–40.

63. Stride E, Pancholi K, Edirisinghe MJ, Samarasinghe S. Increasing the nonlinear character of microbubble oscillations at low acoustic pressures. Journal of The Royal Society Interface. 2008;5(24):807–11.

64. Rayleigh L. VIII. On the pressure developed in a liquid during the collapse of a spherical cavity. Philosophical Magazine Series 6 1917. 34 (200).

65. Plesset MS, Prosperetti A. Bubble dynamics and cavitation. Annual Review of Fluid Mechanics. 1977. 9(1); 145-185.

66. Marmottant P, van der Meer S, Emmer M, Versluis M, de Jong N, Hilgenfeldt S, et al. A model for large amplitude oscillations of coated bubbles accounting for buckling and rupture. The Journal of Acoustical Society of America. 2005;118(6):3499–505.

67. Ferry JD. Viscoelastic Properties of Polymers (3rd Ed.) Wiley, Indianapolis. 1980.

68. A Frinking P, Gaud E, Brochot J, Arditi M. Subharmonic scattering of phospholipid-shell microbubbles at low acoustic pressure amplitudes. IEEE Transaction on Ultrasonics, Ferroelectric and Frequency Control. 2010 Aug 1;57(8):1762–71.

69. de Jong N, Emmer M, Chin CT, Bouakaz A, Mastik F, Lohse D, et al. “Compression-Only” Behavior of Phospholipid-Coated Contrast Bubbles. Ultrasound in Medicine & Biology. 2007 Apr;33(4):653–6.

70. Silj J, Overvelde M, Dollet B, Garbin V, de Jong N, Lohse D, et al. “Compression-only” behavior: A second-order nonlinear response of ultrasound contrast agent microbubbles. The Journal of Acoustical Society of America. 2011;129(4):1729.

71. Katiyar A, Sarkar K. Effects of encapsulation damping on the excitation threshold for subharmonic generation from contrast microbubbles. The Journal of Acoustical Society of America. 2012;132(5):3576–85.

72. Faez T, Emmer M, Docter M, SIJL J, Versluis M, de Jong N. Characterizing the Subharmonic Response of Phospholipid-Coated

Microbubbles for Carotid Imaging. Ultrasound in Medicine & Biology. 2011 Jun;37(6):958–70.

73. Sirsi SR, Borden MA. Microbubble compositions, properties and biomedical applications. Bubble Science, Engineering and Technology. 2009 Nov 1;1(1):3–17.

74. AH M, Nicolaysen H, Toft K. Structure and organization of albumin molecules forming the shell of air-filled microspheres: evidence for a monolayer of albumin molecules of multiple orientations stabilizing the enclosed air. Biotechnology and Applied Biochemistry, 1996;24(2), 145-153.

75. Cavalieri F, Ashokkumar M, Grieser F, Caruso F. Ultrasonic Synthesis of Stable, Functional Lysozyme Microbubbles. Langmuir. 2008 Sep 16;24(18):10078–83.

76. Korpanty G, Grayburn PA, Shohet RV, Brekken RA. Targeting vascular endothelium with avidin microbubbles. Ultrasound in Medicine & Biology. 2005 Sep;31(9):1279–83.

77. Cavalieri F, Hamassi El A, Chiessi E, Paradossi G. Stable Polymeric Microballoons as Multifunctional Device for Biomedical Uses: Synthesis and Characterization. Langmuir. 2005 Sep;21(19):8758–64.

78. Leong-Poi H, Song J, Rim SJ, Christiansen J. Influence of microbubble shell properties on ultrasound signal: Implications for low-power perfusion imaging. Journal of the American Society of Echocardiography, 2002;15(10); 1269-1276.

79. Shchukin DG, Köhler K, Möhwald H, Sukhorukov GB. Gas-Filled Polyelectrolyte Capsules. Angewandte Chemie. 2005 May 20;44(21):3310–4.

80. Lentacker I, De Geest BG, Vandenbroucke RE, Peeters L, Demeester J, De Smedt SC, et al. Ultrasound-Responsive Polymer-Coated Microbubbles That Bind and Protect DNA. Langmuir. 2006 Aug;22(17):7273–8.

81. McKendry JE, Grant CA, Johnson BRG, Coletta PL, Evans JA, Evans SD. Force spectroscopy of streptavidin conjugated lipid coated microbubbles. Bubble Science, Engineering and Technology. 2010 Dec 1;2(2):48–54.

82. Meyer G, Amer NM. Novel optical approach to atomic force microscopy. Applied Physics Letters. 1988;53(12):1045–7.

83. Hoogenboom BW, Frederix PLTM, Fotiadis D, Hug HJ, Engel A. Potential of interferometric cantilever detection and its application for SFM/AFM in liquids. Nanotechnology. 2008 Aug 12;19(38):384019.

84. Ando T. High-speed atomic force microscopy coming of age. Nanotechnology. 2012 Jan 17;23(6):062001.

85. Barrett RC. High-speed, large-scale imaging with the atomic force microscope. Journal of Vacuum Science and Technology B. 1991 Mar;9(2):302.

86. Minne SC, Yaralioglu G, Manalis SR, Adams JD, Zesch J, Atalar A, et al. Automated parallel high-speed atomic force microscopy. Applied Physics Letters. 1998;72(18):2340–2.

87. Sulchek T, Minne SC, Adams JD, Fletcher DA, Atalar A, Quate CF, et al. Dual integrated actuators for extended range high speed atomic force microscopy. Applied Physics Letters. 1999;75(11):1637–9.

88. Ando T, Kodera N, Takai E. A high-speed atomic force microscope for studying biological macromolecules. Proceedings of the National Academy of Sciences, 2001.98(22);12468-12472.

89. Viani MB, Schäffer TE, Paloczi GT, Pietrasanta LI, Smith BL, Thompson JB, et al. Fast imaging and fast force spectroscopy of single biopolymers with a new atomic force microscope designed for small cantilevers. Review of Scientific Instruments. 1999;70(11):4300–3.

90. Kodera N, Yamashita H, Ando T. Active damping of the scanner for high-speed atomic force microscopy. Review of Scientific Instruments. 2005 Apr 26;76(5):053708.

91. Kodera N, Sakashita M, Ando T. Dynamic proportional-integral-differential controller for high-speed atomic force microscopy. Review of Scientific Instruments. 2006 Aug 31;77(8):083704.

92. Ando T, Uchihashi T, Fukuma T. High-speed atomic force microscopy for nano-visualization of dynamic biomolecular processes. Progress in Surface Science. 2008 Nov;83(7-9):337–437.

93. Kodera N, Yamamoto D, Ishikawa R, Ando T. Video imaging of walking myosin V by high-speed atomic force microscopy. Nature. 2010 Oct 10;468(7320):72–6.

94. Yamamoto D, Uchihashi T, Kodera N, Ando T. Anisotropic diffusion of point defects in a two-dimensional crystal of streptavidin observed by high-speed atomic force microscopy. Nanotechnology. 2008 Aug 12;19(38):384009.

95. Shibata M, Uchihashi T, Yamashita H, Kandori H, Ando T. Structural Changes in Bacteriorhodopsin in Response to Alternate Illumination Observed by High-Speed Atomic Force Microscopy. Angewandte Chemie. 2011 Apr 6;123(19):4502–5.

96. Soumpasis DM. Theoretical analysis of fluorescence photobleaching recovery experiments. Biophysical Journal. 1983; 41(1); 95-97.

97. Axelrod D, Koppel DE, Schlessinger J, Elson E, Webb WW. Mobility measurement by analysis of fluorescence photobleaching recovery kinetics. Biophysical Journal. 1976 Sep;16(9):1055–69.

98. Sauerbrey G. Messung von Plattenschwingungen sehr kleiner Amplitude durch Lichtstrommodulation. Z Physik. 1964;178(5):457–71.

99. Voinova MV, Rodahl M, Jonson M, Kasemo B. Viscoelastic Acoustic Response of Layered Polymer Films at Fluid-Solid Interfaces: Continuum Mechanics Approach. Physica Scripta. 2006 Mar 29;59(5):391–6.

100. Liang X, Mao G, Simon Ng KY. Probing small unilamellar EggPC vesicles on mica surface by atomic force microscopy. Colloids and Surfaces B: Biointerfaces. 2004 Mar;34(1):41–51.

101. Richter R, Mukhopadhyay A, Brisson A. Pathways of Lipid Vesicle Deposition on Solid Surfaces: A Combined QCM-D and AFM Study. Biophysical Journal. 2003;85(5);3035-3047.

102. Pardee JD, Spudich JA. Purification of muscle actin. Methods Cell Biol. 1982;24;271-289.

103. Barfoot RJ, Sheikh KH, Johnson BRG, Colyer J, Miles RE, Jeuken LJC, et al. Minimal F-Actin Cytoskeletal System for Planar Supported Phospholipid Bilayers. Langmuir. 2008 Jul;24(13):6827–36.

104. Mimms LT, Zampighi G, Nozaki Y, Tanford C, Reynolds JA. Phospholipid vesicle formation and transmembrane protein incorporation using octyl glucoside. Biochemistry. 1981 Feb;20(4):833–40.

105. Jiskoot W, Teerlink T, Beuvery EC, Crommelin DJA. Preparation of liposomes via detergent removal from mixed micelles by dilution. Pharmaceutisch Weekblad Scientific Edition. 1986 Oct;8(5):259–65.

106. Stark M, Stark RW, Heckl WM, Guckenberger R. Spectroscopy of the anharmonic cantilever oscillations in tapping-mode atomic-force microscopy. Applied Physics Letters. 2000;77(20):3293–5.

107. Butt H-J, Cappella B, Kappl M. Force measurements with the atomic force microscope: Technique, interpretation and applications. Surface Science Reports. 2005 Oct;59(1-6):1–152.

108. Hutter JL, Bechhoefer J. Calibration of atomic-force microscope tips. Review of Scientific Instruments. 1993;64(7):1868.

109. Cheetham MR, Bramble JP, McMillan DG, Krzeminski L, Han X, Johnson BR, et al. Concentrating membrane proteins using asymmetric traps and AC electric fields. Journal of the American Chemical Society. 2011;133(17):6521–4.

110. Hovis JS, Boxer SG. Patterning and composition arrays of supported lipid bilayers by microcontact printing. Langmuir. 2001;17(11);3400-3405.

111. Orth RN, Kameoka J, Zipfel WR, Ilic B, Webb WW, Clark TG, et al. Creating Biological Membranes on the Micron Scale: Forming Patterned Lipid Bilayers Using a Polymer Lift-Off Technique. Biophysical Journal. Elsevier; 2003 Nov;85(5):3066–73.

112. Jackson BL, Groves JT. Scanning Probe Lithography on Fluid Lipid Membranes. J Am Chem Soc. 2004 Nov;126(43):13878–9.

113. Shi J, Chen J, Cremer PS. Sub-100 nm Patterning of Supported Bilayers by Nanoshaving Lithography. J Am Chem Soc. 2008 Mar;130(9):2718–9.

114. Lenhert S, Mirkin CA, Fuchs H. In situ lipid dip-pen nanolithography under water. Scanning. 2010;32:15–23.

115. Lenhert S, Brinkmann F, Laue T, Walheim S, Vannahme C, Klinkhammer S, et al. Lipid multilayer gratings. Nature Nanotechnnology. 2010 Feb 28;5(4):275–9.

116. Hirtz M, Corso R, Sekula-Neuner S, Fuchs H. Comparative Height Measurements of Dip-Pen Nanolithography-Produced Lipid Membrane Stacks with Atomic Force, Fluorescence, and Surface-Enhanced Ellipsometric Contrast Microscopy. Langmuir. 2011 Sep 20;27(18):11605–8.

117. Sekula S, Fuchs J, Weg-Remers S, Nagel P, Schuppler S, Fragala J, et al. Multiplexed Lipid Dip-Pen Nanolithography on Subcellular Scales for the Templating of Functional Proteins and Cell Culture. Small. 2008 Oct;4(10):1785–93.

118. Nissen J, Gritsch S, Wiegand G, Rädler JO. Wetting of phospholipid membranes on hydrophilic surfaces-Concepts towards self-healing membranes. The European Physical Journal B-Condensed Matter and Complex Systems. Springer; 1999;10(2):335–44.

119. Sanii B, Parikh AN. Surface-energy dependent spreading of lipid monolayers and bilayers. Soft Matter. 2007;3(8):974–7.

120. Rädler J, Strey H, Sackmann E. Phenomenology and kinetics of lipid bilayer spreading on hydrophilic surfaces. Langmuir. 1995;11(11):4539–48.

121. May S. A molecular model for the line tension of lipid membranes. The European Physical Journal E. 2000;3(1):37–44.

122. Chernomordik LV, Kozlov MM. Protein-Lipid Interplay in Fusion and Fission of Biological Membranes. Annual Reviews in Biochemistry. 2003 Jun;72(1):175–207.

123. Lipowsky R, Seifert U. Adhesion of Vesicles and Membranes. Molecular Crystals and Liquid Crystals. 1991 Jul;202(1):17–25.

124. Reviakine I, Brisson A. Formation of Supported Phospholipid Bilayers from Unilamellar Vesicles Investigated by Atomic Force Microscopy. Langmuir. 2000 Feb;16(4):1806–15.

125. Portet T, Dimova R. A New Method for Measuring Edge Tensions and Stability of Lipid Bilayers:Effect of Membrane Composition. Biophysical Journal. 2010 Nov 17;99(10):3264–73.

126. West A, Ma K, Chung JL, Kindt JT. Simulation Studies of Structure and Edge Tension of Lipid Bilayer Edges: Effects of Tail Structure and Force-Field. Journal of Physical Chemistry A. 2013 Aug 15;117(32):7114–23.

127. Jiang FY, Bouret Y, Kindt JT. Molecular Dynamics Simulations of the Lipid Bilayer Edge. Biophysical Journal. 2004 Jul;87(1):182–92.

128. Smith AM, Vinchurkar M, Gronbech-Jensen N, Parikh AN. Order at the Edge of the Bilayer: Membrane Remodeling at the Edge of a Planar Supported Bilayer Is Accompanied by a Localized Phase Change. Journal of The American Chemical Society. 2010 Jul 14;132(27):9320–7.

129. Hughes T, Strongin B, Gao FP, Vijayvergiya V, Busath DD, Davis RC. AFM Visualization of Mobile Influenza A M2 Molecules in Planar Bilayers. Biophysical Journal. 2004 Jul;87(1):311–22.

130. Casuso I, Khao J, Chami M, Paul-Gilloteaux P, Husain M, Duneau J-P, et al. Characterization of the motion of membraneproteins using high-speed atomic force microscopy. Nature Nanotechnology. 2012 Jul 24;1–5.

131. Veatch SL, Polozov IV, Gawrisch K, Keller SL. Liquid Domains in Vesicles Investigated by NMR and Fluorescence Microscopy. Biophysical Journal. 2004 May;86(5):2910–22.

132. Salditt T. Thermal fluctuations and stability of solid-supported lipid membranes. Journal of Physics Condensed Matter. 2005 Jan 29;17(6):R287–R314.

133. Veatch SL, Gawrisch K, Keller SL. Closed-Loop Miscibility Gap and Quantitative Tie-Lines in Ternary Membranes Containing Diphytanoyl PC. Biophysical Journal. 2006 Jun;90(12):4428–36.

134. de Almeida RFM, Loura LMS, Fedorov A, Prieto M. Lipid Rafts have Different Sizes Depending on Membrane Composition: A Time-resolved Fluorescence Resonance Energy Transfer Study. Journal of Molecular Biology. 2005 Mar;346(4):1109–20.

135. Connell SD, Smith DA. The atomic force microscope as a tool for studying phase separation in lipid membranes (Review). Molecular Membrane Biology. 2006 Jan;23(1):17–28.

136. Das C, Sheikh KH, Olmsted PD, Connell SD. Phys. Rev. E 82, 041920 (2010) - Nanoscale mechanical probing of supported lipid bilayers with atomic force microscopy. Physical Review E. 2010.

137. Tristram-Nagle S, Nagle JF. Lipid bilayers: thermodynamics, structure, fluctuations, and interactions. Chemistry and Physics of Lipids. 2004 Jan;127(1):3–14.

138. Maulik PR, Shipley GG. N-Palmitoyl Sphingomyelin Bilayers: Structure and Interactions with Cholesterol and Dipalmitoylphosphatidylcholine. Biochemistry. 1996 Jan;35(24):8025–34.

139. Mintzer EA, Waarts BL, Wilschut J, Bittman R. Behavior of a photoactivatable analog of cholesterol, 6-photocholesterol, in model membranes. FEBS Letters. 2002.

140. Radhakrishnan A, McConnell HM. Critical points in charged membranes containing cholesterol. Proceedings of the National Academy of Sciences. 2002 Oct 4;99(21):13391–6.

141. Yuan C, Furlong J, Burgos P, Johnston LJ. The size of lipid rafts: an atomic force microscopy study of ganglioside GM1 domains in sphingomyelin/DOPC/cholesterol membranes. Biophysical Journal. 2002;82(5);2526-2535.

142. Radhakrishnan A, McConnell HM. Condensed Complexes of Cholesterol and Phospholipids. Biophysical Journal. 1999;77(3), 1507-1517.

143. Lee DW, Min Y, Dhar P, Ramachandran A, Israelachvili JN, Zasadzinski JA. Relating domain size distribution to line tension and molecular dipole density in model cytoplasmic myelin lipid monolayers. Proceedings of the National Academy of Sciences. 2011 Jun 7;108(23):9425–30.

144. Haataja M. Critical dynamics in multicomponent lipid membranes. Physical Review E. 2009 Aug;80(2):020902.

145. Han T, Haataja M. Comprehensive analysis of compositional interface fluctuations in planar lipid bilayer membranes. Physical Review E. 2011 Nov;84(5):051903.

146. Fritzsching KJ, Kim J, Holland GP. Biochimica et Biophysica Acta. BBA - Biomembranes. Elsevier B.V; 2013 Jul 31;1828(8):1889–98.

147. Onsager L. Crystal statistics. I. A two-dimensional model with an order-disorder transition. Physical Review. 1944;65(3-4);117.

148. Kusumi A, Honda IK, Suzuki K. Molecular Dynamics and Interactions for Creation of Stimulation-Induced Stabilized Rafts from Small Unstable Steady-State Rafts. Traffic. 2004;5(4);213-230.

150. Brameshuber M, Weghuber J, Ruprecht V, Gombos I, Horvath I, Vigh L, et al. Imaging of Mobile Long-lived Nanoplatforms in the Live Cell Plasma Membrane. Journal of Biological Chemistry. 2010 Dec 24;285(53):41765–71.

151. Schreier H, Moran P, Caras IW. Targeting of liposomes to cells expressing CD4 using glycosylphosphatidylinositol-anchored gp120. Influence of liposome composition on intracellular trafficking. Journal of Biological Chemistry. 1994. 269(12), 9090-9098.

152. de Planque MRR, Killian JA. Protein–lipid interactions studied with designed transmembrane peptides: role of hydrophobic matching and interfacial anchoring (Review). Molecular Membrane Biology. 2003 Jan;20(4):271–84.

153. Hutchison JB, Weis RM, Dinsmore AD. Change of Line Tension in Phase-Separated Vesicles upon Protein Binding. Langmuir. 2012 Mar 20;28(11):5176–81.

154. Alessandrini A, Facci P. Unraveling lipid/protein interaction in model lipid bilayers by Atomic Force Microscopy. Pellequer J-L, Parot P, editors. Journal of Molecular Recognition. 2011 Apr 1;24(3):387–96.

155. Seeger HM, Bortolotti CA, Alessandrini A, Facci P. Phase-Transition-Induced Protein Redistribution in Lipid Bilayers. Journal of Physical Chemistry B. 2009 Dec 31;113(52):16654–9.

156. Schram V, Thompson TE. Influence of the intrinsic membrane protein bacteriorhodopsin on gel-phase domain topology in two-component phase-separated bilayers. Biophysical Journal. 1997 May;72(5):2217–25.

157. Ritchie K, Iino R, Fujiwara T. The fence and picket structure of the plasma membrane of live cells as revealed by single molecule techniques (Review). Membrane Biology. 2003;20(1), 13-18.

158. Murase K, Fujiwara T, Umemura Y, Suzuki K, Iino R, Yamashita H, et al. Ultrafine Membrane Compartments for Molecular Diffusion as Revealed by Single Molecule Techniques. Biophysical Journal. 2004 Jun 1;86(6):4075–93.

159. Shi D, Somlyo AV, Somlyo AP, Shao Z. Visualizing filamentous actin on lipid bilayers by atomic force microscopy in solution. Journal of microscopy. 2001;201(3), 377-382

160. Yamamoto D, Nagura N, Omote S, Taniguchi M, Ando T. Streptavidin 2D Crystal Substrates for Visualizing Biomolecular Processes by Atomic Force Microscopy. Biophysical Journal. 2009 Oct;97(8):2358–67.

161. Bosk S, Braunger JA, Gerke V, Steinem C. Activation of F-Actin Binding Capacity of Ezrin: Synergism of PIP2 Interaction and Phosphorylation. Biophysical Journal. 2011 Apr;100(7):1708–17.

162. Kheya Sengupta, Laurent Limozin, Matthias Tristl, Ilka Haase, Markus Fischer A, Sackmann E. Coupling Artificial Actin Cortices to Biofunctionalized Lipid Monolayers. Langmuir. 2006;22(13):5776–85.

163. Pontani L-L, van der Gucht J, Salbreux G, Heuvingh J, Joanny J-F, Sykes C. Reconstitution of an Actin Cortex Inside a Liposome. Biophysical Journal. 2009 Jan 7;96(1):192–8.

164. Renault A, Lenne P-F, Zakri C, Aradian A, Vénien-Bryan C, Amblard F. Surface-Induced Polymerization of Actin. Biophysical Journal. 1999 Mar;76(3):1580–90.

165. Laliberte A, Gicquaud C. Polymerization of actin by positively charged liposomes. The Journal of Cell Biology. Rockefeller Univ Press; 1988;106(4):1221–7.

166. Wong G, Tang JX, Lin A, Li Y, Janmey PA. Hierarchical Self-Assembly of F-Actin and Cationic Lipid Complexes: Stacked Three-Layer Tubule Networks. Science. 2000 Jun 16;288(5473):2035–9.

167. Henry E, Dif A, Schmutz M, Legoff L, Amblard F, Marchi-Artzner V, et al. Crystallization of Fluorescent Quantum Dots within a Three-Dimensional Bio-Organic Template of Actin Filaments and Lipid Membranes. Nano Letters; 2011 Dec 14;11(12):5443–8.

168. Kouyam T, Mlihash K. Fluorimetry Study of N-(1-Pyrenyl)iodoacetamide-Labelled F-Actin. European Journal of Biochemistry. 2005 Mar 3;114(1):33–8.

169. Kuhn JR, Pollard TD. Real-Time Measurements of Actin Filament Polymerization by Total Internal Reflection Fluorescence Microscopy. Biophysical Journal. 2005 Feb;88(2):1387–402.

170. Lehto T, Miaczynska M, Zerial M, Müller DJ, Severin F. Observing the growth of individual actin filaments in cell extracts by time-lapse atomic force microscopy. FEBS Letters. 2003 Sep;551(1-3):25–8.

171. Koynova R, MacDonald RC. Lipid transfer between cationic vesicles and lipid - DNA lipoplexes: Effect of serum. Biochimica et Biophysica Acta BBA - Biomembranes. 2005;1714(1):63–70.

172. Nagle JF, Tristram-Nagle S. Structure of lipid bilayers. Biochimica et Biophysica Acta (BBA) - Reviews on Biomembranes. 2000 Nov;1469(3):159–95.

173. Reffay M, Gambin Y, Benabdelhak H, Phan G, Taulier N, Ducruix A, et al. Tracking Membrane Protein Association in Model Membranes. PLoS ONE. Public Library of Science; 2009 Apr 1;4(4):e5035.

174. Brown KL, Conboy JC. Electrostatic Induction of Lipid Asymmetry. Journal of The American Chemical Society; 2011 Jun 15;133(23):8794-7.

175. Taylor KA, Taylor DW. Formation of 2-D paracrystals of F-actin on phospholipid layers mixed with quarternary ammonium surfactants. Journal of Structural Biology. 1992 Mar;108(2):140–7.

176. Sept D, McCammon JA. Thermodynamics and Kinetics of Actin Filament Nucleation. Biophysical Journal. 2001 Aug;81(2):667–74.

177. Callan-Jones A, Pelcovits R, Slavin V, Zhang S, Laidlaw D, Loriot G. Simulation and visualization of topological defects in nematic liquid crystals. Physical Review E. 2006 Dec;74(6):061701.

178. Holmes KC, Popp D, Gebhard W, Kabsch W. Atomic model of the actin filament. Nature. 1990 Sep 6;347(6288):44–9.

179. Janmey PA. The Polyelectrolyte Nature of F-actin and the Mechanism of Actin Bundle Formation. Journal of Biological Chemistry. 1996 Apr 12;271(15):8556–63.

180. Richter RP, Maury N, Brisson AR. On the Effect of the Solid Support on the Interleaflet Distribution of Lipids in Supported Lipid Bilayers. Langmuir. 2005 Jan;21(1):299–304.

181. Pan J, Tristram-Nagle S, Kučerka N, Nagle JF. Temperature Dependence of Structure, Bending Rigidity, and Bilayer Interactions of Dioleoylphosphatidylcholine Bilayers. Biophysical Journal. 2008 Jan;94(1):117–24.

182. Andrianantoandro E, Blanchoin L, Sept D, McCammon JA, Pollard TD. Kinetic mechanism of end-to-end annealing of actin filaments. Journal of Molecular Biology. 2001 Sep;312(4):721–30.

183. Popp D, Yamamoto A, Maéda Y. Crowded Surfaces Change Annealing Dynamics of Actin Filaments. Journal of Molecular Biology. 2007 Apr;368(2):365–74.

184. Mogilner A, Oster G. Cell motility driven by actin polymerization. Biophysical Journal. 1996 Dec;71(6):3030–45.

185. Pollard TD, Bhandari D, Maupin P, Wachsstock D, Weeds AG, Zot HG. Direct visualization by electron microscopy of the weakly bound intermediates in the actomyosin adenosine triphosphatase cycle. Biophysical Journal. 1993 Feb;64(2):454–71.

186. Wang F, Sampogna RV, Ware BR. pH dependence of actin self-assembly. Biophysical Journal. 1989 Feb 1;55(2):293–8.

187. Crevenna AH, Naredi-Rainer N, Schonichen A, Dzubiella J, Barber DL, Lamb DC, et al. Electrostatics control actin filament nucleation and elongation kinetics. Journal of Biological Chemistry. 2013 Mar 13.

188. Tanford C, Kirkwood JG. Theory of Protein Titration Curves. I. General Equations for Imprnetrable Spheres. Journal of The American Chemical Society. 1957 Oct 20;79(20):5333–9.

189. Tanford C, Roxby R. Interpretation of protein titration curves. Application to lysozyme. Biochemistry. 1972 May;11(11):2192–8.

190. Shire SJ, Hanania GIH, Gurd FRN. Electrostatic effects in myoglobin. Hydrogen ion equilibriums in sperm whale ferrimyoglobin. Biochemistry. 1974 Jul;13(14):2967–74.

191. Matthew JB. Electrostatic Effects in Proteins. Annual Review of Biophysics and Biophysical Chemistry. 1985 Jun;14(1):387–417.

192. Tamura A, Privalov PL. The entropy cost of protein association. Journal of Molecular Biology. 1997 Nov;273(5):1048–60.

193. Reviakine I, Simon A, Brisson A. Effect of Ca 2+on the Morphology of Mixed DPPC−DOPS Supported Phospholipid Bilayers. Langmuir. 2000 Feb;16(4):1473–7.

194. Hinderliter A, Almeida PFF, Creutz CE, Biltonen RL. Domain Formation in a Fluid Mixed Lipid Bilayer Modulated through Binding of the C2 Protein Motif. Biochemistry. 2001 Apr;40(13):4181–91.

195. Shimokawa N, Hishida M, Seto H, Yoshikawa K. Phase separation of a mixture of charged and neutral lipids on a giant vesicle induced by small cations. Chemical Physics Letters. 2010 Aug;496(1-3):59–63.

196. Borden MA, Longo ML. Dissolution Behavior of Lipid Monolayer-Coated, Air-Filled Microbubbles: Effect of Lipid Hydrophobic Chain Length. Langmuir. 2002 Nov;18(24):9225–33.

197. Mantelli S, Muller P, Harlepp S, Maaloum M. Conformational analysis and estimation of the persistence length of DNA using atomic force microscopy in solution. Soft Matter. 2011;7(7):3412–6.

198. Isambert H, Venier P, Maggs AC, Fattoum A, Kassab R, Pantaloni D, et al. Flexibility of actin filaments derived from thermal fluctuations. Effect of bound nucleotide, phalloidin, and muscle regulatory proteins. Journal of Biological Chemistry. 1995;270(19):11437–44.

199. Lorenz M, Popp D, Holmes KC. Refinement of the F-Actin Model against X-ray Fiber Diffraction Data by the Use of a Directed Mutation Algorithm. Journal of Molecular Biology. 1993 Dec;234(3):826–36.

200. Kabalnov A, Klein D, Pelura T, Schutt E, Weers J. Dissolution of multicomponent microbubbles in the bloodstream: 1. theory. Ultrasound in Medicine & Biology. 1998 Jun;24(5):739–49.

201. Epstein PS, Plesset MS. On the Stability of Gas Bubbles in Liquid-Gas Solutions. Journal of Chemical Physics. 1950;18(11):1505.

202. Grant CA, McKendry JE, Evans SD. Temperature dependent stiffness and visco-elastic behaviour of lipid coated microbubbles using atomic force microscopy. Soft Matter. 2012;8(5):1321–6.

203. Buchner Santos E, Morris JK, Glynos E, Sboros V, Koutsos V. Nanomechanical Properties of Phospholipid Microbubbles. Langmuir. 2012 Apr 3;28(13):5753–60.

204. Helfer E, Harlepp S, Bourdieu L, Robert J, MacKintosh F, Chatenay D. Viscoelastic properties of actin-coated membranes. Physical Review E. 2001 Jan;63(2):021904.

205. Klymenko O, Wiltowska-Zuber J, Lekka M, Kwiatek WM. Energy dissipation in the AFM elasticity measurements. Acta Physica Polonica-Series A General Physics. 2009;115(2):548.

206. Abou-Saleh RH, Peyman S, Critchley K, Evans SD, Thomson NH. Nanomechanics of lipid encapsulated microbubbles with functional coatings. Langmuir. 2013 Feb; 29(12), 4096-4103.

Appendix A

Publications Resulting From This Thesis

1. Heath, George R., Johannes Roth, Simon DA Connell, and Stephen D. Evans. "Diffusion in Low Dimensional Lipid Membranes." *Nano letters* (2014).
2. Connell, Simon D., George Heath, Peter D. Olmsted, and Anastasia Kisil. "Critical point fluctuations in supported lipid membranes." *Faraday Discussions* 161 (2013): 91-111.
3. Heath, George R., Benjamin RG Johnson, Peter D. Olmsted, Simon D. Connell, and Stephen D. Evans. "Actin Assembly at Model-Supported Lipid Bilayers." *Biophysical journal* 105, no. 10 (2013): 2355-2365.
4. Heath, George R., Radwa H. Abou-Saleh, Sally A. Peyman, Benjamin RG Johnson, Simon D. Connell, and Stephen D. Evans. "Self-assembly of actin scaffolds on lipid microbubbles." *Soft Matter* (2014).